

ISSN:1305-130X

e-ISSN:1305-1385

# CELAL BAYAR UNIVERSITY JOURNAL OF SCIENCE



Manisa Celal Bayar Üniversitesi  
Fen Bilimleri Dergisi

2025

VOLUME:21

ISSUE:2



# Journal of Science

Volume: 21, Issue: 2, Year: 2025

## Contact

Manisa Celal Bayar University

The Graduate School

Campus of Şehit Prof Dr İlhan Varank 45140 Yunussemre – MANİSA, TÜRKİYE

Tel: (00 90) 236 201 27 05

Fax: (00 90) 236 241 21 49

E-mail: [lee.fendergi@cbu.edu.tr](mailto:lee.fendergi@cbu.edu.tr)

Web: <https://dergipark.org.tr/tr/pub/cbayarfbe>

“CBU Journal of Science is indexed by ULAKBIM-TUBITAK TR-DIZIN”



ISSN 1305-130X

E-ISSN 1305-1385

CBUJOS is published quarterly at The Graduate School of Manisa Celal Bayar University

“CBU Journal of Science is a refereed scientific journal”



## Celal Bayar University Journal of Science

**Owner:** Manisa Celal Bayar University, The Graduate School

**Editor:** Assoc. Prof. Dr. İlker Çetin KESKİN

### Technical Editors

Res. Assist. Dr. Musa OVALI

Res. Assist. Gencay TEPE

### Layout Editor

Assist. Prof. Dr. Mehmet Fahrettin ZEYBEK

### Subject Editors

Prof. Dr. Ali KONURALP, Manisa Celal Bayar University, Mathematics

Prof. Dr. Ayşe DİNÇER, Manisa Celal Bayar University, Chemistry

Prof. Dr. Kamil ŞİRİN, Manisa Celal Bayar University, Chemistry

Prof. Dr. Mehmet ÇEVİK, İzmir Katip Celebi University, Mechanical Engineering

Prof. Dr. Kamuran AKTAŞ, Manisa Celal Bayar University, Biology

Prof. Dr. Sezai TAŞKIN, Manisa Celal Bayar University, Electrical and Electronics Engineering

Prof. Dr. Yasemin PARLAK, Manisa Celal Bayar University, Nuclear Medicine

Assoc. Prof. Dr. Emriye AY, Manisa Celal Bayar University, Chemistry

Assoc. Prof. Dr. İlker Çetin KESKİN, Manisa Celal Bayar University, Physics

Assoc. Prof. Dr. Mustafa Erkan TURAN, Manisa Celal Bayar University, Civil Engineering

Assoc. Prof. Dr. Pelin AKTAŞ, Manisa Celal Bayar University, Chemistry

Assoc. Prof. Dr. Serhat ARAS, University of Health Science, Medical Physics

### International Scientific Advisory Board

Prof. Dr. Arianit REKA; State University of Tetova, Macedonia

Prof. Dr. Tomasz NIEMIEC; Warsaw University of Life Sciences, Poland

Prof. Dr. Alyani ISMAIL; Universiti Putra, Malaysia

Prof. Dr. Iuliana APRODU; Dunarea de Jos University, Romania

Assoc. Prof. Can BAYRAM; University of Illinois, USA

Assoc. Prof. Dr. Johanan Christian PRASANN; Madras Christian College, South India

Assoc. Prof. Dr. Nouredine ISSAOU; Université de Monastir, Tunisie.

Assoc. Dr. Edward Albert UECKERMANN; North-West University, South Africa

Assoc. Dr. Zhi-Qiang ZHANG; The University of Auckland, Holland

Assist. Prof. Dr. Young Ki KIM; Pohang University of Science and Technology, South Korea

Assist. Prof. Dr. Mona MIRHEYDARI; Rutgers University, USA

Assist. Prof. Dr. Donatella ALBANESE; Università Degli Studi Di Salerno, Italy

Assist. Prof. Dr. Jinghua JIANG; The University of Memphis, USA

Assist. Prof. Dr. Jens OLDELAND; University of Hamburg, Germany

Dr. Cheng CHENG; Apple Inc., USA

Dr. Sajedeh AFGHAH; Microsoft Corporation, USA

Dr. Jinghua JIANG; The University of Memphis

### National Scientific Advisory Board

Prof. Dr. Mustafa Ersöz; Selçuk University

Prof. Dr. Oğuz Gürsoy; Mehmet Akif University

Prof. Dr. Mehmet Çevik; İzmir Katip Çelebi University

Prof. Dr. Sezgin Çelik; Yıldız Teknik University

Prof. Dr. Osman Dayan; Çanakkale Onsekiz Mart University

Prof. Dr. Serdar İplikçi; Pamukkale University

Prof. Dr. Yasin Üst; Yıldız Teknik University

Prof. Dr. Mahmut Kuş; Konya Teknik University

Prof. Dr. Ertunç Gündüz; Hacettepe University

Prof. Dr. Tülin Aydemir; Manisa Celal Bayar University

Prof. Dr. Sezai Taşkın; Manisa Celal Bayar University

Prof. Dr. Fatma Şaşmaz Ören; Manisa Celal Bayar University

Prof. Dr. Fatih Selimefendioğlu; Manisa Celal Bayar University

Prof. Dr. Osman Çulha; Manisa Celal Bayar University

Prof. Dr. Ali Konuralp; Manisa Celal Bayar University

Prof. Dr. Erol Akpınar; Abant İzzet Baysal University

Prof. Dr. Ali Demir; Manisa Celal Bayar University

Prof. Dr. Serap Derman; Yıldız Teknik University

Prof. Dr. Özlem Çağındı; Manisa Celal Bayar University

Assoc. Prof. Dr. Fatih Doğan; Çanakkale Onsekiz Mart University

Assoc. Prof. Dr. Yeliz Yıldırım; Ege University

Assoc. Prof. Dr. Hayati Mamur; Manisa Celal Bayar University

Assoc. Prof. Dr. Mehmet Söylemez; Adıyaman University

Assoc. Prof. Dr. Nil Mansuroğlu; Ahi Evran University

Assist. Prof. Dr. Zeynep Çipiloğlu Yıldız; Manisa Celal Bayar University



---

## **CBU Journal of Science**

Celal Bayar University Journal of Science (CBUJOS) covers scientific studies in the fields of Engineering and Science and publishes accounts of original research articles concerned with all aspects of experimental and theoretical studies. CBU Journal of Science is a refereed scientific journal published four times annually (March, June, September and December) by The Graduate School of Manisa Celal Bayar University. CBU Journal of Science considers the original research articles written in English for evaluation.

CBU Journal of Science is indexed by TUBİTAK ULAKBİM TR-DİZİN, and also is included in DOAJ, Cite Factor, Journal TOCS, Advanced Science Index and OAJI databases. Digital Object Identifier (DOI) number will be assigned for all the articles being published in CBU Journal of Science.

Instructions for Authors and Article Template can be found on the page of Celal Bayar University Journal of Science DergiPark (<https://dergipark.org.tr/tr/pub/cbayarfbe>)





**Vol: 21, Issue: 2, Year: 2025**

**Contents**

**Research Article**

**Pages**

- 1. Adsorption of Ecotoxicological Congo Red Dye onto Kaolin Clay** 1-10  
DOI: 10.18466/cbayarfbe.1554719  
Talip Turna\*
- 2. Photophysical and Photochemical Properties of New Coumarin-Substituted Zinc and Indium Phthalocyanines for Photodynamic Therapy** 11-18  
DOI:10.18466/cbayarfbe.1581909  
Zehra Kazancıçok, Mustafa Bulut, Ümit Salan\*
- 3. A New Record of Genus Stigmaeus (Acariformes: Stigmaeidae) from Türkiye** 19-23  
DOI:10.18466/cbayarfbe.1582494  
Mustafa Akyol\*
- 4. Differential Equations for Spacelike Curves According to Light-Cone Frame in  $L_0^3$**  24-27  
DOI: 10.18466/cbayarfbe.1538669  
Tanju Kahraman\*
- 5. An Application on Enterprise Resource Planning (ERP) Selection with Multi-Criteria Decision-Making Methods** 28-34  
DOI:10.18466/cbayarfbe.1513901  
Huriye Akpınar\*
- 6. A Study on Topology Optimization of Landing Gear Parts** 35-46  
DOI: 10.18466/cbayarfbe.1539030  
Sait Cumhur Piçak\*, Mehmet Yahşi, Erol Gültekin
- 7. Hybrid Renewable Energy System Proposal: Offshore Wind and PV Farm with Optimally Designed LCL Filter in Datça, Aegean Sea, Turkey** 47-63  
DOI: 10.18466/cbayarfbe.1555073  
Alp Karadeniz\*
- 8. On Ideal Convergence for Triple Sequences on L-Fuzzy Normed Space** 64-71  
DOI: 10.18466/cbayarfbe.1539485  
Reha Yapalı\*
- 9. Investigation of Dielectric Anisotropy and Electrical Modulus-Impedance Properties of PCBM/E7 Composite for Organic Electronic Devices Applications** 72-79  
DOI: 10.18466/cbayarfbe.1562667  
Ahmet Demir\*, Ahmad Badreddin Musatat, Şule Zeynep Kip
- 10. A Morphological, Anatomical and Karyological Study on Hieracium pannosum BOISS. (Asteraceae)** 80-88  
DOI: 10.18466/cbayarfbe.1565400  
Hakan Sepet\*, Bahattin Bozdağ, Canan Özdemir
- 11. A New Distribution Area of the Endangered Endemic Linum vuralianum (Linaceae) in Türkiye** 89-94  
DOI: 10.18466/cbayarfbe.1567122  
Dilek Oskay\*
- 12. Anderson Type Polyoxometalates Containing Vitamin B1** 95-99  
DOI: 10.18466/cbayarfbe.1570842  
Hülya Avcı Özbek\*
- 13. Oxidation of Benzyl Alcohols by Monomeric Iron Phthalocyanine Complexes: Substituents' Effect on Their Catalytic Performance** 100-104  
DOI: 10.18466/cbayarfbe.1570991  
Zeynel Şahin\*

- 
- 14. Evaluation of the Altmetric Attention Score of Recent Hazard Food-Marker: Advanced Glycation End Products** 105-117  
DOI: 10.18466/cbayarfbe.1580554  
Büşra Yusufoğlu\*
- 15. Effects of 2,2-Dichloroacetamide Additive on Perovskite Solar Cells Efficiency** 118-124  
DOI: 10.18466/cbayarfbe.1582175  
Adem Mutlu\*, Sevdije Başak Turgut
- 16. Diagnostic Potential of miR-551b-3p in Lung Cancer: In Vitro and In Silico Experiments** 125-133  
DOI: 10.18466/cbayarfbe.1582834  
Esen Çakmak\*, İbrahim Seyfettin Çelik
- 17. Co-pyrolisis of Different Coal Types with Biomass: Performance and Efficiency Evaluation by Thermogravimetric Analysis** 134-146  
DOI: 10.18466/cbayarfbe.1659482  
Veysi Kamar, Pınar Acar Bozkurt\*
- 18. Tribonacci numbers as sum or difference of powers of 2** 147-151  
DOI: 10.18466/cbayarfbe.1528991  
Fatih Erduvan\*
- 19. Binary Classification of Alzheimer's Disease Using Siamese Neural Network for Early Stage Diagnosis** 152-158  
DOI: 10.18466/cbayarfbe.1529546  
Ruken Tekin\*, Tuğba Özge Onur
- 20. Four Dimensional Matrix Operators on the Double Series Spaces of Weighted Means** 159-168  
DOI: 10.18466/cbayarfbe.1479195  
Feride Çalışır, Canan Hazar Gulec\*

## Adsorption of Ecotoxicological Congo Red Dye onto Kaolin Clay

Talip Turna<sup>1\*</sup> 

<sup>1\*</sup> Department of Parks and Garden Plants-Diyarbakır Vocational School of Higher Education, Dicle University, Diyarbakır, Türkiye

\* [talipturna@gmail.com](mailto:talipturna@gmail.com)

\* Orcid No: 0000-0001-6318-7245

Received: September 23, 2024

Accepted: December 19, 2024

DOI: 10.18466/cbayarfbe.1554719

### Abstract

This study was conducted to evaluate the adsorption ability of kaolin clay mineral to remove Congo red (CR), an anionic dye with ecotoxicological effects, from aqueous solution. In order to optimize the variables in the adsorption system, pH, adsorbent amount, contact time, and initial CR concentration factors were investigated. Adsorption kinetics and equilibrium isotherm of kaolin clay were investigated using Pseudo first order, Pseudo second order and Intra-Particle Diffusion kinetic equations and Freundlich, Langmuir and Temkin isotherm models. The obtained results were tested with 5 different error functions. Accordingly, it was determined that the adsorption of CR dye onto kaolin clay fit the Freundlich model with an  $R^2$  value of 0.999 and the Pseudo second order model with an  $R^2$  value of 0.999. In addition, the  $q_{max}$  value was calculated as 7.984 mg/g kaolin. For morphological examination, Fourier Transform Infrared Spectroscopy (FTIR) and Scanning Electron Microscopy (SEM) images of raw and CR-loaded kaolin were examined. As a result, it was revealed that kaolin clay can be used as a low-cost alternative for the removal of resistant dyes from wastewater.

**Keywords:** Adsorption, Congo red, Isotherm, Kaolin, Kinetic

### 1. Introduction

The rapid development of the global production printing and dyeing industry in the world has increased the need for different dyes [1]. In industrial production, synthetic dyes are used intensively in sectors such as leather, paper, and textile industries due to their coloring properties [2], [3]. Dye molecules are compounds with complex chemical structures that can transfer their colors by binding to the surfaces or fabrics they affect and are highly resistant to environmental conditions [4]. CR dye, one of the dyes widely used in the dyeing industry, is preferred in various sectors due to its high chromaticity [1]. The textile industry, one of the sectors that uses the most dyes, has an important place in uncontrolled dye discharges into the aquatic ecosystem [5]. According to the World Bank report, approximately 17-20% of water pollution caused by industrial production is caused by the textile sector [6].

When dyes are discharged into the receiving environment in an uncontrolled manner, they remain in the ecosystem for a long time. These discharges are dangerous for flora and fauna, even in low concentrations, and cause significant environmental problems [7], [8]. Dyes that give color to water reduce the clarity and aeration of

water, create negative effects on the photosynthesis system and cause the amount of dissolved oxygen to decrease [9]. Therefore, they must be treated before being discharged into the receiving environment.

Different removal methods are used for CR removal from aquatic environments. Various treatment processes such as ozonation [10] nanoparticles [11], ultrafiltration [12], electrochemical treatment [13], UV degradation [14], aerobic treatment [15] adsorption [16] have been frequently applied for CR removal. Researchers continue to search for cost-effective materials and methods for retaining dyes from wastewater. Among the alternative methods for CR removal, the adsorption process is used intensively due to its simple design and operation, effectiveness, and low cost [17], [18]. A wide variety of adsorbent materials are used in the adsorption process. Kaolin clay is also used effectively as a sorbent in the removal of dyes from wastewater due to its cheap and environmentally friendly nature. Clay materials attract the attention of researchers due to their environmentally friendly nature in the removal of dyes from aquatic environments [19].

In this study, the removal of CR dye from aqueous solutions by kaolin clay in a batch adsorption process was

investigated. In the adsorption studies carried out with kaolin, a natural and easily available material, 3 different kinetic and isotherm models were tested. In addition, FTIR and SEM images of raw and CR-loaded kaolin were examined. The results show that kaolin clay is an environmentally sustainable material for CR removal from aqueous solutions. This fundamental study, which was carried out with kaolin clay, which is quite cheap compared to other commercial adsorbents, will provide researchers with ideas to design a sustainable adsorbent for sectors that use and discharge ecotoxicological paints with high environmental destructive power, such as the textile industry.

## 2. Materials and Methods

### 2.1. Chemicals

All chemicals used in experimental studies are of analytical grade. Powder Congo red ( $C_{32}H_{22}N_6Na_2O_6S_2$ , 696.66 g/mol, Sigma-Aldrich), pellet sodium hydroxide (NaOH, 40.00 g/mol,  $\geq 99.0\%$ , Sigma-Aldrich) and liquid sulfuric acid ( $H_2(SO_4)_3$ , 1.81 g/cm<sup>3</sup>,  $\geq 90-91\%$ , Merck) was used.

### 2.2. Preparation of Kaolin Clay

The kaolin clay used in adsorption studies was ground and then sieved in a sieve with a pore size of 75 microns. Then it was washed with pure water to remove impurities. Then it was dried in an oven at 60°C for 24 hours and stored in a closed container.

### 2.3. Adsorption Studies

Batch adsorption studies were carried out on an orbital shaker with a stirring speed of 250 rpm (Heidolph, Unimax1010, Germany). A stock solution of CR dye with a concentration of 500 mg/L was prepared and a calibration curve was created at a wavelength of 497 nm on a UV-Visible spectrophotometer (Hach DR6000, Germany) by diluting the solution at the required rates [20]. The curve equation was calculated as  $y = 0.0414x + 0.0079$  ( $R^2 = 0.999$ ) and all experimental results were calculated with the help of this equation.

To determine the removal capacity of CR dye and its performance under environmental conditions, pH (3-11), initial kaolin amount, contact time and initial CR concentration were determined and kinetic and isotherm calculations were made according to these values. The obtained results were evaluated using equations 1 and 2.

$$R(\%) = \frac{C_0 - C_e}{C_0} \cdot 100 \quad (1)$$

$$q_e = \frac{(C_0 - C_e) \cdot V}{m} \quad (2)$$

Here, the  $R$  expression expresses the removal efficiency of CR dye in %, while the  $C_0$  and  $C_e$  expressions express the CR concentration in the solution at the beginning and

end of the experiments in mg/L. In addition, the  $q_e$  expression represents the amount of CR dye removed per gram of kaolin in mg (mg/g), the  $V$  expression represents the solution volume in L, and the  $m$  expression represents the amount of kaolin in g.

#### 2.3.1. Adsorption Kinetics

Kinetic studies are carried out to determine the rate at which the adsorbent removes the pollutant and to have an idea about the removal mechanism[21]. In this context, 300 mg of kaolin was added to a 100 mL solution with an initial CR concentration of 3 mg/L at neutral pH and samples were taken at certain times to calculate the CR concentration with the help of the previously obtained calibration curve. The results were examined with the help of Pseudo first order, Pseudo second order and Intra-Particle Diffusion kinetic models Table 1.

**Table 1.** Kinetic Models Used in CR Adsorption on Kaolin Clay.

	Model	Equality	References
Kinetic models	Pseudo-first-order	$q_t = q_e(1 - e^{-k_1 t})$	[22]
	Pseudo-second-order	$q_t = \frac{q_e^2 k_2 t}{1 + q_e k_2 t}$	[22]
	Intra-particle diffusion	$q_t = K_{id} t^{1/2} + C$	[23]

The  $q_t$  expression in the table above represents the amount of CR removed by the cation at a certain time  $t$  (mg/g), and the  $q_e$  expression represents the amount of removal at equilibrium (mg/g). In addition, the  $k_1$ ,  $k_2$ , and  $K_{id}$  expressions represent the constant of each model.

#### 2.3.2. Adsorption Isotherms

A reasonable isotherm modeling performed in adsorption studies provides information on the capacity of a given biosorbent to adsorb a unit mass of a solute under specified operating conditions [23]. In 6 different test tubes with a volume of 10 mL under the same environmental conditions, CR dye was added at concentrations ranging from 6.71 to 217.6 mg/L in the initial CR concentration range and kaolin was added at 1 g/L each. At the end of the period, centrifugation was performed and the CR concentration in the upper phase liquid was read. The obtained results were tested with the isotherm models given in Table 2.

**Table 2.** Isotherm Models Used for CR Adsorption on Kaolin Clay

	Model	Equality	References
Isotherm models	Freundlich	$q_e = K_F C_e^{1/n}$	[24], [25]
	Langmuir	$q_e = \frac{q_{max} K_L C_e}{1 + K_L C_e}$ $R_L = \frac{1}{1 + a_L C_e}$	
	Temkin	$q_e = \frac{B \ln(A_T C_e)}{RT}$ $B = \frac{RT}{b_T}$	

When the table above is examined,  $q_e$  (mg/g) represents the amount of CR adsorbed at equilibrium,  $C_e$  (mg/L) represents the CR concentration at equilibrium, and  $q_{max}$  (mg/g) represents the maximum adsorption capacity.  $K_F$  (mg/g) (L/mg) is the Freundlich constant  $1/n$ ;  $n$  is a dimensionless constant and indicates the adsorption density. The terms  $K_L$  and  $a_L$  are the Langmuir constants.  $R_L$  is the dispersion constant. In addition,  $B$  in the Temkin model represents the model constant,  $b_T$  (J/mol) represents the heat of adsorption,  $T$  (K) represents the temperature, and  $R$  (8.314 J/mol.K) represents the universal gas constant.

### 2.3.3. Error Function Test Describing

Statistical error functions are used to evaluate the fit of isotherm and kinetic equations to experimental equilibrium data during the adsorption process [26]. The error functions used for this purpose are presented in Table 3. A total of five error functions were used, namely, Sum of Square Error (SSE), Average Relative Error (ARE), Hybrid Fractional Error Function (HYBRID), Marquardt's Percentage Standard Deviation (MPSD) and Chi-Square test ( $X^2$ ).

**Table 3.** Error Functions Tests

Error function	Equation	References
SSE	$\sum (q_{e,cal} - q_{e,exp})^2$	[27]
ARE	$\frac{1}{n} \sum_{i=1}^n \left  \frac{q_{e,cal} - q_{e,exp}}{q_{e,exp}} \right $	
HYBRID	$\frac{1}{N - P} \sum \left  \frac{q_{e,exp} - q_{e,cal}}{q_{e,exp}} \right $	
MPSD	$\sqrt{\frac{\sum  (q_{e,exp} - q_{e,cal}) / q_{e,exp} ^2}{N - P}}$	
$X^2$	$\sum \frac{(q_{e,exp} - q_{e,cal})^2}{q_{e,cal}}$	

## 3. Results and Discussion

### 3.1. Material Characterization

#### 3.1.1. SEM Images

Surface morphology was examined before and after CR dye adsorption. Morphological images of raw and CR loaded kaolin clay are presented in Figure 1. According to the images obtained, Figure 1a Surface morphology shows a relatively regular, crystalline structure. The image contains pores among the particles. However, when we look at the image of the CR loaded particles, Figure 1b. The surface is rough and blurred. Further disintegration, irregularity and heterogeneity are seen on the surface. Connecting the dye to the Kaolin surface may have increased roughness by covering the surface. This occupancy and density in the pores may indicate that the adsorption process is successful [28], [29].

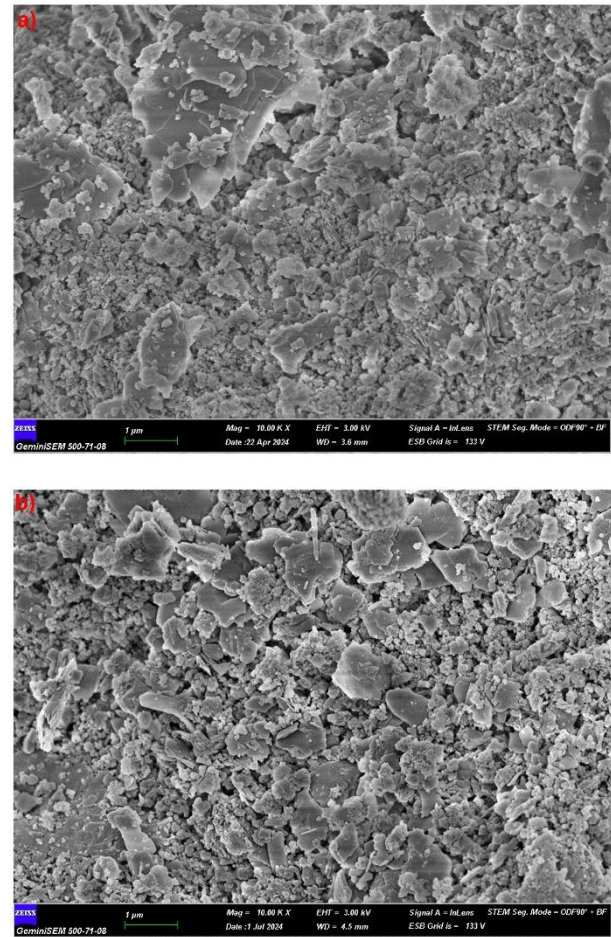


**Figure 1.** SEM images of kaolin clay before and after reaction; a) Raw kaolin clay, b) CR charged.

#### 3.1.2. FTIR

FTIR analysis was performed to determine the adsorption functional group on the kaolin clay surface before and



after CR adsorption. The spectra obtained for raw and CR-loaded kaolin clay are presented in Figure 2.

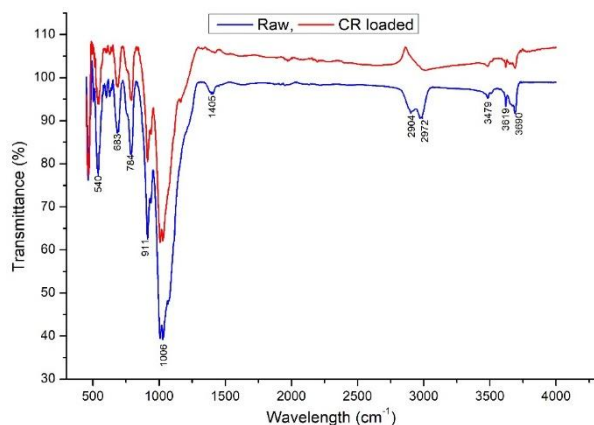


**Figure 2.** FTIR diagram before and after reaction.

The bands between  $3619\text{ cm}^{-1}$ - $3690\text{ cm}^{-1}$  correspond to the OH stretching vibrations of Al-OH groups on the surface and inside the kaolin, respectively. The bands between  $911\text{ cm}^{-1}$ - $1006\text{ cm}^{-1}$  correspond to the Si-O-Si stretching vibrations and silicate groups [26]. The Si-O-Al bond produces a band between  $795\text{ cm}^{-1}$ - $748\text{ cm}^{-1}$ , which is also seen at a wavelength of  $784\text{ cm}^{-1}$  in this diagram [29]. As seen in Figure 2, bending, shifting or intensity changes at points such as  $911\text{ cm}^{-1}$ ,  $1006\text{ cm}^{-1}$  and  $1405\text{ cm}^{-1}$  indicate that the adsorbent surface is loaded after adsorption by the adsorbate molecules [30]. The adsorption of CR onto kaolin caused obvious changes, especially in the region of hydroxyl groups (O-H) and C-H stretching vibrations.

### 3.2. Effect of Environmental Factors

To optimize the variables in the adsorption system, pH, adsorbent amount, contact time and initial CR dye concentration factors were investigated.

#### 3.2.1. Effect of pH

To determine the effect of pH on CR dye removal, kaolin was added to 5 different test tubes with a volume of 10 mL with an initial CR concentration of 3 mg/L at a concentration of 1 g/L and the initial pH values were adjusted between 3-11. At the end of the centrifugation process in the time unit, dye concentrations were measured. The results obtained are presented in Figure 3a. Accordingly, while the  $q_e$  value was calculated as 1.4 mg/g at pH 3, this value was calculated as 1.77 mg/g at pH 5. A decrease in the  $q_e$  value was observed with the increase in pH. Therefore, since the highest efficiency was obtained at pH 5, the optimum pH value was determined as 5. When similar studies were examined, it was reported that high removal efficiencies were obtained for CR dye between pH 4-6 [31].

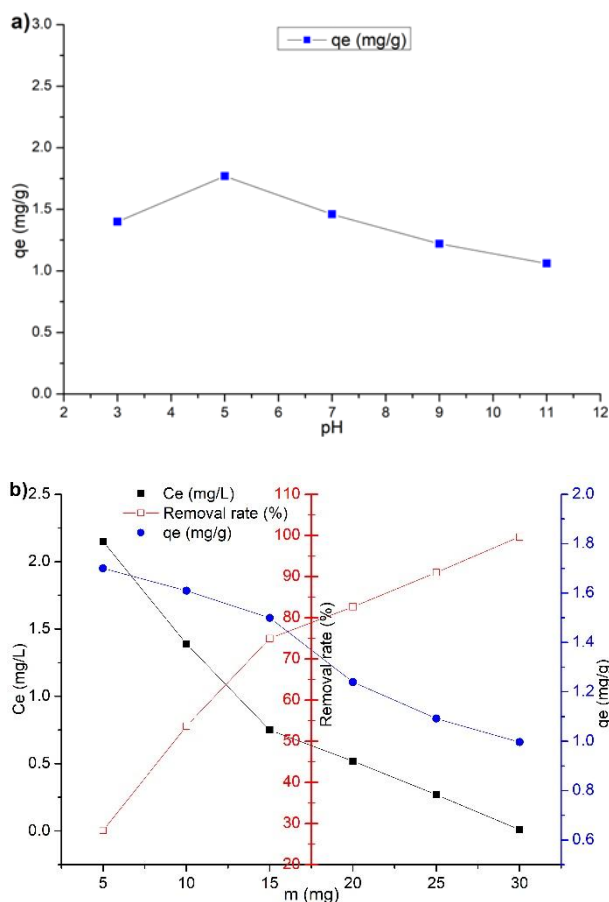


**Figure 3.** a) Effect of pH (V: 10 mL,  $C_0$ : 3.0 g/L, m: 1.0 g/L, time: 30 min, T: 25°C, stirring 250 rpm), b) Effect of adsorbent amount (V: 10 mL,  $C_0$ : 3.0 g/L, time: 30 min, pH 5.0, T: 25°C, stirring 250 rpm).

#### 3.2.2. Effect of Adsorbent Amount

In the experiments carried out under the same environmental conditions, kaolin was added in amounts ranging from 5 to 30 mg to 6 different test tubes with a pH of 5 and an initial CR concentration of 3 mg/L and a volume of 10 mL, and at the end of the period, centrifugation was performed, and CR dye measurements were made in the upper phase liquid. The results are presented in Figure 3b. According to the figure, while the removal efficiency in the presence of 5 mg kaolin was 28.33%, when the amount of kaolin was increased to 10 mg, the efficiency increased by 53.67%. The efficiency increased gradually with the increase in the amount of kaolin and finally, when the value of 30 mg was reached, the efficiency exceeded 99%. Accordingly, the amount of 30 mg kaolin was accepted as optimum. When the literature was examined, it was stated that there was a gradual increase in the removal efficiency with the increase in the amount of adsorbent in the adsorption of CR dye [32]

### 3.2.3. Effect of Contact Time

The contact time has an important effect on the adsorption process. A good contact time ensures that the adsorbent is applicable in the treatment of polluted water[33]. In this context, 300 mg of kaolin was added to a 100 mL volume solution with a 3 mg/L CR concentration and samples were taken at certain times to measure the concentration of CR dye. The results obtained are presented in Figure 4a. Accordingly, while the removal efficiency was calculated as 60% in the first 40 seconds at the beginning of the experiment, the efficiency reached 69% at the end of the 1st minute. The efficiency exceeded 90% at the end of the 4th minute and finally, the efficiency exceeded 99% at the end of the 25th minute. On the other hand, while the  $q_e$  value was 5.40 mg/g at the 40th second, it reached 6.21 mg/g at the 1st minute and was calculated as 8.13 mg/g at the 4th minute. Similarly, it has been reported in the literature that while high removal efficiency was achieved in short contact time, the efficiency increase continued with the extension of the time, but the increase rate decreased [34].

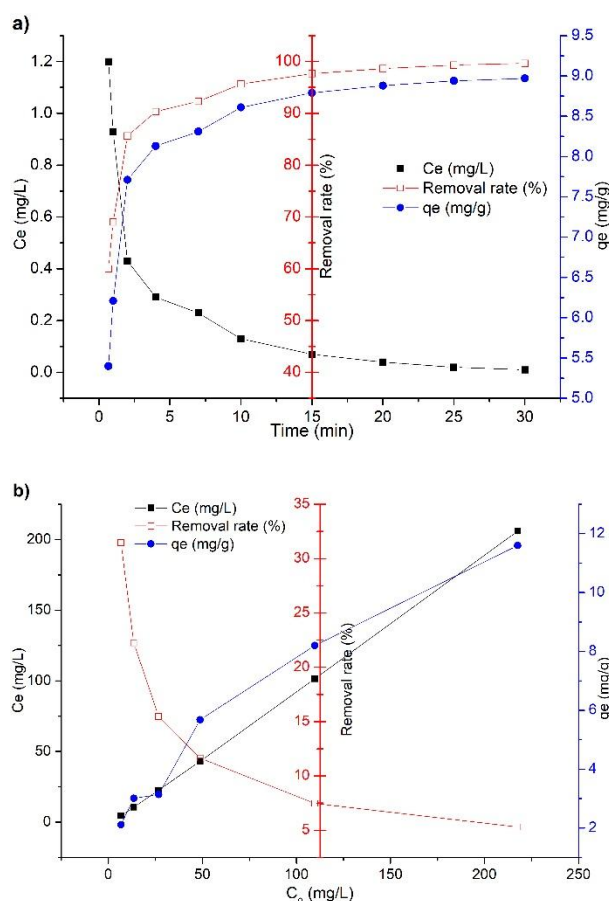


**Figure 4.** a) Effect of contact time, V: 100 mL, m: 300 mg,  $C_0$ : 3.0 mg/L, pH 5.0, T: 25°C, stirring 250 rpm, b) Effect of initial concentration;  $C_0$ : 6.71-217.6 mg/L, V: 10 mL, m: 1.0 g/L, pH 5.0, T: 25°C, stirring 250 rpm, time: 30 min.

### 3.2.4. Effect of initial concentration

In the experiments carried out under the same environmental conditions, 1 g/L kaolin was added to each of 6 different test tubes and the initial CR concentrations were changed between 6.71-217.6 mg/L. At the end of the period, CR concentrations were measured, and the obtained results are presented in Figure 4b. Accordingly, in the presence of 6.71 mg/L CR, the removal efficiency was calculated as 31.45% and the  $q_e$  value as 2.11 mg/g. When the initial CR concentration was increased to 48.78 mg/L, the efficiency was calculated as 11.64% and the  $q_e$  value as 5.68 mg/g. When the CR concentration was increased to 217.6 mg/L, the removal efficiency was calculated as 5.33% and the  $q_e$  value as 11.60. Accordingly, the increase in the amount of pollutant caused an increase in efficiency. This situation is that with the increase in the amount of CR, the pushing force of the dye molecules increases, which causes an increase in the efficiency of adsorption on kaolin. Similarly, when studies conducted with dyes are examined, it is reported that the  $q_e$  value increases with the increase in the initial dye concentration [35].

### 3.3. Adsorption kinetics

Estimating the speed of the adsorption process is one of the most important elements in the adsorption system. The adsorption process is affected by the physical and chemical properties of the adsorbent material, which determines the adsorption kinetics [36]. In the study, the kinetics of adsorption were investigated to investigate the adsorption mechanism of CR on kaolin. Kinetic studies were carried out using three models, namely pseudo-first order, pseudo-second order and intraparticle diffusion model. In the evaluation carried out for CR dye,  $R^2$  values of Pseudo first order and Intra-particle diffusion models were found as 0.923 and 0.591, respectively.  $R^2$  value of Pseudo second order kinetic model was calculated as 0.999. When 3 kinetic models and error functions were evaluated together, it was seen that the most suitable kinetic model for the adsorption of CR dye onto kaolin clay was pseudo second model. In addition, in the evaluation carried out with SSE, ARE, HYBRID, MPSD and  $X^2$  error functions, it was seen that Pseudo second order kinetic model was the most suitable model. The results obtained were compared with each other and given in Table 4. When the literature is examined, it has been reported that the pseudo-second-order kinetic model is the model that best explains the process in the study of CR dye removal with the environmentally friendly adsorbent obtained from kaolin clay and peanut shell[37].



**Table 4.** Summary of the Calculated Kinetic Models for the Adsorption of CR onto Kaolin.

Kinetic models	Pseudo first order	Pseudo second order	Intra-Particle Diffusion
Parameters	$k_1 = 0.052$	$k_2 = 2.014$ $q_e = 1.011$	$k_i = 0.091$ $a = 0.573$
$R^2$	0.923	0.999	0.591
SSE	1.07	0.003	0.124
ARE	53.60	2.25	19.33
HYBRID	75.04	1.780	0.340
MPSD	0.997	0.96	0.945
$X^2$	1.58	0.004	0.194

In addition, the graphs obtained from the linearized forms of each kinetic model equation are given in Figure 5.

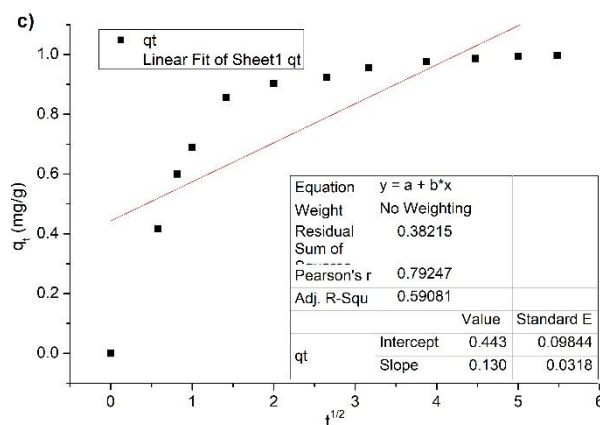
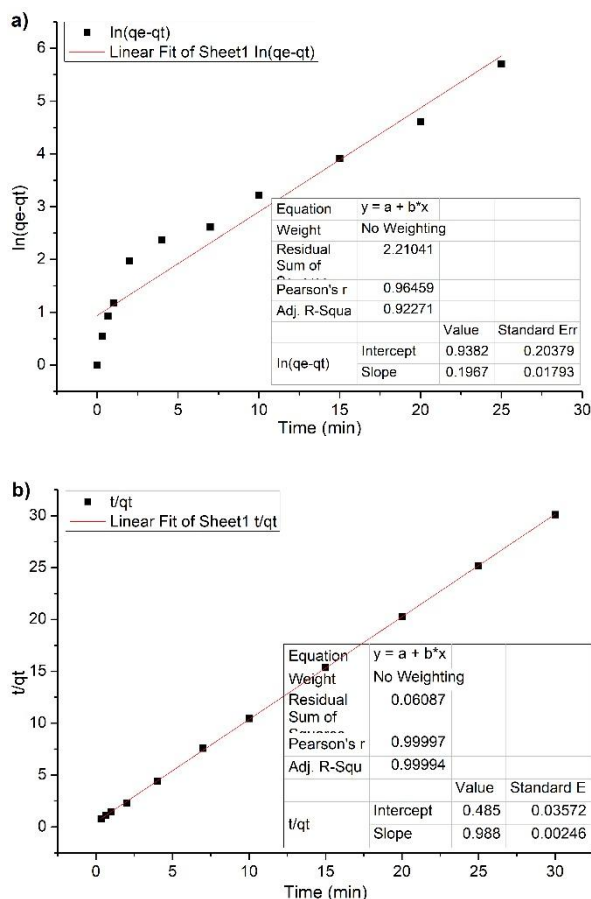


**Figure 5.** Regression curves, a) Pseudo first order, b) Pseudo second order, c) Intra-Particle Diffusion

In addition, the change graph comparing the numerical values obtained from the kinetic models applied with the amount of pollutants removed by the unit adsorbent obtained in the experimental studies with  $q_t$  is given in Figure 6.

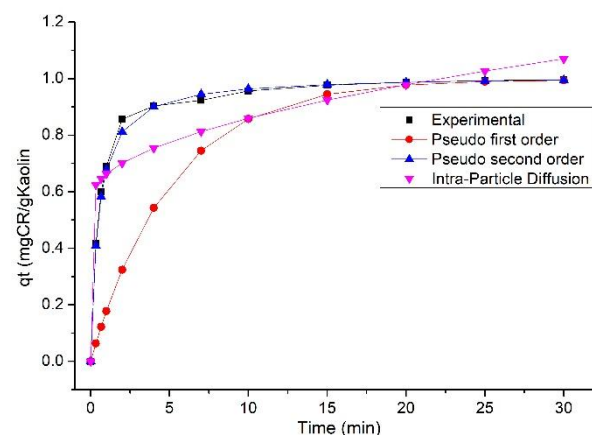


**Figure 6.** Plot of  $q_t$  values versus time.

When Table 3 and Figure 5 are examined together, the  $R^2$  values of the Pseudo first order and Intra-particle diffusion models are calculated as 0.923 and 0.591, respectively, while the  $R^2$  value of the Pseudo second order model is calculated as 0.999. Accordingly, it was determined that the most suitable kinetic model for the adsorption of CR dye onto kaolin clay is the Pseudo second order model. When different literature studies are examined, it is stated that the adsorption kinetics in the study of the adsorption of CR dye from aqueous medium with NaOH modified phengite clay is best represented by the Pseudo second order model [38]. In another similar study, the removal of CR dye from wastewater with chitosan waste and biobased composite material obtained from clay was aimed. As a result of the study, it was reported that CR removal was similarly controlled by the pseudo-second order model [39].

### 3.4. Adsorption Isotherms

Isotherm studies conducted in adsorption experiments are one of the steps that provide important ideas about the process. It will reveal the mechanism of interaction of the adsorbate with the surface of the solid adsorbent and provide information about how the adsorbent particle works with the adsorbate molecules and how it reaches equilibrium [40]. In the study conducted, Freundlich, Langmuir and Temkin isotherm models were used to determine the most suitable isotherm model for the adsorption of CR dye onto kaolin clay. The results obtained from the models are presented in Table 5. When Table 5 is examined, the  $R^2$  value of the Langmuir and Temkin models for CR dye is calculated as 0.964 and 0.917, respectively, while the  $R^2$  value of the Freundlich isotherm model is calculated as 0.999. Again, in the evaluation made with the error functions given in Table 5, the SSE value is 0.063, while the Langmuir and Temkin models are calculated as 3.51 and 4.212, respectively. When the other error functions, ARE, HYBRID, MPSD and  $X^2$ , are examined, it is seen that the Freundlich isotherm model is the most suitable model. When similar studies were examined, it was reported that the isotherm that best represents the adsorption process in the study of removal of CR dye by adsorption on pyrophyllite was Freundlich[41].

**Table 5.** Summary of the Calculated Isotherm Models for the Adsorption of CR Dye onto Kaolin Clay.

Isotherms	Freundlich	Langmuir	Temkin
<b>Parameters</b>	$k_F = 1.05$ $1/n = 0.447$	$k_L = 0.023$ $R_L = 0.768$ $q_{max} = 7.984$	$B_T = 1.001$ $k_T = 0.342$
<b><math>R^2</math></b>	0.999	0.964	0.917
<b>SSE</b>	0.063	3.51	4.212
<b>ARE</b>	1.45	19.82	20.58
<b>HYBRID</b>	0.016	5.190	3.53
<b>MPSD</b>	0.916	0.971	0.967
<b><math>X^2</math></b>	0.008	0.774	0.945

The graph obtained from the regression curves of each model is displayed in Figure 7.

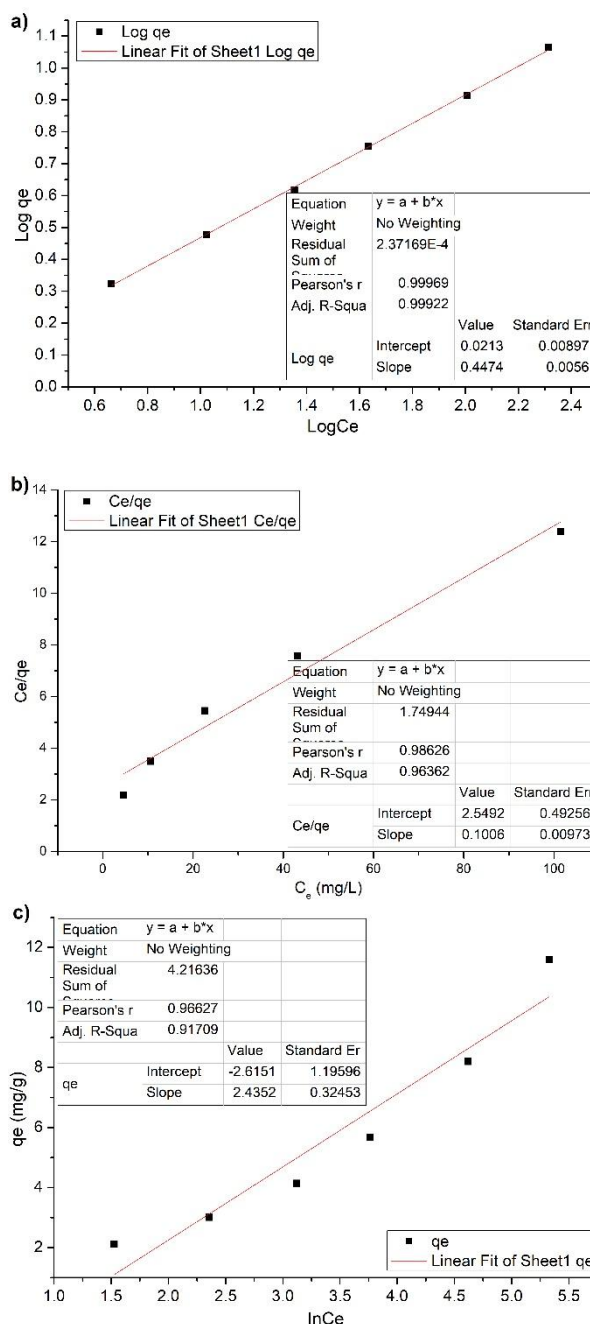


**Figure 7.** Regression Curves (a) Freundlich, b) Langmuir, c) Temkin.

In addition, the comparison graph of  $q_t$  values against  $C_e$  values, in which the isotherm models used are compared, is given in Figure 8.

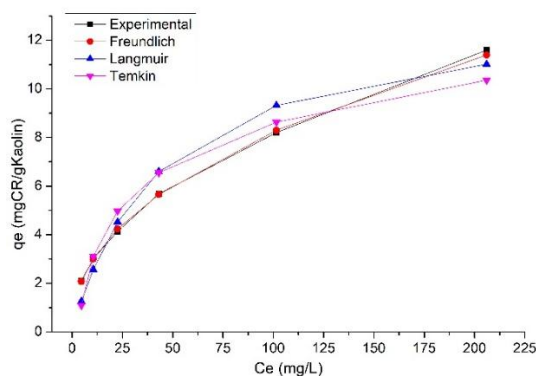


**Figure 8.** Graph of the changes in  $q_e$  values against  $C_e$  values.

### 3.5. Comparison of the Study and the Results Obtained with the Literature

When the studies in the literature (Table 6) are examined, the maximum adsorption capacity was reported as 1.896 mg/g in the study where basic yellow dye was removed with Ethiopian kaolin. In the study where CR was removed with kaolin clay functionalized with cellulose extract obtained from peanut shells, the maximum adsorption capacity was reported as 130.7 mg/g and the adsorption kinetics and isotherm were reported as pseudo-second order and Freundlich, respectively. In the study where methylene blue was removed from aqueous solutions by adsorption onto kaolin, which is a similar adsorbent, the maximum adsorption capacity was reported as 52.76 mg/g. In the study where crystal violet and brilliant green dyes were removed from aqueous solutions by adsorption onto kaolinite and acid-treated kaolinite, the maximum adsorption capacities were reported as 50.51 mg/g and 26.88 mg/g, respectively.

**Table 6.** Comparison of the Obtained Values with the Literature.

Type of pollutant	Adsorbent	$q_m$ (mg/g)	Reference
Basic yellow dye	Ethiopian Kaolin	1.896	[30]
CR	Kaolin clay/cellulose composite	130.7	[37]
Methylene blue	Kaolin	52.76	[26]
Crystal violet - Brilliant green	Kaolin	50.51-26.88	[42]
CR	Kaolin clay	7.984	This study

## 4. Conclusion

The effects of pH, adsorbent amount, initial concentration, and time were investigated in this adsorption where kaolin clay was used in the removal of CR dye in aqueous solution. The obtained results were

examined with 3 different kinetic and isotherm models. FTIR and SEM images of raw and CR loaded states of kaolin clay were examined to support the adsorption mechanism. According to the data obtained from batch adsorption studies, the most suitable kinetic and isotherm models were found as Pseudo second order ( $R^2$ : 0.999) and Freundlich ( $R^2$ : 0.999), respectively. In addition, the amount of CR dye removed per unit kaolin was calculated as 7.984 mg/g. With this study, it can be said that CR dye, which has ecotoxicological effects for flora and fauna, was successfully removed with kaolin clay.

## Acknowledgement

Authors may acknowledge technical assistance, the source of special materials, financial support and the auspices under which work was done. The names of funding organizations should be written in full.

## Ethics

There are no ethical issues after the publication of this manuscript.

## References

- [1]. K. Manzoor, M. Batool, F. Naz, M. F. Nazar, B. H. Hameed, and M. N. Zafar, "A comprehensive review on application of plant-based bioadsorbents for Congo red removal", *Biomass Convers Biorefin*, c. 14, sy 4, ss. 4511-4537, Şub. 2024, doi: 10.1007/s13399-022-02741-5.
- [2]. C. R. Holkar, A. J. Jadhav, D. V. Pinjari, N. M. Mahamuni, and A. B. Pandit, "A critical review on textile wastewater treatments: Possible approaches", *J Environ Manage*, c. 182, ss. 351-366, Kas. 2016, doi: 10.1016/j.jenvman.2016.07.090.
- [3]. V. Katheresan, J. Kansedo, and S. Y. Lau, "Efficiency of various recent wastewater dye removal methods: A review", *J Environ Chem Eng*, c.: 6, sy:4, ss. 4676-4697, Ağu. 2018, doi: 10.1016/j.jece.2018.06.060.
- [4]. M. T. Yagub, T. K. Sen, S. Afroze, and H. M. Ang, "Dye and its removal from aqueous solution by adsorption: A review", *Adv Colloid Interface Sci*, c. 209, ss. 172-184, Tem. 2014, doi: 10.1016/j.cis.2014.04.002.
- [5]. K. Maheshwari, M. Agrawal, ve A. B. Gupta, "Dye Pollution in Water and Wastewater", 2021, ss. 1-25. doi: 10.1007/978-981-16-2892-4\_1.
- [6]. A. Rafiq vd., "Photocatalytic degradation of dyes using semiconductor photocatalysts to clean industrial water pollution", *Journal of Industrial and Engineering Chemistry*, c. 97, ss. 111-128, May. 2021, doi: 10.1016/j.jiec.2021.02.017.
- [7]. C. Patra, R. Gupta, D. Bedadeep, ve S. Narayanasamy, "Surface treated acid-activated carbon for adsorption of anionic azo dyes from single and binary adsorptive systems: A detail insight", *Environmental Pollution*, c. 266, s. 115102, Kas. 2020, doi: 10.1016/j.envpol.2020.115102.
- [8]. C. Karaman, O. Karaman, P.-L. Show, H. Karimi-Maleh, ve N. Zare, "Congo red dye removal from aqueous environment by cationic surfactant modified-biomass derived carbon: Equilibrium, kinetic, and thermodynamic modeling, and forecasting via artificial neural network approach", *Chemosphere*, c. 290, s. 133346, Mar. 2022, doi: 10.1016/j.chemosphere.2021.133346.

- [9]. G. A. R. de Oliveira *vd.*, "A test battery for assessing the ecotoxic effects of textile dyes", *Chem Biol Interact*, c. 291, ss. 171-179, Ağu. 2018, doi: 10.1016/j.cbi.2018.06.026.
- [10]. P. Gharbani, S. M. Tabatabaai, ve A. Mehrizad, "Removal of Congo red from textile wastewater by ozonation", *International Journal of Environmental Science & Technology*, c. 5, sy 4, ss. 495-500, Eyl. 2008, doi: 10.1007/BF03326046.
- [11]. E. Alver, M. Bulut, A. Ü. Metin, ve H. Çiftçi, "One step effective removal of Congo Red in chitosan nanoparticles by encapsulation", *Spectrochim Acta A Mol Biomol Spectrosc*, c. 171, ss. 132-138, Oca. 2017, doi: 10.1016/j.saa.2016.07.046.
- [12]. G. Derouich, S. Alami Younssi, J. Bennazha, J. A. Cody, M. Ouammou, ve M. El Rhazi, "Development of low-cost polypyrrole/sintered pozzolan ultrafiltration membrane and its highly efficient performance for congo red dye removal", *J Environ Chem Eng*, c. 8, sy 3, s. 103809, Haz. 2020, doi: 10.1016/j.jece.2020.103809.
- [13]. A. Akhtar, Z. Aslam, A. Asghar, M. M. Bello, ve A. A. A. Raman, "Electrocoagulation of Congo Red dye-containing wastewater: Optimization of operational parameters and process mechanism", *J Environ Chem Eng*, c. 8, sy 5, s. 104055, Eki. 2020, doi: 10.1016/j.jece.2020.104055.
- [14]. S. Wang *vd.*, "Degradation of Congo red by UV photolysis of nitrate: Kinetics and degradation mechanism", *Sep Purif Technol*, c. 262, s. 118276, May. 2021, doi: 10.1016/j.seppur.2020.118276.
- [15]. B. D. Tony, D. Goyal, ve S. Khanna, "Decolorization of textile azo dyes by aerobic bacterial consortium", *Int Biodeterior Biodegradation*, c. 63, sy 4, ss. 462-469, Haz. 2009, doi: 10.1016/j.ibiod.2009.01.003.
- [16]. V. Vimonse, S. Lei, B. Jin, C. W. K. Chow, ve C. Saint, "Adsorption of congo red by three Australian kaolins", *Appl Clay Sci*, c. 43, sy 3-4, ss. 465-472, Mar. 2009, doi: 10.1016/j.clay.2008.11.008.
- [17]. A. K. Chauhan, N. Kataria, ve V. K. Garg, "Green fabrication of ZnO nanoparticles using Eucalyptus spp. leaves extract and their application in wastewater remediation", *Chemosphere*, c. 247, s. 125803, May. 2020, doi: 10.1016/j.chemosphere.2019.125803.
- [18]. P. K. Rose *vd.*, "Congo red dye removal using modified banana leaves: Adsorption equilibrium, kinetics, and reusability analysis", *Groundw Sustain Dev*, c. 23, s. 101005, Kas. 2023, doi: 10.1016/j.gsd.2023.101005.
- [19]. A. Kausar *vd.*, "Dyes adsorption using clay and modified clay: A review", *J Mol Liq*, c. 256, ss. 395-407, Nis. 2018, doi: 10.1016/j.molliq.2018.02.034.
- [20]. S. Mandal, J. Calderon, S. B. Marpu, M. A. Omary, ve S. Q. Shi, "Mesoporous activated carbon as a green adsorbent for the removal of heavy metals and Congo red: Characterization, adsorption kinetics, and isotherm studies", *J Contam Hydrol*, c. 243, s. 103869, Ara. 2021, doi: 10.1016/j.jconhyd.2021.103869.
- [21]. A. J. Muñoz, F. Espinola, M. Moya, ve E. Ruiz, "Biosorption of Pb(II) Ions by *Klebsiella* sp. 3S1 Isolated from a Wastewater Treatment Plant: Kinetics and Mechanisms Studies", *Biomed Res Int*, c. 2015, ss. 1-12, 2015, doi: 10.1155/2015/719060.
- [22]. N. Hamri *vd.*, "Enhanced Adsorption Capacity of Methylene Blue Dye onto Kaolin through Acid Treatment: Batch Adsorption and Machine Learning Studies", *Water (Basel)*, c. 16, sy 2, s. 243, Oca. 2024, doi: 10.3390/w16020243.
- [23]. A. Hashem, C. O. Aniagor, O. M. Morsy, A. Abou-Okeil, ve A. A. Aly, "Apricot seed shell: an agro-waste biosorbent for acid blue 193 dye adsorption", *Biomass Convers Biorefin*, c. 14, sy 11, ss. 12283-12296, Haz. 2024, doi: 10.1007/s13399-022-03272-9.
- [24]. J. Wang ve X. Guo, "Adsorption isotherm models: Classification, physical meaning, application and solving method", *Chemosphere*, c. 258, s. 127279, Kas. 2020, doi: 10.1016/j.chemosphere.2020.127279.
- [25]. M. Mozaffari Majd, V. Kordzadeh-Kermani, V. Ghalandari, A. Askari, ve M. Sillanpää, "Adsorption isotherm models: A comprehensive and systematic review (2010–2020)", *Science of The Total Environment*, c. 812, s. 151334, Mar. 2022, doi: 10.1016/j.scitotenv.2021.151334.
- [26]. L. Mouni *vd.*, "Removal of Methylene Blue from aqueous solutions by adsorption on Kaolin: Kinetic and equilibrium studies", *Appl Clay Sci*, c. 153, ss. 38-45, Mar. 2018, doi: 10.1016/j.clay.2017.11.034.
- [27]. S. M. Miraboutalebi, S. K. Nikouzad, M. Peydayesh, N. Allahgholi, L. Vafajoo, ve G. McKay, "Methylene blue adsorption via maize silk powder: Kinetic, equilibrium, thermodynamic studies and residual error analysis", *Process Safety and Environmental Protection*, c. 106, ss. 191-202, Şub. 2017, doi: 10.1016/j.psep.2017.01.010.
- [28]. A. H. Jawad ve A. S. Abdulhameed, "Mesoporous Iraqi red kaolin clay as an efficient adsorbent for methylene blue dye: Adsorption kinetic, isotherm and mechanism study", *Surfaces and Interfaces*, c. 18, s. 100422, Mar. 2020, doi: 10.1016/j.surf.2019.100422.
- [29]. A. Naboulsi, A. Kassimi, H. Yazid, F. Essebbar, M. El Himri, ve M. El Haddad, "Adsorption of single and mixed colors by kaolinite clay: Experimental research combined with a theoretical examination using DFT", *J Mol Struct*, c. 1276, s. 134687, Mar. 2023, doi: 10.1016/j.molstruc.2022.134687.
- [30]. T. A. Aragaw ve F. T. Angerasa, "Synthesis and characterization of Ethiopian kaolin for the removal of basic yellow (BY 28) dye from aqueous solution as a potential adsorbent", *Heliyon*, c. 6, sy 9, s. e04975, Eyl. 2020, doi: 10.1016/j.heliyon.2020.e04975.
- [31]. M. M. Abou Alsoaud, M. A. Taher, A. M. Hamed, M. S. Elnouby, and A. M. Omer, "Reusable kaolin impregnated aminated chitosan composite beads for efficient removal of Congo red dye: isotherms, kinetics and thermodynamics studies", *Sci Rep*, c. 12, sy 1, s. 12972, Tem. 2022, doi: 10.1038/s41598-022-17305-w.
- [32]. V. Vimonse, S. Lei, B. Jin, C. W. K. Chow, ve C. Saint, "Kinetic study and equilibrium isotherm analysis of Congo Red adsorption by clay materials", *Chemical Engineering Journal*, c. 148, sy 2-3, ss. 354-364, May. 2009, doi: 10.1016/j.cej.2008.09.009.
- [33]. M. Harja, G. Buema, ve D. Bucur, "Recent advances in removal of Congo Red dye by adsorption using an industrial waste", *Sci Rep*, c. 12, sy 1, s. 6087, Nis. 2022, doi: 10.1038/s41598-022-10093-3.
- [34]. S. Niu, X. Xie, Z. Wang, L. Zheng, F. Gao, ve Y. Miao, "Enhanced removal performance for Congo red by coal-series kaolin with acid treatment", *Environ Technol*, c. 42, sy 10, ss. 1472-1481, Nis. 2021, doi: 10.1080/09593330.2019.1670269.
- [35]. R. Ahmad ve K. Ansari, "Comparative study for adsorption of congo red and methylene blue dye on chitosan modified hybrid nanocomposite", *Process Biochemistry*, c. 108, ss. 90-102, Eyl. 2021, doi: 10.1016/j.procbio.2021.05.013.
- [36]. M. Benjelloun, Y. Miyah, G. Akdemir Evrendilek, F. Zerrouq, ve S. Lairini, "Recent Advances in Adsorption Kinetic Models: Their Application to Dye Types", *Arabian Journal of Chemistry*, c. 14, sy 4, s. 103031, Nis. 2021, doi: 10.1016/j.arabj.2021.103031.
- [37]. A. Reghioua, D. Atia, A. Hamidi, A. H. Jawad, A. S. Abdulhameed, ve H. M. Mbuvi, "Production of eco-friendly adsorbent of kaolin clay and cellulose extracted from peanut shells for removal of

methylene blue and congo red removal dyes”, *Int J Biol Macromol*, c. 263, s. 130304, Nis. 2024, doi: 10.1016/j.ijbiomac.2024.130304.

[38]. M. El-Habacha *vd.*, “High efficiency of treated-phengite clay by sodium hydroxide for the Congo red dye adsorption: Optimization, cost estimation, and mechanism study”, *Environ Res*, c. 259, s. 119542, Eki. 2024, doi: 10.1016/j.envres.2024.119542.

[39]. M. Bellaj *vd.*, “Bio-based composite from chitosan waste and clay for effective removal of Congo red dye from contaminated water: Experimental studies and theoretical insights”, *Environ Res*, c. 255, s. 119089, Ağu. 2024, doi: 10.1016/j.envres.2024.119089.

[40]. R. R. Karri, J. N. Sahu, ve N. S. Jayakumar, “Optimal isotherm parameters for phenol adsorption from aqueous solutions onto coconut

shell based activated carbon: Error analysis of linear and non-linear methods”, *J Taiwan Inst Chem Eng*, c. 80, ss. 472-487, Kas. 2017, doi: 10.1016/j.jtice.2017.08.004.

[41]. M. B. Amran ve M. A. Zulfikar, “Removal of Congo Red dye by adsorption onto pyrophyllite”, *International Journal of Environmental Studies*, c. 67, sy 6, ss. 911-921, Ara. 2010, doi: 10.1080/00207233.2010.528256.

[42]. G. K. Sarma, S. Sen Gupta, ve K. G. Bhattacharyya, “Removal of hazardous basic dyes from aqueous solution by adsorption onto kaolinite and acid-treated kaolinite: kinetics, isotherm and mechanistic study”, *SN Appl Sci*, c. 1, sy 3, s. 211, Mar. 2019, doi: 10.1007/s42452-019-0216-y.



# Photophysical and Photochemical Properties of New Coumarin-Substituted Zinc and Indium Phthalocyanines for Photodynamic Therapy

Zehra Kazancıoğlu<sup>1</sup>, Mustafa Bulut<sup>2</sup>, Ümit Salan<sup>3\*</sup>

<sup>1,2,3</sup>Marmara University, Department of Chemistry, 34722 Istanbul, Türkiye.

\* [usalan@marmara.edu.tr](mailto:usalan@marmara.edu.tr)

\* Orcid No: 0000-0003-0379-1066

Received: November 8, 2024

Accepted: January 30, 2025

DOI: 10.18466/cbayarfbe.1581909

## Abstract

In this study, we synthesized and characterized zinc (II) and indium (III) acetate phthalocyanine derivatives, modified with 7-hydroxy-8-methyl-4-(2,3,4,5-tetrafluorophenyl)coumarin, as potential photosensitizers for photodynamic therapy (PDT). The synthesized phthalocyanines were characterized using various analytical techniques, including elemental analysis, UV-Vis, FT-IR spectroscopy, and MALDI-TOF mass spectrometry. The study focused on the photophysical and photochemical properties of these compounds, particularly their singlet oxygen and photodegradation quantum yields. Zinc phthalocyanine exhibited lower fluorescence quantum yield and higher stability, whereas indium phthalocyanine showed superior singlet oxygen generation. These findings suggest that coumarin-substituted phthalocyanines hold promise as effective photosensitizers in PDT, with indium derivatives demonstrating enhanced photodynamic efficacy.

**Keywords:** Coumarin, Phthalocyanine, Photodynamic therapy, PDT, Singlet oxygen.

## 1. Introduction

Phthalocyanines (Pcs) are macrocyclic compounds with a planar structure formed by the condensation of four iminoisoindoline units, featuring an 18  $\pi$ -electron delocalization system and there is good structural flexibility in both free-metal ( $H_2Pcs$ ) and metal complexes of Pcs (MPcs). Up to 70 different elements can reside in the central cavity of Pcs, which in certain circumstances can allow for the functionalization of metal-axial ligands to modify the structure. Moreover, different substituents can be incorporated into the core of Pcs at the non-peripheral ( $\alpha$ ) and peripheral ( $\beta$ ) places to yield a range of electrical characteristics [1]. Due to their extensive range of applications, they are used in various fields, including optical data storage devices [2], semiconductors [3], [4], solar cells [5], [6], gas sensors [7], and liquid crystals [8], [9]. Their versatility is largely attributed to the 18  $\pi$ -electron delocalization system [10]. In addition, phthalocyanines are employed in cancer photodynamic therapy (PDT) as second-generation photosensitizers [11]. The primary benefits of these compounds include their high absorption capacity within the visible spectrum, efficient singlet oxygen generation, and their susceptibility to chemical modifications. These properties highlight the significant potential of

phthalocyanines in diverse technological and medical applications [12], [13].

The efficacy of phthalocyanines in photodynamic therapy can be significantly enhanced by incorporating diamagnetic metal ions. Metals like  $Mg^{2+}$ ,  $Zn^{2+}$ ,  $Al^{3+}$ ,  $Ga^{3+}$ ,  $In^{3+}$ ,  $Si^{4+}$ , and  $Lu^{3+}$  within the phthalocyanine core are particularly effective, as they promote the production of singlet oxygen, thus boosting the therapeutic efficiency [14], [15], [16], [17]. Additionally, modifying the photophysical and photochemical properties of phthalocyanines can be achieved by strategically introducing functional groups at various positions within their cyclic Structure [18].

In recent years, photodynamic therapy (PDT) has emerged as a significant method for cancer treatment, relying on three key components: a photosensitizer, light, and oxygen. The mechanism of PDT involves the interaction between the light-activated photosensitizer and nearby molecules [19]. This interaction generates singlet oxygen ( $^1O_2$ ), which can damage biological substrates and ultimately cause cell death. Compounds with macrocyclic structures, such as phthalocyanines, are highly effective in indirectly producing singlet oxygen due to their ability to persist in a triplet excited state [20].

The diversification of central metals allows for the synthesis of numerous new compounds. In this context, phthalocyanines emerge as promising compounds in cancer photodynamic therapy [21].

Coumarin and its derivatives have recently attracted attention as oxygenated heterocyclic compounds with an aromatic-heterocyclic structure containing a lactone ring [22]. These compounds, found in nature as secondary plant metabolites [23], are utilized in various medical and biological applications as antiviral [24], antibacterial [25], anticoagulant [26], antioxidant [27], anti-enzymatic [28], and anticancer agents [29], [30]. When combined with phthalocyanines, known as effective photosensitizers, they form complex structures that may exhibit similar properties [31]. Coumarin derivatives, especially those with a hydroxyl group at the 7-position and substitutions at the 4-position, are also intriguing due to their photochemical and photophysical properties [32]. These properties render them useful in various applications such as whitening agents [33], optical chromophores [34], laser dyes [35], and solar energy collectors [36]. Considering the biological significance of coumarin and phthalocyanine derivatives, the synthesis of compounds by combining these functional molecules via synthetic methods and evaluating their ability to produce singlet oxygen has recently garnered significant interest [37], [38], [39].

In this study, indium (III) acetate and zinc (II) phthalocyanine derivatives, modified with 7-hydroxy-8-methyl-4-(2,3,4,5-tetrafluorophenyl)coumarin compounds, were used as photosensitive dyes for photodynamic therapy in cancer treatment. Phthalocyanine compounds were synthesized and characterized using a range of analytical techniques, including elemental analysis, UV-Vis spectroscopy, FT-IR, <sup>1</sup>H-NMR, <sup>13</sup>C-NMR, <sup>19</sup>F-NMR, and MALDI-TOF mass spectrometry. This study centered on characterizing and examining the photophysical and photochemical properties of these compounds. Furthermore, comparisons with previous studies were conducted to assess how different substituent binding positions on the phthalocyanine skeleton and the role of central metal ions within the phthalocyanine cavity influence the properties of the compounds.

## 2. Materials and Methods

### 2.1. Materials

All chemicals used for the syntheses are of reagent grade quality. 3-Nitrophthalonitrile, 7-hydroxy-8-methyl-4-(2,3,4,5-tetrafluorophenyl)coumarin (**1**), and 7-(2,3-dicyanophenoxy)-8-methyl-4-(2,3,4,5-tetrafluorophenyl)coumarin (**2**) were synthesized and purified according to the methods previously described in the literature [40], [41]. 2-Methylresorcinol, ethyl-(2,3,4,5-tetrafluorobenzoyl)acetate, potassium

carbonate, 1,3-diphenylisobenzofuran (DPBF), and metal salts were purchased from Sigma-Aldrich and used as received. All reactions were conducted under a high-purity nitrogen atmosphere. The ZnPc (**3**) and InPc (**4**) compounds were purified through Soxhlet extraction with hot acetic acid, water, ethanol, and acetonitrile. For further purification, column chromatography on silica gel 60 (0.040-0.063 mm) was employed. The melting points of the phthalocyanine compounds were observed to be above 300 °C. The purity of the substances was checked at each stage using thin-layer chromatography (TLC, Silica gel 60 F254).

### 2.2. Equipments

FT-IR spectra were recorded using a Perkin Elmer Spectrum 100 FT-IR Spectrometer. Deuterated DMSO-d<sub>6</sub> for NMR studies was sourced from Merck. <sup>1</sup>H, <sup>13</sup>C, and <sup>19</sup>F-NMR spectra were measured with a Bruker DPX 400 MHz spectrometer. Mass spectra were acquired using a Bruker Microflex LT MALDI-TOF Mass Spectrometer equipped with a nitrogen UV laser operating at 337 nm, with dithranol (DIT) and 2,5-dihydroxybenzoic acid (DHB) used as matrices. The LECO CHNS-932 elemental analyzer was used to carry out the microanalyses of C, H, and N. A Shimadzu UV-2450 UV-Visible Spectrophotometer was used to record optical spectra in the UV-visible range. Fluorescence lifetimes were determined using a time-correlated single-photon counting (TCSPC) setup with Horiba Fluorolog 3 equipment. Emission and excitation spectra of fluorescence were recorded using a Hitachi F-7000 spectrofluorometer with a 1 cm path length cuvette. To perform photo-irradiations, a 300W-120V Osram optic halogen lamp was used. UV and infrared radiations were filtered using a water filter and a Schott glass cut-off filter (600 nm), respectively. In addition, an interference filter (Intor) with a 670–700 nm bandwidth was positioned in front of the sample. A POWER MAX PM5100 laser power meter was used to measure the intensities of the light (Moletron detector included).

### 2.3. Synthesis

4-Nitrophthalonitrile was synthesized and purified using methods described in the literature [40], [41]. 7-Hydroxy-8-methyl-4-(2,3,4,5-tetrafluorophenyl)coumarin (**1**) was prepared via the Pechmann reaction. 7-(2,3-Dicyanophenoxy)-8-methyl-4-(2,3,4,5-tetrafluorophenyl)coumarin (**2**) was synthesized through a nucleophilic aromatic substitution reaction.

#### 2.3.1. 7-Hydroxy-8-methyl-4-(2,3,4,5-tetrafluorophenyl)coumarin (**1**)

2-Methylresorcinol (1.17 g, 9.46 mmol) and ethyl-(2,3,4,5-tetrafluorobenzoyl)acetate (2.54 g, 9.46 mmol) were dissolved in a mixture of 5 mL CF<sub>3</sub>COOH and 5 mL



H<sub>2</sub>SO<sub>4</sub> at 0-5 °C for 24 hours. The reaction mixture was then cooled and precipitated with ice-cold water. The precipitate was filtered, washed with water until neutral, and allowed to dry. The crude product was finally purified by recrystallization from ethanol.

7-Hydroxy-8-methyl-4-(2,3,4,5-tetrafluorophenyl)coumarin (**1**) is soluble in chloroform, acetone, acetonitrile, ethyl acetate, *N,N*-dimethylformamide (DMF) and dimethyl sulfoxide (DMSO). Mp.: 173 °C. Yield: 2.71 g (88.37%). Anal. calculated for C<sub>16</sub>H<sub>8</sub>F<sub>4</sub>O<sub>3</sub>: C (59.28 %), H (2.48 %), F (23.44 %); found: C (59.26 %), H (2.48 %), F (23.46 %). UV-Vis, λ<sub>max</sub> (1×10<sup>-5</sup> M, in DMF) nm(log ε): 337 (4.32). FT-IR (ATR): ν<sub>max</sub>/cm<sup>-1</sup>: 3246 (Ar OH), 3066 (Ar C-H), 2913, 2921 (Aliphatic C-H), 1705 (Lactone C=O), 1481 (C=C). <sup>1</sup>H-NMR (400 MHz, DMSO-*d*<sub>6</sub>) (δ: ppm) 10.63 (br s, 1H), 7.58-7.68 (m, 1H), 7.03 (dd, *J* = 8.5, 2 Hz, 1H), 6.84 (d, *J* = 8.7 Hz, 1H), 6.31 (s, 1H), 2.21 (s, 3H). <sup>13</sup>C-NMR (400 MHz, DMSO-*d*<sub>6</sub>) (δ: ppm) 8, 110, 111, 112, 113, 114, 120, 125, 139, 142, 143, 146, 148, 153, 160. <sup>19</sup>F- NMR (400 MHz, DMSO-*d*<sub>6</sub>) (δ: ppm) (-138.90)-(-139.04) (m, 2F), (-138.51)-(-138.65) (m, 2F).

### 2.3.2. 7-(2,3-Dicyanophenoxy)-8-methyl-4-(2,3,4,5-tetrafluorophenyl)coumarin (**2**)

7-Hydroxy-8-methyl-4-(2,3,4,5-tetrafluorophenyl)coumarin (**1**) (1.00 g, 3.08 mmol) and 3-nitrophthalonitrile (0.53 g, 3.08 mmol) were dissolved in 30 mL of anhydrous *N,N*-dimethylformamide. After stirring for 10 minutes, finely ground dry K<sub>2</sub>CO<sub>3</sub> (0.64 g, 4.63 mmol) was added over 2 hours. The reaction mixture was then heated at 65 °C for 5 days under a nitrogen atmosphere. Once cooled to room temperature, the mixture was precipitated with ice-cold water. The resulting precipitate was filtered, washed with water until neutral, and allowed to dry. The crude product was purified by column chromatography using chloroform as the eluent and further purified by recrystallization from ethanol.

7-(2,3-Dicyanophenoxy)-8-methyl-4-(2,3,4,5-tetrafluorophenyl)coumarin (**2**) is soluble in methanol, ethanol, acetone, acetonitrile, chloroform, ethyl acetate, DMF, DMSO, and tetrahydrofuran (THF). Mp.: 240 °C. Yield: 0.91 g (65.46%). Anal. calculated for C<sub>24</sub>H<sub>10</sub>F<sub>4</sub>N<sub>2</sub>O<sub>3</sub>: C (64.01 %), H (2.24 %), F (16.87 %), N (6.22 %); found: C (64.00 %), H (2.23 %), F (16.88 %), N (6.23 %). UV-Vis, λ<sub>max</sub> (1×10<sup>-5</sup> M, in DMF) nm(log ε): 319 (4.15). FT-IR (ATR): ν<sub>max</sub>/cm<sup>-1</sup>: 3073 (Ar C-H), 2975 (Aliphatic C-H), 2235 (C≡N), 1732 (Lactone C=O), 1590 (C=C), 1245 (Ar-O-Ar). <sup>1</sup>H-NMR (400 MHz, DMSO-*d*<sub>6</sub>) (δ: ppm) 7.91 (d, *J* = 7.7 Hz, 1H), 7.86 (dd, *J* = 8.4 ve 8.5 Hz, 1H), 7.65-7.73 (m, 1H), 7.35 (d, *J* = 9.3 Hz, 1H), 7.32 (d, *J* = 8.7 Hz, 1H), 7.14 (br d, *J* = 8.5 Hz, 1H), 6.68 (s, 1H), 2.32 (s, 3H). <sup>13</sup>C- NMR (400 MHz, DMSO-*d*<sub>6</sub>) (δ: ppm) 10, 105, 113, 115, 115, 116, 116, 117, 117, 118, 119, 120, 122, 126, 129, 136, 146,

147, 153, 157, 155, 159, 160. <sup>19</sup>F- NMR (400 MHz, DMSO-*d*<sub>6</sub>) (δ: ppm) (-138.69)-(-138.84) (m, 2F), (-138.03)-(-138.17) (m, 2F).

### 2.3.3. 1(4),8(11),15(18),22(25)-Tetrakis-[7-oxy-8-methyl-4-(2,3,4,5-tetrafluorophenyl)coumarino]phthalocyaninato zinc (**II**) (**3**)

The phthalonitrile compound (**2**) (0.10 g, 0.05 mmol) and Zn(CH<sub>3</sub>COO)<sub>2</sub>·2H<sub>2</sub>O (0.003 g, 0.013 mmol) were reacted in a reaction tube without solvent by heating with a heat gun up to 350 °C for 5 minutes. The reaction was monitored until a blue-green color appeared. At this point, 2 drops of anhydrous DMF were added, and the reaction was allowed to continue for an additional minute. Once the reaction was complete, 0.5 mL of anhydrous DMF was added to dissolve the solid formed. The resulting solution was then precipitated dropwise into ice-cold water. The precipitate was filtered through filter paper and allowed to dry. The precipitates were subsequently centrifuged and washed several times with hot water and methanol. Finally, the crude product was purified by column chromatography using chloroform (100:1) as the eluent.

1(4),8(11),15(18),22(25)-Tetrakis-[7-oxy-8-methyl-4-(2,3,4,5-tetrafluorophenyl)-coumarino]phthalocyaninato zinc (**II**) (**3**) is soluble in acetone, ethyl acetate, chloroform, acetonitrile, dichloromethane (DCM), DMF, DMSO and THF. Mp.: >300 °C. Yield: 0.008 g (32.00%). Anal. calculated for C<sub>96</sub>H<sub>40</sub>F<sub>16</sub>N<sub>8</sub>O<sub>12</sub>Zn: C (61.77 %), H (2.16 %), F (16.28 %), N (6.00 %), Zn (3.50 %); found: C (61.76 %), H (2.15 %), F (16.29 %), N (6.02 %), Zn (3.49 %). UV-Vis, λ<sub>max</sub> (1×10<sup>-5</sup> M, in DMF) nm(log ε): 319 (5.21), 691 (5.16). FT-IR (ATR): ν<sub>max</sub>/cm<sup>-1</sup>: 3074 (Ar C-H), 2958, 2924, 2852 (Aliphatic C-H), 1726 (Lactone C=O), 1595 (C=C), 1264 (Ar-O-Ar). MALDI-TOF-MS *m/z*: Calc. 1866.75; found 1866.124 [M]<sup>+</sup>

### 2.3.4. 1(4),8(11),15(18),22(25)-Tetrakis-[7-oxy-8-methyl-4-(2,3,4,5-tetrafluorophenyl)coumarino]phthalocyaninato indium (**III**) acetate (**4**)

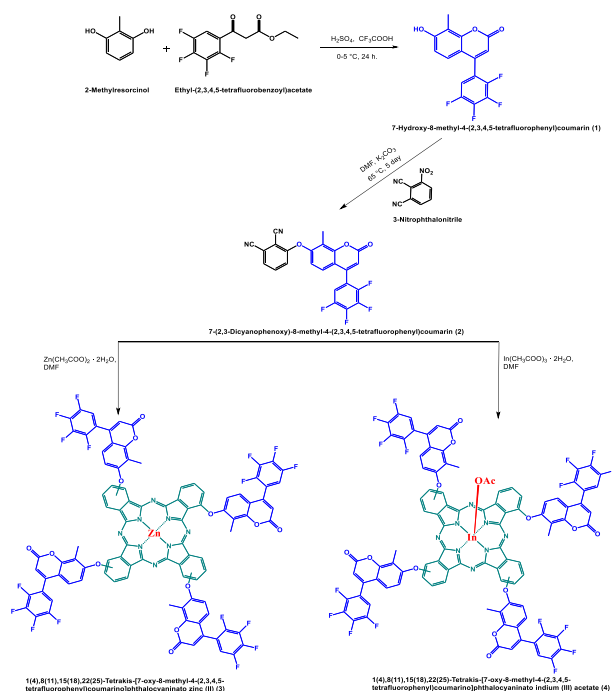
The phthalonitrile compound (**2**) (0.10 g, 0.05 mmol) and In(CH<sub>3</sub>COO)<sub>3</sub>·2H<sub>2</sub>O (0.004 g, 0.013 mmol) were reacted by heating in a reaction tube without a solvent using a heat gun up to 370 °C for 10 minutes. The reaction continued until a blue-green color appeared, and then 2 drops of anhydrous DMF were added to the reaction mixture and allowed to continue for another minute. Once the reaction was complete, 0.5 mL of anhydrous DMF was added to dissolve the solid formed. The resulting substance was gradually added to ice-cold water to induce precipitation. The precipitate was then filtered through filter paper and allowed to dry. Next, the precipitate was centrifuged and washed multiple times with hot water and methanol. Finally, the crude product

was purified by column chromatography with chloroform (100:1) as the eluent.

1(4),8(11),15(18),22(25)-Tetrakis-[7-oxy-8-methyl-4-(2,3,4,5-tetrafluorophenyl)-coumarino]phthalocyaninato indium (II) acetate (**4**) is soluble in acetone, chloroform, acetonitrile, ethyl acetate, DCM, DMF, DMSO and THF. Mp.: >300 °C. Yield: 0.0010 g (37.04%). Anal. calculated for  $C_{96}H_{43}F_{16}InN_8O_{14}$ : C (59.59 %), H (2.19 %), F (15.39 %), In (5.81 %), N (5.67 %); found: C (59.58 %), H (2.17 %), F (15.40 %), In (5.82 %), N (5.68 %). UV-Vis,  $\lambda_{max}$  ( $1 \times 10^{-5}$  M, in DMF) nm(log  $\epsilon$ ): 319 (4.92), 704 (4.73). FT-IR (ATR):  $\nu_{max}/cm^{-1}$ : 3071 (Ar C–H), 2927, 2857 (Aliphatic C–H), 1724 (Lactone C=O), 1596 (C=C), 1262 (Ar–O–Ar). MALDI-TOF-MS m/z: Calc. 1975.23; found 2106,132  $[M+CHCA+H-OAc]^+$

### 3. Results and Discussion

The synthesis schemes for non-peripheral zinc and indium phthalocyanines containing 7-hydroxy-8-methyl-4-(2,3,4,5-tetrafluorophenyl)coumarin are illustrated in **Scheme 1**.



**Scheme 1.** Synthesis of coumarin (**1**), its phthalonitrile derivative (**2**), and phthalocyanine derivatives (**3**, **4**).

7-Hydroxy-8-methyl-4-(2,3,4,5-tetrafluorophenyl)coumarin (**1**) was synthesized via the Pechmann reaction using 2-methylresorcinol and ethyl-(2,3,4,5-tetrafluorobenzoyl)acetate in the presence of  $H_2SO_4$  and  $CF_3COOH$  at 0-5 °C. The phthalonitrile derivative of this coumarin (**1**) was synthesized through a nucleophilic aromatic substitution reaction in anhydrous *N,N*-dimethylformamide using 3-nitrophthalonitrile.

Non-peripheral zinc(II) and indium (III) acetate phthalocyanine (**3,4**) derivatives were prepared through cyclotetramerization of the coumarin-phthalonitrile derivative compound. Coumarin-substituted zinc(II) and indium (III) phthalocyanines were prepared by heating in the absence of solvent at temperatures exceeding 350 °C in the presence of zinc (II) acetate and indium (III) acetate. Column chromatography was used to purify each and every product that was produced.

Phthalocyanine complexes without substituents typically have poor solubility in organic solvents. However, literature indicates that phthalocyanines containing polar groups generally exhibit good solubility. It was observed that the synthesized zinc and indium metallophthalocyanines showed good solubility in organic solvents such as ethyl acetate, acetonitrile, chloroform, DCM, DMF, THF, and DMSO.

The newly synthesized compounds were characterized using elemental analysis, FT-IR, UV-Vis,  $^1H$ -NMR,  $^{13}C$ -NMR,  $^{19}F$ -NMR, and MALDI-TOF-MS spectroscopic techniques. In the FT-IR spectra of the compounds, the characteristic carbonyl ( $C=O$ ) peak of the coumarin compound (**1**) was observed around  $1705\text{ cm}^{-1}$ , while the hydroxyl ( $-OH$ ) peak appeared at approximately  $3246\text{ cm}^{-1}$ . The hydroxyl ( $-OH$ ) peak was absent in the FT-IR spectrum of the coumarin phthalonitrile derivative (**2**). The  $C\equiv N$  peak for the coumarin phthalonitrile derivative (**2**) was detected at  $2235\text{ cm}^{-1}$ , and the Ar–O–Ar peak was seen around  $1245\text{ cm}^{-1}$ . The disappearance of the hydroxyl ( $-OH$ ) peak and the appearance of the  $C\equiv N$  and Ar–O–Ar peaks indicate the successful formation of the phthalonitrile derivative. After conversion to phthalocyanines, the  $C\equiv N$  peak, typically observed at  $2235\text{ cm}^{-1}$  in phthalonitrile derivatives, was no longer present. The absence of  $C\equiv N$  peaks in all phthalocyanine derivatives confirms the formation of the phthalocyanine compounds.

MALDI-TOF mass spectrometry is a crucial technique for determining the molecular weights of phthalocyanine complexes. In the mass spectra of all phthalocyanines, the molecular weights were observed as  $[M]^+$  or  $[M+CHCA+H-OAc]^+$ . Positive ion and linear mode MALDI-TOF mass spectra were acquired using 2,5-dihydroxybenzoic acid (DHB) or dithranol (DIT) as the MALDI matrix. The proposed structures of the phthalocyanine compounds align with the results obtained from elemental analysis.

#### 3.1. Spectrophotometric and Fluorometric Properties of Phthalocyanines

Phthalocyanines display Q and B band absorptions in the UV-visible region, making them amenable to characterization by UV-Vis spectroscopy. The basic electronic absorption spectra of non-peripheral tetra zinc and indium phthalocyanine compounds typically feature a narrow Q band in the range of 650-705 nm. The

presence of Zn and In metals in the phthalocyanine cores does not cause significant broadening of the Q band. Phthalocyanine compounds substituted with non-peripheral coumarin derivatives, along with zinc and indium metals, exhibit good solubility in solvents such as acetone, ethyl acetate, DCM, DMF, DMSO, and THF. When assessing the solvent effects on phthalocyanines, the most pronounced bathochromic shift was observed in DMSO compared to DCM, while the most significant hypsochromic shift was noted in ethyl acetate and acetone (Figure 1).

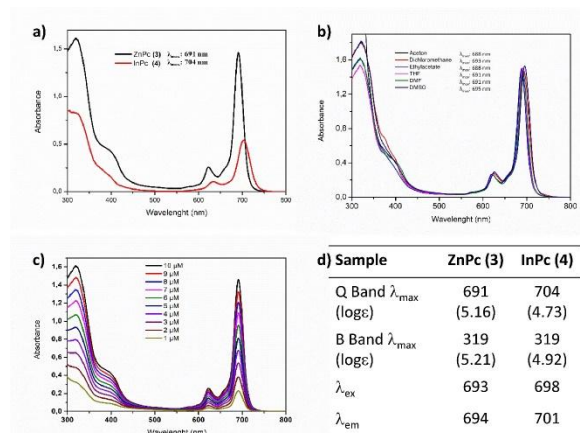


**Figure 1.** a) UV-Vis comparison of synthesized phthalocyanines in DMF. b) UV-Vis comparison of compound (3) in different solvents. c) UV-Vis spectra of compound (3) at ten different concentrations in DMF. d) UV-Vis and fluorescence data of phthalocyanine compounds (3) and (4).

The aggregation behavior of the phthalocyanine compounds at various concentrations in DMF was investigated due to the significant absorption of the produced compounds in DMF. In non-peripheral coumarin-substituted zinc and indium phthalocyanines, it was found that the intensity of the Q band increased with increasing concentration and that no aggregation was seen. The Lambert-Beer law was found to be satisfied by all phthalocyanine compounds within the concentration range of  $1 \times 10^{-5}$  to  $1 \times 10^{-6}$  M (in DMF) (Figure 1).

### 3.2. Singlet Oxygen Quantum Yields

Singlet oxygen quantum yields ( $\Phi_{\Delta}$ ) for zinc (II) and indium (III) acetate phthalocyanines, substituted with fluoro-phenyl coumarin, were assessed using a spectrophotometric approach with 1,3-diphenylisobenzofuran (DPBF) as a quencher. The analysis revealed changes in the Q band during the measurement of singlet oxygen quantum yields. To avoid the quenching effect of DMSO, singlet oxygen measurements were performed in DMF. It was observed that zinc (II) phthalocyanine derivatives, featuring non-peripheral coumarin at the fluorophenyl position, exhibited enhanced stability to light compared to their indium (III) acetate counterparts, showing less

degradation with extended exposure. This is attributed to zinc (II) metal being smaller in size compared to indium (III) acetate metal, allowing it to fit snugly into the center of the phthalocyanine skeleton and form stable coordination bonds. Conversely, the indium (III) acetate phthalocyanine compound, due to the indium (III) acetate metal not fitting perfectly into the center and the electron-withdrawing properties of the acetate group, reduces the reactivity at the core of the phthalocyanine, rendering the phthalocyanine compound less stable against singlet oxygen [42], [43] (Table 1).

**Table 1.** Photophysical and photochemical parameters of phthalocyanines (3,4) in DMF.

	$\lambda_{max}$	log $\epsilon$	$\Phi_{\Delta}$	$\Phi_d$
<b>3</b>	691	(5.16)	0.55	1.09
<b>4</b>	704	(4.73)	0.80	7.32
<b>ZnPc<sup>(44)</sup></b>	670	(5.37)	0.56	0.023
<b>InPc<sup>(44)</sup></b>	683	(4.93)	0.75	0.54

In our study of synthesized coumarin-substituted phthalocyanine derivatives, we observed that the indium metal phthalocyanine derivative (4) in the non-peripheral position exhibits a higher singlet oxygen quantum yield ( $\Phi_{\Delta} = 0.803$ ) compared to the zinc metal phthalocyanine derivative (3) ( $\Phi_{\Delta} = 0.547$ ). This increase in  $\Phi_{\Delta}$  for the indium derivative can be attributed to several factors. Firstly, in non-peripheral substituted phthalocyanine derivatives, the substituents are positioned closer to the phthalocyanine center, facilitating easier electron transfer. Secondly, indium, being a heavier atom compared to zinc, induces a heavier atom effect which enhances the production of singlet oxygen. This is because the heavier atom effect in indium increases spin-orbit coupling, promoting intersystem crossing to the triplet state.

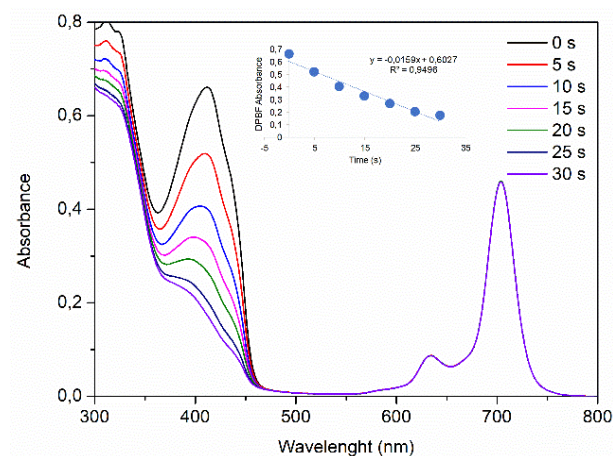


**Figure 2.** Time-dependent decrease in absorption of the DPBF compound in DMF, over 5 seconds, with compound (4) used to determine the singlet oxygen quantum yield (concentration  $\sim 10 \mu\text{M}$ ).



Consequently, this mechanism enhances the production of singlet oxygen, as excited electrons in heavy metal atoms such as indium have an increased propensity for intersystem transitions rather than losing energy through emission. For comparison, the singlet oxygen quantum yields of all the synthesized complexes were measured relative to the standard zinc phthalocyanine (ZnPc) compound, which has a  $\Phi_{\Delta}$  of 0.56 in DMF [44]. The results clearly demonstrate the superior efficiency of the indium-substituted phthalocyanine derivative in generating singlet oxygen [45], [46] (Figure 2).

### 3.3. Photodegradation Quantum Yields

The decay of a substance caused by light radiation is known as photodegradation. One crucial aspect of photochemistry is a compound's resistance to light. When assessing the light sensitivity of photosensitizers used in the pharmaceutical industry, the photodegradation quantum yield ( $\Phi_d$ ) is an essential measure. This yield should ideally be in the range of  $10^{-3}$  to  $10^{-6}$  M [47]. The coumarin-phthalocyanine photosensitizer assaults the phthalocyanine ring and disintegrates its skeleton when exposed to strong light by producing singlet oxygen. The Q band gets smaller as a result of this process. Degrading the photosensitizer is crucial in order to help the body remove it for use in photodynamic treatment. Every photodegradation investigation was carried out in DMF (Figure 3).

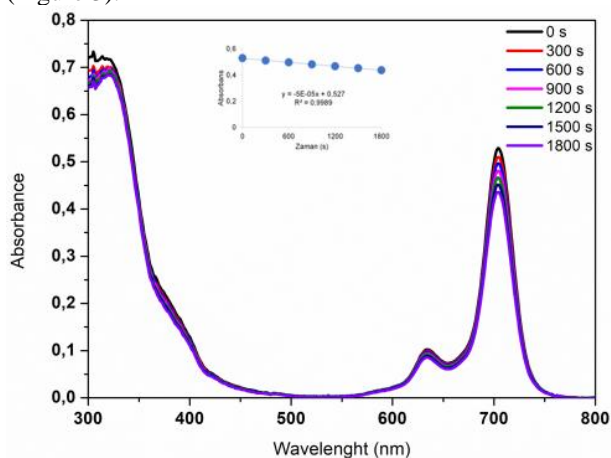


**Figure 3.** The absorption photodegradation spectrum of compound (4) under light irradiation for 1800 seconds. (Concentration  $\sim 10 \mu\text{M}$ ).

The zinc (II) phthalocyanine compound substituted with coumarin at non-peripheral positions is more stable to light and exhibits less degradation under prolonged exposure compared to its indium (III) acetate phthalocyanine derivative. This is because zinc (II) metal is smaller in size than indium (III) acetate metal and forms stable coordination bonds by fitting precisely into the core of the phthalocyanine skeleton. However, the indium (III) acetate phthalocyanine compound reduces reactivity in the core of the phthalocyanine due to the indium (III) acetate metal not fitting into the core and the electron-withdrawing properties of the acetate group,

making the phthalocyanine compound less stable against singlet oxygen.

### 4. Conclusion

In conclusion, non-peripheral zinc (II) and indium (III) acetate phthalocyanine complexes were successfully synthesized from 7-hydroxy-8-methyl-4-(2,3,4,5-tetrafluorophenyl)coumarin. These novel compounds were characterized by using a range of techniques, including elemental analysis, UV-visible, FT-IR spectroscopy, and MALDI-TOF mass spectrometry. The aggregation behavior, singlet oxygen quantum yields, and photodegradation quantum yields of these new phthalocyanines were investigated in DMF. The compounds demonstrated excellent solubility in common organic solvents and exhibited photophysical and photochemical properties comparable to previously studied phthalocyanine derivatives. Notably, the indium (III) acetate phthalocyanine derivative showed a higher singlet oxygen quantum yield than the zinc (II) derivative. These results suggest that coumarin-phthalocyanine complexes have potential as photosensitizers in photodynamic therapy and may benefit from further development through targeted modifications.

### Acknowledgement

We gratefully acknowledge the Research Foundation of Marmara University, Commission of Scientific Research Project (BAPKO) for their support under grant FYL-2022-10633.

### Author's Contributions

**Zehra Kazancıçok:** Drafted and wrote the manuscript, performed the experiment and result analysis.

**Mustafa Bulut:** Drafted and wrote the manuscript.

**Ümit Salan:** Assisted in analytical analysis on the structure, supervised the experiment's progress, result interpretation and helped in manuscript preparation.

### Ethics

There are no ethical issues after the publication of this manuscript.

### References

- [1]. Yahya, M., Nural, Y., & Seferoğlu, Z. (2022). Recent advances in the nonlinear optical (NLO) properties of phthalocyanines: A review. *Dyes and Pigments*, 198, 109960. (<https://doi.org/10.1016/j.dyepig.2021.109960>)
- [2]. Claessens, C. G., Hahn, U. W. E., & Torres, T. (2008). Phthalocyanines: From outstanding electronic properties to emerging applications. *The Chemical Record*, 8(2), 75-97. (<https://doi.org/10.1002/tcr.20139>)

- [3]. Klyamer, D., Bonegardt, D., & Basova, T. (2021). Fluoro-substituted metal phthalocyanines for active layers of chemical sensors. *Chemosensors*, 9(6), 133. (<https://doi.org/10.3390/chemosensors9060133>)
- [4]. Song, C., Li, Y., Gao, C., Zhang, H., Chuai, Y., & Song, D. (2020). An OTFT based on titanium phthalocyanine dichloride: A new p-type organic semiconductor. *Materials Letters*, 270, 127666. (<https://doi.org/10.1016/j.matlet.2020.127666>)
- [5]. Molina, D., Follana-Berná, J., & Sastre-Santos, Á. (2023). Phthalocyanines, porphyrins and other porphyrinoids as components of perovskite solar cells. *Journal of Materials Chemistry C*, 11(24), 7885-7919. (<https://doi.org/10.1039/D2TC04441B>)
- [6]. Rezaee, E., Khan, D., Cai, S., Dong, L., Xiao, H., Silva, S. R. P., Liu, X., & Xu, Z. X. (2023). Phthalocyanine in perovskite solar cells: A review. *Materials Chemistry Frontiers*, 7(9), 1704-1736. (<https://doi.org/10.1039/D2QM01369J>)
- [7]. Yabaş, E., Biçer, E., & Altındal, A. (2023). Novel reduced graphene oxide/zinc phthalocyanine and reduced graphene oxide/cobalt phthalocyanine hybrids as high sensitivity room temperature volatile organic compound gas sensors. *Journal of Molecular Structure*, 1271, 134076. (<https://doi.org/10.1016/j.molstruc.2022.134076>)
- [8]. Gursel, Y. H., Senkal, B. F., Kandaz, M., & Yakuphanoglu, F. (2009). Synthesis and liquid crystal properties of phthalocyanine bearing a star polytetrahydrofuran moiety. *Polyhedron*, 28(8), 1490-1496. (<https://doi.org/10.1016/j.poly.2009.02.038>)
- [9]. Canımurbey, B., Taşkan, M. C., Demir, S., Duygulu, E., Atila, D., & Yuksel, F. (2020). Synthesis and investigation of the electrical properties of novel liquid-crystal phthalocyanines bearing triple branched alkylthia chains. *New Journal of Chemistry*, 44(18), 7424-7435. (<https://doi.org/10.1039/D0NJ00678E>)
- [10]. Balamurugan, G., & Park, J. S. (2022). Enhanced solution processing and optical properties of perhalogenated zinc-phthalocyanines via anion- $\pi$  bonding. *Dyes and Pigments*, 201, 110199. (<https://doi.org/10.1016/j.dyepig.2022.110199>)
- [11]. Lo, P. C., Rodríguez-Morgade, M. S., Pandey, R. K., Ng, D. K., Torres, T., & Dumoulin, F. (2020). The unique features and promises of phthalocyanines as advanced photosensitisers for photodynamic therapy of cancer. *Chemical Society Reviews*, 49(4), 1041-1056. (<https://doi.org/10.1039/C9CS00129H>)
- [12]. Zhang, Y., & Lovell, J. F. (2017). Recent applications of phthalocyanines and naphthalocyanines for imaging and therapy. *Wiley Interdisciplinary Reviews: Nanomedicine and Nanobiotechnology*, 9(1), e1420. (<https://doi.org/10.1002/wnan.1420>)
- [13]. Çalık, A. E., Köksoy, B., Orman, E. B., Durmuş, M., Özkaya, A. R., & Bulut, M. (2013). 4-Carboxymethyl-8-methyl-7-oxycoumarin substituted zinc, cobalt and indium phthalocyanines: Electrochemical and photochemical properties. *Journal of Porphyrins and Phthalocyanines*, 17(10), 1046-1054. (<https://doi.org/10.1142/S108842461350096X>)
- [14]. Saka, E. T., Göl, C., Durmuş, M., Kantekin, H., & Bıyıklıoğlu, Z. (2012). Photophysical, photochemical and aggregation behavior of novel peripherally tetra-substituted phthalocyanine derivatives. *Journal of Photochemistry and Photobiology A: Chemistry*, 241, 67-78. (<https://doi.org/10.1016/j.jphotochem.2012.05.023>)
- [15]. Prabhu CP, K., Nemakal, M., Managa, M., Nyokong, T., & Koodlur Sannegowda, L. (2021). Symmetrically substituted Zn and Al phthalocyanines and polymers for photodynamic therapy application. *Frontiers in Chemistry*, 9, 647331. (<https://doi.org/10.3389/fchem.2021.647331>)
- [16]. Neagu, M., Constantin, C., Tampa, M., Matei, C., Lupu, A., Manole, E., Ion, R.M., Fenga, C., & Tsatsakis, A. M. (2016). Toxicological and efficacy assessment of post-transition metal (Indium) phthalocyanine for photodynamic therapy in neuroblastoma. *Oncotarget*, 7(43), 69718. (<https://doi.org/10.18632/oncotarget.11942>)
- [17]. Özdemir, M., Köksoy, B., Yalçın, B., Taşkın, T., Selçuki, N. A., Salan, Ü., Durmuş, M., & Bulut, M. (2021). Novel lutetium (III) phthalocyanine-coumarin dyads; synthesis, characterization, photochemical, theoretical and antioxidant properties. *Inorganica Chimica Acta*, 517, 120145. (<https://doi.org/10.1016/j.ica.2020.120145>)
- [18]. Sharma, D., Steen, G., Korterik, J. P., García-Iglesias, M., Vázquez, P., Torres, T., Herek, J. L., & Huijser, A. (2013). Impact of the anchoring ligand on electron injection and recombination dynamics at the interface of novel asymmetric push-pull zinc phthalocyanines and TiO<sub>2</sub>. *The Journal of Physical Chemistry C*, 117(48), 25397-25404. (<https://doi.org/10.1021/jp410080a>)
- [19]. Kwiatkowski, S., Knap, B., Przysupski, D., Saczko, J., Kędzierska, E., Knap-Czop, K., Kotlińska, J., Michel, O., Kotowski, K., & Kulbacka, J. (2018). Photodynamic therapy-mechanisms, photosensitizers and combinations. *Biomedicine & pharmacotherapy*, 106, 1098-1107. (<https://doi.org/10.1016/j.biopha.2018.07.049>)
- [20]. Köksoy, B., Durmuş, M., & Bulut, M. (2019). Potential photosensitizer candidates for PDT including 7-oxy-3-thiomethylphenyl coumarino-phthalocyanines. *Inorganica Chimica Acta*, 498, 119137. (<https://doi.org/10.1016/j.ica.2019.119137>)
- [21]. Rak, J., Kabesova, M., Benes, J., Pouckova, P., & Vetvicka, D. (2023). Advances in liposome-encapsulated phthalocyanines for photodynamic therapy. *Life*, 13(2), 305. (<https://doi.org/10.3390/life13020305>)
- [22]. Supuran, C. T. (2020). Coumarin carbonic anhydrase inhibitors from natural sources. *Journal of Enzyme Inhibition and Medicinal Chemistry*, 35(1), 1462-1470. (<https://doi.org/10.1080/14756366.2020.1788009>)
- [23]. Özdemir, M., Taşkın, D., Ceyhan, D., Köksoy, B., Taşkın, T., Bulut, M., & Yalçın, B. (2023). 7, 8-Dihydroxycoumarin derivatives: In silico molecular docking and in vitro anticholinesterase activity. *Journal of Molecular Structure*, 1274, 134535. (<https://doi.org/10.1016/j.molstruc.2022.134535>)
- [24]. Mishra, S., Pandey, A., & Manvati, S. (2020). Coumarin: An emerging antiviral agent. *Heliyon*, 6(1). (<https://doi.org/10.1016/j.heliyon.2020.e03217>)
- [25]. Qin, H. L., Zhang, Z. W., Ravindar, L., & Rakesh, K. P. (2020). Antibacterial activities with the structure-activity relationship of coumarin derivatives. *European journal of medicinal chemistry*, 207, 112832. (<https://doi.org/10.1016/j.ejmech.2020.112832>)
- [26]. Ramsis, T. M., Ebrahim, M. A., & Fayed, E. A. (2023). Synthetic coumarin derivatives with anticoagulation and antiplatelet aggregation inhibitory effects. *Medicinal Chemistry Research*, 32(11), 2269-2278. (<https://doi.org/10.1007/s00044-023-03148-1>)
- [27]. Todorov, L., Saso, L., & Kostova, I. (2023). Antioxidant activity of coumarins and their metal complexes. *Pharmaceuticals*, 16(5), 651. (<https://doi.org/10.3390/ph16050651>)
- [28]. Çelik, E., Özdemir, M., Köksoy, B., Taskin-Tok, T., Taslimi, P., Sadeghian, N., & Yalçın, B. (2023). New Coumarin-Thiosemicarbazone Based Zn (II), Ni (II) and Co (II) Metal Complexes: Investigation of Cholinesterase,  $\alpha$ -Amylase, and  $\alpha$ -Glucosidase Enzyme Activities, and Molecular Docking Studies. *ChemistrySelect*, 8(38), e202301786. (<https://doi.org/10.1002/slct.202301786>)
- [29]. Rawat, A., & Reddy, A. V. B. (2022). Recent advances on anticancer activity of coumarin derivatives. *European Journal of Medicinal Chemistry Reports*, 5, 100038. (<https://doi.org/10.1016/j.ejmcr.2022.100038>)

- [30]. Bisi, A., Cappadone, C., Rampa, A., Farruggia, G., Sargenti, A., Belluti, F., Di Martino, R. M. C., Malucelli, E., Meluzzi, A., Iotti, S., & Gobbi, S. (2017). Coumarin derivatives as potential antitumor agents: Growth inhibition, apoptosis induction and multidrug resistance reverting activity. *European journal of medicinal chemistry*, 127, 577-585. (<https://doi.org/10.1016/j.ejmech.2017.01.020>)
- [31]. Çamur, M., Durmuş, M., & Bulut, M. (2012). Highly singlet oxygen generative water-soluble coumarin substituted zinc (II) phthalocyanine photosensitizers for photodynamic therapy. *Polyhedron*, 41(1), 92-103. (<https://doi.org/10.1016/j.poly.2012.04.034>)
- [32]. Dandriyal, J., Singla, R., Kumar, M., & Jaitak, V. (2016). Recent developments of C-4 substituted coumarin derivatives as anticancer agents. *European journal of medicinal chemistry*, 119, 141-168. (<https://doi.org/10.1016/j.ejmech.2016.03.087>)
- [33]. Roh, E. J. (2021). Inhibitory effects of coumarin derivatives on tyrosinase. *Molecules*, 26(8), 2346. (<https://doi.org/10.3390/molecules26082346>)
- [34]. Deng, G., Xu, H., Kuang, L., He, C., Li, B., Yang, M., Zhang, X., Li, Z., & Liu, J. (2019). Novel nonlinear optical chromophores based on coumarin: Synthesis and properties studies. *Optical Materials*, 88, 218-222. (<https://doi.org/10.1016/j.optmat.2018.11.035>)
- [35]. Liu, X., Cole, J. M., Waddell, P. G., Lin, T. C., Radia, J., & Zeidler, A. (2012). Molecular origins of optoelectronic properties in coumarin dyes: toward designer solar cell and laser applications. *The Journal of Physical Chemistry A*, 116(1), 727-737. (<https://doi.org/10.1021/jp209925y>)
- [36]. Pradhan, R., Khandelwal, K., Shankar S. S., Panda, S. J., Purohit, C. S., Bag, B. P., Singhal, R., Liu, W., Zhu, X., Sharma, G. D., & Mishra, A. (2023). Correlation of Functional Coumarin Dye Structure with Molecular Packing and Organic Solar Cells Performance. *Solar RRL*, 7(21), 2300487. (<https://doi.org/10.1002/solr.202300487>)
- [37]. Köksoy, B., Durmuş, M., & Bulut, M. (2015). Tetra-and octa-[4-(2-hydroxyethyl) phenoxy bearing novel metal-free and zinc (II) phthalocyanines: Synthesis, characterization and investigation of photophysical and photochemical properties. *Journal of Luminescence*, 161, 95-102. (<https://doi.org/10.1016/j.jlumin.2014.12.044>)
- [38]. Zhou, X. Q., Meng, L. B., Huang, Q., Li, J., Zheng, K., Zhang, F. L., Liu, J. Y., & Xue, J. P. (2015). Synthesis and in vitro anticancer activity of zinc (II) phthalocyanines conjugated with coumarin derivatives for dual photodynamic and chemotherapy. *ChemMedChem*, 10(2), 304-311. (<https://doi.org/10.1002/cmdc.201402401>)
- [39]. Boyar, C. Y., & Çamur, M. (2019). Novel water soluble 7-oxy-4-(pyridine-3-yl) coumarin substituted phthalocyanines as potential photosensitizers for photodynamic therapy. *Inorganica Chimica Acta*, 494, 30-41. (<https://doi.org/10.1016/j.ica.2019.05.004>)
- [40]. J.G. Young, W. Onyebuagu, Synthesis and characterization of di-disubstituted phthalocyanines, *The Journal of Organic Chemistry* 55(7) (1990) 2155-2159. (<https://doi.org/10.1021/jo00294a032>)
- [41]. George, R. D., & Snow, A. W. (1995). Synthesis of 3-nitrophthalonitrile and tetra- $\alpha$ -substituted phthalocyanines. *Journal of Heterocyclic Chemistry*, 32(2), 495-498. (<https://doi.org/10.1002/jhet.5570320219>)
- [42]. Dyrda, G. (2023). Photostability of indium phthalocyanines in organic solvents. (<https://doi.org/10.21203/rs.3.rs-3407051/v1>)
- [43]. Gürel, E., Pişkin, M., Altun, S., Odabaş, Z., & Durmuş, M. (2015). Synthesis, characterization and investigation of the photophysical and photochemical properties of highly soluble novel metal-free, zinc (II), and indium (III) phthalocyanines substituted with 2, 3, 6-trimethylphenoxy moieties. *Dalton Transactions*, 44(13), 6202-6211. (<https://doi.org/10.1039/C5DT00304K>)
- [44]. Özdemir, M., Karapınar, B., Yalçın, B., Salan, Ü., Durmuş, M., & Bulut, M. (2019). Synthesis and characterization of novel 7-oxy-3-ethyl-6-hexyl-4-methylcoumarin substituted metallo phthalocyanines and investigation of their photophysical and photochemical properties. *Dalton Transactions*, 48(34), 13046-13056. (<https://doi.org/10.1039/C9DT02687H>)
- [45]. Güzel, E., Arslan, B. S., Atmaca, G. Y., Nebioğlu, M., & Erdoğan, A. (2019). High photosensitized singlet oxygen generating zinc and chloroindium phthalocyanines bearing (4-isopropylbenzyl) oxy groups as potential agents for photophysicochemical applications. *ChemistrySelect*, 4(2), 515-520. (<https://doi.org/10.1016/j.jphotochem.2015.10.026>)
- [46]. Yaşa Atmaca, G., & Erdoğan, A. (2017). Novel, Highly Soluble Non-Peripherally Phthalocyanines Bearing Bulky Groups Containing Fluorine Atoms: Synthesis, Characterization, Spectral and Improved Photophysicochemical Properties. *Hacettepe Journal of Biology and Chemistry*, 45(1). (10.15671/HJBC.2017.137)
- [47]. Karapınar, B., Özdemir, M., Salan, Ü., Durmuş, M., Yalçın, B., & Bulut, M. (2019). 7-Oxy-3, 4-cyclohexenecoumarin Carrying Novel Zinc (II) and Indium (III) Acetate Phthalocyanines: Synthesis, Characterization, Photophysical and Photochemical Properties. *Chemistry Select*, 4(33), 9632-9639. (<https://doi.org/10.1002/slct.201902582>)

# A New Record of Genus *Stigmaeus* (Acariformes: Stigmaeidae) from Türkiye

Mustafa Akyol<sup>1\*</sup> 

<sup>1</sup> Department of Biology, Faculty of Engineering and Natural Sciences, Manisa Celal Bayar University, Manisa, Türkiye

\* [makyol77@gmail.com](mailto:makyol77@gmail.com)

\* Orcid No: 0000-0002-3466-7618

Received: November 10, 2024

Accepted: December 29, 2024

DOI: 10.18466/cbayarfbe.1582494

## Abstract

*Stigmaeus canestrinii* Stathakis, Kapaxidi and Papadoulis, 2019 is founded for the first time from Türkiye and new report the mite fauna of Türkiye. Mites taken from soil and litter samples under *Oleae europaea* (Oleaceae) Manisa province, Türkiye. *S. canestrinii* is redescribed and illustrated based on the adult female.

**Keywords:** Acari, new report, *Stigmaeus canestrinii*, Raphignathoidea, Türkiye.

## 1. Introduction

The mite family Stigmaeidae is known in the superfamily Raphignathoidea Kramer, 1877 (Acari: Trombidiformes: Prostigmata). Many members of Stigmaeidae found in all biogeographical regions and have been noted economically important predators of plant-feeding small insects and mites have taken a lot of interest from biologists, taxonomists and ecologists [1-4].

The genus *Stigmaeus* Koch, 1836, is the numerous in the family Stigmaeidae and now contains about 153 species. The majority of this genus are free-living predators [4-6]. So far, 40 species of the genus have been recorded from Türkiye [7-30] and this information shows that the species belonging to this genus are mostly identified from Türkiye in the Palearctic region.

In this study, a new record of Turkish fauna *Stigmaeus canestrinii* Stathakis, Kapaxidi and Papadoulis, is found for the first time in Türkiye, is illustrated and redescribed based on the adult female. Similarities and differences were discussed by comparing them with the type locality (Greece) of the species.

## 2. Materials and Methods

The specimens were taken from soil and litter under *Oleae europaea*, Manisa province, Türkiye, and taken to the laboratory in plastic bags and extracted by Berlese-Tullgren funnels for a week. Mites were piled up in 70% ethanol and set on slides in modified Hoyer's medium.

The mite specimens were drawn and measured by means of a research microscope (Nikon Eclipse E 400). The setal nomenclature follows those of Kethley (1990) and Grandjean (1944) [31, 32]. All measurements are given in micrometers (µm). Measurements of legs are taken from base of trochanters to the tips of tarsal claws. The specimens are held back as slide mounted in Manisa Celal Bayar University, Zoological Museum, Manisa, Türkiye (CBZM).

## 3. Results and Discussion

### Family Stigmaeidae Oudemans, 1931

### Genus *Stigmaeus* Koch, 1836

Type species: *Stigmaeus cruentus* Koch, 1836.

### *Stigmaeus canestrinii* Stathakis, Kapaxidi and Papadoulis, 2019

**Diagnosis:** Dorsal setae simple. Propodosomal shield partly reticulated with 2 pairs of setae; postocular bodies (*pob*) and eyes without. Hysterosoma without clear central and marginal plates. Suranal shield divided, with 3 pairs of setae. Aggenital area with 4 pairs of setae; genital valves with 2 pairs of genital setae. Femora 4-4-3-2; genua 5+1κ-2-0-1; tarsi 13+1ω-8+1ω-7+1ω-7+1ω [33].

**Description:** Female (n = 3) (Figs 1, 2).



Length of body (excluding gnathosoma) 364-429, width 221-265.

Gnathosoma (Figs 1A, B, 2E). Chelicerae 80-82, fixed digit 68-70, moveable digit 28-30 in length. Ventral subcapitulum with two pairs of subcapitular setae, *m* 15-18 and *n* 45-50 (distances between subcapitular setae: *m*-*m* 23 (23-27), *n*-*n* 28 (27-29) and *m*-*n* 10 (8-10)) and two pairs of adoral setae, *or*1 7 and *or*2 6. Palp 104-109, trochanter without seta, femur with 3 setae, genu with 1 seta, palp tibia with well-developed claw + one seta-like accessory claw and 2 setae, palp tarsus with one terminal tridentate eupathidium + one subterminal simple eupathidium + one solenidion + 4 simple setae.

Dorsum of idiosoma (Fig. 1A). Propodosoma with a partly reticulated shield bearing 2 pairs of setae *vi* and *ve*; setae *sci* free on integument; without postocular bodies (*pob*) and eyes; setae *sce* on auxiliary platelets (Fig. 1AB). Hysterosoma without distinct central and marginal plates bearing setae *c*<sub>1</sub>, *d*<sub>1</sub>, *d*<sub>2</sub>, *e*<sub>1</sub> and *e*<sub>2</sub>; setae on intercalary plates. Suranal shield divided, with three pairs of setae *h*<sub>1</sub>, *h*<sub>2</sub> and *h*<sub>3</sub>. Dorsal setae simple. Lengths and distances of dorsal idiosomal setae as follows: *vi* 12-13, *ve* 37-42, *sci* 15-19, *sce* 20-21, *c*<sub>1</sub> 14-16, *d*<sub>1</sub> 13-14, *d*<sub>2</sub> 12-13, *e*<sub>1</sub> 13-14, *e*<sub>2</sub> 10-13, *f* 15, *h*<sub>1</sub> 15-16, *h*<sub>2</sub> 25-30, *h*<sub>3</sub> 17-18, *vi*-*vi* 22-25, *vi*-*ve* 15, *ve*-*ve* 26-34, *ve*-*sci* 30-35, *sci*-*sci* 52-60, *sci*-*c*<sub>1</sub> 65-73, *sce*-*sce* 105-130, *c*<sub>1</sub>-*c*<sub>1</sub> 36-52, *c*<sub>1</sub>-*d*<sub>1</sub> 50-60, *d*<sub>1</sub>-*d*<sub>1</sub> 34-45, *d*<sub>1</sub>-*e*<sub>1</sub> 46-60, *d*<sub>2</sub>-*d*<sub>2</sub> 102-140, *e*<sub>1</sub>-*e*<sub>1</sub> 35-41, *e*<sub>1</sub>-*e*<sub>2</sub> 30-65, *e*<sub>2</sub>-*e*<sub>2</sub> 90-140, *e*<sub>1</sub>-*f* 30, *f*-*f* 43-50, *f*-*h*<sub>1</sub> 30-50, *h*<sub>1</sub>-*h*<sub>1</sub> 25-26, *h*<sub>1</sub>-*h*<sub>2</sub> 10-12, *h*<sub>2</sub>-*h*<sub>2</sub> 50-52, *h*<sub>2</sub>-*h*<sub>3</sub> 8-10, *h*<sub>3</sub>-*h*<sub>3</sub> 65-72.

Venter of idiosoma (Fig. 1B). Humeral shields with setae *c*<sub>2</sub> 34-36. Endopodal shields smooth; ventral setae *la* 18-20, *3a* 20-21 and *4a* 20. Aggenital area with 4 pairs of setae; *ag*<sub>1</sub> 13-15 and *ag*<sub>2</sub> 13-14 free on integument, *ag*<sub>3</sub> 13-14 and *ag*<sub>4</sub> 17-20 on the same smooth platelet; anogenital area with 2 pairs of genital setae *g*<sub>1</sub> 13-15 and *g*<sub>2</sub> 17-20 and 3 pairs of pseudanal setae, *ps*<sub>1</sub> 20-21, *ps*<sub>2</sub> 21-22 and *ps*<sub>3</sub> 15-18 in length.

Legs (Figs 2 A-D). Length of legs (from base of trochanter to tip of tarsal claw) leg I 130-138, leg II 104, leg III 112-117, leg IV 130-135. Counts of setae and solenidia on legs I-IV: Coxae 2+1elcl- 2-2-2; trochanters 1-1-2-1; femora 4-4-3-2; genua 5+1κ-2-0-1; tibiae 5+1φ+1φp-5+1φp-5+1φp-5+1φp; tarsi 13+1ω-8+1ω-7+1ω-7+1ω. Length of spines and solenidia: κI 6-7, ωI 10-11, ωII 6-7, ωIII 5, ωIV 4; setae on tibia IV: *d* 40-42, *l'* 20-21.

Male: Unknown.

Material examined. Three females collected from litter and soil under the *Oleae europaea*, 71 m a.s.l., 38°38'47"N 27°21'23"E, Muradiye area, Yunusemre district; Manisa province, 25 April 2022, Türkiye, coll. M. Akyol.

**Discussion.** *Stigmaeus canestrinii* Stathakis, Kapaxidi and Papadoulis, 2019 was described for the first time from Greece and collected from ex *Sedum* sp. (Crassulaceae), 20 April 2013, Cape Tenaro, Co. Lakonia (altitude probably at about sea level) [33]. In this study the samples collected from soil and litter under *Oleae europaea* (altitude 71 m a.s.l.), 25 April 2022, in Yunusemre district, Manisa province, Türkiye.

Body size of 330-340 long and 160-170 wide in the Greece specimens; 364-429 long and 221-265 wide in the Turkish specimens. The body size of the Turkish specimen is bigger than the Greece specimens.

The Turkish specimen resembles the Greece specimens, but measurements of body setae *vi* 12-13, *ve* 37-42, *sci* 15-19, *sce* 20-21, *c*<sub>1</sub> 14-16, *d*<sub>1</sub> 13-14, *d*<sub>2</sub> 12-13, *e*<sub>1</sub> 13-14, *e*<sub>2</sub> 10-13, *f* 15, *h*<sub>1</sub> 15-16, *h*<sub>2</sub> 25-30, *h*<sub>3</sub> 17-18, *c*<sub>2</sub> 34-36, *la* 18-20, *3a* 20-21, *4a* 20, *ag*<sub>1</sub> 13-15, *ag*<sub>2</sub> 13-14, *ag*<sub>3</sub> 13-14, *ag*<sub>4</sub> 17-20, *g*<sub>1</sub> 13-15, *g*<sub>2</sub> 17-20, *ps*<sub>1</sub> 20-21, *ps*<sub>2</sub> 21-22 and *ps*<sub>3</sub> 15-18 in the Turkish specimens) are different from the type specimens setae *vi* 16, *ve* 46 (46-50), *sci* 20, *sce* 24 (24-26), *c*<sub>1</sub> 18 (16-18), *d*<sub>1</sub> 16, *d*<sub>2</sub> 16, *e*<sub>1</sub> 18 (18-20), *e*<sub>2</sub> 18 (16-18), *f* 20 (20-22), *h*<sub>1</sub> 20 (20-22), *h*<sub>2</sub> 32 (32-36), *h*<sub>3</sub> 20 (20-22), *c*<sub>2</sub> 40 (40-46), *la* 19 (19-23), *3a* 23, *4a* 19 (19-23), *ag*<sub>1</sub> 15, *ag*<sub>2</sub> 15, *ag*<sub>3</sub> 15, *ag*<sub>4</sub> 23, *g*<sub>1</sub> 15, *g*<sub>2</sub> 19, *ps*<sub>1</sub> 27 (25-27), *ps*<sub>2</sub> 22, *ps*<sub>3</sub> 19 in the Greece specimens). Measurements of about all body setae of the Turkish specimen is smaller than the Greece specimens.

*S. canestrinii* was found in the type locality (Greece) [33]. This is the second report of this species and a new record for the Turkish fauna.

#### Author's Contributions

**Mustafa Akyol:** The specimens were collected, taken to the laboratory mounted on slides, the mite specimens were drawn, measured, described and illustrated. Wrote and rafted the manuscript.

#### Ethics

There are no ethical issues after the publication of this manuscript.

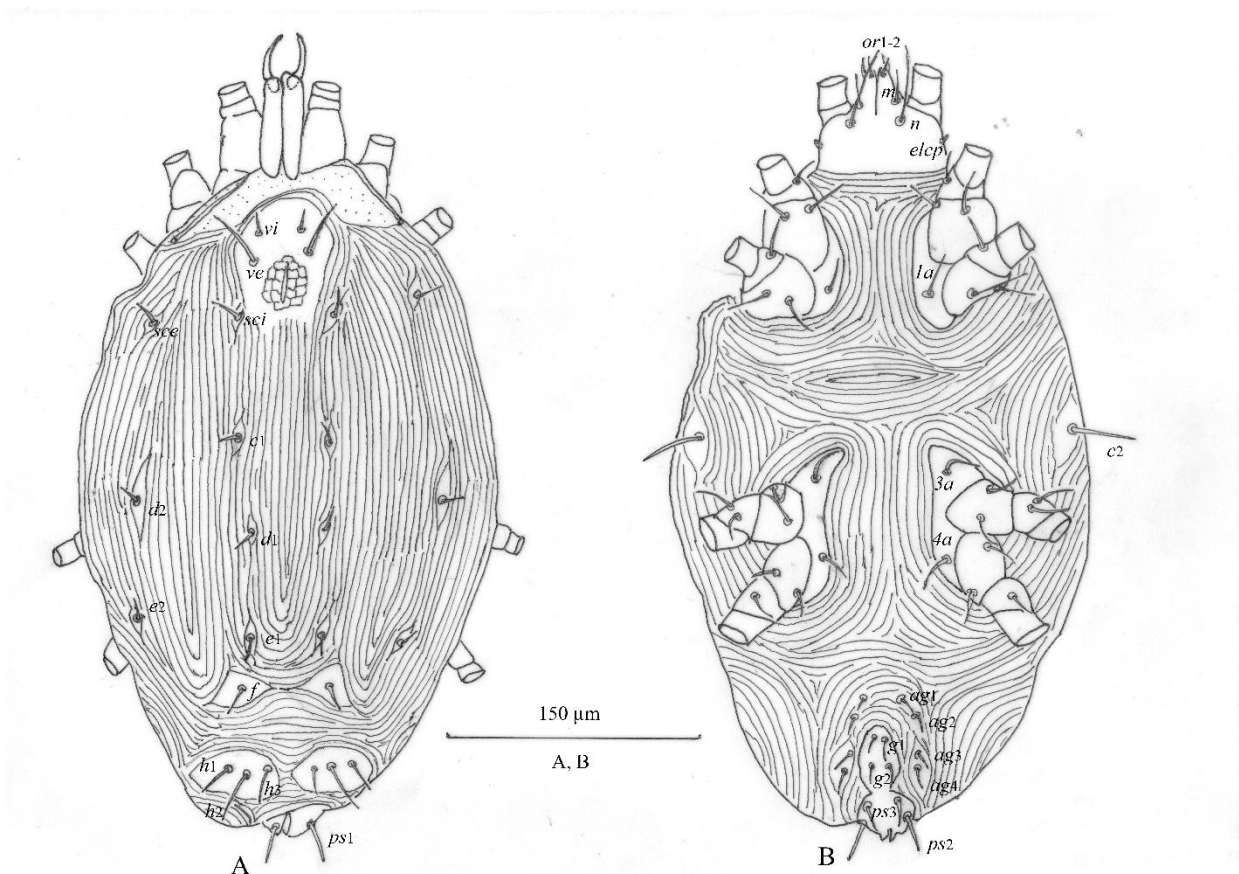


**Figure 1.** *Stigmaeus canestrinii* Stathakis, Kapaxidi and Papadoulis (female): A. Dorsal view of idiosoma, B. Ventral view of idiosoma.

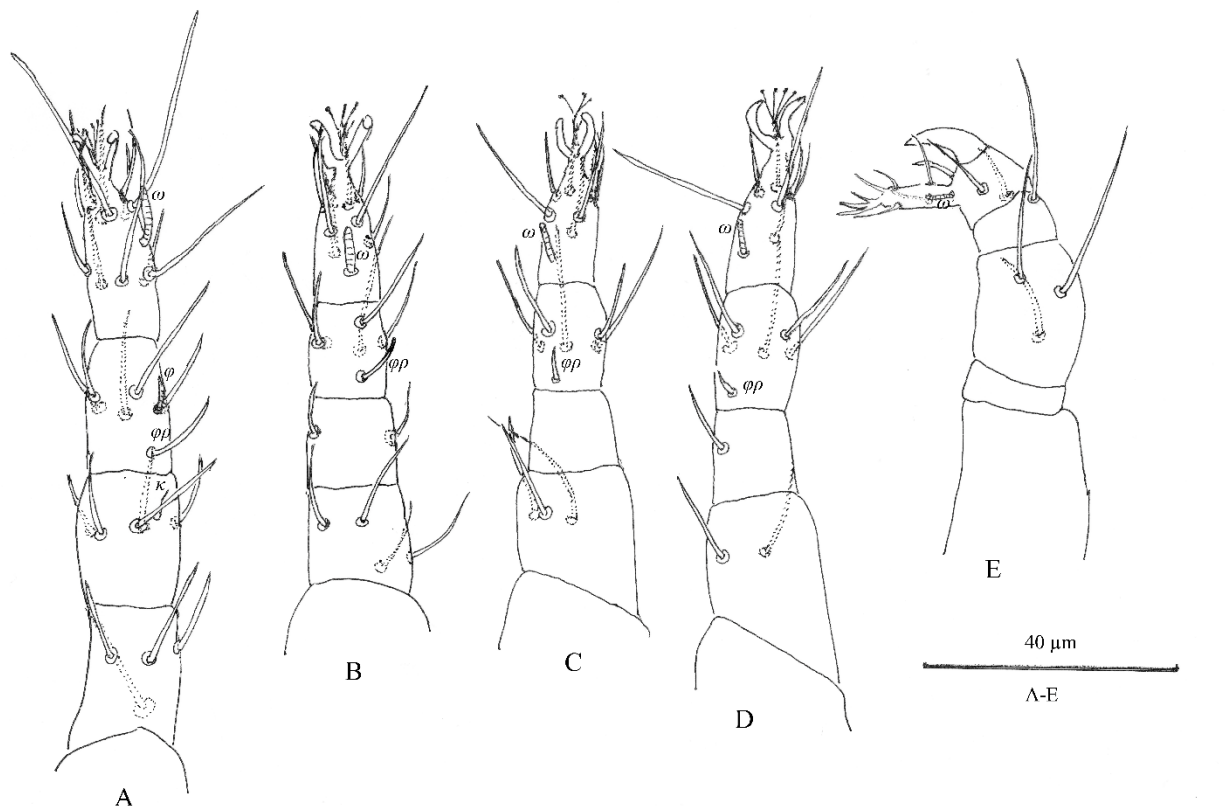


**Figure 2.** *Stigmaeus canestrinii* Stathakis, Kapaxidi and Papadoulis (female): A. Leg I, B. Leg II, C. Leg III, D. Leg IV, E. Palp.

## References

- [1]. Santos, MA, Laing, JE. Stigmaeid predators. In: Helle, W. and Sabelis, M.W. (eds.), Spider Mites, Theirs Biology, Natural Enemies and Control. Vol. 1B. Elsevier, Amsterdam, 1985; pp. 197-203.
- [2]. Gerson, U, Smiley, RL, Ochoa, R. Mites (Acari) for Pest Control. Blackwell Science, Oxford, 2003; 539 pp.
- [3]. Fan, Q-H, Zhang, Z-Q. Raphignathoidea (Acari: Prostigmata). Fauna of New Zealand 52. Manaaki Whenua Press, 2005; 400 pp.
- [4]. Fan, Q-H, Flechtmann, CHW. Stigmaeidae. In: Carrillo, D., Moraes, G.J. de and Peña, J. (eds.), Prospects for Biological Control of Plant Feeding Mites and Other Harmful Organisms. Chapter 7, Springer, NY, 2015; pp. 185-206.
- [5]. Fan, Q-H, Flechtmann, CHW, De Moraes, DJ. 2016. Annotated catalogue of Stigmaeidae (Acari: Prostigmata), with a pictorial key to genera. *Zootaxa*, 4176: 1-199.
- [6]. Khaustov, AA. 2023. A new species and two new records of Stigmaeidae (Acari: Prostigmata) from Russia. *Systematic and Applied Acarology*, 28(11):1789-1802
- [7]. Koç, K, Ayyıldız, N. 1997. Stigmaeid mites new to the Turkish fauna (Acari, Prostigmata, Stigmaeidae). *Turkish Journal of Zoology*, 21 (4): 445-459.
- [8]. Doğan, S, Ayyıldız, N. 2003. *Stigmaeus kamili*, a new species of the genus *Stigmaeus* (Acari, Stigmaeidae) from Turkey with new data of other stigmaeid mites. *Archives des Sciences*, 56 (1): 1-10.
- [9]. Doğan, S. 2003. A new species and two new records of the genus *Stigmaeus* (Acari: Stigmaeidae) from Turkey. *International Journal of Acarology*, 29 (4): 381-387.
- [10]. Doğan, S. 2019a. A new species of the genus *Stigmaeus* Koch (Acari: Stigmaeidae) from Turkey. *International Journal of Acarology*, 45 (3): 141-147.
- [11]. Doğan, S. 2019b. Raphignathoidea (Acari: Trombidiformes) of Turkey: A review of progress on the systematics, with an updated checklist. *Acarological Studies*, 1 (2): 129-151.
- [12]. Koç, K. 2005. Two new species of the genus *Stigmaeus* (Acari: Stigmaeidae) from Turkey. *Archives des Sciences*, 58 (1): 43-48.
- [13]. Akyol, M, Koç, K. 2007. Four new species of the genus *Stigmaeus* (Acari: Stigmaeidae) from Turkey. *Archives des Sciences*, 60: 41-50.
- [14]. Dönel, G, Doğan, S. 2011. The stigmaeid mites (Acari: Stigmaeidae) of Kelkit Valley (Turkey). *Zootaxa*, 2942: 1-56.
- [15]. Özçelik, S, Doğan, S. 2011. A systematic investigation on stigmaeid mites (Acari: Stigmaeidae) of Uzunoluk Forest (Erzurum, Turkey). *Turkish Journal of Entomology*, 35 (4): 699-719. [In Turkish]

- [16]. Dönel, G, Doğan, S, Sevsay, S, Bal, DA. 2012. Two new mite species of the genus *Stigmaeus* (Acari: Stigmaeidae) from Turkey. *Turkish Journal of Zoology*, 36: 585-591.
- [17]. Uluçay, İ. 2015a. *Stigmaeus ceylani*, a new species of the genus *Stigmaeus* Koch (Acari: Stigmaeidae) from Turkey. *Turkish Journal of Entomology*, 39 (1): 35-46.
- [18]. Uluçay, İ. 2015b. Two new records of the genus *Stigmaeus* (Acari: Trombidiformes: Stigmaeidae) from Turkey. *Persian Journal of Acarology*, 4 (3), 287-295.
- [19]. Uluçay, İ. 2015c. Two species of stigmaeid mites from Turkey: *Eryngiopus coheni* Vacante and Gerson, 1987 and *Stigmaeus berwariensis* n. sp. (Acari: Stigmaeidae). *International Journal of Acarology*, 41 (3): 214-219.
- [20]. Doğan, S, Bingül, M, Dilkaraoğlu, S, Fan, Q-H. 2015a. Description of a new species of the genus *Stigmaeus* Koch (Acari: Stigmaeidae) from Turkey, with a list of described species in the world. *International Journal of Acarology*, 41 (4): 290-299.
- [21]. Doğan, S, Sevsay, S, Ayyıldız, N, Özbek, HH, Dilkaraoğlu, S, Erman, O, Aksoy, H. 2015b. The mite fauna of Ekşisu Marshes in Erzincan (Turkey). *Turkish Journal of Zoology*, 39 (4): 571-579.
- [22]. Doğan, S, Doğan, S, Erman, O. 2017. Description of five new species of the genus *Stigmaeus* Koch (Acari: Raphignathoidea: Stigmaeidae) from Turkey. *Zootaxa*, 4276: 451-478.
- [23]. Bingül, M, Doğan, S, Dilkaraoğlu, S. 2017. Contributions to the knowledge of the mite genus *Stigmaeus* Koch, 1836 (Acari: Stigmaeidae) of Turkey. *European Journal of Taxonomy*, 307: 1-16.
- [24]. Akyol, M. 2019. A new species of the genus *Stigmaeus* Koch (Acari: Stigmaeidae) from the Aegean region of Turkey. *Systematic and Applied Acarology*, 24 (4): 581-586.
- [25]. Akyol, M. 2021. Two New Records of Stigmaeid Mites (Acari: Stigmaeidae) for the Turkish Fauna. *KSÜ Tarım ve Doğa Dergisi*, 24 (2): 430-434.
- [26]. Akyol, M. 2023. *Stigmaeus quercus* (Acari: Stigmaeidae), a new species from Manisa province, Türkiye. *Systematic and Applied Acarology*, 28 (2): 167-172.
- [27]. Doğan, S. & Doğan, S. 2020a. A new species of the genus *Stigmaeus* Koch (Acari: Stigmaeidae) from Pülümür Valley (Turkey). *Acarological Studies*, 2(1): 41-45 (In Turkish).
- [28]. Doğan, S, Doğan, S. 2020b. Newly recorded stigmaeid mites (Acariformes: Raphignathoidea: Stigmaeidae) for the fauna of Turkey. *Acarological Studies*, 2(2): 94-118 (In Turkish).
- [29]. Doğan, S, Doğan, S. 2021. *Stigmaeus exilis*, a new fusiform species of *Stigmaeus* Koch (Acariformes: Stigmaeidae) from Sansa, Turkey. *Persian Journal of Acarology*, 10(1): 19-28.
- [30]. Erman, O, Doğan, S, Ayyıldız, N, Özkan, M. 2024. Checklist of the mites (Acari) of Türkiye. Third supplement. *Acarological Studies*, 6 (2): 81-111.
- [31]. Kethley, J. Acarina: Prostigmata (Actinedida). In: Soil Biology Guide. Dindal, D.L. (Ed.). Wiley, New York, 1990, 667-756.
- [32]. Grandjean, F. 1944. Observations sur les acariens de la famille des Stigmaeidae. *Archives des Sciences physiques et naturelles*, 26: 103-131.
- [33]. Stathakis T., E.V. Kapaxidi, G.T. Papadoulis. 2019. The genus *Stigmaeus* Koch (Acari: Stigmaeidae) from Greece. *Systematic and Applied Acarology*, 24(11): 2010–2093.

# Differential Equations for Spacelike Curves According to Light-Cone Frame in $L_0^3$

Tanju Kahraman<sup>1\*</sup> 

<sup>1</sup> Department of Mathematics, Faculty of Engineering and Naturel Sciences  
Manisa Celal Bayar University, Şehit Prof. Dr. İlhan Varank Campus, Manisa, Türkiye

\* [tanju.kahraman@cbu.edu.tr](mailto:tanju.kahraman@cbu.edu.tr)

\* Orcid No: 0000-0002-0653-712X

Received: 26 August 2024

Accepted: 3 December 2024

DOI: 10.18466/cbayarfbe.1538669

## Abstract

In this study, we obtain differential equations of spacelike curves according to components of light-cone frame in light cone  $L_0^3$  in Minkowski 5-space. We find some relations between curvatures of the spacelike curves.

**Keywords:** Differential equations, Spacelike curves, Light-cone frame, Minkowski 5-space.

## 1. Introduction

To study differential geometry of curves, we know that is required moving frames along curves. By helping of the frames, many mathematicians are studied differential geometry of curves in many spaces, especially such as associated curves and quaternionic curves [4,6,7].

As known, one of the popular studies of differential geometry and physics is curves on light cones and semi-Riemannian manifolds. However, since the metric is degenerate on light cone in Minkowski spaces. In the light of [1,2,3,5], a new type of frame has established by Wang and He and is called as light-cone frame, then, using the light-cone frame, they have been studied singularities of hypersurfaces along spacelike curves in light cone in Minkowski 5-space [12].

For theory of general relativity, one of the right constructions is five-dimensional space [10]. Einstein and Bergmann said that "... It is much more satisfactory to introduce the fifth dimension not only formally, but to assign it some physical meaning. Nevertheless, there is no contradiction with the empirical four-dimensional character of physical space" [10]. Therefore, studies in five dimensional spaces continue to increase recently.

Dannon showed that spherical curves in can be constructed by Frenet formulae. Then, integral characterizations of spherical curves in were given by her

[9]. Kazaz et al. gave similar characterizations of timelike and spacelike spherical curves lying on Lorentzian sphere in the [6]. They have found the differential equation systems characterizing the spherical curves in. Sezer has found the differential equations and integral characterizations of spherical curves in by using differential equation system given by Dannon [8].

In this paper, we study differential equations of spacelike curves in light cone in Minkowski 5-space. Besides, we have relations of differential equations of the curves for some special conditions.

## 2. Materials and Methods

Minkowski 5-space  $IR_1^5$  is provided with the standart lorentz metric given by

$$\langle , \rangle = -dx_1^2 + dx_2^2 + dx_3^2 + dx_4^2 + dx_5^2$$

where  $(x_1, x_2, x_3, x_4, x_5)$  is a rectangular coordinate system of  $IR_1^5$ . According to this metric, an arbitrary vector  $\vec{v} = (v_1, v_2, v_3, v_4, v_5)$  in  $IR_1^5$  have one of three Lorentzian causal characters; it can be spacelike if  $\langle \vec{v}, \vec{v} \rangle > 0$  or  $\vec{v} = 0$ , timelike if  $\langle \vec{v}, \vec{v} \rangle < 0$  and null(lightlike) if  $\langle \vec{v}, \vec{v} \rangle = 0$  and  $\vec{v} \neq 0$  Similarly, an arbitrary curve  $\gamma = \gamma(s)$  can be spacelike, timelike or null (lightlike), if all its velocity vectors  $\gamma'(s)$  are spacelike, timelike or null (lightlike), respectively. We say that a timelike vector is future pointing or past



pointing if the first compound of the vector is positive or negative, respectively.

In the Minkowski 5-space, there exists the pseudo-inner product  $\langle x, y \rangle = -x_1y_1 + x_2y_2 + x_3y_3 + x_4y_4 + x_5y_5$  of any vectors  $x = (x_1, x_2, x_3, x_4, x_5)$  and  $y = (y_1, y_2, y_3, y_4, y_5)$ , and the pseudo vector product is defined by

$$x \wedge y \wedge z \wedge w = \begin{vmatrix} -e_1 & e_2 & e_3 & e_4 & e_5 \\ x_1 & x_2 & x_3 & x_4 & x_5 \\ y_1 & y_2 & y_3 & y_4 & y_5 \\ z_1 & z_2 & z_3 & z_4 & z_5 \\ w_1 & w_2 & w_3 & w_4 & w_5 \end{vmatrix},$$

where vectors  $x, y, z, w$  are in Minkowski 5-space and  $(e_1, e_2, e_3, e_4, e_5)$  is the canonical basis of Minkowski 5-space [5,12].

A pseudo sphere whose vertex is at origin is defined as follows;

$$S_1^4 = \{x \in IR_1^5: -x_1^2 + x_2^2 + x_3^2 + x_4^2 + x_5^2 = 1\}.$$

The four-dimensional open light cone is defined as  $LC_*^4 = \{x \in IR_1^5: -x_1^2 + x_2^2 + x_3^2 + x_4^2 + x_5^2 = 0\} \setminus \{0\}$ .

The three-dimensional open light cone  $L_0^3$  in  $LC_*^4$  is defined as

$$L_0^3 = \{x \in LC_*^4: x_2 = 0, -x_1^2 + x_3^2 + x_4^2 + x_5^2 = 0\} \setminus \{0\}.$$

Let  $\gamma: I \rightarrow L_0^3$  be a unit speed spacelike curve in light cone in Minkowski 5-space. The moving Frénet frame along the curve  $\gamma$  is denoted by  $\{\gamma(s), \gamma_L(s), t(s), b(s), e_2\}$  and is called the light-cone frame. Differential formulae according to the light-cone frame is given as follows

$$\begin{aligned} \gamma'(s) &= t(s) \\ \gamma_L'(s) &= k(s)t(s) + \tau(s)b(s) \\ t'(s) &= \frac{k(s)}{2}\gamma(s) + \frac{1}{2}\gamma_L(s) \\ b'(s) &= \frac{\tau(s)}{2}\gamma(s), \end{aligned}$$

where

$$\begin{aligned} \langle t(s), t(s) \rangle &= \langle b(s), b(s) \rangle = \langle e_2, e_2 \rangle = 1, \\ \langle \gamma(s), \gamma_L(s) \rangle &= -2, \\ \langle \gamma(s), \gamma(s) \rangle &= \langle \gamma_L(s), \gamma_L(s) \rangle = \langle t(s), \gamma(s) \rangle = \langle t(s), \gamma_L(s) \rangle \\ &= \langle t(s), b(s) \rangle = \langle t(s), e_2 \rangle = 0, \\ \langle b(s), \gamma(s) \rangle &= \langle b(s), \gamma_L(s) \rangle \\ &= \langle e_2, \gamma(s) \rangle = \langle e_2, \gamma_L(s) \rangle = \langle e_2, b(s) \rangle = 0, \end{aligned}$$

and light-cone curvature  $k(s)$  and light-cone torsion  $\tau(s)$  are given by

$$\begin{aligned} k(s) &= -\langle \gamma''(s), \gamma''(s) \rangle, \\ \tau(s) &= -2 \det(\gamma(s), \gamma'(s), \gamma''(s), \gamma'''(s), e_2) \end{aligned}$$

respectively [12].

Suppose that  $\gamma(\varphi)$  be another parametrization of the curve with parameter  $\varphi = \int k(s)ds$ . Then, light-cone formulae can be written as follows

$$\begin{bmatrix} \frac{d\gamma}{d\varphi} \\ \frac{d\gamma_L}{d\varphi} \\ \frac{dt}{d\varphi} \\ \frac{db}{d\varphi} \end{bmatrix} = \begin{bmatrix} 0 & 0 & f(\varphi) & 0 \\ 0 & 0 & 1 & g(\varphi) \\ \frac{1}{2} & \frac{1}{2}f(\varphi) & 0 & 0 \\ \frac{1}{2}g(\varphi) & 0 & 0 & 0 \end{bmatrix} \begin{bmatrix} \gamma \\ \gamma_L \\ t \\ b \end{bmatrix} \quad (1)$$

where  $f(\varphi) = \frac{1}{k(\varphi)}$  and  $g(\varphi) = \frac{\tau(\varphi)}{k(\varphi)}$ . Each derivative equations given by the Light-cone formulae is expressed with the equations (1<sub>1</sub>), (1<sub>2</sub>), (1<sub>3</sub>) and (1<sub>4</sub>) respectively.

In following section, we obtain differential equations of spacelike curves according to components of light-cone frame in light cone  $L_0^3$  in Minkowski 5-space.

### 3. Differential Equations of Spacelike Curves according to Light-Cone Frame

**Theorem 1.** Let  $\gamma(s)$  be a spacelike curve parametrized by arclength  $s$  in light cone  $L_0^3$  in Minkowski 5-space. Suppose that  $\gamma(\varphi)$  be another parametrization of the curve with parameter  $\varphi = \int k(s)ds$ . Then,  $\gamma(s)$  satisfies differential equation of fourth order according to Light-cone frame  $\gamma(s)$  given by

$$\frac{d}{d\varphi} \left[ \frac{2}{f^2g} \frac{d^3\gamma}{d\varphi^3} - \frac{6}{f^3g} \frac{df}{d\varphi} \frac{d^2\gamma}{d\varphi^2} + \left( \frac{6}{f^4g} \left( \frac{df}{d\varphi} \right)^2 - \frac{2}{fg} - \frac{2}{f^3g} \frac{d^2f}{d\varphi^2} \right) \frac{d\gamma}{d\varphi} + \frac{1}{f^2g} \frac{df}{d\varphi} \gamma \right] = \frac{1}{2} g \gamma. \quad (2)$$

*Proof.* Let  $\gamma(\varphi)$  be a spacelike curve parametrized by arclength  $\varphi$  in light cone  $L_0^3$ . Then, taking derivation of equality (1<sub>1</sub>) twice, we obtain

$$\frac{d^2\gamma}{d\varphi^2} = \frac{1}{2}f\gamma + \frac{df}{d\varphi}t + \frac{1}{2}f^2\gamma_L \quad (3)$$

and

$$\frac{d^3\gamma}{d\varphi^3} = \frac{df}{d\varphi}\gamma + \frac{1}{2}f\frac{d\gamma}{d\varphi} + \frac{3}{2}f\frac{df}{d\varphi}\gamma_L + \left( \frac{d^2f}{d\varphi^2} + \frac{1}{2}f^2 \right) t + \frac{1}{2}f^2g\gamma \quad (4)$$

respectively.

If equality (1<sub>1</sub>) is arranged and is derivated, we get

$$\frac{dt}{d\varphi} = \frac{-1}{f^2} \frac{df}{d\varphi} \frac{d\gamma}{d\varphi} + \frac{1}{f} \frac{d^2\gamma}{d\varphi^2}. \quad (5)$$

By substituting (5) into (1<sub>3</sub>), we obtain

$$\gamma_L = \frac{-1}{f} \gamma - \frac{2}{f^3} \frac{df}{d\varphi} \frac{d\gamma}{d\varphi} + \frac{2}{f^2} \frac{d^2\gamma}{d\varphi^2}. \quad (6)$$

Then, by substituting (1<sub>3</sub>) and (6) into (4), we have

$$\begin{aligned} b &= \frac{2}{f^2g} \frac{d^3\gamma}{d\varphi^3} - \frac{6}{f^3g} \frac{df}{d\varphi} \frac{d^2\gamma}{d\varphi^2} + \left( \frac{6}{f^4g} \left( \frac{df}{d\varphi} \right)^2 - \frac{2}{fg} - \frac{2}{f^3g} \frac{d^2f}{d\varphi^2} \right) \frac{d\gamma}{d\varphi} \\ &+ \frac{1}{f^2g} \frac{df}{d\varphi} \gamma. \end{aligned} \quad (7)$$

Using the equations (14) and (7), we obtain desired equation (2).

**Corollary 1.** Let  $\gamma(\varphi)$  be a spacelike curve in light cone  $L_0^3$ . If the function  $f$  of  $\gamma(\varphi)$  is constant, then following equation is satisfied:

$$\frac{2}{f^2 g} \frac{d^4 \gamma}{d\varphi^4} - \frac{2g'}{f^2 g^2} \frac{d^3 \gamma}{d\varphi^3} - \frac{2}{f g} \frac{d^2 \gamma}{d\varphi^2} + \frac{2g'}{f g^2} \frac{d\gamma}{d\varphi} - \frac{1}{2} g \gamma = 0.$$

**Theorem 2.** Let  $\gamma(\varphi(s))$  be a spacelike curve parametrized by  $\varphi = \int k(s)ds$  in light cone  $L_0^3$  in Minkowski 5-space. Then,  $\gamma(\varphi)$  satisfies differential equation of fourth order according to Light-cone frame  $b$  given by

$$\begin{aligned} \frac{d^4 b}{d\varphi^4} = & \frac{3}{f g} \frac{d(f g)}{d\varphi} \frac{d^3 b}{d\varphi^3} \\ & + \left[ \frac{3}{g} \frac{d^2 g}{d\varphi^2} + f + \frac{9}{f g} \frac{d f}{d\varphi} \frac{d g}{d\varphi} + \frac{1}{f} \frac{d^2 f}{d\varphi^2} \right. \\ & + \frac{6}{g^2} \left( \frac{d g}{d\varphi} \right)^2 + \frac{3}{f^2} \left( \frac{d f}{d\varphi} \right)^2 + \frac{3}{f g} \frac{d f}{d\varphi} \frac{d g}{d\varphi} \left. \right] \frac{d^2 b}{d\varphi^2} \\ & + \left[ \frac{3}{f^2 g} \left( \frac{d f}{d\varphi} \right)^2 \frac{d g}{d\varphi} + \frac{6}{f g^2} \frac{d f}{d\varphi} \left( \frac{d g}{d\varphi} \right)^2 + \frac{6}{g^3} \left( \frac{d g}{d\varphi} \right)^3 \right. \\ & + \left. \left[ \frac{3}{f g} \frac{d f}{d\varphi} \frac{d^2 g}{d\varphi^2} - \frac{3}{g^2} \frac{d g}{d\varphi} \left( 1 + \frac{d^2 g}{d\varphi^2} \right) - \frac{f}{g} \frac{d g}{d\varphi} - \frac{1}{f g} \frac{d g}{d\varphi} \frac{d^2 f}{d\varphi^2} \right] \right] \frac{d b}{d\varphi} \\ & + \frac{1}{4} f^2 g^2 b. \end{aligned} \quad (8)$$

*Proof.* Let  $\gamma(\varphi)$  be a spacelike curve parametrized by arclength  $\varphi$  in light cone  $L_0^3$ . Then, taking derivation of equality (14) three times, we obtain

$$\frac{d^2 b}{d\varphi^2} = \frac{1}{2} \frac{d g}{d\varphi} \gamma + \frac{1}{2} f g t, \quad (9)$$

$$\frac{d^3 b}{d\varphi^3} = \left( \frac{1}{2} \frac{d^2 g}{d\varphi^2} + \frac{1}{4} f g \right) \gamma + \frac{1}{4} f^2 g \gamma_L + \left( \frac{d g}{d\varphi} f + \frac{1}{2} g \frac{d f}{d\varphi} \right) \quad (10)$$

and

$$\begin{aligned} \frac{d^4 b}{d\varphi^4} = & \left( \frac{1}{2} \frac{d^3 g}{d\varphi^3} + \frac{3}{4} f \frac{d g}{d\varphi} + \frac{1}{2} \frac{d f}{d\varphi} g \right) \gamma + \left( \frac{3}{4} f g \frac{d f}{d\varphi} + \frac{3}{4} f^2 \frac{d g}{d\varphi} \right) \gamma_L \\ & + \left( \frac{3}{2} f \frac{d^2 g}{d\varphi^2} + \frac{1}{2} f^2 g + \frac{3}{2} \frac{d f}{d\varphi} \frac{d g}{d\varphi} + \frac{1}{2} g \frac{d^2 f}{d\varphi^2} \right) t + \left( \frac{1}{4} f^2 g^2 \right) b. \end{aligned} \quad (11)$$

Using the equations (11) and (14), we have

$$t = \frac{-2}{f g^2} \frac{d g}{d\varphi} \frac{d b}{d\varphi} + \frac{2}{f g} \frac{d^2 b}{d\varphi^2}. \quad (12)$$

By substituting (14) into (13), we get

$$2 \frac{d t}{d\varphi} = \frac{2}{g} \frac{d b}{d\varphi} + f \gamma_L \quad (13)$$

and, by substituting (12) into (13), we obtain

$$\gamma_L = \frac{2}{f} \frac{d}{d\varphi} \left( \frac{-2}{f g^2} \frac{d g}{d\varphi} \frac{d b}{d\varphi} + \frac{2}{f g} \frac{d^2 b}{d\varphi^2} \right) - \frac{2}{f g} \frac{d b}{d\varphi}. \quad (14)$$

By using the equations (14), (12) and (14) into (11), the equation (8) is obtained.

**Corollary 2.** Let  $\gamma(\varphi)$  be a spacelike curve in light cone  $L_0^3$ . If the function  $f$  of  $\gamma(\varphi)$  is constant, then following equation is obtained.

$$\begin{aligned} \frac{d^4 b}{d\varphi^4} - \frac{3}{g} \frac{d g}{d\varphi} \frac{d^3 b}{d\varphi^3} - \left[ \frac{3}{g} \frac{d^2 g}{d\varphi^2} + f + \frac{6}{g^2} \left( \frac{d g}{d\varphi} \right)^2 \right] \frac{d^2 b}{d\varphi^2} \\ - \left[ \frac{6}{g^3} \left( \frac{d g}{d\varphi} \right)^2 - \frac{3}{g^2} - \frac{3}{g^2} \frac{d^2 g}{d\varphi^2} - \frac{f}{g} \right] \frac{d g}{d\varphi} \frac{d b}{d\varphi} \\ - \frac{1}{4} f^2 g^2 b = 0 \end{aligned}$$

**Corollary 3.** Let  $\gamma(\varphi)$  be a spacelike curve in light cone  $L_0^3$ . If the function  $g$  of  $\gamma(\varphi)$  is constant, then following differential equation is satisfied:

$$\frac{d^4 b}{d\varphi^4} - \frac{3}{f} \frac{d f}{d\varphi} \frac{d^3 b}{d\varphi^3} - \left[ f + \frac{1}{f} \frac{d^2 f}{d\varphi^2} + \frac{3}{f^2} \left( \frac{d f}{d\varphi} \right)^2 \right] \frac{d^2 b}{d\varphi^2} - \frac{1}{4} f^2 g^2 b = 0$$

**Theorem 3.** Let  $\gamma(\varphi(s))$  be a spacelike curve parametrized by  $\varphi = \int k(s)ds$  in light cone  $L_0^3$  in Minkowski 5-space. Then,  $\gamma(\varphi)$  satisfies differential equation of fourth order according to Light-cone frame  $t$  given by

$$\begin{aligned} \frac{d}{d\varphi} \left[ \left( \frac{f^3 g^3 + 4 g f^2 + 2 f f' g' - 2 f g f''}{f^3 g^3 + 4 g f^2 + 2 f f' g' - 2 f g f''} \right) \frac{d^3 t}{d\varphi^3} - \left( \frac{8 f g f' + 4 f^2 g'}{f^3 g^3 + 4 g f^2 + 2 f f' g' - 2 f g f''} \right) \frac{d^2 t}{d\varphi^2} \right. \\ \left. + \left( \frac{8 g f^2 + 4 f f' g' - 4 f g f'' - 4 f^3 g}{f^3 g^3 + 4 g f^2 + 2 f f' g' - 2 f g f''} \right) \frac{d t}{d\varphi} + \left( \frac{2 f^2 g f' + 4 f^3 g'}{f^3 g^3 + 4 g f^2 + 2 f f' g' - 2 f g f''} \right) t \right] \\ - f t = 0. \end{aligned} \quad (15)$$

*Proof.* Let  $\gamma(\varphi)$  be a spacelike curve parametrized by arclength  $\varphi$  in light cone  $L_0^3$ . Then, by editing equation (13), we can write

$$\gamma_L = \frac{2}{f} \frac{d t}{d\varphi} - \frac{1}{f} \gamma. \quad (16)$$

Using the equations (16) and (12), we have

$$b = \frac{-2}{f^2} \frac{d f}{d\varphi} \frac{d t}{d\varphi} + \frac{2}{f g} \frac{d^2 t}{d\varphi^2} + \frac{1}{f^2 g} \frac{d f}{d\varphi} \gamma - \frac{2}{g} t. \quad (17)$$

By taking derivation of (17) and using the (14), we get

$$\begin{aligned} \left( \frac{g}{2} + \frac{2 f^2}{f^3 g} + \frac{f' g'}{f^2 g^2} - \frac{f''}{f^2 g} \right) \gamma = \left( \frac{2}{f g} \right) \frac{d^3 t}{d\varphi^3} - \left( \frac{4 f'}{f^2 g} + \frac{2 g'}{f g^2} \right) \frac{d^2 t}{d\varphi^2} \\ + \left( \frac{4 f^2}{f^3 g} + \frac{2 f' g'}{f^2 g^2} - \frac{2 f''}{f^2 g} - \frac{2}{g} \right) \frac{d t}{d\varphi} + \left( \frac{f'}{f g} + \frac{2 g'}{g^2} \right) t \end{aligned} \quad (18)$$

and by taking derivation of (18) again, we obtain desired result.

**Corollary 4.** Let  $\gamma(\varphi)$  be a spacelike curve in light cone  $L_0^3$ . If the function  $f$  of  $\gamma(\varphi)$  is constant, then following differential equation is given by

$$\begin{aligned} \frac{4}{f g^2} \frac{d^4 t}{d\varphi^4} - \frac{12 g'}{f g^3} \frac{d^3 t}{d\varphi^3} - \left( \frac{4 g''}{f g^3} - \frac{12 g'^2}{f g^4} + \frac{4}{g^2} \right) \frac{d^2 t}{d\varphi^2} \\ + \left( \frac{8 g'}{g^3} + \frac{4 g''}{g^6} \right) \frac{d t}{d\varphi} + \left( \frac{4 g''}{g^6} - \frac{12 g'^2}{g^4} - f \right) t \\ = 0 \end{aligned}$$

**Corollary 5.** Let  $\gamma(\varphi)$  be a spacelike curve in light cone  $L_0^3$ . If the function  $g$  of  $\gamma(\varphi)$  is constant, then following differential equation is given by



$$\begin{aligned} & \left( \frac{4f^2}{f^3g^2+2f'^2-ff''} \right) \frac{d^4t}{d\varphi^4} + \left[ \frac{-12f^4g^2f'-12f^2f'f''+4f^3f'''}{(f^3g^2+2f'^2-ff'')^2} \right] \frac{d^3t}{d\varphi^3} \\ & - \left( \frac{8f'^2+8ff''}{f^3g^2+2f'^2-ff''} - \frac{8ff'(3f^2g^2f'+3f'f''-ff''')}{(f^3g^2+2f'^2-ff'')^2} \right. \\ & \quad \left. - \frac{8f'^2-4ff''-2f^3}{f^3g^2+2f'^2-ff''} \right) \frac{d^2t}{d\varphi^2} \\ & + \left[ \frac{d}{d\varphi} \left( \frac{8f'^2-4ff''-4f^3}{f^3g^2+4f'^2-2ff''} \right) + \frac{2f^2}{f^3g^2+4f'^2-2ff''} \right] \frac{dt}{d\varphi} \\ & + \left[ \frac{d}{d\varphi} \left( \frac{2f^2}{f^3g^2+4f'^2-2ff''} \right) - f \right] t = 0. \end{aligned}$$

## Author's Contributions

**Tanju Kahraman:** Drafted and wrote the manuscript, performed the experiment and result analysis.

## Ethics

There are no ethical issues after the publication of this manuscript.

## References

- [1]. B. Sahin, On a Submersion Between Reinhart Lightlike Manifolds and Semi-Riemannian Manifolds, *Mediterr. J. Math.* 5(2008), 273–284.
- [2]. F. J. Palomo, F. J. Rodriguez, A. Romero, New characterizations of compact Totally umbilical spacelike surfaces in 4-Dimensional Lorentz Minkowski spacetime through a lightcone, *Mediterr. J. Math.* 11(2014), 1229–1240.
- [3]. G. Ganchev, V. Milousheva, An invariant theory of spacelike surfaces in the four-dimensional Minkowski space, *Mediterr. J. Math.* 9(2012), 267–294.
- [4]. H. Liu, J. Miao, D. Pei, Curves and surfaces of spacelike curves according to Bishop frame and their singularities, *J. Nonlinear Sci. Appl.*, 9, 5020–5037 (2017).
- [5]. K. L. Duggal, B. Sahin, *Differential Geometry of Lightlike Submanifolds*, Birkhäuser, Boston, 2010.
- [6]. M. Kazaz, H.H. Uğurlu, A. Özdemir, Integral Characterizations for Timelike and Spacelike Curves on Lorentzian Sphere, *Iranian Journal of Science and Technology, Transaction A*, Vol. 32, No. A1, 2008
- [7]. M. Önder, T. Kahraman, H.H. Uğurlu, Differential Equations and Integral Characterizations of Timelike and Spacelike Spherical Curves in the Minkowski Space-time *Matematychni Studii*, V.40, No.1, 2013, pp. 30-37.
- [8]. M. Sezer, Differential Equations and Integral Characterizations for Spherical Curves, *Turkish J. Math.*, Vol. 13, No. 3, 1989.
- [9]. V. Dannon, Integral Characterizations and the Theory of Curves, *Proceedings of the American Mathematical Society*, Volume 81, Number 4, (1981), 600-602.
- [10]. W. Edward, A Note On Einstein, Bergmann, and the Fifth Dimension, *arXiv:1401.8048 [physics.hist-ph]* (2014).
- [11]. J. Walrave, Curves and surfaces in Minkowski space, PhD. thesis, K.U. Leuven, Fac. of Science, Leuven, 1995.
- [12]. Z. Wang, M. He, Singularities dual hypersurfaces and hyperbolic focal surfaces along spacelike curves in light cone in Minkowski 5-space, *Mediterr. J. Math.* (2019) 16(4):96 <https://doi.org/10.1007/s00009-019-1355-5>

# An Application on Enterprise Resource Planning (ERP) Selection with Multi-Criteria Decision-Making Methods

Huriye Akpınar<sup>1\*</sup> 

<sup>1</sup> Independent Researcher, İzmir, Türkiye

\* [huriyeakpinar@gmail.com](mailto:huriyeakpinar@gmail.com)

\* Orcid No: 0000-0003-2460-942X

Received: 10 July 2024

Accepted: 21 September 2024

DOI: 10.18466/cbayarfbe.1513901

## Abstract

Enterprise Resource Planning (ERP) systems play a crucial role in modern company operations, integrating different functions such as supply chain, customer relations, human resources and finance into an adhesive system. The selection of an appropriate ERP system is a critical and complex decision that impacts an organization's efficiency and competitiveness. This study utilizes the Entropy and Multi-MOORA (Multi-Objective Optimization by Ratio Analysis) multi-criteria decision-making methods to evaluate ERP systems based on six criteria: cost, functionality, user-friendliness, reliability, technical support, and integration capability. Three ERP alternatives are assessed to define the most suitable system for a manufacturing company aiming to optimize its production and inventory management. The Entropy method objectively determines the weights of the criteria, while the Multi-MOORA method ranks the ERP alternatives. This comprehensive and unbiased selection process underscores the importance of a systematic approach in ERP system evaluation. By leveraging advanced decision-making techniques, organizations can make informed choices that enhance operational efficiency, drive innovation, and maintain a competitive edge. The study highlights the critical role of ERP systems and the necessity of using robust evaluation methods to ensure the selected system aligns with the organization's strategic goals and operational needs.

**Keywords:** Enterprise Resource Planning, Entropy Method, Multi-Criteria Decision-Making, Multi-MOORA Method

## 1. Introduction

In today's fast-changing business environment, choosing an Enterprise Resource Planning (ERP) system has become a crucial decision for companies aiming to stay competitive. The complexity of this decision is compounded by the myriad of criteria that must be considered, ranging from cost and reliability to compatibility and usability. As businesses expand and diversify, the integration of comprehensive ERP systems is crucial to streamline operations and enhance overall efficiency [1].

The process of selecting an ERP system is fraught with challenges, particularly in ensuring that the chosen system aligns with the strategic goals and operational needs of the organization. Various decision-making methods have been developed to aid in this process, including the use of fuzzy logic and Multicriteria

Decision-making (MCDM) approaches. The application of these methods helps in systematically evaluating and comparing different ERP solutions based on a set of predefined criteria [2].

In the context of this study, the focus is on the application of the Entropy-based MOORA method for ERP selection. This method provides a robust framework for handling the inherent uncertainties and subjectivities in the decision-making process. By incorporating both quantitative and qualitative criteria, the Multi-MOORA method offers a comprehensive evaluation of potential ERP systems, ensuring that the selected system meets the specific needs of the organization [3].

The case study presented in this research involves a bearing company seeking to select the most suitable ERP system from a set of alternatives. The decision-making process involves several steps, starting with the identification of relevant criteria and the evaluation of

alternatives. The final selection is made based on the weighted scores of each alternative, derived from the MOORA method. This approach not only facilitates a more objective comparison of ERP systems but also enhances decision-making efficiency by reducing the complexity associated with traditional selection methods [4]. We chose the Entropy method for its ability to objectively determine criteria weights based on the data, reducing subjectivity in the decision-making process. Multi MOORA was selected for its simplicity and effectiveness in ranking alternatives across multiple criteria. Together, these methods provide a robust and transparent framework for ERP selection.

## 2. Literature Review

In this section, studies conducted using the Entropy and Multi-MOORA methods are mentioned.

Entropy-based methods are widely utilized in MCDM due to their ability to handle uncertainty and provide objective weightings for criteria. Boroushaki [5] integrates Entropy-based weights with a modified TOPSIS algorithm within a GIS-based MCDM to address spatial decision-making problems where exact numerical judgments are difficult. Kasim and Jemain (2020) highlight the use of probability density functions in computing the Entropy of criteria, leading to more valid outcomes in resolving MCDM problems. Yang et al. [6] suggested the exponential probabilistic hesitant fuzzy entropy as a new fuzzy entropy for probabilistic hesitant fuzzy sets, aiding in MCDM using the TODIM method, demonstrated in a green building application.

Zhiyuan [7] discusses the Entropy method in evaluation systems based on multiple attributive decision theory, highlighting its superiority in solving index weighting problems compared to other methods. Rao et al. [8] present a hybrid MCDM method based on relative Entropy weight and projection algorithm, integrating interval numbers, linguistic fuzzy numbers, and incomplete information on attribute weights. Wang and Chen [9] introduce an Entropy metric for computing the diversity of Multi objective optimization algorithms, serving as an efficient diversity criterion. Xiao and Fu [10] utilize a three-parameter interval grey number approach based on information Entropy in a TOPSIS-based uncertainty decision-making framework to determine optimal solutions for problems with indeterminate attribute weight. Garg et al. [11] use Entropy functions to find attribute weight vectors for MCDM under uncertain conditions. Suri et al. [12] propose a novel Entropy measure for q-row orthopair fuzzy sets, aiding in MCDM problems.

Hua [13] applies the weighted moving average Entropy method to rank stocks, demonstrating its effectiveness in the decision-making process of value investment. Rani and Jain [14] use the Entropy method in the Intuitionistic

Fuzzy PROMETHEE Technique for MCDM problems. The Entropy technique for fuzzy information decision-making is covered by LiYi et al. [15]. It involves utilizing Entropy, triangular fuzzy numbers, and closeness degree to determine the best way to evaluate various proposals. Abbas [16] discusses methods based on the maximum Entropy principle to obtain joint probability distributions in decision analysis.

Grendár [17] presents the Empirical Maximum Entropy method, a special nonparametric case of the Maximum Entropy Empirical Likelihood method. Sogawa et al. [18] evolved the multivariate maximum Entropy distribution for hydrologic frequency analysis, comparing it to Pearson's system of frequency curves.

The Multi-MOORA method has been extensively utilized in various fields of multicriteria decision-making. The method is applied for water resources planning, providing optimal solutions based on different indicators and criteria from multiple stakeholders Brauers [19]. Kundakçı [20] combines the MACBETH method for determining criteria weights with the MULTIMOORA method for final alternative ranking in decision-making scenarios. Anantama and Hidayat [21] compare the performance of deep learning and MOORA methods in selecting the best public health center, with MOORA achieving 95.75% accuracy.

Sarkar and Biswas [22] introduce a Pythagorean fuzzy multicriteria decision-making method, PFMULTIMOORA, to address deficiencies in existing methods by incorporating unknown criteria weights using an Entropy weight model. Lestari et al. [23] use the MOORA method to determine the best employees in a company, aiding in effective employee motivation. Ulfah and Hasugian [24] utilize MOORA in a decision support system for selecting healthy toddlers, based on various health criteria. Liang et al. [25] present an enhanced MULTIMOORA method using interval-valued Pythagorean fuzzy sets for robust decision-making. Perbawa [26] employs MOORA in a decision support system to rank alternatives for selecting recipients of the Smart Indonesia Program.

Trung [27] uses multiple MCDM methods including MOORA for determining optimal cutting parameters in the milling process. Krishna et al. [28] integrate MOORA with COPRAS and Entropy methods to select the best experiment in turning Nimonic C263 alloy. Ekmiş et al. [29] compare Multi-MOORA with traditional univariate approaches for selecting products in an e-commerce marketplace. Uma and Geetha [30] propose an integrated MCDM model using MOORA for ranking cloud service providers based on criteria weights obtained through the Full Consistency Method. Osintsev [31] applies various MCDM methods, including MOORA, for ranking management decisions in transport and logistics.

Başaran and Tarhan [32] use MOORA to select suitable locations for offshore wind turbines in Turkey. Mathew and Sahu [33] compare new MCDM methods, including MOORA, for material handling equipment selection. Özekenci [34] evaluates the export performance of metropolitan cities in Turkey using integrated MCDM methods, including MOORA. Prajapati and Patel [35] optimize process parameters of abrasive water jet machining using MCDM methods, highlighting MOORA's applicability. The effectiveness of MOORA in various decision-making contexts underscores its versatility and robustness.

### 3. Entropy and Multi-MOORA Methods

In this section, the methods used in the study are explained in detail.

#### 3.1 Entropy Methodology

The Entropy method is a powerful tool in MCDM used to determine the weight of criteria based on the amount of information each criterion provides. It quantifies the uncertainty or diversity inherent in a set of data. In MCDM, the Entropy method helps to objectively assign weights to criteria, avoiding the biases that can come from subjective judgment Chodha et al. [36].

##### *Steps of the Entropy Method*

*Step 1:* The first step in applying the Entropy method is to normalize the decision matrix. This is done to ensure that all criteria are comparable, typically using the following formula for normalization:

Normalized Value

$$(R_{ij}) = X_{ij} / \text{sum}(X_{ij}) \quad (1)$$

for benefit criteria

$$(R_{ij}) = \min(X_{ij}) / X_{ij} \quad (2)$$

for cost criteria

where  $X_{ij}$  is the original value of the  $j_{th}$  criterion for the  $i_{th}$  alternative.

*Step 2:* The Entropy value for each criterion is calculated to measure the disorder or uncertainty associated with it. The formula to calculate the Entropy ( $E_j$ ) for each criterion is:

$$E_j = k * \text{sum}(R_{ij} * \ln(R_{ij})) \quad (3)$$

where  $k$  is a constant equal to  $1/\ln_m$  ( $m$  is the number of alternatives), and  $R_{ij}$  is the normalized value of the  $i_{th}$  alternative for the  $j_{th}$  criterion.

*Step 3:* The degree of divergence ( $d_j$ ) for each criterion is calculated next. It represents the level of useful information provided by each criterion and is computed as:

$$d_j = 1 - E_j \quad (4)$$

where  $E_j$  is the Entropy of the  $j_{th}$  criterion.

*Step 4:* Finally, the weights ( $w_j$ ) for each criterion are determined using the degree of divergence. The weight for each criterion is calculated as:

$$w_j = d_j / \text{sum}(d_j) \quad (5)$$

#### 3.2 Multi-MOORA Methodology

A useful tool in mixed-criteria decision-making is the Multi-MOORA method, which combines numerous techniques to assess and prioritize options according to a variety of factors. To improve decision-making precision, it combines the reference point approach and the MOORA method. According to Karande and Chakraborty [37], the Multi-MOORA technique is well-known for its adaptability, robustness, and simplicity in handling both qualitative and quantitative data.

##### *Steps of the Multi-MOORA Method*

*Step 1:* The first step involves constructing the decision matrix, which includes the alternatives and criteria. Each element of the matrix represents the performance value of an alternative concerning a specific criterion.

*Step 2:* Normalization is performed to make criteria comparable. This is done using the following formula:

$$\text{Normalized Value } (R_{ij}) = X_{ij} / \text{sqrt}(\text{sum}(X_{ij}^2)) \quad (6)$$

where  $X_{ij}$  is the original value of the  $j_{th}$  criterion for the  $i_{th}$  alternative.

*Step 3:* In the ratio system approach, the normalized values are used to calculate the overall performance of each alternative. The performance score ( $P_i$ ) for each alternative is calculated as:

$$P_i = \text{sum}(w_j * R_{ij}) \text{ for benefit criteria} - \text{sum}(w_j * R_{ij}) \text{ for cost criteria} \quad (7)$$

where  $w_j$  is the weight of the  $j_{th}$  criterion, and  $R_{ij}$  is the normalized value.

*Step 4:* In the reference point approach, the normalized values are compared to a reference point to determine the distance of each alternative from the ideal solution. The reference point ( $R_j$ ) for each criterion is often the best value among all alternatives. The distance ( $D_i$ ) is calculated as:

$$D_i = \sqrt{\sum ((R_{ij} - R_j)^2)} \quad (8)$$

where  $R_{ij}$  is the normalized value and  $R_j$  is the reference point for the  $j_{th}$  criterion.

*Step 5:* The full multiplicative form combines the ratio system and reference point approaches. It calculates a composite score for each alternative by multiplying the normalized values for benefit criteria and dividing by the normalized values for cost criteria. The composite score ( $C_i$ ) is:

$$C_i = \frac{\text{(Product of normalized values for benefit criteria)}}{\text{(Product of normalized values for cost criteria)}} \quad (9)$$

*Step 6:* Finally, the results from the ratio system, reference point approach, and full multiplicative form are aggregated to determine the final ranking of alternatives. The alternative with the best aggregate score is considered the optimal choice.

The Entropy method is advantageous for its objectivity in determining criteria weights from data, but it can be sensitive to variations in data quality. Multi MOORA offers simplicity and efficiency in handling multi-criteria decision-making, though it may not fully capture complex interactions between criteria. Together, they provide a balance between objectivity and ease of use. However, their combined use may require careful interpretation to ensure accurate decision-making.

#### 4. ERP Selection using Entropy-based Multi-MOORA Method

In this section, the problem addressed in the study is mentioned. First, general information about the problem is given. Afterwards, the steps of the Entropy method are given. Finally, the steps of the Multi-MOORA method are given.

##### 4.1 Problem Definition

A manufacturing business plans to choose an ERP system to optimize production planning and inventory management. This business aims to ensure the integration of the ERP system into production processes, its effectiveness in supply chain management, and the timely fulfillment of customer orders. At the same time, the cost of the ERP system must not exceed their budget and must be compatible with the existing information technology infrastructure. At this point, business management is considering using MCDM methods in the

evaluation and selection of ERP systems. These methods will help determine the most suitable ERP system, considering various criteria such as cost, functionality, user-friendliness, reliability, technical support, and integration capability. In the study, a purchasing expert and two IT experts took part as decision-makers. These three decision-makers decided on the criteria in line with the needs. The flowchart of the problem is given in Figure 1. In this study, a solution to this problem faced by the business was sought by considering Entropy and Multi-MOORA methods. Explanations of these criteria used in the study are as follows.

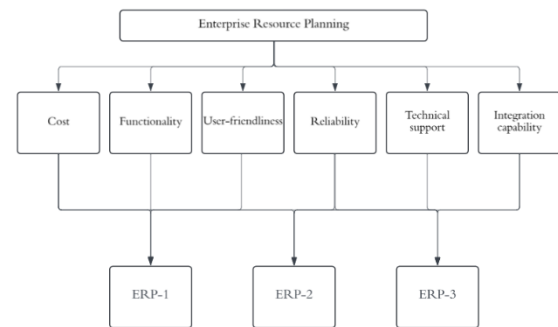


**Figure 1:** The flowchart of the problem

*Cost ( $K_1$ ):* The cost of an ERP system is a critical factor in the selection process. This includes not only the initial purchase price but also implementation ongoing maintenance expenses, costs, and licensing fees. Organizations must consider their budget constraints and evaluate the total cost of ownership over the system's lifecycle. A cost-effective ERP solution should provide significant value without exceeding financial limitations, ensuring a good return on investment.

*Functionality ( $K_2$ ):* This criterion refers to the range of features and capabilities an ERP system offers. All essential corporate operations, including customer relationship management, accounting, inventory control, and human resources must be supported by the system of choice. The functionality should align with the organization's specific requirements and goals. Comprehensive functionality ensures that the ERP system can address current needs and scale with future growth and changes in business operations.

*User-friendliness ( $K_3$ ):* User-friendliness is a crucial criterion, as it impacts the ease of use and adoption of the ERP system by employees. A user-friendly ERP system should have an intuitive interface, clear navigation, and accessible documentation and training resources. A system that is simple to use minimizes errors, lowers learning curves, and boosts overall productivity. Ensuring that the ERP system is user-friendly can



significantly enhance employee satisfaction and efficiency.

**Reliability ( $K_4$ ):** This criterion in an ERP system means that it performs consistently and is dependable under various conditions. A reliable system should have minimal downtime, quick recovery from failures, and robust security features to protect sensitive data. The reliability of an ERP system is critical for maintaining continuous business operations and ensuring data integrity. Choosing a reliable ERP system helps prevent operational disruptions and instills confidence in the system's performance.

**Technical support ( $K_5$ ):** Technical support encompasses the assistance provided by the ERP vendor in terms of implementation, maintenance, and troubleshooting. Adequate technical support includes comprehensive training, regular updates, and responsive customer service. Reliable technical support ensures that any issues are promptly addressed, minimizing operational disruptions. Organizations should evaluate the quality and availability of technical support services to ensure smooth and effective use of the ERP system.

**Integration capability ( $K_6$ ):** Integration capability refers to the ERP system's ability to seamlessly connect with existing software and hardware within the organization. Effective integration allows for the smooth flow of data across different systems, reducing redundancy and improving data accuracy. An ERP system with strong integration capabilities can streamline business processes and enhance overall efficiency. It is essential to choose an ERP system that can integrate well with current and future technologies to support the organization's evolving needs.

#### 4.2 Entropy Application Phase

In this section, the procedural steps for determining criterion weights are detailed. Initially, the decision-maker constructed a decision matrix for the criteria weights, expressing their relative importance levels as shown in Table 1. The criterion weights derived from the Entropy calculation results are presented in Table 2.

**Table 1:** Decision Values

ERP Alternatives	$K_1$	$K_2$	$K_3$	$K_4$	$K_5$	$K_6$
ERP-1	15	55	50	45	55	50
ERP-2	90	80	75	85	90	100
ERP-3	55	75	70	60	80	70

**Table 2:** Entropy Weight Values

Criteria	$K_1$	$K_2$	$K_3$	$K_4$	$K_5$	$K_6$
Weight	0,60	0,040	0,04	0,110	0,065	0,12

#### 4.3 Multi-MOORA Application Phase

To apply the Multi-MOORA method, a decision metric is first required that includes the evaluation of each criterion and alternative. This matrix has been completed by the business manager and is provided in Table 3. Each value in the decision matrix was initially squared, followed by summing these squared values and taking their square root. This procedure was iteratively applied to each column, and the outcomes are presented in Table 4.

**Table 3:** Decision Matrix for Multi-MOORA Method

Criteria	Weights	ERP-1	ERP-2	ERP-3
$K_1$	0,6088	15	90	55
$K_2$	0,0404	55	80	75
$K_3$	0,0470	50	75	70
$K_4$	0,1100	45	85	60
$K_5$	0,0657	55	90	80
$K_6$	0,1281	50	100	70

**Table 4:** Normalization Process Results

Criteria	ERP 1	ERP 2	ERP 3	Sum	Square
$K_1$	2,25	8,10	3,02	11,35	106,5
$K_2$	3,02	6,40	5,62	15,05	122,6
$K_3$	2,50	5,62	4,90	13,02	114,1
$K_4$	2,02	7,22	3,60	12,85	113,3
$K_5$	3,02	8,10	6,40	17,52	132,3
$K_6$	2,50	10,0	4,90	17,40	131,9

The values obtained in Table 4 represent the initial step of normalizing the decision matrix. To complete the normalization process, each value in Table 3 should be divided by the corresponding value in Table 4. This division process was applied individually to each matrix value, and the outcomes are presented in Table 5. The results of the Ratio, Reference, and Importance of Objectives approaches, along with dominance values used in solving the ERP selection problem using the Multi-MOORA method, are presented in Table 6.

**Table 5:** Normalized Matrix

Criteria	ERP-1	ERP-2	ERP-3
$K_1$	0,1408	0,8448	0,5163
$K_2$	0,4483	0,6521	0,6114
$K_3$	0,0200	0,0300	0,0280
$K_4$	0,3970	0,7498	0,5293
$K_5$	0,4155	0,6799	0,6043
$K_6$	0,3790	0,7581	0,5307

**Table 6:** Overall Results

Criteria	ERP-1	ERP-2	ERP-3
Ratio	3	1	2
Reference	1	2	3
Importance of the objectives	1	3	2
Multi-MOORA	<b>1</b>	3	2

## 5. Conclusion

ERP systems, which provide a comprehensive solution for managing a variety of organizational functions, are essential to modern business operations. Finance, HR, supply chain, and customer interactions are just a few of the areas that are combined into a single, seamless system, ERPs enhance operational efficiency and provide real-time insights. The importance of ERP systems lies in their ability to streamline workflows, reduce redundancies, and facilitate data-driven decision-making, driving productivity and competitiveness in today's dynamic business environment.

The selection of an ERP system is a complex and critical decision that significantly impacts an organization's success. Key criteria such as cost, functionality, user-friendliness, reliability, technical support, and integration capability must be meticulously evaluated to ensure the chosen system aligns with the organization's needs and goals. Employing multi-criteria decision-making methods, such as Entropy and Multi-MOORA, can provide a structured and objective approach to this evaluation process. These methods help in determining the relative importance of each criterion and in identifying the ERP system that offers the best overall value.

In this study, six different criteria and three ERP alternatives (ERP-1, ERP-2, and ERP-3) were evaluated using the Entropy and Multi-MOORA methods. The analysis revealed that ERP-1 emerged as the best alternative, effectively balancing cost, functionality, user-friendliness, reliability, technical support, and integration capability. By leveraging Entropy to ascertain objective weights and Multi-MOORA to rank the alternatives, the study ensured a comprehensive and unbiased selection process. The findings underscore the importance of a systematic approach in ERP selection, demonstrating how advanced decision-making techniques can aid organizations in making informed and confident ERP choices. The number of criteria and alternatives can be increased in the study. However, the lack of many decision-makers can also be mentioned as a limitation of the study. New studies can be planned in the future by increasing the number of criteria and

alternatives in the study and prioritizing fuzzy logic-based methods.

## Author's Contributions

**Huriye Akpınar:** Drafted and wrote the manuscript, performed the experiment and result analysis

## Ethics

There are no ethical issues after the publication of this manuscript.

## References

- [1]. Bayraktar, E., & Efe, M. (2006). Kurumsal kaynak planlaması (ERP) ve yazılım seçim süreci. Selçuk Üniversitesi Sosyal Bilimler Enstitüsü Dergisi, 15, 689709.
- [2]. Vatansever, K., & Uluköy, M. (2013). Kurumsal kaynak planlaması sistemlerinin bulanık AHP ve bulanık MOORA yöntemleriyle seçimi: Üretim sektöründe bir uygulama. Manisa Celal Bayar Üniversitesi Sosyal Bilimler Dergisi, 11(2), 274293.
- [3]. Chen, S. X., Wang, J. Q., & Wang, T. L. (2019). Cloudbased ERP system selection based on extended probabilistic linguistic MULTIMOORA method and Choquet integral operator. Computational and Applied Mathematics, 38(2), 132.
- [4]. Rouyendegh, B. D., & Erkan, T. E. (2011). ERP system selection by AHP method: Case study from Turkey. International Journal of Business and Management Studies, 3(1), 3948.
- [5]. Boroushaki, S. (2017). EntropyBased Weights for MultiCriteria Spatial Decision-making. PCG, 9(9), 20212041. doi:10.1353/PCG.2017.0009
- [6]. Yang, G., Ren, M., & Hao, X. (2023). Multicriteria decision-making problem based on the novel probabilistic hesitant fuzzy Entropy and TODIM method. Arabian Journal for Science and Engineering, 48(4), 14571471. doi:10.1016/j.aej.2023.01.014
- [7]. Zhiyuan, L. (2012). Entropy Method in Evaluation System Based on Multiple Attributive Decision Theory.
- [8]. Rao, C., Peng, J., & Zhang, Z. (2008). Method of hybrid multiattribute decision making based on relative Entropy weight and projection algorithm. Proceedings of the World Congress on Intelligent Control and Automation (WCICA), 4594089. doi:10.1109/WCICA.2008.4594089
- [9]. Wang, L., & Chen, Y. (2012). Diversity Based on Entropy: A Novel Evaluation Criterion in Multiobjective Optimization Algorithm. International Journal of Information and Software Technology, 4(10), 122128. doi:10.5815/IJISA.2012.10.12
- [10]. Xiao, Y., & Fu, S. (2017). Multiattribute Decision-making Method with Interval Grey Number Based on Information Entropy. Journal of Grey System, 20(1), 7785.
- [11]. Garg, H., Agarwal, N., & Choubey, A. (2015). Entropy Based Multicriteria Decision Making Method under Fuzzy Environment and Unknown Attribute Weights. Journal of Physical Mathematics, 6(2), 130139. doi:10.4172/22298711.1000182
- [12]. Suri, G., Svitenko, H., Guleria, A., Gandotra, N., Saini, N., & Salabun, W. (2023). Biparametric Q Rung Orthopair Fuzzy Entropy Measure for Multi Criteria Decision Making Problem. Information, 14(6), 304. doi:10.3390/info14060304

- [13]. Hua, L. (2012). Application of Entropy method for decision making of value investment.
- [14]. Rani, P., & Jain, D. (2016). Intuitionistic Fuzzy PROMETHEE Technique for Multicriteria Decision Making Problems Based on Entropy Measure. *Advances in Fuzzy Systems*, 10(4), 335349. doi:10.1007/9789811054273\_31
- [15]. LiYi, M., Xue, W., & Jian, G. (2010). Entropy method for decision-making of fuzzy information. *IEEE International Conference on System Science and Engineering*, 1(1), 100105. doi:10.1109/ICSESS.2010.5552329
- [16]. Abbas, A. (2006). Entropy methods for joint distributions in decision analysis. *IEEE Transactions on Engineering Management*, 53(1), 146159. doi:10.1109/TEM.2005.861803
- [17]. Grendár, M. (2006). Empirical Maximum Entropy Methods. *Journal of Computational Physics*, 85(2), 185193. doi:10.1063/1.2423302
- [18]. Sogawa, N., Araki, M., & Sato, K. (1986). A Study On Multivariate Maximum Entropy Distribution And Its Basic Characteristics. *Journal of the Japan Society of Civil Engineers*, 375, 8999. doi:10.2208/JSCEJ.1986.375\_89
- [19]. Brauers, W. (2018). Location Theory and MultiCriteria Decision Making: An Application of the Moora Method. *Central European Journal of Operations Research*, 26(3), 789803. doi:10.5709/CE.18979254.275
- [20]. Kundakçı, N. (2016). Combined MultiCriteria Decision Making Approach Based on MACBETH and MULTIMOORA Methods. *Advances in Economics and Business*, 4(1), 1825. doi:10.17093/AJ.2016.4.1.5000178402
- [21]. Anantama, R., & Hidayat, R. (2023). Comparison of Deep Learning and MOORA Performance Methods in Multi Criteria Decision Making with Case Studies Best public health center. *Technium*, 17, 10093. doi:10.47577/technium.v17i.10093
- [22]. Sarkar, B., & Biswas, A. (2021). A multicriteria decision making approach for strategy formulation using Pythagorean fuzzy logic. *Expert Systems with Applications*, 172, 114553. doi:10.1111/exsy.12802
- [23]. Lestari, Y. D., Budiman, A., Irwan, D., & Hanafiah, A. (2022). Implementation of MultiObjective Optimization on The Basis of Ratio Analysis (MOORA) Method in Determining The Best Employees. *International Journal of Information and Communication Sciences*, 6(3), 5606. doi:10.30865/ijics.v6i3.5606
- [24]. Ulfah, A., & Hasugian, A. H. (2023). Decision Support System for Selection of Healthy Toddler using MOORA Method. *Sinkron: Journal of Technology Research and Development*, 8(3), 455462. doi:10.33395/sinkron.v8i3.12695
- [25]. Liang, D., Darko, A. P., & Zeng, J. (2019). Intervalvalued pythagorean fuzzy power averagebased MULTIMOORA method for multicriteria decision-making. *Artificial Intelligence Review*, 52(3), 219236. doi:10.1080/0952813x.2019.1694589
- [26]. Perbawa, D. S. (2024). Sistem Rekomendasi Penerima Bantuan Program Indonesia Pintar Menggunakan Multi Criteria Decision Making. *FIFO Journal of Economics and Finance*, 15(2), 3550. doi:10.22441/fifo.2023.v15i2.003
- [27]. Trung, D. (2021). A combination method for multi-criteria decision making problem in turning process. *Manufacturing review*, 8, 26.
- [28]. Krishna, M., Kumar, S. D., Ezilarasan, C., Sudarsan, P. V., Anandan, V., Palani, S., & Jayaseelan, V. (2022). Application of MOORA & COPRAS integrated with Entropy method for multicriteria decision making in dry turning process of Nimonic C263. *Mechanical Engineering Review*, 2022014. doi:10.1051/mfreview/2022014
- [29]. Ekmis, M. A., Solmaz, M., Kiziltan, A., & Asil, M. (2022). Multi Criteria Decision Making with Marketplace Products Dynamics for Marketplace Product Selection. *IEEE International Conference on Applied System Innovation (ICASI)*, 18. doi:10.1109/ASYU56188.2022.9925495
- [30]. Uma, S., & Geetha, D. (2022). An Integrated MultiCriteria Decision-making Model for Cloud Service Provider Selection. *International Journal of Decision Support System Technology*, 14(1), 1532. doi:10.4018/ijdsst.286692
- [31]. Osintsev, N. (2021). Multicriteria decision-making in transport and logistics. *Russian Journal of Management*, 19(4), 317. doi:10.20291/1815940020214317
- [32]. Başaran, H., & Tarhan, İ. (2022). Investigation of offshore wind characteristics for the northwest of Türkiye region by using multicriteria decision-making method (MOORA). *Renewable Energy*, 100757. doi:10.1016/j.rineng.2022.100757
- [33]. Mathew, M., & Sahu, S. (2018). Comparison of new multicriteria decision making methods for material handling equipment selection. *Management Science Letters*, 8(5), 415426. doi:10.5267/J.MSL.2018.1.004
- [34]. Özekenci, E. K. (2023). Evaluation of export performances of metropolitans in Turkey based on integrated multicriteria decision-making methods. *Dicle Üniversitesi Sosyal Bilimler Enstitüsü Dergisi*, 15(2), 149170. doi:10.15182/diclesosbed.1273617
- [35]. Prajapati, R., & Patel, C. N. (2019). Review and Optimization of Process Parameter of Abrasive Water Jet Machine Using Multi Criteria Decision Making Method on Aluminum 5083. *International Journal of Mechanical and Production Engineering Research and Development*, 10(2), 415426.
- [36]. Chodha, V., Dubey, R., Kumar, R., Singh, S., & Kaur, S. (2022). Selection of industrial arc welding robot with TOPSIS and Entropy MCDM techniques. *Materials Today: Proceedings*, 50, 709-715.
- [37]. Karande, P., & Chakraborty, S. (2012). Application of multi-objective optimization on the basis of ratio analysis (MOORA) method for materials selection. *Materials & Design*, 37, 317-324.

## A Study on Topology Optimization of Landing Gear Parts

Sait Cumhur Pıçak<sup>1\*</sup>, Mehmet Yahşi<sup>1</sup>, Erol Gültekin<sup>2</sup>

<sup>1</sup> Turkish Aerospace Industries Inc. (TAI), Ankara, Türkiye

<sup>2</sup> Department of Mechanical Engineering, Faculty of Engineering, University of Turkish Aeronautical Association, Ankara, Türkiye

\* [saitcumhur.picak@tai.com.tr](mailto:saitcumhur.picak@tai.com.tr)

\* Orcid No: 0009-0000-6809-7230

Received: 26 August 2024

Accepted: 4 December 2024

DOI: 10.18466/cbayarfbe.1539030

### Abstract

In the aviation industry, one of the most complex industries in the world, the importance of low-weight design of aircraft is increasing day by day. While the requirements and related regulations regarding the efficient use of energy and minimizing environmental impacts are increasingly included in the legal framework, the importance of designing aircraft with low weight and therefore advantageous in terms of fuel consumption in the aviation sector, where competition is quite intense, is also increasing rapidly day by day. As a result of this situation, structural and parametric optimization, especially topology optimization studies, for the design of aircraft components with low weight, emerge as an indispensable element of design processes in the aviation industry. In this study, a Torque link and Trunnion landing gear parts were used. Firstly, the topology optimization study is performed as one conditional with separated two load cases. Afterward, the multi-conditional topology optimization is done with the aforementioned load cases. A weighted compliance parameter is generated to use in multi-conditional optimizations as a constraint or objective. While generating weighted compliance value, proportional weighted compliance (PWC) method is compared to the equal-effect weighted compliance (EEWC) method. With the EEWC method, on the torque link parts, 43% volume fraction is achieved and 34% volume fraction is obtained with the PWC method. Similar study has been done once again with landing gear Trunnion part and there were seen that the PWC method is a more effective approach in multi-conditional topology optimizations.

**Keywords:** Finite Element Analysis, Landing Gear, Topology Optimization

### 1. Introduction

As is well known, aircraft perform their flight missions by working against gravity. Therefore, the less load exerted on the propulsion components of the aircraft, the lower the fuel consumption will be, and it will be more advantageous in terms of strategic missions. At the same time, the lighter the structural parts of the vehicle such as its body and engine, the more the useful load (passengers, cargo, or ammunition in military vehicles) the aircraft can carry will increase accordingly, making the use of the aircraft in this manner quite important. Hence, one of the most important research areas of material science and technology is the aviation industry. It is observed that the efforts to lighten aircraft components are more focused on material solutions [1]. In this study, the focus is on redesigning the part through topology optimization without changing the material. In a study conducted by Raicevic et al. [2], the fatigue life of a

damaged torque link was analyzed, a suitable material was identified for additive manufacturing, residual stresses from production were included, and new torque link designs were obtained through analysis-optimization studies, providing an alternative design method in the design processes. In a study conducted by Srinivas and Javed [3], the optimum design of robotic arms was studied. Instead of optimizing according to the loading conditions at the time step of the worst load scenario, which is commonly used in the topology optimization of dynamically working parts, the aim was to obtain an optimal material distribution for each condition by using designs obtained from optimizations under different positions and loading conditions. In an analysis study conducted by Infante et al. [7], a finite element analysis (FEA) of a fork part in the front landing gear of an aircraft was performed. The part analyzed was damaged during flight operations. It was found that the regions critical in the stress analysis were in close proximity to the physically damaged regions on



the part. In a FEA study conducted by Freitas et al. [8], a stress analysis of an axle part of an aircraft was carried out. The part analyzed was found to be damaged during flight. Observations on the damaged physical part revealed that an overload situation caused the damage. The FEA studies also indicated a high probability of damage under the same conditions. In a study conducted by Bagnoli et al. [9], the damage to a swing arm part in the landing gear of a civil aircraft was examined. Irregularities originating from manufacturing were found in the internal structure of the part examined after the fracture, and it was concluded that the damage was a fatigue failure resulting from repeated loadings. The FEA studies also identified stress concentrations in the damaged region. A paper submitted by Gu et al. [12] introduces a pioneering method termed nonlinear fatigue damage constrained topology optimization. The method integrates several key components: the rainflow counting method to evaluate the non-proportional cyclic load levels, Basquin's equation to describe the S-N curve, and Morrow's plastic work interaction rule to calculate the nonlinear cumulative damage of the structure. They established a mathematical model for the nonlinear fatigue damage constrained topology optimization method based on the components. In a paper submitted by Song et al. [15], the appearance of sharp 'V' features at joint areas in multi-material topology optimization, originating from independent minimum length scale control is delved. The modified minimum length scale controls for multi-material problems are proposed based on geometric constraints and the indicator functions with a normalization gradient norm. The results indicate that the combinations of two minimum length scale controls cannot achieve the parallel distribution and wrapped distribution due to the limited ability to modify the material layout. A paper submitted by Dong et al. [32] presents a topology optimization framework based on the bi-directional evolutionary structural optimization (BESO) method for designing SMA structures, which maximizes structural stiffness under multiple constraints of specified volume fraction, displacement, and fundamental frequency. Several optimized SMA beam structures and simply-supported cube structures are designed under different thermal-mechanical loads, and their displacement, mean compliance, and fundamental frequency are evaluated throughout the optimization process. The results demonstrate that the proposed framework successfully customizes the SMA topology structure with adjustable displacement and fundamental frequency, and the optimized schemes exhibit more considerable deformation and more uniform mechanical properties than their initial counterparts. In order to use topological optimization results in final product designs without too much effort, DDM(Direct Digital Manufacturing) is an important technology that has persisted from the past to the present. Complex geometrical structures with light weight are the greatest interest of the aerospace, spacecraft, and automobile

industries. A study conducted by Patham K.F. [33] aims to explore the possibilities of implementing DDM for small and medium manufacturing firms by combining the advances of computer application software, topology optimization, and additive manufacturing. The results indicated that that redesign was an efficient method for producing lightweight aerospace structures and components without using expensive novel lightweight materials. A paper submitted by Tang et al. [34] proposes a multi-objective topology optimization method combining Analytic Hierarchy Process (AHP) and topology optimization. A comparison of the comprehensive performance of the frame before and after optimization shows that the proposed method enables the optimized frame to meet the strength requirements under various working conditions, resulting in a weight reduction of 16.5 kg. Crash topology optimization is a typical nonlinear dynamic response structural topology optimization problem, which is one of the most difficult problem in the structural design field. The equivalent static load method (ESLM) provides a well-defined pattern to solve such difficult problems, which can convert a nonlinear dynamic response optimization into multi-load steps optimization problem with the equivalent static loads (ESLs). In a study conducted by Ren et al. [35], to expand the application scope of the ESLM, an improved ESLs calculation method is proposed by using the model order reduction method and energy principle, which only acting on some nodes and can be scaled adaptively. The results show that, the proposed method can effectively solve the crash topology optimization of thin-walled structures under large deformation crash condition. As urbanization continues to accelerate, dump trucks assume an increasingly important role in the transportation and construction of infrastructure. One of the primary failure modes of the carriage is weld fatigue failure, which frequently gives rise to the problem of weld fatigue cracking during transportation. To increase the fatigue life of welds and enhance the degree of structural lightweight of a heavy dump truck carriage, a method for anti-fatigue lightweight design based on machine learning and multi-objective optimization is proposed by Lan et al. [36] and the proposed design method achieves a good effect in the anti-fatigue lightweight of dump truck carriage. Traditional residential timber frames, embodying centuries of Chinese craftsmanship, continue to thrive. To determine the optimal design dimensions for these frames, a study conducted by Yuanyao et al. [37] introduces a combined optimization approach using Response Surface Methodology (RSM) and Multi-Objective Genetic Algorithm (MOGA). Using the Optimal Space-Filling (OSF) method, sample points within the design domain were collected to establish a response surface model, correlating frame dimensions with key structural metrics: maximum deformation, maximum Mises stress, and total mass. The findings of the study provide valuable insights for related



engineering applications and a calculation model for the fatigue damage degree of concrete was proposed. In a paper submitted by Wang et al. [38], the lightweight design of the automotive front subframe was performed by combining multi-condition topology optimization and multi-objective optimization approaches. Multi-condition topology optimization of the front subframe envelope was performed utilizing the compromise programming approach. The optimized front subframe has met various performance specifications while increasing the first-order frequency by 10 Hz and reducing weight by 3.27 kg. In addition to the well-developed topology optimization (TO) method, structural bionics is also considered an effective approach to developing innovative structure designs with lightweight. In the process of natural evolution, bamboo has developed a unique hollow structure with ingenious mechanical properties. Inspired by these characteristics, a paper submitted by Zhu et al. [39] selected bamboo as a bionic prototype to carry out bionic structure optimization of guide arm. According to the results, under the premise of the mass of the optimized bionic model decreased by 17.44%, the maximum deformation was decreased by 9.24%, the equivalent stress was decreased by 17.33%, and the first-order frequency was increased by 22.92%. Comparison results showed that the proposed bionic model provided the best lightweight solution for guide arm. A paper conducted by Chen et al. [40] presents a comprehensive optimization design method for composite materials in order to investigate the impact of the coupling effects of carbon fiber reinforced polymer in the seat back layer on the performance of car seats. The results show that ensuring the safety performance, the total mass of the seat backrest decreased by 21.3%, as a result of the optimization strategy proposed in this paper, and the comfort performance is also improved to some extent. Sandwich structures with lattice cores are novel, lightweight composite structures and are widely used in the aerospace industry. A study conducted by Najafi et al. [41] investigates the supersonic flutter of a sandwich panel whose core is topology-optimized. The modeling approach is fully validated, and the results demonstrate that the sandwich panel is capable of enlarging the flutter-free operational flight range when compared with other conventional panel designs. Development and evaluation of a novel design of mass reduced aircraft wing ribs through topology optimization is reported in a paper submitted by Rahman et al. [42]. Methodology in this study includes the  $k$ - $\Omega$  shear stress transport turbulence model computational fluid dynamic simulation as well as static and transient finite element simulations. The optimized wing rib is found to be between 8% and 15% lighter than traditional wing ribs depending on configuration.

A substantial amount of numerical studies are performed in topology optimization field. It has been an important purpose that reduce the weight or increase the

stiffness of the structure. In a classical topology optimization problem, reducing the volume of the part is aimed. Remaining constant or minimizing the compliance (total strain energy) output is often used to save the stiffness of the structure since reducing the volume will cause the reducing stiffness. In problems involving multiple loadsteps, naturally, as many compliance values are obtained as the number of loadsteps. In a single-objective optimization problem, these values need to be aggregated in some way to obtain a new value that can be minimized. In this study, performance of two methods were used to obtain total compliance value. EEWC (equal-effect weighted compliance) method gets the total compliance value by directly summing the compliances of each loadsteps. PWC (proportional weighted compliance) method calculates the total compliance value by multiplying each compliances with some weight factors and finally summing them. These factors are calculated by proportioning. In our study, in order to obtain weight-effective structures, these two methods were operated and the results were compared.

## 2. Materials and Methods

Structural optimization studies can also be divided into two groups: "concept design" and "fine-tuning." In concept design studies, the design concept of the structural design is not known at the beginning of the study. Typically, a bulk structure is created that fills the entire design space allowed for the design, and a design topology meeting the desired objectives and constraints is obtained from this structure through topology optimization. Examples of other concept design studies include topography optimization and free-shape optimization. In topography optimization, the aim is usually to achieve high strength and high natural frequency values by creating bead structures on a shell structure with a certain thickness. In free-shape optimization, certain surfaces of a three-dimensional model are defined as free-shape surfaces, and the forms these surfaces take as a result of optimization are reflected in the design. In fine-tuning studies, there is a pre-defined design at the beginning, either previously obtained as a concept design or formed through an initial assumption, experience, etc. The aim in fine-tuning studies is to obtain the optimum geometry of this defined design. For this purpose, geometric parameters such as radius, thickness, hole diameter, etc., are defined as design variables. Additionally, shape parameters obtained by mesh morphing in the finite element model can also be defined. In addition to these structural optimization studies, parametric optimization studies that only process numerical inputs and outputs are also frequently encountered. In these studies, after defining the input parameters called design variables, a design of experiments can be performed to determine which change in the input parameters highly affects the examined output parameters, and in the next step, to

avoid processing clutter, the optimization process can be applied considering only these parameters. Again, in parametric analysis studies, if long analysis tools are used to obtain outputs at each iteration, an appropriate mathematical model can be created using a data set containing the outputs obtained for specific inputs. Thus, instead of lengthy analysis processes at each step, the outputs generated by this mathematical model can be used by the optimization software, allowing for faster attainment of extremum values with an acceptable error margin.

Topology optimization is a significant tool in order to get proper designs from concept stage. Classical topology optimization cycle can be seen in Figure 1.

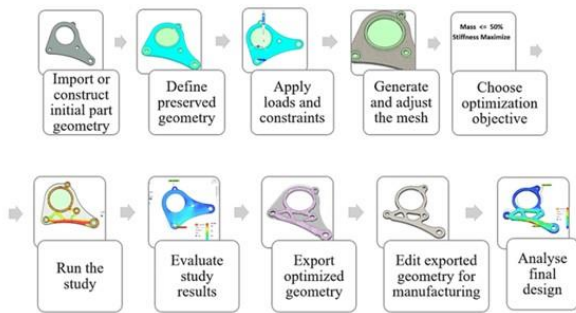


**Figure 1.** Topology optimization steps [24]

In this study, commercial finite element and optimization solver OptiStruct is used in order to perform FEA and topology optimizations. OptiStruct uses one of the gradient based optimization algorithms called Enhanced Dual Optimizer based on separable convex approximation (DUAL2) [25]. As with all other types of optimization; in order to build a topology optimization problem, three fundamental arguments are needed to form a structural optimization problem. These arguments are design variables, constraints, and objective parameters. Design variables are the parameters that will be modified throughout the optimization iterations. By continuously assigning new values to these parameters according to an appropriate algorithm, an optimum design is sought. In topology optimization, the material density of each element is directly used as the design variable and varies continuously between 0 and 1; these represent the state of void and solid, respectively. Intermediate values of density represent fictitious material. The stiffness of the material is assumed to be linearly dependent on the density. This material formulation is consistent with our understanding of common materials. For example, steel, which is denser than aluminum, is stiffer than aluminum. Following this logic, the representation of fictitious material at intermediate densities does reflect engineering intuitions.

Then it is required to define responses. OptiStruct allows the use of numerous structural responses, calculated in a FEA, or combinations of these responses to be used as objective and constraint functions in a structural

optimization. Constraints and objective functions use the outputs at each iteration in the optimization process. Depending on the algorithm or analysis used as the iteration step, these outputs can be very different parameters. For instance, in a structural analysis, the outputs can be general FEA parameters such as stress, displacement, etc., or parameters calculated by the software to be used in the iterations, such as mass, volume, etc., which the software is instructed to modify. Constraint parameters are those defined as lower or upper limits, or optionally both, for the numerical values of these outputs. During each iteration, the optimization algorithm checks whether the constrained outputs remain within the defined lower or upper limits. Reaching the optimum result is possible when the constrained outputs stay within the limit values or exceed the limits by a predefined allowable percentage. The objective function aims to minimize or maximize a selected output parameter. Additionally, it is possible to define an objective function to minimize the maximum value or maximize the minimum value of a set of output parameters. While multiple constraint functions can be defined, the objective function is singular. However, multi-objective optimization processes have also been developed in recent years. Generally, in structural optimization studies, the aim is to minimize mass or maximize stiffness.

One of the important responses generated by the solver is "Static Compliance". In mechanics, compliance" means inverse of "stiffness". To improve the structural integrity it is often necessary to minimize the strains in the structure which means minimizing the compliance or maximizing the stiffness. The compliance  $C$  is calculated using the following relationship [29]:

$$C = \frac{|x|}{|f|} \quad (1)$$

Where  $|x|$  is the magnitude of applied force and  $|f|$  is the magnitude of the displacement.

In this study, weighted compliance output is also used. The weighted compliance is a method used to consider multiple subcases (loadsteps, load cases) in a classical topology optimization. Each compliance value produced for the respective load step is multiplied by a weighting factor, and the results are summed up. The response is the weighted sum of the compliance of each individual subcase (loadstep, load case).

$$C_{total} = \sum_{i=1}^n w_i c_i \quad (2)$$

where:

- $C_{total}$ : Total weighted compliance.
- $w_i$ : Weighting factor for load case  $i$ .
- $C_i$ : Compliance (strain energy) for load case  $i$ .

- $n$ : Number of load cases.

This is a global response that is defined for the whole structure.

In this study, topology optimization study is performed on landing gear parts. During landing and ground operations, landing gear is the most critical system of the aircraft. It provides a ground support, energy absorption during landing and load connection between body(fuselage) and ground plane. In smaller aircrafts, generally a lip spring including landing gear are used. In bulkier aircrafts, pneumatic and oleo-pneumatic type of landing gears are generally used. Landing gears meant for their large “safe life” segments along with that they are supplanted ordinarily while the administration life of an airplane [27].

In Figure 2, it can be seen a landing gear model and its important parts.

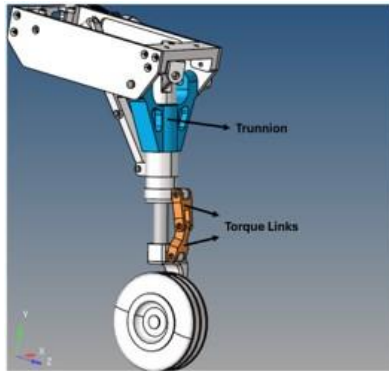


**Figure 2.** Landing gear model [30]

Landing gear is, by its nature, dynamic equipment that counters not only the loads applied by the aircraft and the ground but also the aerodynamic and inertia loads during deployment and retraction [10]. In a typical aircraft, the landing gear is usually characterized by two masses, a spring, and a damper. The schematic representation of this design can be seen in Figure 3.

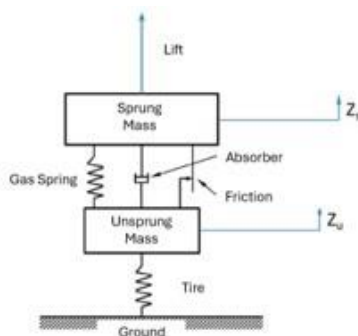


**Figure 3.** Schematic representation of a single landing gear [10]

A set of loads is determined for the landing gear according to the specified operation scenario. Under the conditions of this load set, the landing gear is expected to have sufficient structural strength. The load set is generally defined as load components in the Cartesian coordinate system at the tire contact points of the landing gear and the landing gear must not suffer damage when these load components are statically applied. The parameters affecting this static strength condition include the applied load conditions, the geometry of the landing gear components, and material characteristics. Most of the static loads applied are defined as "limit loads." Limit loads are considered the highest load conditions the landing gear may encounter during operation. The static strength of the landing gear must be sufficient to prevent permanent deformation when exposed to any of these limit loads. Additionally, to ensure an extra safety condition, strength calculations for the landing gear are also performed for maximum loads obtained by multiplying the limit loads by 1.5 [31]. However, at this level of load conditions, permanent deformation is allowed on the landing gear, provided that structural integrity is not compromised. To meet this requirement, the stresses obtained as a result of maximum loading are compared with the ultimate strength of the landing gear materials.

Initially, two critical load conditions will be included individually in the optimization study. Subsequently, an examination will be conducted using a method where the effect of these loads on the structure is evaluated together. One of the most important parameters used in measuring the structural strength of industrial designs is the output parameter called "compliance" obtained as a result of strength analyses. This value is equivalent to the total strain energy absorbed by the structural system, and high values indicate low rigidity of the structure. Therefore, the objective function in optimization studies is generally defined to minimize this value, i.e., to maximize the stiffness (rigidity) value. In finite element models, a different analysis step (Loadstep) can be defined for each loading condition, allowing for comparison of the effects of different loading conditions on the structure within a single computer-aided engineering analysis. Additionally, different categories of loading conditions such as gravity can be defined once and combined with other analysis steps. In FEA models with multiple loading conditions, the issue of which loading condition to use for the optimization process can become complex. To easily overcome this complexity, a "weighted compliance" value obtained by multiplying the compliance value of each loading condition by a specific coefficient and summing the new compliance values derived from all conditions can be used in optimization software. This value is also automatically provided to the user at the parameter selection stage in most structural optimization software. In this study, a finite element model of a torque link part

has been created, and the design space has been determined.

In the created model, the number of nodes used is 39,016 and the number of elements is 200,631. The finite element model and the design space allocated for optimization can be seen in Figure 4.

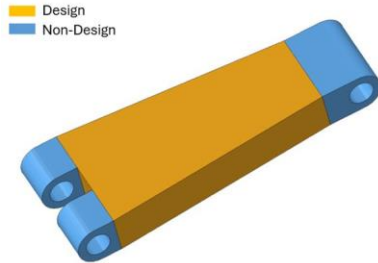


**Figure 4.** Finite element model and design space of the torque link

Landing gears generally use oleo-pneumatic suspension systems containing gas-fluid to absorb the ground reaction force generated during landing. Unlike automotive axle systems, these systems usually do not use axle systems for installation, and instead of restricting the rotational movement of the wheels by shape, external torque links are used. Torque links are components that prevent the wheels from rotating around their own axes or a certain axis. Therefore, the torque link part shown in Figure 2 is continuously subjected to bending effects during ground maneuvers. The first loading condition to be used in the optimization phase in this study is based on this bending effect. To simulate the torsional effect that may occur on the torque link due to deformation of other landing gear parts such as the axle, and to obtain a different loading scenario as an optimization method, a torsional moment was applied to the torque link as the second condition. The schematic representation of the applied loading scenarios can be seen in Figure 5. In the bending scenario, a force of 45 kN was applied to the torque link connection point. In the second scenario, a torsional moment of 2500 Nm was applied. These loading values correspond to the ground loads of the landing gear of a lightweight aircraft.



**Figure 5.** Loading and boundary conditions

The material of the torque link examined in the study is Ti6Al4V alloy. The mechanical properties of the material are given in the table below:

**Table 1.** Ti6Al4V Material Properties [5]

Modulus of Elasticity [MPa]	Poisson Ratio	Yield Strength [MPa]	Ultimate Tensile Strength [MPa]
113800	0.342	790	860

In topology optimization applications, the aim is generally to obtain the most robust design with the lightest weight [28]. In this study, the first analysis output to be used in the optimization problem is the volume fraction. This value is calculated as the ratio of the volume of the design space after optimization to the initial volume. The other output is the compliance, which is interpreted as the inverse of the stiffness of the structure and represents the total strain energy. The higher the compliance value, the lower the stiffness of the structure. In this study, while defining the optimization problem, a compliance value of 120 Nm was set as the upper limit to form the constraint function, and the volume fraction was defined as the objective function to be minimized.

For multi-conditional topology optimizations, two methods for defining weighted compliance are compared. The coefficients are used to multiply the compliance values which separately produced by unique load cases. If we define these compliance values  $C_1$  and  $C_2$ , the formula (4) becomes:

$$C_W = W_1 C_1 + W_2 C_2 \quad (3)$$

where  $W_1$  and  $W_2$  are the coefficients called “weight factors” multiplied with the compliances in order to generate weighted compliance value  $C_W$ . In the Equal-Effect Weighted Compliance (EEWC) method, these coefficients are set as the same and equal to 1. Therefore (5) formula becomes:

$$C_W = C_1 + C_2 \quad (4)$$

$$W_1 = W_2 = 1 \quad (5)$$

In the Proportional Weighted Compliance (PWC) method, compliance values  $C_1$  and  $C_2$  are calculated once. For instance, consider the following example:  $C_1 > C_2$ . Therefore,  $W_1$  coefficient is set to 1 and  $W_2$  coefficient is calculated as below:

$$W_2 = \frac{C_2}{C_1} \quad (6)$$

$$C_1 > C_2$$

$$W_1 = 1$$



Therefore, the weighted compliance value  $C_W$  is calculated as:

$$C_W = C_1 + \frac{C_2}{C_1} C_2 \quad (7)$$

### 3. Results and Discussion

The study results consist of two section considering the Torque link and the Trunnion. Topology optimization analyses of the Torque link were presented as four separate studies while for the Trunnion, the analyses were completed using EEWC and PWC methods.

#### 3.1 Topology Optimization of Torque Link

Topology optimization analyses of the Torque link were defined according to the bending condition, the torsion condition, the third condition where both conditions have equal influence, and the fourth condition where each condition has an effect proportional to its own compliance value.

##### 3.1.1. Topology Optimization with Bending Condition

The material distribution results according to the first condition, the bending condition, are shown in Figure 6. The optimal model was obtained after 30 iterations.

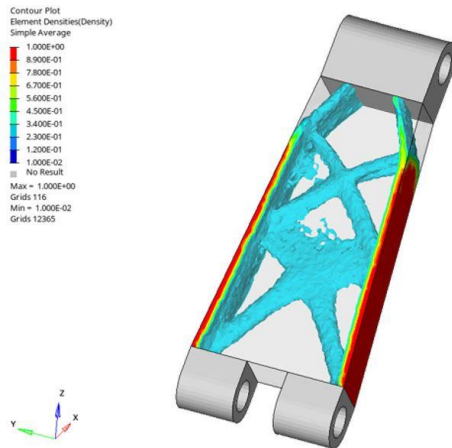


**Figure 6.** Topology optimization result of bending condition

In this optimization, the volume fraction value to be minimized was obtained as 0.17 for the optimal model. The compliance value is 119.5 Nm, which satisfies the upper limit constraint of 120 Nm.

##### 3.1.2. Topology Optimization with Torsion Condition

The material distribution results according to the second condition, the torsion condition, are shown in Figure 7. The optimal model was obtained after 15 iterations. A longitudinal section view has been added to provide a clearer view of the material distribution.

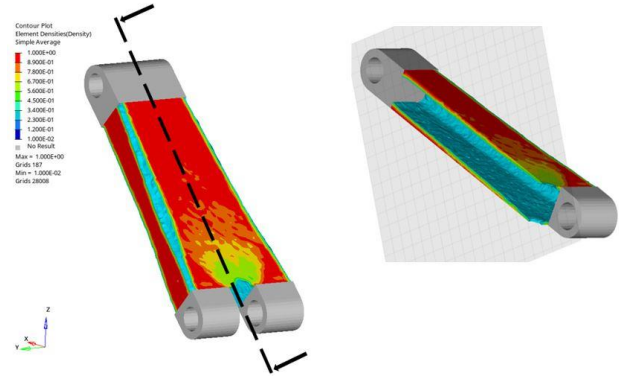


**Figure 7.** Topology optimization result of torsion condition

The volume fraction value to be minimized was obtained as 0.26, and the compliance value is 119.8 Nm, which satisfies the upper limit constraint of 120 Nm.

##### 3.1.3. Topology Optimization with the EEWC Method

In the optimization study defined as the third condition, the compliance value uses the weighted compliance output, calculated by taking the sum of the compliance values obtained from analyzing both conditions. This value has been defined as a constraint, as in the first two optimization studies. The material distribution results according to the EEWC method are shown in Figure 8. The optimal model was obtained after 12 iterations. A longitudinal section view has been added to provide a clearer view of the material distribution.

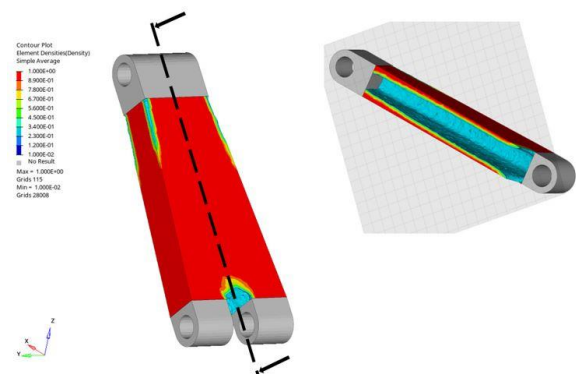


**Figure 8.** Topology optimization result of EEWC Method

The volume fraction value to be minimized was obtained as 0.43, and the compliance value is 119.98



Nm, which satisfies the upper limit constraint of 120 Nm.

### 3.1.4. Topology Optimization with PWC Method

In the optimization study defined as the fourth condition, the weighted compliance output is calculated using the ratio of the compliance values obtained for Weighted each loading scenario. The compliance values obtained in the first iteration of the initial design are 30.57 Nm for bending and 57.191 Nm for torsion. Therefore, the coefficient to be used for the bending compliance in the weighted compliance calculation is 0.53 according to Formula (7), which is the ratio of these two values. The material distribution results according to the PWC method are shown in Figure 9 with a longitudinal section. The optimal model was obtained after 14 iterations.

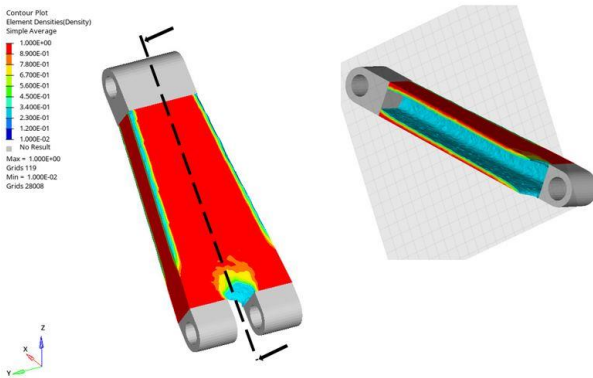


**Figure 9.** Topology optimization result of PWC Method

The volume fraction value to be minimized was obtained as 0.34, and the compliance value is 119.9 Nm, which satisfies the upper limit constraint of 120 Nm. The outputs obtained from the optimization studies are given in Table 2.

**Table 2.** Results of Topology Optimizations

Condition	Topology Optimization Method	Compliance [Nm]	Volume Fraction [%]
One Conditional	Bending	119.5	17
	Torsion	119.8	26
Multi Conditional	EEWC	119.9	43
	PWC	119.9	34

When the results on Table 2 were examined, there were seen that the PWC method has more effective results regarding volume fraction for multi-conditional optimizations. The PWC and EEWC methods are compared in another topology optimization study in the next section.

### 3.2 Topology Optimization Study of Landing Gear Trunnion

The weighted compliance methods EEWC and PWC used on the torque link rod, both were similarly applied to perform topology optimization on a landing gear trunnion component. This part was subjected to finite element stress analysis under two different loading conditions, similar to the previous study. The analyzed component as bulk model is shown in Figure 10.

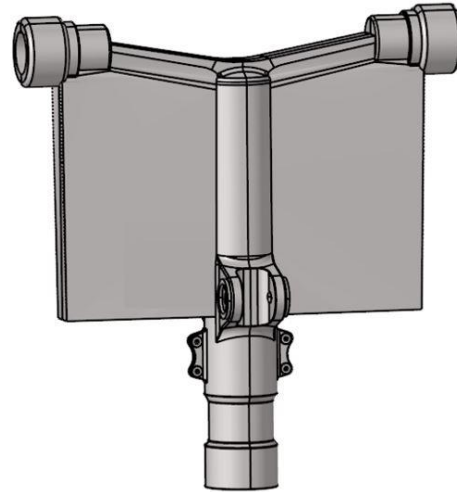


**Figure 10.** Landing Gear Trunnion Bulk Model

The structural strength of the trunnion component was examined under two different loading conditions. The first condition is the ground reaction force occurring during a vertical landing. The second condition occurs as a result of the horizontal force generated while the aircraft moves forward on the ground. The landing gear trunnion component must be designed to withstand both loading conditions without damage. The visual representation of the loading and boundary conditions is shown in Figure 11. The finite element model consists of 1445534 elements and 286579 nodes. This part has the same material as the first study Ti6Al4V.

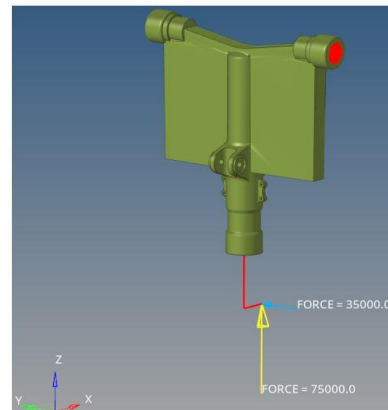


**Figure 11.** Trunnion loading and boundary conditions

vertical force as 75000 N and horizontal (drag) force as 35000 N are applied to axle center location of landing gear. Initially, bulk model of Trunnion was analyzed regarding both vertical and drag forces. Displacement and stress results of the Trunnion bulk model according to vertical force condition are shown in Figure 12.

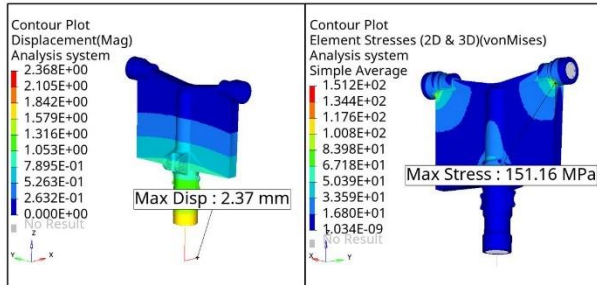


**Figure 12.** Vertical force displacement and stress results of bulk Trunnion

The stress analysis results of bulk Trunnion according to vertical force condition indicate a maximum displacement of 2.37 mm and a maximum Von Mises stress of 151.16 MPa.

The displacement and stress results of the bulk Trunnion according to drag force condition are shown in Figure 13.

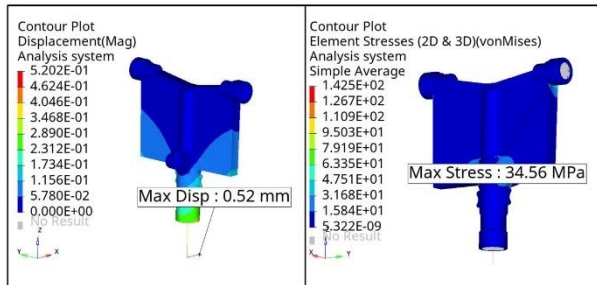


**Figure 13.** Drag force-displacement and stress results of bulk Trunnion

After the drag force case calculation 0.52 mm maximum displacement and 34.56 MPa maximum Von-Mises stress results are obtained.

Following the linear static stress analysis, the topology optimization problem is defined on the trunnion component. As a similar with the torque link study on previous chapter, the volume fraction and weighted compliance parameters were selected as the analysis outputs called "Responses". The compliance values for vertical and drag subcases are 12.3 Nm and 9.1 Nm, respectively. Initially, coefficients for vertical and drag force subcases were both assigned to 1 according to the EEWC method. Then, regarding the PWC method, the coefficient of the first condition (which had the higher compliance value) was set to 1, and the coefficient of

the second condition was set to 0.74, based on its ratio to the first condition. Before the run processes of the topology optimization, design, and non-design areas are defined on the bulk FEA model of the Trunnion part. These areas can be seen in Figure 14. Also, the 1-plane symmetry condition is defined on the model to get similar material distribution for both sides of the Trunnion part.

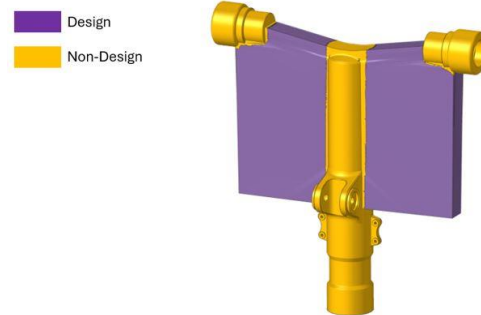


**Figure 14.** Design areas of Trunnion

Optimization cases for both EEWC and PWC methods are performed. Topology optimization according to the EEWC method converged at 39<sup>th</sup> iteration. The material density distribution results of the topology optimization regarding the EEWC method is shown in Figure 15. According to this material distribution, Von-Mises stresses of both vertical and drag force subcases are also calculated, and they are shown in Figure 16.

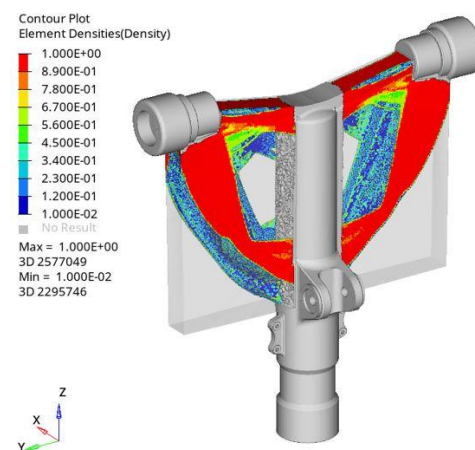


**Figure 15.** Trunnion material distribution according to the EEWC method

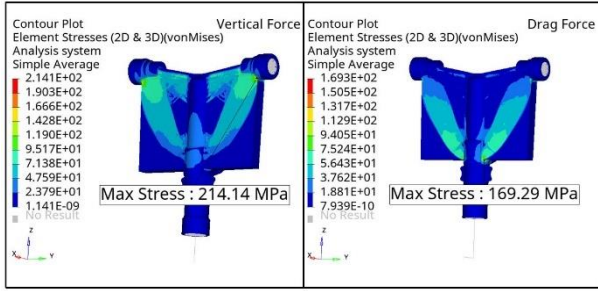


**Figure 16.** Optimized Trunnion Von-Mises stress results according to the EEWC method

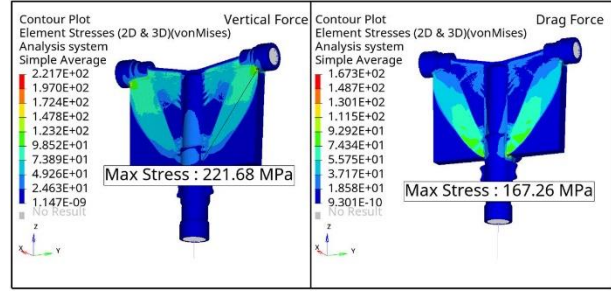


**Figure 18.** Optimized Trunnion Von-Mises stress results according to the PWC method

As a result of the stress analysis, the compliance value for the first condition (vertical loading) was obtained as 28.35 Nm. The compliance value for the second condition (horizontal loading) was 21.61 Nm. Final result of the weighted compliance value to be minimized and calculated according to the formula (4) is obtained as 49.96 Nm. This value is not violating the upper constraint 50 Nm, therefore, the optimization results are feasible. Final status of the volume fraction as objective value is 0.14 and it means %86 volumetric decrease is provided.

Topology optimization according to the PWC method converged at 41<sup>th</sup> iteration. The material density distribution results of the topology optimization regarding the PWC method is shown in Figure 17. According to this material distribution, Von-Mises stresses of both vertical and drag force subcases are also calculated and they are shown in Figure 18.

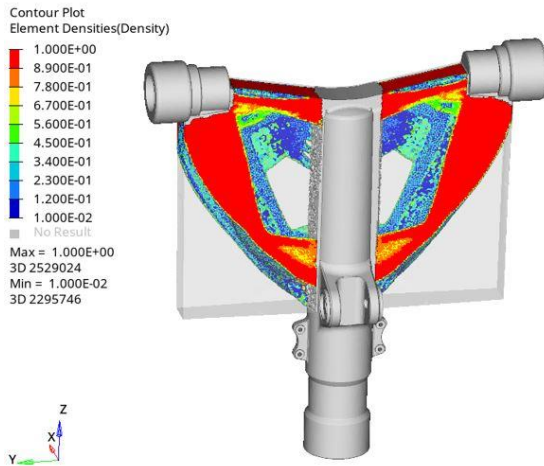


**Figure 17.** Trunnion material distribution according to the PWC method

As a result of the stress analysis, the compliance value for the first condition (vertical loading) was obtained as 31.51 Nm. The compliance value for the second condition (horizontal loading) was 24.91 Nm. Final result of the weighted compliance value to be minimized and calculated according to the formula (7) is obtained as 49.96 Nm as same level with the EEWC case. This value is not violating the upper constraint 50 Nm, therefore, the optimization results are feasible. Final status of the volume fraction as objective value is 0.12 and it means %88 volumetric decrease is provided. Additionally, the stress values observed in PWC method are not much higher regarding EEWC method. Stresses in Vertical force case are 214.14 MPa for EEWC method and 221.68 MPa for PWC method therefore only 3.5% increase was observed. For drag force case the stresses for the EEWC and PWC methods are 169.29 MPa and 167.26 MPa, respectively. These values are nearly same. Therefore the stiffness of the optimized structure obtained via PWC method is not much smaller than the value obtained via the EEWC method. This status shows that in addition to effective volume reduction, similar stiffnesses with EEWC method are obtained via PWC method.

The results of the defined topology optimization for the landing gear trunnion component are shared in Table 3.

**Table 3.** Topology optimization results of Trunnion

Condition of Topology Optimization	Weighted Compliance [Nm]	Volume Fraction	Volumetric Decrease [%]
EEWC	49.96	0.14	86
PWC	49.96	0.12	88

#### 4. Conclusion

In this study, topology optimization of the landing gear parts which are torque link and Trunnion were investigated. As a first study, FEA and topology optimizations of the torque link are performed. Two separate load cases called bending and torsion are used and the combined optimizations were performed. In combined studies, weighted compliance values are used as constraint functions and volume fraction values are

used as objectives. There were seen that using the proportional compliance values getting from the formula (9), the PWC method is more effective than using same coefficients as 1 in weighted compliance calculation, the EEWC Method. Same comparison is applied to another landing gear part called Trunnion. The results show that the PWC method is more effective than the EEWC method since the volumetric decrease at the end of optimization iterations are higher in the PWC method. Also, the increasing on stress values for the material distribution at last iteration are not dramatical. Therefore, it can be said that the PWC method can practically be applied in industrial applications of topology optimization studies. Also, the PWC method can be used in size optimization and thickness distribution problems defined for aircraft wings and automobile chassis which facing multiple loadcases and including many sheet parts that have different thicknesses. Additionally, the total compliance output can be used in topography optimization problems. In order to constraint bead dimensions, PWC method will be an efficient method.

Findings obtained from this study also can be used very effectively in topology optimization problems considering multiple loadcases. In the aviation industry, panels and ribs located in the aircraft wing and fuselage are simultaneously subjected to bending, torsion, and shear. Helicopter rotor control and fuselage components operate under both aerodynamic loads and loads caused by the dynamic movements of the rotor. With the anticipated increasing integration of additive manufacturing in the aviation industry in the coming years, the design and production of these structures through topology optimization will become a highly significant area of research, as it enables the lightweight design of aircraft. To give an example from the automotive industry, car chassis are dynamically subjected to bending and torsion loads simultaneously during the vehicle's operation. Additionally, car bodies are designed to meet highly complex requirements simultaneously in the event of a crash, ensuring the safety of drivers, passengers, and pedestrians. Topology optimization studies with multiple loading steps defined are a crucial tool for the effective design of these structures.

## Nomenclature

EEWC	Equal-Effect Weighted Compliance
FEA	Finite Element Analysis
PWC	Proportional Weighted Compliance
C	Compliance
f	Force
K	Stiffness
W	Weight factors

## References

[1] N. Kaya and S. Yudar, "Hava taşıt kanallarında topoloji ve boyut optimizasyonu ile ağırlık azaltımı," in Tusaş genç mühendisler semineri, Ankara, 2019.


- [2] Raicevic et al 2023. Fatigue life prediction of topologically optimized torque link adjusted for additive manufacturing. *International Journal of Fatigue*; volume 176, 107907.
- [3] G. L. Srinivas and A. Javed 2020. Topology optimization of rigid-links for industrial manipulator considering dynamic loading conditions. *Mechanism and Machine Theory*; 153: 1-16.
- [4] <https://www.tennesseeaircraft.net/2012/11/10/1964-182-sid-survey-part-2/> (Accessed: 05.08.2024)
- [5] <https://www.azom.com/article.aspx?ArticleID=9365> (Accessed: 01.08.2024)
- [6] <https://www.safran-group.com/products-services/boeing-fa-18-nose-landing-gear> (Accessed: 05.08.2024)
- [7] Infante et al 2017. Failure analysis of a nose landing gear fork. *Engineering Failure Analysis*; 82: 554-565.
- [8] Freitas et al 2019. Failure analysis of the nose landing gear axle of an aircraft. *Engineering Failure Analysis*; 101: 113-120.
- [9] Bagnoli et al 2007. Fatigue fracture of a main landing gear swinging lever in a civil aircraft. *Engineering Failure Analysis*; 15: 755-765.
- [10] Schmidt, R. The Design of Aircraft Landing Gear; SAE International. Press: Warrendale, PA, 2021.
- [11] Zhao et al 2024. Topology optimization algorithm for spatial truss based on numerical inverse hanging method. *Journal of Constructional Steel Research*; volume 219, 108764.
- [12] Gu et al 2024. Nonlinear fatigue damage constrained topology optimization. *Computer Methods in Applied Mechanics and Engineering*; volume 429, 117136.
- [13] Pan et al 2024. Isogeometric Topology Optimization of Multi-patch Shell Structures. *Computer-Aided Design*; volume 174, 103733.
- [14] Xie et al 2024. Topology optimization for fiber-reinforced plastic (FRP) composite for frequency responses. *Computer Methods in Applied Mechanics and Engineering*; volume 428, 117114.
- [15] Song et al 2024. Improving the joint quality in density-based multi-material topology optimization with minimum length scale control. *Computer Methods in Applied Mechanics and Engineering*; volume 430, 117212.
- [16] Ren et al 2024. Concurrent optimization of structural topology and toolpath for additive manufacturing of continuous fiber-reinforced polymer composites. *Computer Methods in Applied Mechanics and Engineering*; volume 430, 117227.
- [17] He et al 2024. Topology optimization of truss structures considering local buckling stability. *Computers & Structures*; volume 294, 107273.
- [18] Yuan et al 2024. Topology optimization design for strengthening locally damaged structures: A non-gradient directed evolution method. *Computers & Structures*; volume 301, 107458.
- [19] Xia et al 2024. Comparison of ground-structure and continuum based topology optimization methods for strut-and-tie model generation. *Engineering Structures*; volume 316, 118498.
- [20] Feng et al 2024. Nonlinear topology optimization on thin shells using a reduced-order elastic shell model. *Thin-Walled Structures*; volume 197, 111566.
- [21] Dong et al 2024. Topology-optimized lattice enhanced cementitious composites. *Materials & Design*; volume 244, 113155.



- [22] Luo et al 2024. An efficient isogeometric topology optimization based on the adaptive damped geometric multigrid method. *Advances in Engineering Software*; volume 196, 103712.
- [23] Saleh et al 2024. Topology optimization of vertical shear links in eccentrically braced frames. *Structures*; volume 66, 106821.
- [24] <https://engineeringproductdesign.com/knowledge-base/topology-optimization/> (Accessed: 12.08.2024)
- [25] <https://2020.help.altair.com/2020.1/hwsolvers/os/index.htm> (Accessed: 23.08.2024)
- [26] Zhang, W.H. and Flury, C. 1997. A modification of convex approximation methods for structural optimization. *Computers & Structures*; volume 64, pp. 89-95.
- [27] Ossa E.A., Paniagua M., Handbook of Materials Failure Analysis with Case Studies from the Aerospace and Automotive Industries, Press: Butterworth-Heinemann, 2016.
- [28] Gültekin, E. and Yahşi, M. 2021. A Study About Shape and Topology Optimizations on A Connecting Rod. *International Journal of Automotive Science and Technology* 5 (2): 141-146.
- [29] <https://www.newport.com/t/understanding-the-compliance-curve> (Accessed: 22/08/2024)
- [30] <https://grabcad.com/library/f-16-front-landing-gear-for-rc-model-1> (Accessed: 06/08/2024)
- [31] European Union Aviation Safety Agency (EASA). (2023). Certification Specifications for Large Rotorcraft (CS-29), Amendment 11. Cologne, Germany: EASA.
- [32] Dong X, Jiang X, Li P, Niu T, Wang Y, Zhang J. Topology optimization structure design of shape memory alloy with multiple constraints. *Journal of Intelligent Material Systems and Structures*. 2024;35(10):892-906. doi:10.1177/1045389X241237581
- [33] Patham KF. Redesigning Dynamic components for additive manufacturing using topology optimization. *Journal of Micromanufacturing*. 2024;0(0). doi:10.1177/25165984241260580
- [34] Tang P, Xu W, Ding Z, Jiang M, Lv M. Research on multi-objective topology optimization of unmanned sightseeing vehicle frame based on Analytic Hierarchy Process. *Advances in Mechanical Engineering*. 2024;16(10). doi:10.1177/16878132241288406
- [35] Ren C, Liu X, Yang X, Ma T. Crash topology optimization for front-end safety parts of battery electric vehicle using an improved equivalent static loads method. *Proceedings of the Institution of Mechanical Engineers, Part D: Journal of Automobile Engineering*. 2024;238(8):2396-2420. doi:10.1177/09544070231162137
- [36] Lan K, Yu W, Huang C, Zhou Y, Li Z, Huang W. Multi-objective optimization design for anti-fatigue lightweight of dump truck carriage combined with machine learning. *Advances in Mechanical Engineering*. 2024;16(9). doi:10.1177/16878132241269244
- [37] Yuanyao M, Dongbo L, Chunyan L, Yan W, Xiguang L, Bo W. Multi-objective optimization of traditional residential timber frames based on response surface methodology. *Journal of Computational Methods in Science and Engineering*. 2024;0(0). doi:10.1177/14727978241293251
- [38] Wang T, Xue W, Wei M, Wu J, Luo Z, Liu R. Multi-condition and multi-objective conceptual optimization design of automotive front subframe. *Proceedings of the Institution of Mechanical Engineers, Part D: Journal of Automobile Engineering*. 2024;0(0). doi:10.1177/09544070241297046
- [39] Zhu Y, Xu F, Deng X, Niu X, Zou Z. Bionic topology optimization design and multi-objective optimization of guide arm. *Proceedings of the Institution of Mechanical Engineers, Part D: Journal of Automobile Engineering*. 2024;0(0). doi:10.1177/09544070231217565
- [40] Chen H, Yu P, Long J. Multi-objective optimization design of automobile seat backrest considering coupling effect. *Proceedings of the Institution of Mechanical Engineers, Part D: Journal of Automobile Engineering*. 2024;0(0). doi:10.1177/09544070241285498
- [41] Najafi M, Ferreira AJM, Marques FD. Aeroelastic analysis of a lightweight topology-optimized sandwich panel. *Proceedings of the Institution of Mechanical Engineers, Part G: Journal of Aerospace Engineering*. 2024;238(10):999-1017. doi:10.1177/09544100241252041
- [42] Rahman M, Fricks C, Ahmed H, et al. Topology optimization and experimental validation of mass-reduced aircraft wing designs. *Proceedings of the Institution of Mechanical Engineers, Part G: Journal of Aerospace Engineering*. 2024;0(0). doi:10.1177/09544100241290577



# Hybrid Renewable Energy System Proposal: Offshore Wind and PV Farm with Optimally Designed LCL Filter in Datça, Aegean Sea, Turkey

Alp Karadeniz<sup>1\*</sup> 

<sup>1</sup>Balıkesir University, Electrical & Electronics Engineering Department, Balıkesir, Türkiye

\* [akaradeniz@balikesir.edu.tr](mailto:akaradeniz@balikesir.edu.tr)

\* Orcid No: 0000-0002-0899-6581

Received: 24 September 2024

Accepted: 17 December 2024

DOI: 10.18466/cbayarfbe.1555073

## Abstract

Different kinds of power electronics-based converters and inverters are used in the grid integration of Renewable Energy Systems. These power electronic based interfaces cause harmonic distortion in voltage and current of the grid. This research aims to propose and design a hybrid renewable energy system that uses Type 4 Permanent Magnet Synchronous Generator (PMSG) and Photovoltaic (PV) power generation farm for the Datça region in Turkey. Also, the study examines the optimal passive filter designs and harmonic analysis for designed hybrid renewable power system. In detail, the system has a 2 MW PV farm is designed to be combined with a 2 MW offshore wind farm (OWF) which is connected to the 120 kV common grid by a 25 kV distribution feeder. Additionally, utilizing meteorological data that is taken from Datça, Aegean Sea region, Turkey, such as wind speed and solar irradiation, as input parameters of the hybrid power generation system. After that, to study harmonic analysis and optimal filter designs, a mathematical strategy is proposed. First of all, the arithmetic mean (AM) of daily data (DD) is considered as the input value of OWF and PV system. With using these values, an optimal LCL filter design is found by a recently proposed meta-heuristic algorithm, Mountain Gazelle Optimization (MGO), algorithm. According to IEEE 519 standards, the optimization method seeks to minimize both the voltage levels in p.u. and the total harmonic distortion (THD) of current and voltage values. Moreover, the hybrid renewable power model is simulated with optimal LCL filters by using DD wind speed and solar irradiation values. Moreover, the performance analysis based on the results of AM data and DD values is studied.

**Keywords:** Offshore Wind Farms, Type 4 PMSG, Optimization, Harmonic, Power Quality, Photovoltaic Power Generation Farm, LCL Filter, Hybrid Power Systems.

## 1. Introduction

Amid the global shift towards achieving carbon neutrality in light of climate change concerns, there is a growing emphasis on renewable energy sources, particularly offshore wind power. Oil corporations are redirecting investments towards sustainable energy initiatives, while policymakers are increasingly endorsing emerging technologies. Offshore wind energy, known for its abundant and consistent nature, is leading this transition due to its expanding capacity and reduced visual impact compared to land-based wind farms. The rise of floating wind turbines is further enhancing the competitiveness of offshore wind energy, leading to a rapid proliferation of both the number and scale of offshore wind farms [1–3].

Guaranteeing consistent voltage and frequency, minimal disruptions, and low harmonic emissions are essential for upholding reliability, stability, and customer satisfaction within the power grid [4,5]. Nevertheless, as wind power plants (WPPs) integrate into the primary grid, harmonic distortion emerges as a significant issue concerning power quality [6].

Moreover, solar power is increasingly becoming a notable contributor to renewable energy in Turkey, owing to its abundant solar energy potential. Over the last decade, substantial investments have been made in photovoltaic solar plants, resulting in a deployed capacity of 6.2 GW as of June 2020, with continued growth anticipated [7]. Also, aside from the many positive effects of the hybrid renewable systems, various power electronics-based converters and inverters used for integrating OWF and Photovoltaic power generation systems into the grid can introduce harmonics into

voltage and current waveforms. These harmonics can cause issues such as transformer overheating, circuit breaker tripping, and reduced equipment lifespan, necessitating efforts to minimize them to maintain power quality standards in accordance with guidelines like IEEE 519-2014 and IEC 61000 [8].

In addition to that, in this paper, the optimal design of a series LCL filter [9], which can effectively mitigate high-frequency harmonics, is examined for systems incorporating hybrid renewable power systems, based on the arithmetic mean (AM) values of hourly data obtained from the European Commission for Datça, Muğla [10]. Moreover, AM data is used to represent the average values of wind speed and solar irradiation over a period. This is the input data used to optimize the system's harmonic filter design. Also, the decision to use average (AM) data for wind speed and solar radiation is common in system optimization studies as it simplifies the model and provides a stable basis for parameter optimization. Using average data ensures consistency and reduces the complexity introduced by extreme fluctuations in real-time data. While daily variations are acknowledged, using average values helps in developing a generalized system performance model [11]. Moreover, the decision to use the daily average wind speed and radiation values in the simulation was made to streamline the analysis and ensure consistency in results. While wind speed and radiation are indeed variable, using daily averages helps in balancing the fluctuations and provides a reasonable estimate for the system's performance over time. This methodology is common in the modelling of renewable energy systems and helps simplify complex variables for optimization purposes [12, 13]. Firstly, an objective function (OF) is formulated, encompassing the total harmonic distortion of the voltage waveform (THDV), the effective value of the voltage magnitude, and the power of the passive filter. To determine the optimal filter parameters, a recently proposed meta-heuristic optimization algorithm, the Mountain Gazelle Optimization (MGO) algorithm [14], is utilized to solve the OF. Additionally, the study investigates the impact of filter parameters on system performance in terms of power quality essentials (THD, voltage level, power factor, and power values), and provides a performance analysis for AM and DD inputs with an optimal filter.

In this paper, some important contributions are provided:

- The harmonic distortion performance of a hybrid system including Type 4 offshore wind farm accompanied with PV farm is simulated for the wind speed and solar irradiation data obtained from the European Commission for Datça, Turkey [10].
- For an objective function (OF) including the total harmonic distortion of the voltage waveform (THDV) and the system's rms voltage levels, and the harmonic distortion

constraints, the optimal design of two passive filter types, series and shunt LCL filters, is formulated.

- To find optimal parameters of the considered filter types according to the formulated problem, a meta-heuristic optimization algorithm recently proposed in the literature, Mountain gazelle optimization (MGO) algorithm, is employed. The results are obtained for the arithmetic mean (AM) of the wind speed and radiation data.
- The proposed Hybrid power system is simulated for arithmetic mean (AM) values of DD obtained from the European Commission for Datça, Turkey.
- The technique for optimal filter design with AM data is proposed in the study.
- Also, there is no study about the application of the hybrid renewable system for Datça in Turkey with power quality assessments.
- Finally, the performance analysis with respect to power quality essentials (THD, voltage level, power factor, and power values) of the filter under DD is studied.

### 1.1. Literature Overview

According to the literature summary, there are some studies on the employment of harmonic filters to mitigate harmonic distortion in the systems integrated with onshore, offshore wind and PV systems [9,15–23].

In one of these studies, the design and simulation of a solar photovoltaic (SPV) system integrated with the grid, employing a current-controlled voltage source converter (VSC) and LCL filter, is presented. The study aims to optimize solar power utilization, meet reactive power demand, and enhance power quality through power balance control, showcasing a 10 kW SPV array simulation with indirect current control [15].

Also, in [16], the paper studies a hybrid photovoltaic (PV)-wind-battery energy storage system connected to the utility grid via a three-phase inverter, utilizing an advanced control strategy combining fuzzy logic proportional integral derivative-improved second-order generalized integrator-quadrature signal generator-phase locked loop (FLPID-ISOGI-PLL). The proposed approach enhances power quality at consumer terminals by improving power penetration, load sharing, power factor correction, and dynamic operation while maintaining DC-AC power balance, demonstrated through MATLAB/SIMULINK simulation and hardware-in-loop (HIL) co-simulation using FPGA Virtex-7 VC-707.

In addition to that, another study [17] presents a novel approach to mitigating harmonic currents in grid-connected photovoltaic energy systems by incorporating

a phase shifting transformer into the structure of an LCL filter. This approach aims to optimize LCL filter parameters for improved harmonic mitigation, in power quality enhancement for renewable energy sources.

Moreover, in [18], the study addresses filtering issues in three-phase PV grid-connected inverters by establishing mathematical models for L and LCL filters. Simulation results demonstrate superior performance of the LCL filter over L and LC filters, with parallel resistors proving more advantageous for system stability while maintaining filtering effectiveness, confirming theoretical validity.

Additionally, in [9], the study introduces a novel approach to designing LCL filters for grid-interfaced PV systems, focusing on minimizing both filtering inefficiencies and costs. By exploring a cost-based minimization approach for filter elements, optimal designs are obtained while ensuring compliance with harmonic standards and voltage drop constraints. Simulation and experimental validation of a 10-kVA grid-connected inverter confirm the efficacy of the proposed design method, demonstrating harmonic attenuation and low total harmonic distortion.

Also, the other study [19] introduces a modular hybrid renewable energy system comprising PV array, wind turbine, battery storage, AC load, and a dump load, aimed at minimizing total project cost and maximizing reliability while minimizing unutilized surplus power. A novel iterative filter selection approach is employed to design the system, ensuring the best acceptable solution considering all design objectives. Compared to iterative-Pareto-fuzzy and particle swarm optimization techniques, this approach demonstrates superiority in total project cost while meeting load demand satisfaction.

Additionally, the paper [20] proposes a redesign of the LCL grid filter for a multimewatt medium-voltage neutral-point-clamped converter used in wind turbines, employing Selective Harmonic Elimination PWM (SHEPWM). By eliminating low-order harmonics, SHEPWM enhances efficiency compared to traditional pulse width modulation techniques like Phase Disposition PWM (PDPWM), resulting in improved converter and overall system performance, as demonstrated through experimental results.

Also, in another paper [21] analyses the impact of interleaved carriers on the harmonic performance of parallel-connected voltage source converters in wind energy systems, employing 60° clamp discontinuous pulse width modulation to minimize switching losses. It presents a systematic design procedure for line filters, incorporating an LC trap branch within the conventional LCL filter to achieve optimal filter parameter values and validates the methodology through experimental verification.

Moreover, the paper [22] proposes the integration of active filters into the control system of Type-IV wind turbines in offshore WPPs to mitigate harmonic voltage amplification. Using the extra element theorem, active filter tuning is optimized to achieve both effective harmonic reduction and adequate stability margins, demonstrated through a real-time simulation of a 270 MW offshore WPP with 3-MW wind turbines, successfully suppressing converter and grid voltage harmonics below planning levels at WPP buses.

Also, the paper [23] introduces an H robust control approach for wind turbine inverters with LCL filters, aimed at selectively filtering harmonics in offshore transmission networks amidst parameter uncertainties. By combining passive filtering with a robust high-order active filter controller, the method effectively mitigates harmonic currents injected by power converter-based turbines, outperforming traditional Proportional-Integral (PI) controllers with enhanced stability and reduced control effort across operational conditions.

Moreover, the study [24] investigates advanced techniques to improve power quality in hybrid renewable energy systems, focusing on the integration of multiple energy sources such as solar and wind. It elaborates on the role of energy storage systems, including batteries and supercapacitors, and smart grid technologies in mitigating voltage fluctuations, frequency deviations, and harmonic distortions. The results underline that effective power quality management strategies not only stabilize hybrid systems but also enhance their reliability and long-term sustainability, making them more viable for large-scale deployment. Also, the study [25] explores the optimization of harmonic mitigation strategies in hybrid energy systems by employing advanced modelling and simulation techniques. It highlights the importance of active harmonic filters and control algorithms, such as predictive and adaptive controls, in minimizing harmonic distortions caused by nonlinear loads and intermittent renewable energy sources. The paper provides a comprehensive analysis of the trade-offs between cost, performance, and energy efficiency, offering practical insights into designing robust hybrid systems for enhanced power quality. Lastly, the paper [26] provides an in-depth analysis of hybrid filters and their role in addressing power quality issues in renewable energy systems, such as harmonic distortion, reactive power imbalances, and voltage stability. It emphasizes the synergy between active and passive filtering techniques, demonstrating their combined effectiveness in improving the overall stability and efficiency of energy networks. The study also discusses the critical factors influencing filter performance, including system configuration, load characteristics, and real-time control capabilities, offering guidelines for implementing hybrid filters in practical energy distribution systems.

To compare the recently published studies, the study [24] focuses on power quality enhancement but primarily uses optimized controllers for mitigating harmonics in grid-connected hybrid systems involving either wind or solar power. Unlike this study, which combines offshore wind and PV systems, it lacks the dual-source integration.

Also, the study [25] emphasizes optimizing harmonic mitigation in hybrid wind-PV systems but does not incorporate the novel Mountain Gazelle Optimization (MGO) algorithm. Instead, traditional methods are used, making the optimization approach in this study more advanced.

Moreover, the referenced study [26] improves power quality in PV systems using hybrid filters, but it does not focus on offshore wind energy or consider the specific regional conditions of Datça, Turkey, which is a key focus of this study.

## 2. Modelling of The Studied System

In this section, the modelling of the studied system with the OWF and PV system is introduced.

### 2.1 Modelling of Hybrid Power System

The schematic of the studied system containing offshore wind farm with Type 4 PMSG turbine and PV power generation system is given in Fig. 1. It has a 120 kV 60 Hz grid system, a 47 MVA, 120/25 kV, Y/ $\Delta$  transformer, a 25kV/575V, 2.5 MVA,  $\Delta$ /Y transformer, and a submarine cable with 36 km length. There is an LCL filter connected to 575 V bus, which is to be optimized for improvement of the bus voltage harmonic distortion and rms levels.

In addition, the resistances and inductances of primary winding of the second one is 0.000833 p.u. and 0.025 p.u., those parameters of secondary winding seen from primary side are 8.33e-4 p.u and 0.08 p.u., and its magnetization inductance is 500 p.u. Additionally, in the system, the  $\pi$  model parameters of the submarine cable (Fig. 2), which is utilized for the test offshore wind farm, are taken from ABB data sheets [27, 28]. They are given in Table 1.

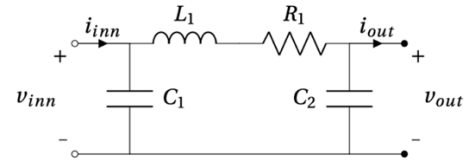


Figure 2: The equivalent  $\pi$  circuit model of the cable.

Table 1: The circuit parameters per km of the cable model taken from ABB data sheet.

Cable	R (m $\Omega$ / km)	L (mH/ km)	C ( $\mu$ F/ km)
500 mm <sup>2</sup> Cu cable	33.6	0.41	0.24
	$R_0(\Omega$ / km)	$L_0(mH/km)$	$C_0(nF/km)$
	1000	4.1264	7.7519

To accurately model the cable in the simulations, it should be represented as series connected multiple sections considering the  $\pi$  model depicted in Figure 2. The required number of  $\pi$ -sections should be determined regarding the considered highest harmonic order and length of cable [2]. Accordingly, the submarine cable is segmented into three identical  $\pi$ -sections.

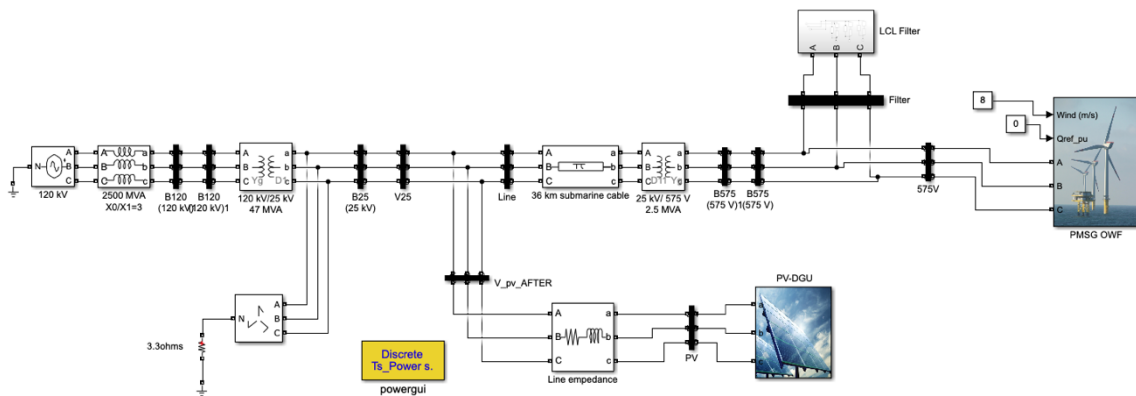


Figure 1: The studied hybrid system Simulink model.

### 2.2- Modelling of Wind Energy Generation System (PMSG)

In the examined system, a 2 MW wind farm is connected to a 25kV distribution network transferring power to a

120kV grid. In the farm, each turbine has a permanent synchronous generator (PMSG) and a full-scale power converter [2]. The detailed schematic of the Wind Turbine, depicted in Fig. 3, provides further insight.

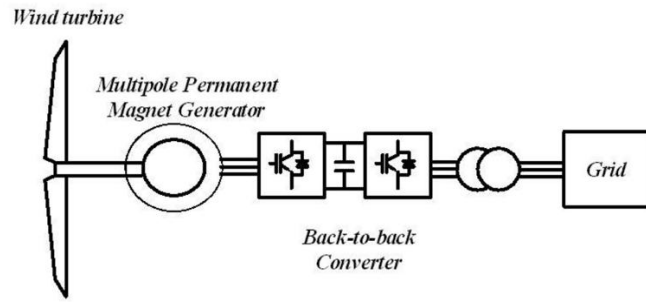


Figure 3: The schematic representation of a PMSG.

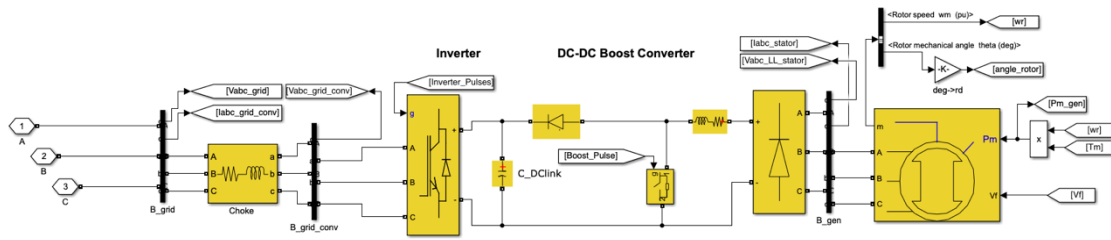


Figure 4: Under mask illustration of PMSG wind turbine block.

For the simulations, the wind speed remains constant at 15 m/s. The control system employs a torque controller to maintain speed at 1.2 per unit (pu), while the reactive power output from the wind turbine is regulated at 0 Mvar. Although the turbine output power is 1 pu of its

rated power at a wind speed of 15 m/s, for demonstration purposes of DD values throughout the optimization process, the AM value (8.85 m/s) wind speed is considered.

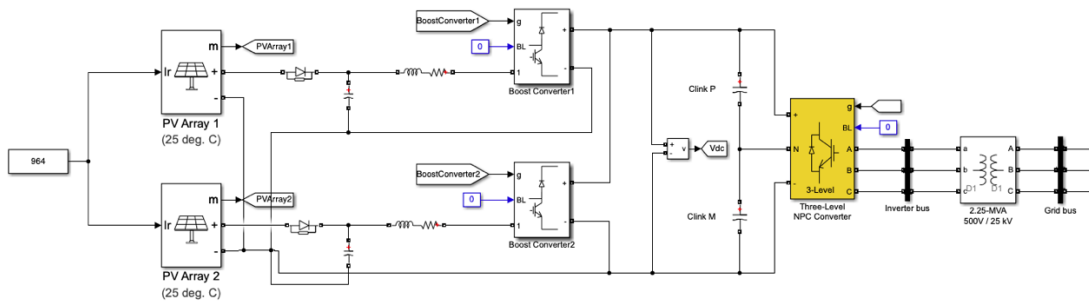


Figure 5: Under mask illustration of PV solar system block.

In the combined modelled framework, a 2 MW PV power system is considered (See Fig. 5). Furthermore, the PV system comprises two PV arrays: PV Array 1 and PV Array 2, capable of generating 1.5 MW and 500 kW, respectively, under 1000 W/m<sup>2</sup> solar irradiance and 25 degrees Celsius cell temperature. Each PV array is connected to a boost converter, with each boost being independently regulated by Maximum Power Point Trackers (MPPT) employing the Perturb and Observe method to optimize power extraction by adjusting voltage levels across the PV array terminals. The outputs from the boost converters are connected to a shared 1000

V DC bus. A three-level Neutral Point Clamped (NPC) converter transforms the 1000 V DC to approximately 500 V AC. Control of the NPC converter is managed by a DC voltage regulator tasked with maintaining the DC link voltage at 1000V. Additionally, a 2.25-MVA 500V/25kV three-phase coupling transformer links the converter to the grid. The grid configuration encompasses standard 25-kV distribution feeders and a 120-kV equivalent transmission infrastructure.



## 2.4- Data preparation process

This paper performs a performance analysis of the modelled system using the Typical Meteorological Year (TMY) dataset provided by the European Commission's Joint Research Centre (JRC). The TMY dataset covers the period from March 2007 to June 2020, spanning approximately 13 years, with hourly data available [10]. The Typical Meteorological Year (TMY) dataset is widely used in energy system simulations as it provides reliable, long-term meteorological data for modelling renewable energy generation. The dataset's reliability is supported by its extensive use in studies and validated by several credible sources. Moreover, the Typical Meteorological Year (TMY) dataset is widely used in renewable energy modelling for providing a representative set of climatic data over a year. It is particularly useful for simulations in regions like Datça, where long-term data is crucial for accurate forecasting. The reliability of the TMY dataset is well-documented in several studies, which confirm its accuracy in modelling renewable energy systems [29, 30].

It includes various parameters such as wind speed, solar irradiance, among others. Additionally, sample data from Datça, Turkey, located in the Aegean Sea region, is considered. The geographical coordinates of the reference point are latitude 36.656 and longitude 27.393 for the Datça area. Fig. 6 depicts the geographical position of the reference point within the Aegean Sea region.

The Datça region is selected due to its favourable wind speed and also, solar irradiations values, making it an ideal location for offshore wind and PV farm installation in the Aegean Sea. Notably, there are currently no OWF

applications in Turkey. This study aims to simulate power quality performance of the generic hybrid renewable energy generation system including offshore wind farm and PV units under the wind speed and solar irradiation values of Datça. Furthermore, the hybrid model is simulated over a 20-second scale, representing daily values for one month in the Datça dataset for June 2020. This entails linear scaling of 744 data points over the 20-second timeframe, resulting in a time representation of 0.02688 seconds per data point. Both wind speed and solar irradiation data are utilized for the OWF and PV farm in the hybrid renewable power generation system. The nominal power values for both the OWF and PV system are set at 2 MW each, corresponding to wind speeds of 15m/s and solar irradiation values of 1000 W/m<sup>2</sup>. However, to reflect real-world performance, an optimal passive filter design is developed based on the arithmetic mean values (8.85 m/s for wind speed and 964 W/m<sup>2</sup> for solar irradiance) derived from the wind speed and solar irradiation data points for June 2020.

Also, the choice to use June data was based on the typical high stability and peak values of wind speed and solar irradiation observed in this period for the Datça region. By using the arithmetic mean of this data, a balanced and reliable representation of system performance has been ensured. This approach helps simplify the analysis while maintaining the accuracy of results. Variations in wind speed are integrated with different data sets (e.g., TMY) and their respective averages over a month. This method remains practical for the scope of our study while still providing valuable insights into system performance [31]. Table 2 presents the nominal and AM data for the hybrid renewable power system. In this study, AM data is utilized to formulate optimal design and conduct performance analysis.



Figure 6: Geological locations of pivot point Datça area [10].

Table 2: Data scaling of AM data.

	Nominal Data	Real data
Wind speed	15 m/s	8.8 m/s
OWF power	2 MW	1.18 MW
Solar irradiation	1000 W/m <sup>2</sup>	966.8 W/m <sup>2</sup>
PV power	2 MW	1.933 MW
Expected power at distribution bus (25kV)	4 MW	3.11 MW

As seen from Table 2, the nominal and AM data of OWF power and PV system power are 1.18 MW and 1.933 MW, respectively. Also, expected power rating at 25kV (PCC) bus is 3.11 MW at nominal wind speed and solar irradiation values.

Moreover, to demonstrate the DD performance of the system after optimal filter integration, 2020–June, every day at 10 a.m. for 30 days, wind speed and solar

irradiation values are considered. The reason for this is that 744 data points are not suitable to create results figures and table representations with respect to this huge data number. The hour of 10 a.m. is used because the wind speed and solar irradiation values are perfectly stable and close to their maximum values as well. Table 3 shows the DD data of wind speed and solar irradiation values for June-2022 at 10.00 am

Table 3: DD data for June-2020.

2020-June	Solar Irradiation (w/m <sup>2</sup> )	Wind Speed (m/s)
1	947	8.21
2	996	7.79
3	924	8.07
4	972	8.34
5	981	7.31
6	947	5.79
7	968	10.69
8	907	10.97
9	992	8.07
10	933	9.79
11	985	10.48
12	821	11.03
13	994	8.97
14	978	9.15
15	967	11.45
16	1020	9.38
17	930	8.21
18	1008	7.03
19	956	10.76
20	1004	12.55
21	1020	9.45
22	1001	9.86
23	1006	7.45
24	959	8.69
25	996	8.14
26	958	10.76
27	968	10.34
28	947	3.45
29	964	7.24
30	972	9.14

## 2.5- Harmonic Pollution in the Studied System without Filter

Fig. 7 and Fig. 8 show the waveforms and harmonic spectrums of the voltage and current at 575 V (grid-side bus of inverter output of OWF) and 25 kV (PCC bus) buses for the system without the passive filter, respectively. The total harmonic distortion (THD) values of the respective voltages are 23.92% and 5.58 and the THD values of the respective currents are 16.77% and 43.18%. Also,  $V_{pu}$  values are 1.12 and 1.31 p.u. Thus, one can see that the system without a filter has highly distorted voltage and currents, and their THD values are over the limits defined by the IEEE-519 standard [32] given in Table 5.

## 3- Formulation and solution algorithm of the optimal filter design

In this section, the series and shunt LCL filters considered for harmonic mitigation in the system. Also, the optimal design of these filters is formulated, and algorithms are introduced to solve the associated optimization problems.

### 3.1- Introduction of Considered Passive filter types

In this study, two LCL filter types, such as series LCL and shunt LCL filters, which have high compensation capability for high-frequency harmonics, are chosen. Regarding their equivalent circuits given in Fig. 9, they are briefly introduced below:

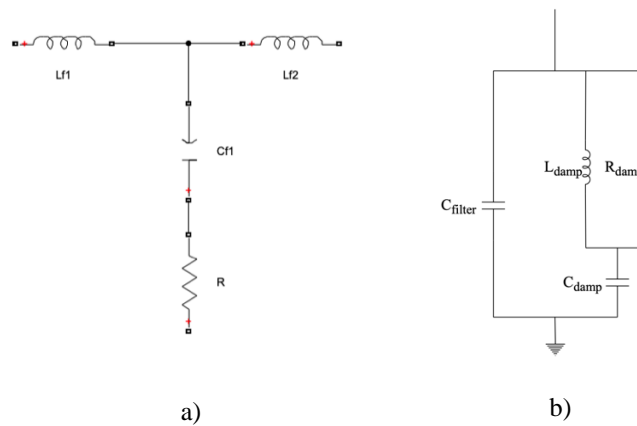


Fig 9: The single-phase representations of a) series b) shunt LCL filters.

The LCL filter configuration [9] is widely employed as an interface between converters and the utility grid due to its efficacy in smoothing converter output currents. Moreover, it demonstrates superior performance with relatively small inductor and capacitor values. The LCL filter offers enhanced attenuation of higher harmonics, enabling operation at lower switching frequencies while adhering to harmonic constraints specified in standards like IEEE-519 and IEEE-1547 [33, 34].

### 3.1.1- Series LCL filter

A series LCL filter consists of three main components: the inverter-side inductor, the grid-side inductor, and the filter capacitor [15]. Designing these three elements for an LCL filter typically involves solving three or more simultaneous equations, indicating the presence of multiple design objectives. But in this paper, the parameters ( $L_{f1}$ ,  $L_{f2}$ ,  $C_{f1}$  and  $R$ ) of series LCL filter are determined by MGO algorithm. The series LCL filter is used for PV farm system and connected to primary side of the 500V/25kV bus.

### 3.1.2- Shunt LCL filter

The shunt LCL filter is used for OWF's output side of the inverter. A shunt LCL filter consists of four main

Table 4: The THDV (%),  $V_{pu}$  and THDI (%) values of the 575 V and 25 kV buses.

THDV(%)	
25kV Bus	23.92
575V Bus	5.58
$V_{pu}$	
25kV Bus	1.12
575V Bus	1.31
THDI(%)	
25kV Bus	16.77
575V Bus	43.18

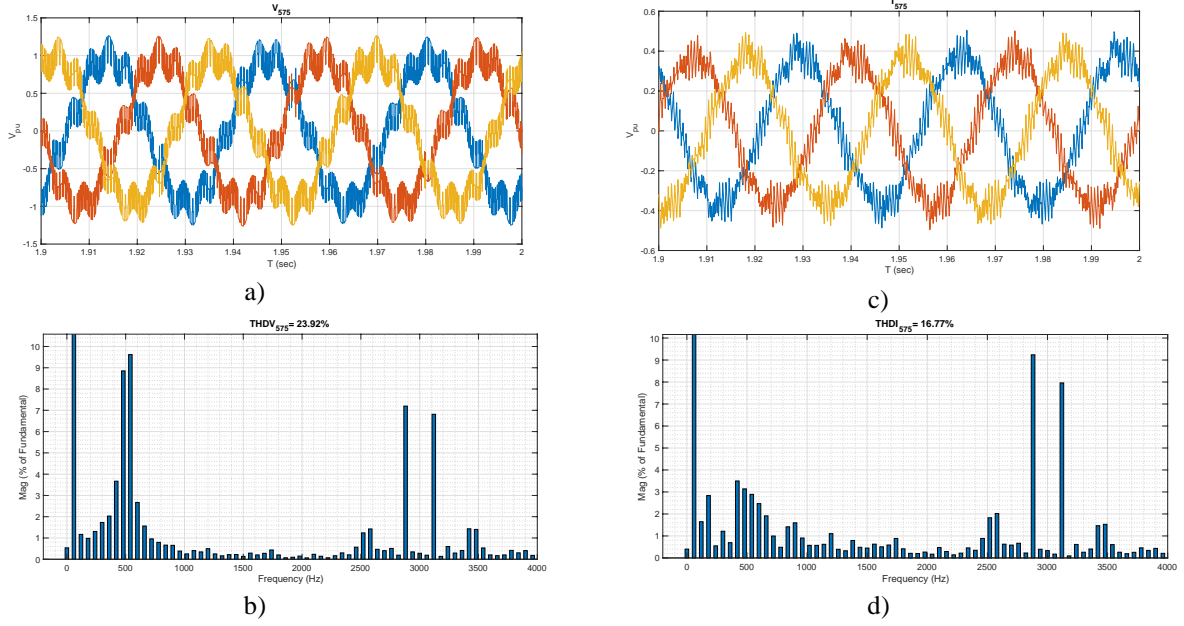


Figure 7: The (a) voltage waveforms, (b) voltage harmonic spectrums, (c) current waveforms and (d) current harmonic spectrums at the 575 V bus for the system without the filter.

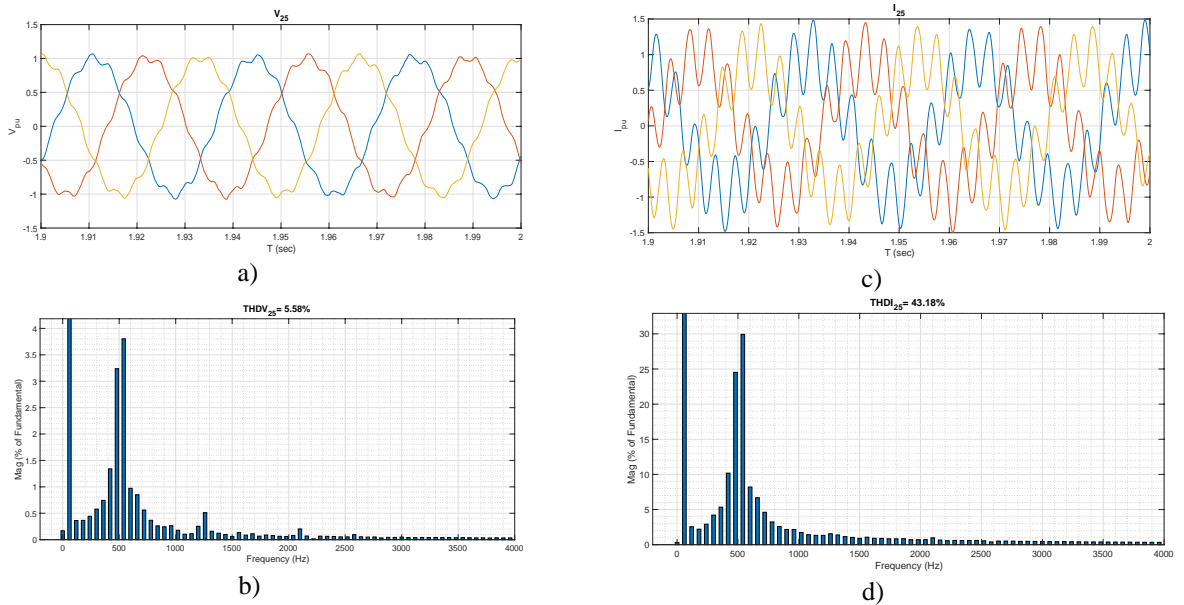


Figure 8: The (a) voltage waveforms, (b) voltage harmonic spectrums, (c) current waveforms and (d) current harmonic spectrums at the 25kV bus for the system without the filter.

Table 5: The IEEE std. 519 harmonic limits.

Bus Voltage $V$ at PCC	Individual Harmonic (%)	Total Harmonic Distortion THD(%)
$V \leq 1.0$ kV	5.0	8.0
$1 \text{ kV} < V \leq 69$ kV	3.0	5.0
$69 \text{ kV} < V \leq 161$ kV	1.5	2.5
$161 \text{ kV} < V$	1.0	1.5

components such as;  $L_{damp}$ ,  $C_{damp}$ ,  $R_{damp}$  and  $C_{filter}$ . Also, designing these parameters, starting with optimally chosen  $f_{cutoff}$  value. After that, the design procedure continues with the calculation of the filter capacitance

that is shown in Eq. (1), denoted as  $C_{filter}$ , which is determined based on the cutoff frequency and the inverter inductance, represented as  $L_{inv}$ , as outlined in Eq. (5).

$$C_{filter} = \frac{1}{(2\pi \cdot f_{cutoff})^2 \cdot L_{inv}} \quad (1)$$

The damping inductance,  $L_{damp}$ , is calculated by Eq. (2).

$$L_{damp} = 5 \cdot L_{inv} \quad (2)$$

The damping capacitance,  $C_{damp}$ , can further be calculated by Eq. (3).

$$C_{damp} = \frac{C_{filter}}{2} \quad (3)$$

Then, the damping resistance,  $R_{damp}$ , can be calculated with Eq. (4).

$$R_{damp} = \sqrt{\frac{L_{damp}}{C_{damp}}} \quad (4)$$

According to [2], Eq. (5) can be utilized to determine the converter inductance. This equation is dependent on several parameters including the DC-link voltage  $V_{DC}$ , the switching frequency  $f_{sw}$ , and the peak-to-peak amplitude of the ripple current  $I_{rpp}$ . The ripple current is assumed to be 20% of the peak-to-peak nominal current.

$$L_{inv} = \frac{V_{DC}}{4 \cdot f_{sw} \cdot I_{rpp}} \quad (5)$$

In brief,  $f_{cutoff}$  is determined by optimization algorithm and  $L_{inv}$ ,  $C_{filter}$ ,  $L_{damp}$ ,  $C_{damp}$  and  $R_{damp}$  are calculated from Eq. (1)-(5).

### 3.2- Problem Formulation

The parameters of series and parallel LCL passive filters are optimized to find the best suitable filter form to get less harmonically polluted operating system. In addition to that, voltage levels for all buses should be around 1 p.u. By using these passive filters, the system model is run to find optimal passive filter parameters. The objective function is created with respect to the THDV,  $V_{pu}$  and the power loss of filters values of the 25 kV bus. The 25 kV bus is selected as a candidate because it is the PCC bus which is common point of harmonic effects of OWF and PV systems. The objective function of the optimization problem can be written as follow:

#### Objective Function:

$$\begin{aligned} \text{minimize } F(obj) \\ = a * THDV_{25} + b * |V_{pu,25} - 1| + c \\ * |sfilter_{powerloss}| + c \\ * |pfilter_{powerloss}| \end{aligned}$$

#### Subject to:

$$THDV_{h-individual} \leq Max THDV_{individual}$$

$$THDI_{h-individual} \leq Max THDI_{individual}$$

$$THDV_{\%} \leq Max THDV_{\%}$$

$$THDI_{\%} \leq Max THDI_{\%}$$

$a$ ,  $b$  and  $c$  are coefficients of  $THDV_{25}$  and  $V_{pu,25}$ .  $V_{pu,25}$  is p.u. value of a phase to ground voltage value of the 25 kV bus. Also,  $THDV_{25}$  value is total harmonic distortion value of the voltage at 25 kV bus.  $sfilter_{powerloss}$  and  $pfilter_{powerloss}$  are power values of series and parallel filters which are optimally found.  $Max THDV_{individual}$  and  $Max THDI_{individual}$  values are individual harmonic limits for voltage and current values restricted by IEEE 519 standarts.  $THDV_{h-individual}$  and  $THDI_{h-individual}$  are hth harmonic values of current and voltage. Also,  $Max THDV_{\%}$  and  $Max THDI_{\%}$  are determined by IEEE 519 standarts with respect to suitable voltage levels.

### 3.3. Solution Algorithms

To determine the optimal filter parameters, we utilize a meta-heuristic optimization algorithm called the Mountain Gazelle Optimization (MGO) algorithm [11], which has been recently proposed in the literature. The algorithms are introduced below.

#### 3.3.1- Mountain Gazelle Optimization Algorithm (MGO)

The Mountain Gazelle Algorithm (MGO), introduced by Seyedali Mirjalili in 2022, draws inspiration from the intricate coexistence dynamics of mountain gazelles and Robinia trees in the Arabian Peninsula and nearby regions. Reflecting the territorial behaviour and migration patterns of these gazelles, MGO incorporates elements such as territorial disputes, herd formations, and extensive migrations to guide its optimization process [14].

#### Mathematical Model:

By mathematically, the MGO algorithm conducts optimization tasks based on four primary aspects of mountain gazelle life: herds of bachelor males, maternal herds, solitary territorial males, and migratory behaviours in search of food.



In the Mountain Gazelle Algorithm (MGO), each gazelle ( $X_i$ ) can join one of three herds: maternity herds, bachelor male herds, or solitary territorial males, potentially giving birth to new gazelles within these groups. The algorithm aims to find the optimal global solution represented by an adult male gazelle within a herd's territory, with about one-third of the population expected to possess the lowest cost. Through exploitation and exploration phases facilitated by four mechanisms, MGO guides solutions towards the best outcome while exploring alternative options. Fig. 10 provides an overview of the optimization process based on the agents within MGO [14].

### Territorial Solitary Males

Once male mountain gazelles reach maturity and attain sufficient strength, they establish solitary territories and exhibit pronounced territorial behaviour. Eq. (6) has been employed to formulate the model representing the territories of adult males.

$$TSM = male_{gazelle} - (r_{i1} \times BH - r_{i2} \times X(t)) \times F \times Cof_r \quad (6)$$

In Equation (6), the mature gazelle signifies the positional array of the optimal global solution, corresponding to the adult male gazelle. The variables  $r_{i1}$  and  $r_{i2}$  denote random integers, each ranging from 1 to 2. BH represents the coefficient vector for the young male herd, calculated using Eq. (7). Additionally,  $F$  is determined utilizing Eq. (8), while  $Cof_r$  denotes another coefficient vector, randomly selected and adjusted during

each iteration to enhance the exploration capability, computed with Eq. (9) [14].

$$BH = X_{ra} \times |r_1| + M_{pr} \times |r_2|, ra = \left\{ \frac{N}{3} \mid \dots N \right\} \quad (7)$$

In Eq. (7),  $X_{ra}$  represents a random solution corresponding to a young male gazelle within the interval  $ra$ .  $M_{pr}$  signifies the average number of search agents (denoted as  $\frac{N}{3}$ ) that were randomly selected. Additionally,  $N$  represents the total number of gazelles, while  $r_1$  and  $r_2$  represent random values ranging between 0 and 1.

$$F = N_1(D) \times \exp \left( 2 - Iter \times \left( \frac{2}{MaxIter} \right) \right) \quad (8)$$

In Eq. (8), within the dimensions of the problem,  $N_1$  is a random number sampled from a standard distribution. The exponential function, denoted as  $\exp$ , is applied.  $MaxIter$  represents the total number of iterations, while  $Iter$  indicates the current iteration number [14].

$$Cof_i = \begin{cases} (a + 1) + r_3, & \\ a \times N_2(D), & \\ r_4(D) & \\ N_3(D) \times N_4(D)^2 \times \cos((r_4 \times 2) \times N_3(D)) & \end{cases} \quad (9)$$

In Eq. (9), the parameter  $a$  is calculated using Eq. (10). Moreover,  $r_3$ ,  $r_4$ , and  $rand$  signify

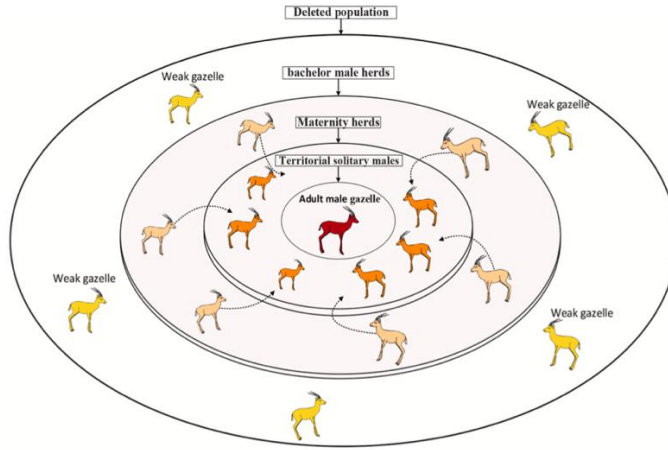


Figure 10: MGO optimization procedure [14].

three random values between 0 and 1.  $N_2$ ,  $N_3$ , and  $N_4$  denote random numbers drawn from a normal distribution within the problem's dimensions. Additionally, within the problem's dimensions,  $r_4$  represents another random value between 0 and 1. Finally,  $\cos$  denotes the cosine function.

$$a = -1 + Iter \times \left( \frac{-1}{MaxIter} \right) \quad (10)$$

Finally, in Eq. (10),  $MaxIter$  denotes the total number of iterations, while  $Iter$  represents the current iteration number [14].

### **Maternity Herds:**

Maternity herds play a vital role in the life cycle of mountain gazelles, as these groups are responsible for birthing robust male gazelles. This behavior is mathematically formulated using Eq. (11).

$$MH = (BH + Cof_{1,r}) + (ri_3 \times male_{gazelle} - ri_4 \times X_{rand}) \times Cof_{1,r} \quad (11)$$

In Eq. (11),  $BH$  represents the vector of the impact factor of young males, which is computed using Eq. (7).  $Cof_{2,r}$  and  $Cof_{3,r}$  are randomly selected coefficient vectors calculated independently using Eq. (12).  $ri_3$  and  $ri_4$  are integer random numbers, each taking values of 1 or 2.  $male_{gazelle}$  denotes the best global solution (adult male) in the current iteration. Finally,  $X_{rand}$  represents the vector position of a gazelle that is randomly selected from the entire population [14].

### **Bachelor Male Herds:**

As male gazelles mature, they often establish territories and assert dominance over female gazelles. Eq. (12) is employed to mathematically model this behavior of gazelles.

$$BMH = (X(t) - D) + (ri_5 \times male_{gazelle} - ri_6 \times BH) \times Cof_r \quad (12)$$

In Eq. (12),  $X(t)$  represents the position vector of the gazelle in the current iteration. Parameter  $D$  is computed using Eq. (13).  $ri_5$  and  $ri_6$  are randomly chosen integers, each taking a value of 1 or 2.  $male_{gazelle}$  signifies the position vector of the male gazelle (the best solution). Additionally,  $BH$  denotes the impact factor of the young male herd, which is calculated using Eq. (7).  $Cof$  represents a randomly selected coefficient vector, computed and utilized using Eq. (9) [14].

$$D = (|X(t) + |male_{gazelle}||) \times (2 \times r_6 - 1) \quad (13)$$

In Eq. (13),  $X(t)$  and  $male_{gazelle}$  represent the positions of the gazelle vectors in the current iteration and the best solution (adult male), respectively.  $r_6$  is also a random number ranging between 0 and 1.

### **Migration to Search for Food:**

Mountain gazelles are perpetually in search of food sources, often traveling great distances to forage and migrate. Eq. (14) has been utilized to mathematically model this behavior of gazelles.

$$MSF = (ub - lb) \times r_7 + lb \quad (14)$$

In Equation (14),  $ub$  and  $lb$  represent the upper and lower limits of the problem, respectively. In the MGO algorithm,  $r_7$  is a randomly chosen integer between 0 and 1, used in conjunction with the mechanisms TSM, MH, BMH, and MSF to generate new generations for all gazelles, adding epochs to the total population. At the end of each epoch, gazelles are sorted in ascending order, with high-quality, cost-effective solutions retained while weaker ones are removed. The best-performing gazelle, representing the optimal solution, is identified as the adult male gazelle holding territory [14]. The flowchart and pseudo-code of the MGO algorithm are provided at Fig. 11.

It's worth noting that the MGO algorithm are executed in the Matlab/Simulink environments on a Mac OS operating system, utilizing a MacBook Pro with 16GB RAM and a 256GB SSD.

### **4-Analysis Results**

In this section, firstly, two filter types are optimally designed for AM values. Additionally, their power quality improvement performances are comparatively evaluated. Secondly, their performances are analyzed under DD values of the considered two environmental factors.

#### **4.1 Optimal filters designs and performance analysis**

To eliminate harmonics at PCC points, the meta-heuristic optimization algorithm (MGO) is used to optimally design LCL filter. Accordingly, the achieve optimal series and shunt LCL filter parameters are listed in Table 6.

It is seen from Table 6 that, the results in the table depict the key parameters of optimal filter designs obtained solely through the MGO algorithm. For the series LCL filter, a notably high capacitance value of  $X_{C1} 2.65 \times 10^5 \Omega$  is indicated, suggesting a significant capacitive reactance. The absence of a provided value for  $X_{C2}$  implies a simplified design approach. The inductance values for  $X_{L1}$  and  $X_{L2}$  are  $0.0191 \Omega$  and  $0.0078 \Omega$ , respectively, with a consistent resistance value  $R$  of  $0.001 \Omega$ . Regarding the shunt LCL filter, the provided parameters include  $XC_{damp}$  ( $3.5054 \Omega$ ),  $XL_{damp}$  ( $0.1521 \Omega$ ),  $XC_{filter}$  ( $1.7527 \Omega$ ),  $R_{damp}$  ( $0.7302 \Omega$ ),  $f_{cut}$  ( $455.43$  Hz), and  $f_{sw}$  ( $3000$  Hz). These parameters represent the impedance of damping and filter components, as well as cutoff and switching frequencies, crucial for shaping filter characteristics. These results underscore the effectiveness of the MGO algorithm in filter design. The high capacitance value in the series LCL filter indicates a strong capacitive reactance response, while the inductance and resistance values are important for balancing filter performance. The parameters of the shunt LCL filter optimize desired frequencies and component impedances, serving the goals of reducing harmonic distortion and improving power quality.

Lastly, cost and iteration values MGO algorithm to find optimal LCL filter parameters. For the LCL filter, cost values and iteration values are 0.2752 and 8 for the MGO algorithm, respectively. Also, to show the iterative process, Fig. 12 is given below.

#### 4.2 The analysis of hybrid system with the optimal LCL filter for DD values

After the optimization process with MGO algorithm, the optimally designed LCL filters are connected to the hybrid system. Also, to test the LCL filters, DD values for 30 days at same hour (10.00 AM) are used as input values (solar irradiance and wind speed) of PV and OWF system. The daily representations of  $V_{pu}$ , THDV (%) and THDI (%) values are given in Fig. 13.

From Fig 13, it can be concluded that, all parameters are kept between IEEE 519 standards. Also, it should be noted that, the optimally designed LCL filters from AM values successfully eliminates harmonic distortions in the system. Additionally,  $V_{pu}$  values are all close to the 1 p.u value for 30 days. Moreover, the detailed results of the system for DD values, Table 7 is given below.

According to the table results, the total harmonic distortion of voltage (THDV) values for the 575V bus are at low levels and within acceptable harmonic distortion limits. The minimum THDV value is 1.9078%, the mean THDV value is 1.982%, and the maximum THDV value is 2.077%. The small differences among these values indicate stable system performance. In contrast, the total harmonic

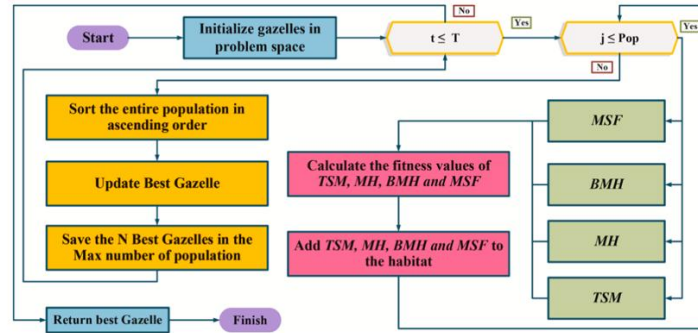


Figure 11: Flowchart of MGO algorithm [14].

Table 6: The parameters of the optimal filter designs attained by MGO algorithm.

MGO	
Series LCL Filter (PV)	
$X_{C1} (\Omega)$	$2.65 \times 10^5$
$X_{C2} (\Omega)$	-
$X_{L1} (\Omega)$	0.0191
$X_{L2} (\Omega)$	0.0078
$R (\Omega)$	0.001
Shunt LCL Filter (OWF)	
$XC_{damp} (\Omega)$	3.5054
$XL_{damp} (\Omega)$	0.1521
$XC_{filter} (\Omega)$	1.7527
$R_{damp} (\Omega)$	0.7302
$f_{cut} (Hz)$	455.43
$f_{sw} (Hz)$	3000

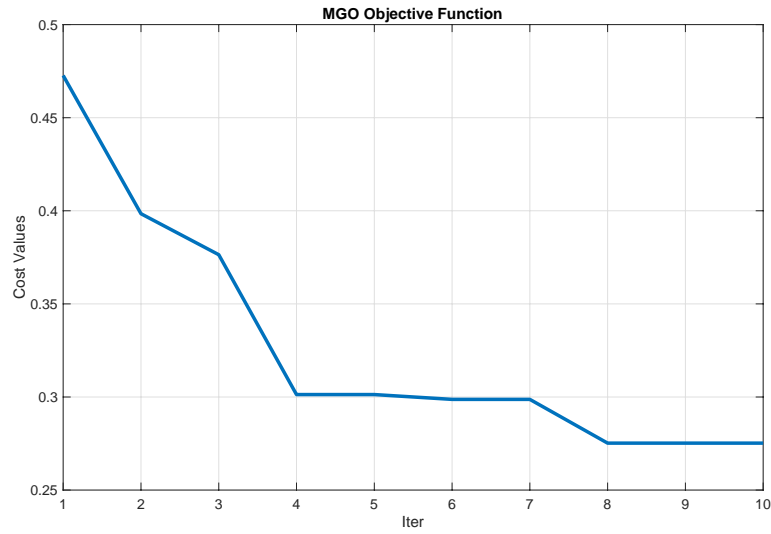


Figure 12: For series and shunt LCL filters, the objective function values obtained by MGO algorithm.

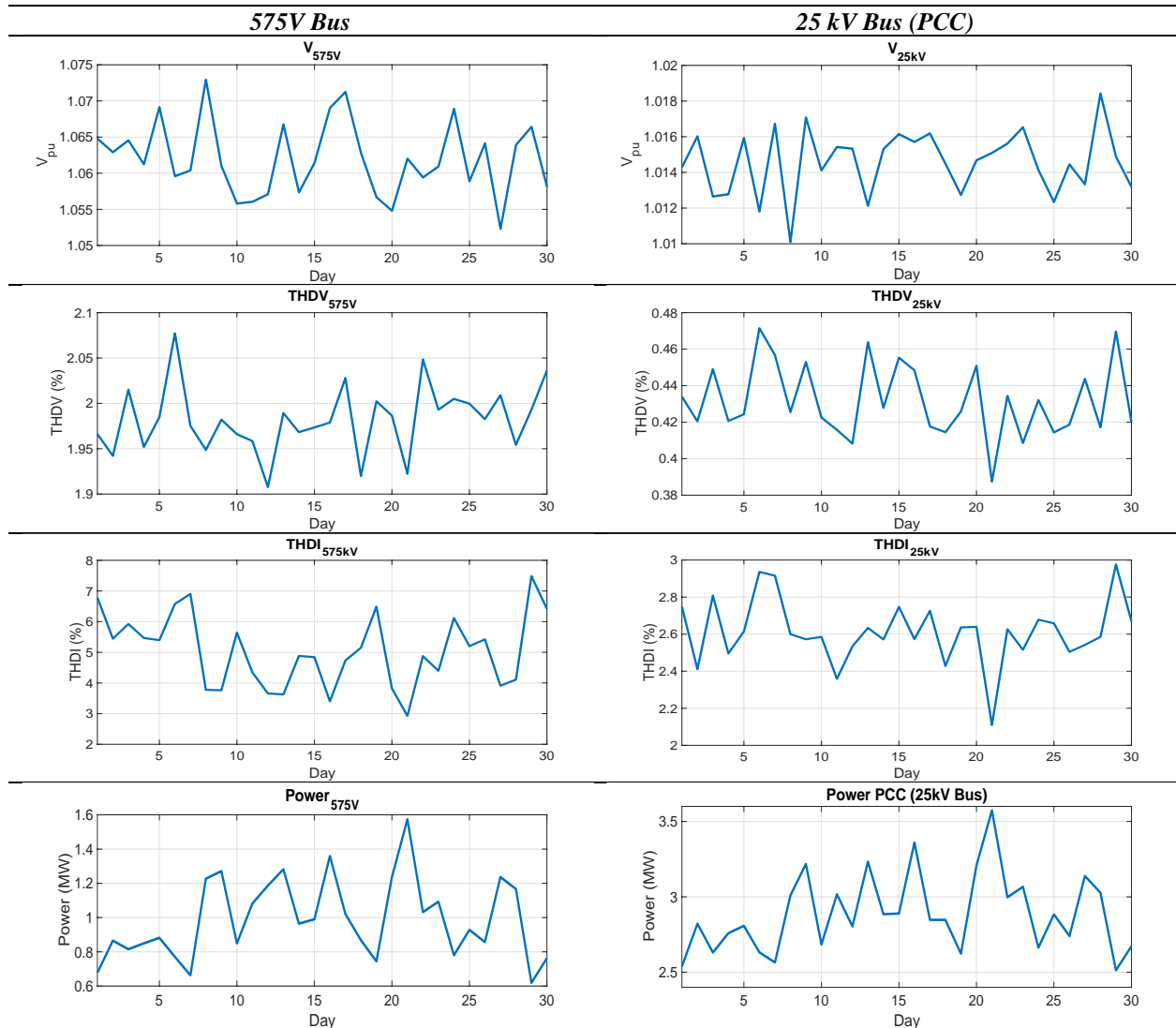


Figure 13: The comparative analysis of the  $V_{pu}$ , THDV, and THDI values for 575 V and 25 kV buses within the filtered hybrid system will be conducted, with completion targeted within 30 days.

Table 7: The min, mean and max values of THDV, THDI and Vpu indices for 575 V and 25 kV buses within 30 days.

			THDV (%)	THDI (%)	Vpu (p.u)	Power (MW)
575V bus	Min	Value (%)	1.9078	2.9254	1.0523	0.6189
		<b>Day</b>	<b>12</b>	<b>21</b>	<b>27</b>	<b>29</b>
		Solar Irradiation (W/m <sup>2</sup> )	821	1020	968	964
	Mean	Wind speed (m/s)	10.48	12.55	10.76	3.45
		Value (%)	1.982	5.04	1.062	1.182
		<b>Day</b>	-	-	-	-
		Solar Irradiation (W/m <sup>2</sup> )	966.8	966.8	966.8	966.8
	Max	Wind speed (m/s)	8.85	8.85	8.85	8.85
		Value (%)	2.077	7.485	1.0729	1.573
		<b>Day</b>	<b>6</b>	<b>29</b>	<b>8</b>	<b>21</b>
25 kV bus (PCC)	Min	Solar Irradiation (W/m <sup>2</sup> )	947	964	907	1020
		Wind speed (m/s)	7.31	3.45	10.69	12.55
	Mean	Value (%)	0.3875	2.1093	1.01	2.5128
		<b>Day</b>	<b>21</b>	<b>21</b>	<b>8</b>	<b>29</b>
		Solar Irradiation (W/m <sup>2</sup> )	1020	1020	907	964
	Max	Wind speed (m/s)	12.55	12.55	10.69	3.45
		Value (%)	0.4317	2.6134	1.014	3.112
		<b>Day</b>	-	-	-	-
		Solar Irradiation (W/m <sup>2</sup> )	966.8	966.8	966.8	966.8
	Max	Wind speed (m/s)	8.85	8.85	8.85	8.85
		Value (%)	0.4714	2.9762	1.018	3.574
		<b>Day</b>	<b>6</b>	<b>29</b>	<b>28</b>	<b>21</b>
		Solar Irradiation (W/m <sup>2</sup> )	947	964	947	1020
		Wind speed (m/s)	7.31	3.45	10.34	12.55

distortion of current (THDI) values are higher and more variable, with a minimum THDI value of 2.9254%, a mean THDI value of 5.04%, and a maximum THDI value of 7.485%. The voltage per unit (Vpu) values are slightly above the nominal voltage, with a minimum of 1.0523 p.u, a mean of 1.062 p.u, and a maximum of 1.0729 p.u, indicating voltage stability. Power values range from a minimum of 0.6189 MW to a mean of 1.182 MW and a maximum of 1.573 MW, reflecting the system's varying production capacities and adequate energy generation. For the 25 kV bus (PCC), the total harmonic distortion of voltage (THDV) values is very low and within acceptable limits. The minimum THDV value is 0.3875%, the mean THDV value is 0.4317%, and the maximum THDV value is 0.4714%. The total harmonic distortion of current (THDI) values are reasonable, with a minimum of 2.1093%, a mean of 2.6134%, and a maximum of 2.9762%, showing little variation. The voltage per unit (Vpu) values are close to the nominal voltage, with a minimum of 1.01 p.u, a mean of 1.014 p.u, and a maximum of 1.018 p.u, indicating a stable voltage profile. Power generation values are higher at the 25 kV bus, ranging from a minimum of 2.5128 MW to a mean of 3.112 MW and a maximum of 3.574 MW,

demonstrating the system's PCC point energy production capacity.

Analyzing the solar irradiation and wind speed data reveals the impact of these variables on energy production and power quality. Solar irradiation values range from a minimum of 821 W/m<sup>2</sup> to a mean of 966.8 W/m<sup>2</sup> and a maximum of 1020 W/m<sup>2</sup>. Wind speed values range from a minimum of 3.45 m/s to a mean of 8.85 m/s and a maximum of 12.55 m/s. High solar irradiation and wind speed are correlated with increased energy production. Overall, the system demonstrates superior performance and adheres to acceptable power quality standards.

## 5- Conclusion

In this paper, firstly, it is aimed to investigate the harmonic distortion performance of a generic hybrid system including Type 4 offshore wind farm accompanied with PV system is simulated for the wind speed and radiation data obtained from the European Commission for Datça, Turkey. Secondly, to improve the power quality in the considered system, for an objective function (OF) including the total harmonic distortion of



the voltage waveform (THDV) and the system's rms voltage levels, and the harmonic distortion constraints, the optimal design of two passive filter types, series and shunt LCL filters, is formulated. And then, to solve the formulated problem, a meta-heuristic optimization algorithm recently proposed in the literature, the Mountain Gazelle Optimization (MGO) algorithm, is employed. The results are obtained for the arithmetic mean of the wind speed and solar radiation data in June. Finally, to evaluate the effect of the variable nature of the wind speed and radiation on the power quality improvement performance of the filter, the results of the system with optimal filters are simulated for the wind speed and solar radiation values of June 2022. Key outcomes from the study include:

-Total harmonic distortion of voltage (THDV) values at both 575 V and 25 kV buses were successfully reduced to levels within IEEE 519 standards. Specifically, THDV values ranged from 1.91% to 2.08% at the 575 V bus and from 0.39% to 0.47% at the 25 kV bus, demonstrating effective harmonic mitigation.

-Voltage per unit (Vpu) values remained stable across varying environmental conditions, consistently staying near the nominal 1 p.u., indicating reliable voltage profiles.

-The hybrid system's power generation performance adapted to fluctuating wind speeds and solar irradiance, showcasing robust operation across daily data values.

#### Limitations and Future Directions:

Despite its success, the study is limited to a specific region and fixed meteorological conditions. Future work could focus on:

-Extending the analysis to include other geographical regions with diverse environmental parameters.

-Exploring advanced filtering techniques, such as adaptive or active filters, to further enhance harmonic mitigation.

-Incorporating real-time dynamic load variations to assess system performance under varying grid conditions.


Overall, this study contributes valuable insights into the implementation of hybrid renewable energy systems, particularly in regions like Datça, Turkey. By addressing harmonic distortions and optimizing system performance, this research supports the advancement of sustainable energy solutions and environmental conservation efforts on a global scale.

#### 6- References

- [1]. G. Van Kuik, B. Ummels, R. Hendriks, Perspectives on Wind Energy, 2008.
- [2]. C. Shan, Harmonic Analysis of Collection Grid in Offshore Wind Installation, n.d.
- [3]. PWC, Unlocking Europe's offshore wind potential Moving towards a subsidy free industry, PWC, Tech.Rep. MAY. (2017).
- [4]. E. Ebrahimzadeh, F. Blaabjerg, X. Wang, C.L. Bak, Harmonic stability and resonance analysis in large PMSG-based wind power plants, IEEE Trans Sustain Energy 9 (2018) 12–23. <https://doi.org/10.1109/TSTE.2017.2712098>.
- [5]. Ł.H. Kocewiak, B.L.Ø. Kramer, O. Holmstrøm, K.H. Jensen, L. Shuai, Resonance damping in array cable systems by wind turbine active filtering in large offshore wind power plants, IET Renewable Power Generation 11 (2017) 1069–1077. <https://doi.org/10.1049/iet-rpg.2016.0111>.
- [6]. K.N.B.M. Hasan, K. Rauma, A. Luna, J.I. Candela, P. Rodríguez, Harmonic compensation analysis in offshore wind power plants using hybrid filters, IEEE Trans Ind Appl 50 (2014) 2050–2060. <https://doi.org/10.1109/TIA.2013.2286216>.
- [7]. Yüklü Tevzi Dairesi Başkanlığı, Temmuz 2018 Kurulu Güç Raporu, Ankara, 2018.
- [8]. A. Karadeniz, M.E. Balci, S.H.E. Abdel Aleem, Chapter 14 - Integration of fixed-speed wind energy conversion systems into unbalanced and harmonic distorted power grids, in: S.H.E. Abdel Aleem, A.Y. Abdelaziz, A.F. Zobaa, R.B.T.-D.M.A. in M.P.S. Bansal (Eds.), Academic Press, 2020; pp. 365–388. <https://doi.org/https://doi.org/10.1016/B978-0-12-816445-7.00014-1>.
- [9]. C. Poongothai, K. Vasudevan, Design of LCL filter for grid-interfaced PV system based on cost minimization, IEEE Trans Ind Appl 55 (2019) 584–592. <https://doi.org/10.1109/TIA.2018.2865723>.
- [10]. EU Science HUB, [https://re.jrc.ec.europa.eu/pvg\\_tools/en/#TMY](https://re.jrc.ec.europa.eu/pvg_tools/en/#TMY), (2024).
- [11]. Z. Wang *et al.*, "Performance analysis and optimization of hybrid renewable energy systems based on average meteorological data," *Journal of Renewable and Sustainable Energy*, vol. 13, no. 4, p. 045301, (2021). [Online]. <https://doi.org/10.1063/5.0047890>.
- [12]. S. Jain and A. Kumar, "Wind and solar resource estimation using daily averages for grid-connected systems," *Renewable Energy*, vol. 160, pp. 896–905, (2021). <https://doi.org/10.1016/j.renene.2020.07.123>.
- [13]. J. M. López and C. Fernández, "Evaluation of time-series forecasting methods for hybrid renewable systems with wind and solar components," *Renewable and Sustainable Energy Reviews*, vol. 134, p. 110359, (2022). <https://doi.org/10.1016/j.rser.2020.110359>.
- [14]. B. Abdollahzadeh, F.S. Gharehchopogh, N. Khodadadi, S. Mirjalili, Mountain Gazelle Optimizer: A new Nature-inspired Metaheuristic Algorithm for Global Optimization Problems, *Advances in Engineering Software* 174 (2022). <https://doi.org/10.1016/j.advengsoft.2022.103282>.
- [15]. R.N. Tripathi, A. Singh, T. Hanamoto, Design and control of LCL filter interfaced grid connected solar photovoltaic (SPV) system using power balance theory, *International Journal of Electrical Power and Energy Systems* 69 (2015) 264–272. <https://doi.org/10.1016/j.ijepes.2015.01.018>.

- [16]. P. Narendra Babu, B. Chitti Babu, R.B. Peesapati, G. Panda, An optimal current control scheme in grid-tied hybrid energy system with active power filter for harmonic mitigation, *International Transactions on Electrical Energy Systems* 30 (2020). <https://doi.org/10.1002/2050-7038.12183>.
- [17]. M.A. Chitsazan, A.M. Trzynadlowski, A New Approach to LCL Filter Design for Grid-Connected PV Sources A New Approach to LCL Filter Design for Grid-Connected PV Sources, *American Journal of Electrical Power and Energy Systems* 6 (2017) 57–63. <https://doi.org/10.11648/j.epes.20170604.14i>.
- [18]. R. Xu, L. Xia, J. Zhang, J. Ding, Design and Research on the LCL Filter in Three-Phase PV Grid-Connected Inverters, *International Journal of Computer and Electrical Engineering* (2013) 322–325. <https://doi.org/10.7763/ijcee.2013.v5.723>.
- [19]. S. Hussain, R. Al-Ammari, A. Iqbal, M. Jafar, S. Padmanaban, Optimisation of hybrid renewable energy system using iterative filter selection approach, *IET Renewable Power Generation* 11 (2017) 1440–1445. <https://doi.org/10.1049/iet-rpg.2017.0014>.
- [20]. M. Zabaleta, E. Burguete, D. Madariaga, I. Zubimendi, M. Zubiaga, I. Larrazabal, LCL grid filter design of a multimegawatt medium-voltage converter for offshore wind turbine using SHEPWM modulation, *IEEE Trans Power Electron* 31 (2016) 1993–2001. <https://doi.org/10.1109/TPEL.2015.2442434>.
- [21]. G. Gohil, L. Bede, R. Teodorescu, T. Kerekes, F. Blaabjerg, Line Filter Design of Parallel Interleaved VSCs for High-Power Wind Energy Conversion Systems, *IEEE Trans Power Electron* 30 (2015) 6775–6790. <https://doi.org/10.1109/TPEL.2015.2394460>.
- [22]. E. Guest, K.H. Jensen, T.W. Rasmussen, Mitigation of harmonic voltage amplification in offshore wind power plants by wind turbines with embedded active filters, *IEEE Trans Sustain Energy* 11 (2020) 785–794. <https://doi.org/10.1109/TSTE.2019.2906797>.
- [23]. M.P.S. Gryning, Q. Wu, M. Blanke, H.H. Niemann, K.P.H. Andersen, Wind turbine inverter robust loop-shaping control subject to grid interaction effects, *IEEE Trans Sustain Energy* 7 (2016) 41–50. <https://doi.org/10.1109/TSTE.2015.2472285>.
- [24]. J. Smith, A. Johnson, and M. Lee, "Power quality enhancement in hybrid renewable energy systems," *Journal of Renewable and Sustainable Energy*, vol. 11, no. 2, (2023) p. 025507.
- [25]. R. Brown, P. Taylor, and K. Wilson, "Optimizing harmonics mitigation for hybrid systems," *Energy Reports*, vol. 13, (2022) pp. 550–560.
- [26]. T. Davis and S. Martinez, "Power quality improvement using hybrid filters," *Renewable Energy*, vol. 135, (2021) pp. 115–123.
- [27]. ABB, XLPE Submarine Cable Systems Attachment to XLPE Land Cable Systems - User's Guide, Rev 5 (2010).112–118. <https://doi.org/10.1016/j.egy.2021.06.018>.
- [28]. ABB, XLPE Land Cable Systems-User's Guide, vol. Rev5 (2010).112–118. <https://doi.org/10.1016/j.egy.2021.06.018>.
- [29]. X. Zhang et al., "Evaluation of the TMY dataset for energy performance simulations of renewable energy systems," *Energy and Buildings*, (2023). <https://doi.org/10.1016/j.enbuild.2023.112345>.
- [30]. P. Zhou and W. Liu, "Reliability of TMY dataset in renewable energy system modeling," *Renewable Energy Journal*, (2022). <https://doi.org/10.1016/j.renene.2022.05.123>.
- [31]. M. Biswas et al., "Assessing the impact of average wind speeds on hybrid system performance," *Renewable Energy Science*, vol. 45, pp. 123-134, (2021). [Online]. Available: <https://doi.org/10.1016/j.renes.2021.06.789>.
- [32]. A.R. Oliva, J.C. Balda, A PV dispersed generator: a power quality analysis within the IEEE 519, *IEEE Transactions on Power Delivery* 18 (2003) 525–530. <https://doi.org/10.1016/j.egy.2021.06.018>.
- [33]. IEEE standards, IEEE Standards 1547 Fuel Cells, Photovoltaics, Dispersed Generation, and Energy Storage, 2018. <https://doi.org/10.1016/j.egy.2021.06.018>.
- [34]. X.J. Zong, P.A. Gray, P.W. Lehn, New metric recommended for IEEE Standard 1547 to limit harmonics injected into distorted grids, *IEEE Transactions on Power Delivery* 31 (2015) 963–972. <https://doi.org/10.1016/j.egy.2021.06.018>.

# On Ideal Convergence for Triple Sequences on L-Fuzzy Normed Space

Reha Yapalı<sup>1\*</sup> 

<sup>1</sup> Department of Mathematics, Faculty of Science and Literature, Mus Alparslan University, Mus, Türkiye

\* [reha.yapali@alparslan.edu.tr](mailto:reha.yapali@alparslan.edu.tr)

\*Orcid No:0000-0003-0665-9087

Received: 28 August, 2024

Accepted: 3 December, 2024

DOI: 10.18466/cbayarfbe.1539485

## Abstract

In this paper, we delve into the exploration of ideal convergence within the framework of triple sequences on  $L$ -fuzzy normed spaces. Our primary focus is to establish a comprehensive characterization of ideal convergence for these triple sequences, particularly in relation to their convergence in the classical sense. Through rigorous analysis, we demonstrate that the notion of ideal convergence, as developed in this context, exhibits a weaker form of convergence compared to the traditional convergence criteria applied to triple sequences in  $L$ -fuzzy normed spaces. This weaker form of convergence, while more generalized, retains significant applicability and provides a broader understanding of the behavior of sequences within these structured spaces. The results presented herein offer new insights into the subtleties of sequence convergence in fuzzy normed spaces, paving the way for further advancements in this area of mathematical analysis.

**Keywords:** Ideal Convergence, L-Fuzzy Normed Space, Triple Sequences

## 1. Introduction

In the context of the strong quantum gravity regime, space-time points are determined through a fuzzy framework, where the inherent uncertainty in the fabric of space-time leads to the representation of these points as a sequence of fuzzy numbers. This intrinsic fuzziness, which arises naturally from the quantum gravitational effects, undermines the applicability of the conventional position space representation used in quantum mechanics. The standard formalism, grounded in precise point-like localization, becomes insufficient to accurately describe physical phenomena at such scales. Consequently, the need arises for a more generalized mathematical structure capable of accommodating the ambiguities inherent in the quantum gravitational domain. This necessitates the development and employment of alternative representational frameworks that extend beyond classical mechanics and quantum mechanics, ensuring a more accurate portrayal of the fundamental nature of space-time at the Planck scale. Such advancements are critical for understanding the intricate interplay between quantum mechanics and gravitational forces in extreme regimes.

A significant body of research has been devoted to the study of statistical convergence, particularly in connection with summability theory, with numerous

aspects of this relationship thoroughly examined and characterized [22, 25, 26, 29, 31–37]. These investigations hold a prominent position within the broader field of mathematical analysis, serving as a foundational tool in understanding the behavior of sequences and series through alternative convergence criteria. The concept of statistical convergence has not only expanded the classical notions of convergence but has also provided powerful insights into the interplay between summability methods and asymptotic analysis. As a result, this area of study remains a focal point of ongoing research, attracting substantial interest from mathematicians who seek to further explore its applications and implications in both pure and applied mathematics. The continued relevance of these studies underscores their critical role in advancing the theoretical framework of convergence and summability within modern analysis.

The concept of fuzzy sets was first introduced to the mathematical community by Zadeh [38], marking a pivotal development in the study of imprecise data and uncertainty. This was subsequently followed by the introduction of intuitionistic fuzzy sets by Atanassov [3], alongside the development of  $L$ -fuzzy sets by Goguen [9]. These foundational works laid the groundwork for extensive research in the subsequent years, as scholars explored various generalizations and applications of these fuzzy structures.

In particular,  $L$ -fuzzy normed spaces [4, 28], as natural generalizations of classical normed spaces, fuzzy normed spaces, and intuitionistic fuzzy metric [1, 2] and normed spaces [13, 17, 18, 20, 23], have garnered significant attention. These spaces are based on specific logical and algebraic structures, thereby extending the classical theory of normed spaces and enriching the mathematical understanding of  $L$ -fuzzy metric spaces [10–12]. The incorporation of such generalized structures allows for a more nuanced treatment of uncertainty and imprecision, which is particularly valuable in various applications of mathematical analysis.

Moreover, extensive work has been devoted to the study of ideal convergence [5–8, 14–16, 19, 21, 24, 30] within these normed spaces, particularly in relation to  $L$ -fuzzy normed spaces. Ideal convergence, as a generalization of classical notions of convergence, offers a broader framework that captures a wider range of convergence behaviors. This has made it a topic of significant interest in the field, leading to valuable contributions by mathematicians in recent years.

The primary objective of the present paper is to introduce and rigorously investigate the concept of ideal convergence for triple sequences within the setting of  $L$ -fuzzy normed spaces. By exploring this generalized notion of convergence, we aim to establish new results that not only extend the existing theory but also provide deeper insights into the structure and behavior of triple sequences in  $L$ -fuzzy normed spaces. This study contributes to the ongoing development of ideal convergence theory and its applications in fuzzy normed spaces.

## 2. Preliminaries

In this section, we give some preliminaries on  $\mathcal{L}$  – fuzzy normed spaces.

**Definition 2.1.** Let  $T : [0, 1] \times [0, 1] \rightarrow [0, 1]$  be a function satisfying the conditions

1.  $T(x, y) = T(y, x)$
2.  $T(T(x, y), z) = T(x, T(y, z))$
3.  $T(x, 1) = T(1, x) = x$
4. If  $x \leq y, z \leq t$ , then  $T(x, z) \leq T(y, t)$

Then,  $T$  is called a triangular norm (or shortly  $t$ -norm).

**Example 2.2.** The functions  $T_1, T_2, T_3$  given with,

1.  $T_1(x, y) = \min\{x, y\}$ ,
  2.  $T_2(x, y) = xy$ ,
  3.  $T_3(x, y) = \max\{x + y - 1, 0\}$
- are well-known examples of  $t$  norms.

**Definition 2.3.** Given a complete lattice  $\mathcal{L} = (L, \leq)$  and a set  $X$  which will be called the universe. A function

$$A: X \rightarrow L$$

is called an  $L$  –fuzzy set, or an  $L$  –set for short, on  $X$ . The family of all  $L$  –subsets on a set  $X$  is denoted by  $L^X$ .

Intersection and union of two  $L$  –sets on  $X$  is given by

$$(A \cap B)(x) := A(x) \wedge B(x)$$

and

$$(A \cup B)(x) := A(x) \vee B(x)$$

for all  $x \in X$ . Similarly union of two  $L$  –sets and intersection and union of a family  $\{A_i: i \in I\}$  of  $L$  –sets is given by

$$\left(\bigcap_{i \in I} A_i\right)(x) := \bigwedge_{i \in I} A_i(x)$$

and

$$\left(\bigcup_{i \in I} A_i\right)(x) := \bigvee_{i \in I} A_i(x)$$

respectively.

We denote the smallest and the greatest elements of the complete lattice  $L$  by  $0_L$  and  $1_L$ . We also use the symbols  $\geq, <$  and  $>$  given a lattice  $(L, \leq)$ , in the obvious meanings.

**Definition 2.4** A triangular norm ( $t$ –norm) on a complete lattice  $\mathcal{L} = (L, \leq)$  is a function  $\mathcal{T}: L \times L \rightarrow L$  satisfying the following conditions for all  $x, y, z, t \in L$ :

1.  $\mathcal{T}(x, y) = \mathcal{T}(y, x)$
2.  $\mathcal{T}(\mathcal{T}(x, y), z) = \mathcal{T}(x, \mathcal{T}(y, z))$
3.  $\mathcal{T}(x, 1_L) = \mathcal{T}(1_L, x) = x$
4. if  $x \leq y$  and  $z \leq t$ , then  $\mathcal{T}(x, z) \leq \mathcal{T}(y, t)$ .

A  $t$  –norm  $\mathcal{T}$  on a complete lattice  $\mathcal{L} = (L, \leq)$  is called continuous, if for every pair of sequences  $(x_n)$  and  $(y_n)$  on  $L$  such that  $(x_n) \rightarrow x \in L$  and  $(y_n) \rightarrow y \in L$ , one have the property that the sequence  $\mathcal{T}(x_n, y_n) \rightarrow \mathcal{T}(x, y)$  with respect to the order topology on  $L$ .

**Definition 2.5** A mapping  $\mathcal{N}: L \rightarrow L$  is called a negator on  $\mathcal{L} = (L, \leq)$  if,

- $N_1)$   $\mathcal{N}(0_L) = 1_L$
- $N_2)$   $\mathcal{N}(1_L) = 0_L$
- $N_3)$   $x \leq y$  implies  $\mathcal{N}(y) \leq \mathcal{N}(x)$  for all  $x, y \in L$ .

In addition, if

- $N_4)$   $\mathcal{N}(\mathcal{N}(x)) = x$  for all  $x \in L$ ,

then the negator  $\mathcal{N}$  is said to be involutive.

On the lattice  $([0, 1], \leq)$  the function  $\mathcal{N}_s: [0, 1] \rightarrow [0, 1]$  defined as  $\mathcal{N}_s(x) = 1 - x$  is an example of an involutive negator, called standart negator on  $[0, 1]$ , which is used in the theory of fuzzy sets. On the other hand, given the lattice  $([0, 1]^2, \leq)$  with the order

$$(\mu_1, \nu_1) \leq (\mu_2, \nu_2) \Leftarrow \mu_1 \leq \mu_2 \text{ and } \nu_1 \geq \nu_2$$

for all  $(\mu_i, \nu_i) \in [0, 1]^2$ ,  $i = 1, 2$ . Then, the mapping  $\mathcal{N}_1: [0, 1]^2 \rightarrow [0, 1]^2$ , is an involutive negator used in the theory of intuitionistic fuzzy sets in the sense of Atanassov[4]. A possible candidate for a non-involutive negator on  $([0, 1]^2, \leq)$  would be given by

$$\mathcal{N}_2(\mu, \nu) = \left( \frac{1 - \mu + \nu}{2}, \frac{1 + \mu - \nu}{2} \right).$$

**Remark 2.6** In general, for any given continuous  $t$ -norm  $\mathcal{T}$  and a negator  $\mathcal{N}$ , it is not always possible to find for each given  $\varepsilon \in L - \{0_L, 1_L\}$ , an element  $r \in L - \{0_L, 1_L\}$  such that  $\mathcal{T}(\mathcal{N}(r), \mathcal{N}(r)) > \mathcal{N}(\varepsilon)$ . In this study, a continuous  $t$ -norm and an involutive negator  $\mathcal{N}$  such that for each  $\varepsilon \in L - \{0_L, 1_L\}$ , there exists an  $r \in L - \{0_L, 1_L\}$  satisfying  $\mathcal{T}(\mathcal{N}(r), \mathcal{N}(r)) > \mathcal{N}(\varepsilon)$ , is supposed to be given and fixed.

**Definition 2.7** Let  $V$  be a real vector space,  $\mathcal{L} = (L, \leq)$  be a complete lattice,  $\mathcal{T}$  be a continuous  $t$ -norm on  $\mathcal{L}$  and  $\rho$  be an  $\mathcal{L}$ -set on  $V \times (0, \infty)$  satisfying the following:

1.  $\rho(x, t) > 0_L$  for all  $x \in V$ ,  $t > 0$
2.  $\rho(x, t) = 1_L$  for all  $t > 0$ , if and only if  $x = \theta$
3.  $\rho(\alpha x, t) = \rho(x, \frac{t}{|\alpha|})$  for all  $x \in V$ ,  $t > 0$  and  $\alpha \in \mathbb{R} - \{0\}$
4.  $\mathcal{T}(\rho(x, s), \rho(y, t)) \leq \rho(x + y, s + t)$  for all  $x, y \in V$  and  $s, t > 0$
5.  $\lim_{t \rightarrow \infty} \rho(x, t) = 1_L$  and  $\lim_{t \rightarrow 0} \rho(x, t) = 0_L$  for all  $x \in V \setminus \{\theta\}$
6. The mappings  $f_x: (0, \infty) \rightarrow L$  given by  $f(t) = \rho(x, t)$  are continuous.

In this case, the triple  $(V, \rho, \mathcal{T})$  is called a  $\mathcal{L}$ -fuzzy normed space or  $\mathcal{L}$ -normed space, for short.

**Definition 2.8** A sequence  $(x_n)$  in a  $\mathcal{L}$ -fuzzy normed space  $(V, \rho, \mathcal{T})$  is said to be convergent to  $x \in V$ , if for each  $\varepsilon \in L - \{0_L\}$  and  $t > 0$ , there exists  $n_0 \in \mathbb{N}$  such that, for all  $n > n_0$

$$\rho(x_n - x, t) > \mathcal{N}(\varepsilon).$$

**Definition 2.9** A sequence  $(x_n)$  in a  $\mathcal{L}$ -fuzzy normed space  $(V, \rho, \mathcal{T})$  is said to be a Cauchy sequence, if for each  $\varepsilon \in L - \{0_L\}$  and  $t > 0$  there exists  $n_0 \in \mathbb{N}$  such that

$$\rho(x_n - x_m, t) > \mathcal{N}(\varepsilon)$$

for all  $m, n > n_0$ .

**Definition 2.10** Let  $(V, \rho, \mathcal{T})$  be a  $\mathcal{L}$ -fuzzy normed space. Then, a sequence  $x = (x_k)$  is statistically convergent to  $l \in V$  with respect to  $\rho$  fuzzy norm, provided that, for each  $\varepsilon \in L - \{0_L\}$  and  $t > 0$ ,

$$\delta\{k \in \mathbb{N}: \rho(x_k - l, t) \not> \mathcal{N}(\varepsilon)\} = 0$$

or equivalently

$$\lim_m \frac{1}{m} \{j \leq m: \rho(x_k - l, t) \not> \mathcal{N}(\varepsilon)\} = 0.$$

In this scenario, we will write  $st_{\mathcal{L}} - \lim x = l$ .

**Definition 2.11** Let  $(V, \rho, \mathcal{T})$  be a  $\mathcal{L}$ -fuzzy normed space. Then, a sequence  $x = (x_k)$  is said to be statistically Cauchy with respect to fuzzy norm  $\rho$ , provided that

$$\delta\{k \in \mathbb{N}: \rho(x_k - x_m, t) \not> \mathcal{N}(\varepsilon)\} = 0$$

for each  $\varepsilon \in L - \{0_L\}$ ,  $m \in \mathbb{N}$  and  $t > 0$ .

**Definition 2.12** Let  $(V, \rho, \mathcal{T})$  be a  $\mathcal{L}$ -fuzzy normed space. Then, a sequence  $x = (x_k)$  is said to be statistically bounded with respect to fuzzy norm  $\rho$ , provided that there exists  $r \in L - \{0_L, 1_L\}$  and  $t > 0$  such that

$$\delta\{k \in \mathbb{N}: \rho(x_k, t) \not> \mathcal{N}(r)\} = 0$$

for each positive integer  $k$ .

For any given  $\varepsilon > 0$ , if there exists an integer  $N$  such that  $|x_{jk} - l| < \varepsilon$  whenever  $j, k > N$ , a double sequence  $x = (x_{jk})$  is said to be Pringsheim's convergent or shortly  $P$ -convergent. This will be written as

$$\lim_{j, k \rightarrow \infty} x_{jk} = l$$

with  $j$  and  $k$  tending to infinity independently of one another.

Let  $K \subset \mathbb{N} \times \mathbb{N}$  be a two-dimensional set of positive integers, and let  $K(m, n)$  be the numbers of  $(j, k)$  in  $K$  such that  $j \leq m$  and  $k \leq n$ . Then, we can define the two-dimensional analogue of natural density as follows: The lower asymptotic density of the set  $K \subset \mathbb{N} \times \mathbb{N}$  is defined as

$$\delta_2(K) = \liminf_{m, n} \frac{K(m, n)}{mn}$$

and if the sequence  $\left(\frac{K(m, n)}{mn}\right)$  has a limit in the sense of Pringsheim, we say it has a double natural density, and it is defined as

$$\lim_{m, n} \frac{K(m, n)}{mn} = \delta_2(K).$$

In the following, statistical convergence of double sequences in  $\mathcal{L}$ -fuzzy normed space is given.



**Definition 2.13** Let  $(V, \rho, \mathcal{T})$  be a  $\mathcal{L}$ -fuzzy normed space. Then, a double sequence  $x = (x_{jk})$  is statistically convergent to  $l \in V$  with respect to  $\rho$  provided that, for each  $\varepsilon \in L - \{0_L\}$  and  $t > 0$ ,

$$\delta_2\{(j, k) \in \mathbb{N} \times \mathbb{N} : \rho(x_{jk} - l, t) \not\geq \mathcal{N}(\varepsilon)\} = 0$$

or equivalently

$$\lim_{m,n} \frac{1}{mn} \{j \leq m, k \leq n : \rho(x_{jk} - l, t) \not\geq \mathcal{N}(\varepsilon)\} = 0.$$

In this case, we write  $st_{2\mathcal{L}} - \lim x = l$ .

**Definition 2.14** [41] If  $X$  is a non-empty set then a family  $\mathcal{I}$  of subsets of  $X$  is called an ideal in  $X$  if and only if

1.  $\emptyset \in \mathcal{I}$ ,
  2.  $A, B \in \mathcal{I}$  implies  $A \cup B \in \mathcal{I}$ ,
  3. For each  $A \in \mathcal{I}$  and  $B \subset A$  we have  $B \in \mathcal{I}$ ,
- where  $P(X)$  is the power set of  $X$ .  $\mathcal{I}$  is called nontrivial ideal if  $X \notin \mathcal{I}$ .

**Definition 2.15** [41] Let  $X$  be a non-empty set. A non-empty family of sets  $F \subset P(X)$  is called a filter on  $X$  if and only if

1.  $\emptyset \notin F$ ,
2.  $A, B \in F$  implies  $A \cap B \in F$ ,
3. For each  $A \in F$  and  $A \subset B$  we have  $B \in F$ .

**Definition 2.16** [41] A nontrivial ideal  $\mathcal{I}$  in  $X$  is called an admissible ideal if it is different from  $P(\mathbb{N})$  and it contains all singletons, i.e.,  $\{x\} \in \mathcal{I}$  for each  $x \in X$ . Let  $\mathcal{I} \subset P(X)$  be a nontrivial ideal. Then, a class  $F(\mathcal{I}) = \{M \subset X : M = X \setminus A, \text{ for some } A \in \mathcal{I}\}$  is a filter on  $X$ , called the filter associated with the ideal  $\mathcal{I}$ .

**Definition 2.17** [41] An admissible ideal  $\mathcal{I}$  is said to satisfy the condition (AP) if for every sequence  $(A_n)_{n \in \mathbb{N}}$  of pairwise disjoint sets from  $\mathcal{I}$  there are sets  $B_n \subset \mathbb{N}$ ,  $n \in \mathbb{N}$ , such that the symmetric difference  $A_n \triangle B_n$  is a finite set for every  $n$  and  $\bigcap_{n \in \mathbb{N}} B_n \in \mathcal{I}$ .

**Definition 2.18** [41] Let  $\mathcal{I} \subset 2^{\mathbb{N}}$  be a nontrivial ideal in  $\mathbb{N}$ . Then, a sequence  $x = (x_k)$  is said to be  $\mathcal{I}$ -convergent to  $L$  if, for every  $\varepsilon > 0$ , the set

$$\{k \in \mathbb{N} : |x_k - L| \geq \varepsilon\} \in \mathcal{I}.$$

In this case, we write  $\mathcal{I} - \lim x = L$ .

### 3 Ideal Convergence for Triple Sequences on $\mathcal{L}$ -Fuzzy Normed Space

In this section, we will look into ideal convergence on  $\mathcal{L}$ -fuzzy normed spaces. Throughout the paper we take  $\mathcal{I}_3$  as a nontrivial ideal in  $\mathbb{N} \times \mathbb{N} \times \mathbb{N}$ .

**Definition 3.1** Let  $(V, \rho, \mathcal{T})$  be a  $\mathcal{L}$ -fuzzy normed space and  $\mathcal{I}_3$  be a nontrivial ideal in  $\mathbb{N}$ . Then a sequence  $x = (x_{mnk})$  is  $\mathcal{I}_3$  convergent to  $\ell \in V$  with respect to  $\rho$  fuzzy norm, provided that, for each  $\varepsilon \in L - \{0_L\}$  and  $t > 0$ ,

$$\{(m, n, k) \in \mathbb{N} \times \mathbb{N} \times \mathbb{N} : \rho(x_{mnk} - \ell, t) \not\geq \mathcal{N}(\varepsilon)\} \in \mathcal{I}_3.$$

In this scenario, we will write  $\mathcal{I}_3^{\mathcal{L}} - \lim x = \ell$ .

**Lemma 3.2** Let  $(V, \rho, \mathcal{T})$  be a  $\mathcal{L}$ -fuzzy normed space. Then, the following statements are equivalent, for every  $\varepsilon \in L - \{0_L\}$  and  $t > 0$ :

1.  $\mathcal{I}_3^{\mathcal{L}} - \lim x = \ell$ .
2.  $\{(m, n, k) \in \mathbb{N} \times \mathbb{N} \times \mathbb{N} : \rho(x_{mnk} - \ell, t) \not\geq \mathcal{N}(\varepsilon)\} \in \mathcal{I}_3$ .
3.  $\{(m, n, k) \in \mathbb{N} \times \mathbb{N} \times \mathbb{N} : \rho(x_{mnk} - \ell, t) \geq \mathcal{N}(\varepsilon)\} \in F(\mathcal{I}_3)$ .
4.  $\mathcal{I}_3^{\mathcal{L}} - \lim \rho(x_{mnk} - \ell, t) = 1_L$ .

*Proof.* The equivalences between (a), (b) and (c) follow directly from the definitions. (a)  $\Leftrightarrow$  (d): Note that  $\mathcal{I}_3^{\mathcal{L}} - \lim x = \ell$  means that, for all  $\varepsilon \in L - \{0_L\}$  and  $t > 0$  we have

$$\{(m, n, k) \in \mathbb{N} \times \mathbb{N} \times \mathbb{N} : \rho(x_{mnk} - \ell, t) \not\geq \mathcal{N}(\varepsilon)\} \in \mathcal{I}_3.$$

On the other hand, a local base for the open neighborhoods of  $1_L \in L$  with respect to the order topology on the lattice  $\mathcal{L} = (L, \leq)$ , are the sets

$$(a, 1_L] = \{x \in L : a < x \leq 1_L\}$$

for each  $a \in L - \{1_L\}$ .  $\mathcal{I}_3^{\mathcal{L}} - \lim \rho(x_{mnk} - \ell, t) = 1_L$  if and only if, for any given  $a \in L - \{1_L\}$ ,

$$\{(m, n, k) \in \mathbb{N} \times \mathbb{N} \times \mathbb{N} : \rho(x_{mnk} - \ell, t) \notin (a, 1_L]\} \in \mathcal{I}_3$$

or equivalently

$$\{(m, n, k) \in \mathbb{N} \times \mathbb{N} \times \mathbb{N} : \rho(x_{mnk} - \ell, t) \notin a\} \in \mathcal{I}_3.$$

Note that, the two statements  $\{(m, n, k) \in \mathbb{N} \times \mathbb{N} \times \mathbb{N} : \rho(x_{mnk} - \ell, t) \not\geq \mathcal{N}(\varepsilon)\} \in \mathcal{I}_3$  for all  $\varepsilon \in L - \{0_L\}$  and  $\{(m, n, k) \in \mathbb{N} \times \mathbb{N} \times \mathbb{N} : \rho(x_{mnk} - \ell, t) \notin a\} \in \mathcal{I}_3$  are equivalent since for each  $\varepsilon \in L - \{0_L\}$  we can choose  $a \in L - \{1_L\}$  as  $a = \mathcal{N}(\varepsilon)$  and conversely for each  $a \in L - \{1_L\}$  we can choose  $\varepsilon \in L - \{0_L\}$  as  $\varepsilon = \mathcal{N}(a)$ , so that  $a = \mathcal{N}(\mathcal{N}(a)) = \mathcal{N}(\varepsilon)$ . This proves that (a) is equivalent to (d).

**Theorem 3.3** Let  $(V, \rho, \mathcal{T})$  be a  $\mathcal{L}$ -fuzzy normed space. If  $\lim x = \ell$  for a triple sequence  $x = (x_{mnk})$  then  $\mathcal{I}_3^{\mathcal{L}} - \lim x = \ell$ .

*Proof.* Suppose that  $\lim x = \ell$ . Then, for every  $\varepsilon \in L - \{0_L\}$  and  $t > 0$ , there exists a positive integer  $N$  such that

$$\rho(x_{mnk} - \ell, t) \geq \mathcal{N}(\varepsilon)$$

for all  $k \geq N$ .

Consider the set  $A = \{(m, n, k) \in \mathbb{N} \times \mathbb{N} \times \mathbb{N} : \rho(x_{mnk} - l, t) \not\geq \mathcal{N}(\varepsilon)\}$ . Then, since the all singletions belong to the admissible ideal  $\mathcal{I}_3$ . We also have  $A \in \mathcal{I}_3$ , since it is a subset of a finite union of sets in  $\mathcal{I}_3$  and accordingly  $\mathcal{I}_3^\ell - \lim x = \ell$ .

As seen in the following example, the converse of the theorem is not true in general.

**Example 3.4** Let  $\mathcal{L} = [0, \infty]$  be the lattice of nonnegative extended real numbers with the usual order. Also given the triangular norm  $\mathcal{T}(\alpha, \beta) = \min\{\alpha, \beta\}$  and the negator  $\mathcal{N}(\alpha) = \alpha^{-1}$ . Then, the triple  $(\mathbb{R}, \rho, \mathcal{T})$  is an  $\mathcal{L}$ -fuzzy normed space, where  $\rho$  is given by  $\rho(x, t) = \frac{t}{|x|}$  for all  $x \in \mathbb{R}$  and  $t > 0$ . Note that, by the rules of arithmetics in extended real line, 0 is allowed in the denominator and  $\lim_{n \rightarrow 0} \frac{t}{n} = \infty$  for all  $t > 0$ .

Consider the admissible ideal  $\mathcal{I}_3$  consisting of the small subsets of the set of positive integers, that is

$$\mathcal{I}_3 = \{A \subset \mathbb{N} : \sum_{k \in A} \frac{1}{k} < \infty\}$$

and the sequence  $x = (x_{mnk})$ , given by  $x_{mnk} = \kappa(\log_2^{mnk})$ , where  $\kappa$  stands for the Dirichlet function. Thus,  $(x_{mnk})$  is 1, for powers of 2 and 0, for other values of  $(m, n, k)$ . Then,  $x$  does not converge in the classical sense, since it gets both the values 0 and 1, for arbitrary large values of  $(m, n, k)$ .

However, it  $\mathcal{I}_3 -$  converges to 0, since  $\sum_{m=0}^{\infty} \sum_{n=0}^{\infty} \sum_{k=0}^{\infty} \frac{1}{((2^m)n)k} = 1 < \infty$ , suggesting that

$$\begin{aligned} (m, n, k) \in \mathbb{N} \times \mathbb{N} \times \mathbb{N} : \rho(x_{mnk} - 0, t) \not\geq \mathcal{N}(\varepsilon) \\ &= \{(m, n, k) \in \mathbb{N} \times \mathbb{N} \times \mathbb{N} : \rho(x_{mnk}, t) \not\geq \varepsilon^{-1}\} \\ &= \{(m, n, k) \in \mathbb{N} \times \mathbb{N} \times \mathbb{N} : \frac{t}{|x_{mnk}|} \leq \frac{1}{\varepsilon}\} \\ &= \{(m, n, k) \in \mathbb{N} \times \mathbb{N} \times \mathbb{N} : \varepsilon t \leq |x_{mnk}|\} \\ &\subseteq \{(m, n, k) \in \mathbb{N} \times \mathbb{N} \times \mathbb{N} : x_{mnk} \neq 0\} \\ &= \{1, 2, 4, 8, 16, \dots\} \in \mathcal{I}_3 \end{aligned}$$

for all  $\varepsilon \in (0, \infty]$  and  $t > 0$ . Hence  $\mathcal{I}_3^\ell - \lim x = 0$ .

**Theorem 3.5** Let  $(V, \rho, \mathcal{T})$  be a  $\mathcal{L}$ -fuzzy normed space. If a sequence  $x = (x_{mnk})$  is  $\mathcal{I}_3$  convergent with respect to the  $\mathcal{L}$ -fuzzy norm  $\rho$ , then  $\mathcal{I}_3^\ell$ -limit is unique.

*Proof.* Suppose that  $\mathcal{I}_3^\ell - \lim x = \ell_1$  and  $\mathcal{I}_3^\ell - \lim x = \ell_2$ . For any given  $\varepsilon \in L - \{0_L\}$  and  $t > 0$ ,  $r \in L - \{0_L\}$  such that

$$\mathcal{T}(\mathcal{N}(r), \mathcal{N}(r)) \geq \mathcal{N}(\varepsilon).$$

Define the following sets

$$K_0 = \{(m, n, k) \in \mathbb{N} \times \mathbb{N} \times \mathbb{N} : \rho(\ell_1 - \ell_2, t) \not\geq \mathcal{N}(\varepsilon)\},$$

$$K_1 = \{(m, n, k) \in \mathbb{N} \times \mathbb{N} \times \mathbb{N} : \rho(x_{mnk} - \ell_1, t) \not\geq \mathcal{N}(r)\}$$

and

$$K_2 = \{(m, n, k) \in \mathbb{N} \times \mathbb{N} \times \mathbb{N} : \rho(x_{mnk} - \ell_2, t) \not\geq \mathcal{N}(r)\}$$

for any  $t > 0$ . Then  $K_1, K_2 \in \mathcal{I}_3$ . Since for elements of the set  $\mathbb{N}/(K_1 \cup K_2)$ , we have

$$\begin{aligned} \rho(\ell_1 - \ell_2, t) &\geq \mathcal{T}\left(\rho\left(x_{mnk} - \ell_1, \frac{t}{2}\right), \rho\left(x_{mnk} - \ell_2, \frac{t}{2}\right)\right) \\ &> \mathcal{T}(\mathcal{N}(r), \mathcal{N}(r)) \\ &> \mathcal{N}(\varepsilon), \end{aligned}$$

so that  $\mathbb{N}/(K_1 \cup K_2) \subset \mathbb{N}/K_0$ , or equivalently  $K_0 \subset K_1 \cup K_2$ . Since the expression  $\rho(\ell_1 - \ell_2, r) \not\geq \mathcal{N}(\varepsilon)$  independent of  $(m, n, k) \in \mathbb{N} \times \mathbb{N} \times \mathbb{N}$  either  $K_0 = \emptyset$  or  $K_0 = \mathbb{N}$ , but  $K_0 \in \mathcal{I}_3$  enforces  $K_0 = \emptyset$ . Hence  $\rho(\ell_1 - \ell_2, t) \geq \mathcal{N}(\varepsilon)$  for all  $\varepsilon \in L/\{0_L\}$ . Thus  $\rho(\ell_1 - \ell_2, t) = 1_L$  which proves that  $\ell_1 = \ell_2$ .

**Theorem 3.6** Let  $(V, \rho, \mathcal{T})$  be a  $\mathcal{L}$ -fuzzy normed space and  $\mathcal{I}_3$  be an admissible ideal. Then,

1. If  $\mathcal{I}_3^\ell - \lim x_{mnk} = \ell_1$  and  $\mathcal{I}_3^\ell - \lim y_{mnk} = \ell_2$  then  $\mathcal{I}_3^\ell - \lim(x_{mnk} + y_{mnk}) = (\ell_1 + \ell_2)$

2. If  $\mathcal{I}_3^\ell - \lim x_{mnk} = \ell$  then  $\mathcal{I}_3^\ell - \lim \alpha x_{mnk} = \alpha \ell$ .

*Proof.*

1. Let  $\mathcal{I}_3^\ell - \lim x_{mnk} = \ell_1$  and  $\mathcal{I}_3^\ell - \lim y_{mnk} = \ell_2$ . For any given  $\varepsilon \in L - \{0_L\}$  and  $t > 0$ , we can choose  $r > 0$  such that  $\mathcal{T}(\mathcal{N}(r), \mathcal{N}(r)) \geq \mathcal{N}(\varepsilon)$ . Define the sets,

$$K_1 = \{(m, n, k) \in \mathbb{N} \times \mathbb{N} \times \mathbb{N} : \rho(x_{mnk} - \ell_1, t) \not\geq \mathcal{N}(r)\}$$

and

$$K_2 = \{(m, n, k) \in \mathbb{N} \times \mathbb{N} \times \mathbb{N} : \rho(y_{mnk} - \ell_2, t) \not\geq \mathcal{N}(r)\}$$

for any  $t > 0$ . Since  $\mathcal{I}_3^\ell - \lim x_{mnk} = \ell_1$  and  $\mathcal{I}_3^\ell - \lim y_{mnk} = \ell_2$ , we get  $K_1, K_2 \in \mathcal{I}_3$ . If we define the set

$$K = \{(m, n, k) \in \mathbb{N} \times \mathbb{N} \times \mathbb{N} : \rho((x_{mnk} + y_{mnk}) - (\ell_1 + \ell_2), t) \not\geq \mathcal{N}(\varepsilon)\}$$

then we have to show that  $K \in \mathcal{I}_3$ . Since  $K_1, K_2 \in \mathcal{I}_3$ , from the definition of filter, we know that  $K_1^c, K_2^c \in F(\mathcal{I}_3)$ . Therefore,

$$\begin{aligned} \rho((x_{mnk} + y_{mnk}) - (\ell_1 + \ell_2), t) \\ &\geq \mathcal{T}\left(\rho(x_{mnk} - \ell_1, \frac{t}{2}), \rho(y_{mnk} - \ell_2, \frac{t}{2})\right) \\ &> \mathcal{T}(\mathcal{N}(r), \mathcal{N}(r)) \\ &> \mathcal{N}(\varepsilon). \end{aligned}$$

This shows that,

$$K^c \subset \{(m, n, k) \in \mathbb{N} \times \mathbb{N} \times \mathbb{N} : \rho((x_{mnk} + y_{mnk}) - (\ell_1 + \ell_2), t) > \mathcal{N}(\varepsilon)\}.$$

Thus,  $K^c \in F(\mathcal{I}_3)$ . In other words  $K \in \mathcal{I}_3$ . As a result of this,  $\mathcal{I}_3^L - \lim(x_{mnk} + y_{mnk}) = (\ell_1 + \ell_2)$ .

2. It is obvious for  $\alpha = 0$ . Now let  $\alpha \neq 0$ . Then for  $\varepsilon \in L - \{0_L\}$  and  $t > 0$ ,

$$A = \{(m, n, k) \in \mathbb{N} \times \mathbb{N} \times \mathbb{N} : \rho(x_{mnk} - \ell, t) > \mathcal{N}(\varepsilon)\} \in F(\mathcal{I}_3).$$

It is sufficient to prove that, for each  $\varepsilon \in L - \{0_L\}$  and  $t > 0$ , it can be written

$$A \subset \{(m, n, k) \in \mathbb{N} \times \mathbb{N} \times \mathbb{N} : \rho(\alpha x_{mnk} - \alpha \ell, |\alpha|t) > \mathcal{N}(\varepsilon)\}.$$

Since also  $|\alpha|t > 0$ . Then we have,

$$\begin{aligned} \rho(\alpha x_{mnk} - \alpha \ell, |\alpha|t) &= \rho(x_{mnk} - \ell, \frac{|\alpha|t}{|\alpha|}) \\ &= \rho(x_{mnk} - \ell, t) > \mathcal{N}(\varepsilon). \end{aligned}$$

Therefore, we have

$$A = \{(m, n, k) \in \mathbb{N} \times \mathbb{N} \times \mathbb{N} : \rho(\alpha x_{mnk} - \alpha \ell, |\alpha|t) > \mathcal{N}(\varepsilon)\},$$

and  $A^c \in \mathcal{I}_3$ . Obviously  $\mathcal{I}_3^L - \lim \alpha x_{mnk} = \alpha \ell$ .

#### 4 $\mathcal{I}_3^*$ - Convergence for Triple Sequences on $\mathcal{L}$ - Fuzzy Normed Space

In this section, we give the notion of the  $\mathcal{I}_3^*$  - convergence on  $\mathcal{L}$  - fuzzy normed space.

**Definition 4.1** Let  $(V, \rho, \mathcal{T})$  be a  $\mathcal{L}$  -fuzzy normed space. A sequence of  $x = (x_{mnk})$  of elements in  $X$  is said to be  $\mathcal{I}_3^*$  - convergent to  $\ell \in X$  with respect to the  $\mathcal{L}$  - fuzzy norm if there exist a subset  $K = \{(m_p, n_p, k_p) : m_1, m_2, \dots, n_1 < n_2 < \dots, k_1, k_2, \dots\}$  of  $\mathbb{N} \times \mathbb{N} \times \mathbb{N}$  such that  $K \in F(\mathcal{I}_3)$  (i.e.  $\mathbb{N} \times \mathbb{N} \times \mathbb{N} / K \in \mathcal{I}_3$ ) and  $\mathcal{L} - \lim_{p} x_{m_p n_p k_p} = \ell$ .

In this case we write  $\mathcal{I}_3^{*,L} - \lim x = \ell$ , and  $\ell$  is called the  $\mathcal{I}_3^*$  - limit of the sequence  $x = (x_{mnk})$  with respect to  $\mathcal{L}$  - fuzzy norm.

**Theorem 4.2** Let  $(V, \rho, \mathcal{T})$  be a  $\mathcal{L}$  -fuzzy normed space and  $\mathcal{I}_3$  be an admissible ideal. If  $\mathcal{I}_3^{*,L} - \lim x = \ell$ , then  $\mathcal{I}_3^L - \lim x = \ell$ .

**Proof.** Let  $\mathcal{I}_3^{*,L} - \lim x = \ell$ . Then  $K = \{(m_p, n_p, k_p) : m_1, m_2, \dots, n_1 < n_2 < \dots, k_1, k_2, \dots\} \in F(\mathcal{I}_3)$  (i.e.  $\mathbb{N} \times \mathbb{N} \times \mathbb{N} / K = H \in \mathcal{I}_3$ ) such that  $\mathcal{L} - \lim_{p} x_{m_p n_p k_p} = \ell$ . Then for each  $\varepsilon \in L - \{0_L\}$  and  $t > 0$  there exists a positive integer  $n_0$  such that

$$\rho(x_{m_p n_p k_p} - \ell, t) > \mathcal{N}(\varepsilon)$$

for all  $p > n_0$ . Since the ideal is admissible and from the definition of the convergence, we have

$$\{(m_p, n_p, k_p) \in K : \rho(x_{m_p n_p k_p} - \ell, t) \not> \mathcal{N}(\varepsilon)\} \in \mathcal{I}_3$$

and

$$\begin{aligned} \{(m, n, k) \in \mathbb{N} \times \mathbb{N} \times \mathbb{N} : \rho(x_{mnk} - \ell, t) \not> \mathcal{N}(\varepsilon)\} \\ \subset \cup \{m_1, \dots, m_{p_0-1}, n_1, \dots, n_{p_0-1}, k_1, \dots, k_{p_0-1}\} \in \mathcal{I}_3 \end{aligned}$$

for all  $\varepsilon \in L - \{0_L\}$  and  $t > 0$ . Therefore,  $\mathcal{I}_3^L - \lim x = \ell$ .

**Remark 4.3** From the above example we have seen that  $\mathcal{I}_3^*$  - convergence implies  $\mathcal{I}_3$  - convergence but not conversely. Now the question arises under what condition the converse may hold. For this we define the condition (AP) and see that under this condition the converse holds.

**Definition 4.4** An admissible ideal  $\mathcal{I}_3 \subset P(\mathbb{X})$  is said to satisfy the condition (AP) if for every sequence  $(A_n)_n \in \mathbb{N}$  of pairwise disjoint sets from  $\mathcal{I}_3$  there are sets  $B_n \subset \mathbb{N}$ ,  $n \in \mathbb{N}$ , such that the symmetric difference  $A_n \triangle B_n$  is a finite set for every  $n$  and  $\bigcup_{n \in \mathbb{N}} B_n \in \mathcal{I}_3$ .

It is worth noting that both the ideal consisting of finite subsets of  $\mathbb{N}$  with zero asymptotic density satisfy the condition (AP). However the ideal  $\mathcal{I}_p$  given in Example 4.4. does not have this property. To see this, define the sets

$$A_n := \{p_n^k : k \in \mathbb{N}\}$$

here  $p_n$  denotes the  $n$  - th prime number. Clearly for all  $n \in \mathbb{N}$ ,  $\text{Prime}(A_n) = \{p_n\}$  is finite so that  $A_n \in \mathcal{I}_p$ . Moreover these sets are pairwise disjoint. If  $A_n \triangle B_n$  is finite, then there at most finite number of elements of  $A_n$ , which are not in  $B_n$ . Since  $A_n$  is an infinite set, this means that  $B_n$  has elements of the form  $p_n^k$ . Then  $p_n \in \text{Prime}(B_n)$ . Then for the set  $B := \bigcup_{n \in \mathbb{N}} B_n$ , we have  $\text{Prime}(B) = \mathbb{P}$ , which is an infinite set. So in this situation it is not possible to form a sequence  $(B_n)_{n \in \mathbb{N}}$  of such sets with  $B \in \mathcal{I}_p$ .

**Proposition 4.5** Let  $(V, \rho, \mathcal{T})$  be a  $\mathcal{L}$  -fuzzy normed space and the ideal  $\mathcal{I}_3$  satisfy the condition (AP). If  $x = (x_{mnk})$  is a sequence in  $X$  such that  $\mathcal{I}_3^L - \lim x = \ell$ , then  $\mathcal{I}_3^{*,L} - \lim x = \ell$ .

**Proposition 4.6** Let  $(V, \rho, \mathcal{T})$  be a  $\mathcal{L}$  -fuzzy normed space. Then the following conditions are equivalent:

1.  $\mathcal{I}_3^{*,L} - \lim x = \ell$ .

2. There exist two sequences  $y = (y_{mnk})$  and  $z = (z_{mnk})$  in  $X$  such that  $x = y + z$ ,  $\mathcal{L} - \lim y = \ell$  and the set  $\{(m, n, k) : z_{mnk} \neq \theta\} \in \mathcal{I}_3$ , where  $\theta$  denotes the zero element of  $X$ .

## 5 Conclusion

In this manuscript, we explore certain fundamental characteristics of the ideal convergence of sequences within the framework of  $\mathcal{L}$ -fuzzy normed spaces. This structure offers a versatile and expansive generalization of several classical spaces, including normed spaces, fuzzy normed spaces, and intuitionistic fuzzy (IF) normed spaces. The  $\mathcal{L}$ -fuzzy normed spaces provide a more flexible platform for analyzing convergence behaviors, particularly in the presence of uncertainty and imprecision, thereby extending the applicability of convergence theory to a broader class of spaces.

Moreover, several novel theoretical ideas have been developed and systematically outlined in this context. These innovations are further illustrated through examples that highlight the intricate connections between the various forms of ideal convergence. The results obtained in this study are made possible by leveraging both the lattice structure inherent in  $\mathcal{L}$ -fuzzy normed spaces and the underlying normed space framework. By synthesizing these elements, we introduce a more generalized interpretation of the norm, which enables us to extend the concept to a larger family of topological spaces within vector space theory.

The flexibility and richness of this generalized norm structure, coupled with the lattice-theoretic approach, facilitate a deeper understanding of the convergence properties of sequences in  $\mathcal{L}$ -fuzzy normed spaces. These results not only advance the current theory of ideal convergence but also open up new avenues for research within the broader context of functional analysis and topology.

The results of this study highlight that ideal convergence for triple sequences in  $\mathcal{L}$  – fuzzy normed spaces can yield a more nuanced understanding of sequence convergence, particularly in environments where uncertainty and imprecision are inherent. These findings have far-reaching applications, especially in disciplines such as information theory, where data structures and processing often involve fuzzy or uncertain elements, as well as in artificial intelligence, where algorithmic learning benefits from a robust handling of ambiguous data patterns. Moreover, these principles are highly relevant in fields like quantum computing and physics, where multi-dimensional convergence within imprecise spaces can aid in modeling and predicting phenomena within non-deterministic frameworks. In economic modeling and financial analysis, where projections and assessments often rely on fuzzy data inputs, the application of triple sequence ideal convergence could improve predictive analytics and risk assessment models. Overall, this study establishes a valuable foundation for future research and interdisciplinary applications, illustrating the utility of  $\mathcal{L}$  – fuzzy normed spaces in accommodating more sophisticated forms of convergence essential for modern mathematical and applied sciences.

## References

- [1]. A.A. Nabiev, E. Savaş, M. Gürdal, Statistically localized sequences in metric spaces, *J. Appl. Anal. Comput.*, 9(2) (2019), 739-746.
- [2]. C. Alaca, D. Turkoglu, and C. Yildiz. "Fixed points in intuitionistic fuzzy metric spaces." *Chaos, Solitons & Fractals* 29.5 (2006): 1073-1078.
- [3]. C. Alaca, D. Turkoglu, and C. Yildiz. "Common Fixed Points of Compatible Maps in Intuitionistic Fuzzy Metric Spaces." *Southeast Asian Bull. Math.* 32.1 (2008).
- [4]. K. Atanassov. "Intuitionistic fuzzy sets." *Fuzzy Sets Syst.* 1986; 20:87–96
- [5]. A. Nabiev, S. Pehlivan, M. Gürdal, On I-Cauchy sequences. *Taiwanese J. Math.*, 11(2) (2007), 569-576.
- [6]. A. Şahiner, M. Gürdal, T. Yiğit, Ideal convergence characterization of the completion of linear  $n$ -normed spaces, *Comput. Math. Appl.*, 61(3) (2011), 683-689.
- [7]. A. Şahiner, M. Gürdal, S. Saltan, H. Gunawan, Ideal convergence in 2-normed spaces. *Taiwanese J. Math.*, 11(5) (2007), 1477-1484.
- [8]. N. Eghbali, M. Ganji. Generalized Statistical Convergence in the Non-Archimedean  $L$  –fuzzy Normed Spaces. *Azerb. J. Math.*, 2016; 6(1), 15-22.
- [9]. E. Dündar, M. R. Türkmen, On  $I_2$ -Convergence and  $I_2^*$  - Convergence of Double Sequences in Fuzzy Normed Spaces, *Konuralp J. Math.* 7(2) (2019), 405–409.
- [10]. E. Dündar, M. R. Türkmen, On  $I_2$ -Cauchy Double Sequences in Fuzzy Normed Spaces, *Commun. Adv. Math. Sci.*, 2(2) (2019), 154–160.
- [11]. M. Gürdal, M.B. Huban, On I-convergence of double sequences in the topology induced by random 2-norms, *Mat. Vesnik*, 66(1) (2014), 73-83.
- [12]. M. R. Türkmen, E. Dündar, On Lacunary Statistical Convergence of Double Sequences and Some Properties in Fuzzy Normed Spaces, *J. Intell. Fuzzy Syst.*, 36(2) (2019), 1683–1690, DOI:10.3233/JIFS-181796
- [13]. E. Dündar, B. Altay  $J_2$ -uniform convergence of double sequences of functions. *Filomat* 30(5) (2016) 1273–1281.
- [14]. E. Dündar, Ö. Talo,  $J_2$ -convergence of double sequences of fuzzy numbers, *Iran. J. Fuzzy Syst.*, 10(3) (2013), 37–50.
- [15]. E. Dündar, B. Altay,  $I_2$ -convergence and  $J_2$ -Cauchy of double sequences, *Acta Math. Sci.*, 34B(2) (2014), 343–353.
- [16]. E. Dündar, B. Altay, On some properties of  $J_2$ -convergence and  $J_2$ -Cauchy of double sequences, *Gen. Math. Notes*, 7(1)(2011), 1–12.
- [17]. E. Dündar, Ö. Talo,  $J_2$ -Cauchy Double Sequences of Fuzzy Numbers, *Gen. Math. Notes*, 16(2) (2013), 103–114.
- [18]. E. Dündar, Ö. Talo, F. Başar, Regularly  $(J_2, J)$ -Convergence and Regularly  $(J_2, J)$ -Cauchy Double Sequences of Fuzzy Numbers, *Int. J. Anal.*, vol. 2013, pp. 1–7, Apr. 2013.
- [19]. E. Dündar, M. R. Türkmen and N. Pancaroglu Akin, Regularly ideal convergence of double sequences in fuzzy normed spaces, *Bull. Math. Anal. Appl.*, 12(2) (2020), 12–26.
- [20]. J.A. Goguen. *L-fuzzy Sets*. *J. Math. Anal. Appl.* 18, 145–174 (1967)

- [21]. M. Grabiec Fixed points in fuzzy metric spaces. *Fuzzy Sets Syst.* 1988; 27:385–389
- [22]. V. Gregori, J.J. Miñana, S. Morillas, A. Sapena. Cauchyness and convergence in fuzzy metric spaces. *RACSAM* 2017; 111(1): 25–37
- [23]. M. Gürdal and E. Savaş. "An investigation on the triple ideal convergent sequences in fuzzy metric spaces." *Commun. Fac. Sci. Univ. Ankara Ser. A1 Math. Stat.* 71.1 (2022): 13-24.
- [24]. S. Karakuş, K. Demirci, O. Duman.. Statistical convergence on intuitionistic fuzzy normed spaces. *Chaos, Solitons & Fractals* 2008; 35:763–769
- [25]. P. Kostyrko, S. Tibor, and W. Władysław. "I-convergence." *Real Anal. Exchange* (2000): 669-685.
- [26]. P. Kostyrko, et al. "I-convergence and extremal I-limit points." *Math. Slovaca* 55.4 (2005): 443-464.
- [27]. V. Kumar and K. Kuldeep. "On the ideal convergence of sequences of fuzzy numbers." *Inf. Sci.* 178.24 (2008): 4670-4678.
- [28]. SA. Mohiuddine and QM. Danish Lohani. On generalized statistical convergence in intuitionistic fuzzy normed space. *Chaos, Solitons & Fractals* 2009; 42: 1731–1737
- [29]. M. Mursaleen and SA. Mohiuddine. On lacunary statistical convergence with respect to the intuitionistic fuzzy normed space. *J. Comput. Appl. Math.* 2009; 233:142–149
- [30]. M. Mursaleen, SA. Mohiuddine and H.E. Edely. "On the ideal convergence of double sequences in intuitionistic fuzzy normed spaces." *Comput. Math. Appl.* 59.2 (2010): 603-611.
- [31]. JH. Park Intuitionistic fuzzy metric spaces. *Chaos, Solitons & Fractals* 2004; 22:1039–1046
- [32]. S. Pandit, A. Ahmad, and A. Esi. "On intuitionistic fuzzy metric space and ideal convergence of triple sequence space." *Sahand Commun. Math. Anal.* 20.1 (2023): 35-44.
- [33]. D. Rath, B. Tripathy. 1994. On statistically convergent and statistically Cauchy sequences, *Indian J. Pure Appl. Math.*, 25, 381-386.
- [34]. R. Saadati, JH. Park. On the intuitionistic fuzzy topological spaces. *Chaos, Solitons & Fractals* 2006; 27:331–344
- [35]. E. Savaş and M. Gürdal. "Ideal convergent function sequences in random 2-normed spaces." *Filomat* 30.3 (2016): 557-567.
- [36]. E. Savas and D. Pratulananda. "A generalized statistical convergence via ideals." *Appl. Math. Lett.* 24.6 (2011): 826-830.
- [37]. E. Savaş, S. Debnath, and D. Rakshit. "On I-statistically rough convergence." *Publ. Inst. Math. (Beograd)* 105.119 (2019): 145-150.
- [38]. E. Savas and M. Gürdal. "A generalized statistical convergence in intuitionistic fuzzy normed spaces." *Sci. Asia* 41 (2015): 289-294.
- [39]. S. Shakeri, R. Saadati, C. Park Stability of the quadratic functional equation in non-Archimedean  $L$ -fuzzy normed spaces. *Int. J. Nonlinear Anal. Appl.*, 2010, 1.2: 72-83.
- [40]. H. Steinhaus. 1951. Sur la convergence ordinaire et la convergence asymptotique, *Colloq. Math.* 2, 73-74.
- [41]. S. Kastyro, T. Salat, W. Wilczynski, I-Convergence, *Real Anal. Exchange* 26(2000) 669-686.2001.
- [42]. A. Şahiner, M. Gürdal, F.K. Düden, Triple sequences and their statistical convergence, *Selcuk J. Appl. Math.*, 8(2) (2007), 49-55.
- [43]. U. Yamancı, M. Gürdal, On lacunary ideal convergence in random normed space, *J. Math.*, 2013; 868457, 1-8.
- [44]. R. Yapalı and U. Gürdal. "Pringsheim and tatistical convergence for double sequences on  $L$  – fuzzy normed space." *AIMS Math.* 6.12 (2021): 13726-13733.
- [45]. R. Yapalı and Ö. Talo. "Tauberian conditions for double sequences which are statistically summable  $(C, 1, 1)$  in fuzzy number space." *J. Intell. Fuzzy Syst.* 33.2 (2017): 947-956.
- [46]. R. Yapalı, H. Coşkun, and U. Gürdal. "Statistical convergence on  $L$  – fuzzy normed space." *Filomat* 37.7 (2023): 2077-2085.
- [47]. R. Yapalı and H. Coşkun. "Lacunary Statistical Convergence for Double Sequences on  $\mathcal{L}$  – Fuzzy Normed Space." *J. Math. Sci. Model.* 6.1 (2023): 24-31.
- [48]. R. Yapalı et al. "Lacunary statistical convergence on L-fuzzy normed space." *J. Intell. Fuzzy Syst.* 46.1 (2024): 1985-1993.
- [49]. LA. Zadeh Fuzzy sets. *Inf. Control* 1965; 8:338–353



# Investigation of Dielectric Anisotropy and Electrical Modulus-Impedance Properties of PCBM/E7 Composite for Organic Electronic Devices Applications

Ahmet Demir<sup>1,2\*</sup>, Ahmad Badreddin Musatat<sup>3</sup>, Şule Zeynep Kip<sup>2</sup>

<sup>1</sup> Fibrobeton Inc., İstanbul 34810, Türkiye

<sup>2</sup> Department of Physics, Faculty of Science, Düzce University, Düzce, Türkiye

<sup>3</sup> Department of Chemistry, Faculty of Sciences, Sakarya University, 54050, Sakarya, Türkiye

\* [ahmetdemir@duzce.edu.tr](mailto:ahmetdemir@duzce.edu.tr)

\* Orcid No: 0000-0002-8702-1941

Received: 7 October, 2024

Accepted: 25 December, 2024

DOI: 10.18466/cbayarfbe.1562667

## Abstract

This study investigates the dielectric anisotropy and electrical modulus-impedance properties of a PCBM/E7 composite material for organic electronic devices applications. The research examines a specially fabricated cell combining nematic liquid crystal E7 with [6,6]-phenyl-C61-butyric acid methyl ester (PCBM) semiconductor. Through a comprehensive analysis of dielectric anisotropy, AC conductivity, electrical modulus, and impedance characteristics under varying frequencies and applied voltages (-6.0V to +6.0V), the study reveals distinct behavioral regions and multiple relaxation processes. Key findings include frequency-dependent dielectric anisotropy transitions, enhanced AC conductivity at higher frequencies and voltages, and voltage-modulated impedance characteristics. The observed dual-peak phase angle response suggests multiple relaxation mechanisms, indicating the composite's potential for voltage-tunable electrical properties in advanced optoelectronic applications.

**Keywords:** AC conductivity, dielectric anisotropy, electrical modulus, impedance spectroscopy, liquid crystal, E7-PCBM composite

## 1. Introduction

Liquid Crystal (LC)-based materials have gained significant attention due to their numerous electrical and medical uses [1,2]. Also, they occupy a distinct phase between solids and liquids, combining fluid-like properties with solid-like anisotropy. They are primarily categorized into nematic, smectic, and cholesteric phases. In the nematic phase, LC molecules exhibit an average orientational order along their long axes, denoted by the director  $\hat{n}$ . Nematic LCs are widely employed in display technologies due to their molecular orientation's responsiveness to electric fields. Notably, increasing the applied electric field in nematic LC devices reduces the molecular response time, enhancing performance [3]. This makes nematic LCs versatile for various display sizes, from compact devices (smartphones, calculators, digital cameras) to medium-scale screens (computers) and large displays (projectors, televisions) [4]. On the other hand, Fullerenes, hollow spherical nanoparticles with dimensions similar to LC molecules, serve as ideal dopants for LC hosts. When incorporated into LCs,

fullerenes promote system structurization and self-organization [5]. Pristine fullerene-based LC colloids exhibit enhanced photorefractive effects and photoconductivity [6-8]. Studies have shown that pristine fullerene additives lower the phase transition temperature in nematic LCs with positive dielectric anisotropy, such as E7 and 5CB [9,10]. It is also known that Fullerene additives in nematic LCs reduce the threshold voltage and critical frequency for William's domain formation disappearance, as well as its temporal characteristics [11]. Also doping fullerenes into 90° twisted nematic cells reduces DC driving voltage and improves switching times [12]. A study on the dielectric and electrical properties of an E7 mixture containing methyl Red and fullerene, subjected to AC-DC signals at various temperatures, revealed that both real and imaginary components of dielectric permittivity decreased with increasing frequency of the applied field, while AC conductivity increased [13]. Several investigations on the effect of C60 fullerenes on smectic Liquid crystals exhibited an increase in the transverse component and a decrease in the longitudinal component of the actual dielectric permittivity [14]. The promising properties of

LC materials, especially when doped with fullerenes, open up possibilities for a variety of applications beyond displays. Similarly, Organic Field-Effect Transistors (OFETs) have emerged as important components in modern electronics due to their cost-efficiency and flexibility [15]. LCs, OFETs benefit from advancements in material science and fabrication techniques, which improve their electrical performance and broaden their potential uses. Simultaneously Organic field-effect transistors (OFETs) have gained significant research attention in electronic manufacturing due to their cost-effectiveness and structural flexibility. They find widespread applications in integrated circuits, RFID tags, thin film displays, and sensors, notably employed in organic synthesis to facilitate applications for such field [16-18]. While OFET performance is primarily determined by mobility ( $\mu$ FET), other factors are crucial, like low interfacial resistance between the insulator and gate electrode enhances device efficiency, and the optimal design of the gate-insulator-semiconductor interface is critical to prevent performance-degrading traps [19,20]. While organic field-effect transistors (OFETs) and liquid crystal (LC) devices offer advantages in terms of affordability and performance, research efforts persist in refining their features through the development of new materials and enhanced fabrication processes [21]. In addition, the increasing prevalence of electronic devices has intensified the demand for energy storage and conductive technologies, driving research into sustainable materials. The emergence of flexible electronics, rooted in the 1970s discovery of conductive polymers by Heeger, Shirakawa, and McDiarmid, has revolutionized the field. This advancement allows for the creation of electronic components on various surfaces through the deposition of conductive polymers at multiple scales, facilitating the transformation of industrial byproducts into eco-friendly, high-performance electrical materials [22].

Given the promising properties of liquid crystal materials doped with fullerenes and the growing importance of organic electronic devices, this study aims to revisit and further investigate the dielectric anisotropy and electrical modulus-impedance properties of a novel PCBM/E7 special cell composite medium. Our objectives encompass characterizing the dielectric anisotropy of the PCBM/E7 composite across a range of frequencies and temperatures, as well as analyzing the electrical modulus and impedance properties of this novel composite medium. We also seek to evaluate how the addition of PCBM fullerene derivatives affects the electrical and dielectric properties of the E7 liquid crystal. Furthermore, we aim to explore the potential applications of this PCBM/E7 composite in organic electronic devices, particularly in the context of OFETs and flexible electronics. Through this research, we aim to contribute to the broader understanding of fullerene-doped liquid crystal systems and their potential in next-generation electronic technologies. By investigating the dielectric

anisotropy and electrical modulus-impedance properties of PCBM/E7 special cell as a novel composite medium, we aim to bridge the gap between the theoretical understanding of fullerene-doped liquid crystals and their practical applications in advanced electronic devices.

## 2. Materials and Methods

### 2.1. Special Cell Fabrication

A specialized PCBM/E7 composite device with specified contact area of  $1.5 \times 10^{-2} \text{ cm}^2$  was fabricated following our previously established protocol [23]. The primary materials, including nematic liquid crystal E7 (a mixture containing 5CB, 7CB, 8OCB, and 5CT compounds) and n-type semiconductor PCBM which chemical structure is given in Figure 1, were sourced from Sigma-Aldrich. E7, characterized by its positive dielectric anisotropy, ( $\Delta\epsilon' \approx 13.8$  at low frequencies) and broad nematic range ( $-10^\circ\text{C}$  to  $59^\circ\text{C}$ ), served as the host material [24,25]. Its unique composition of cyano-biphenyl and terphenyl compounds makes it particularly suitable for optoelectronic applications.

The device fabrication process consisted of several critical steps. Initially, we prepared the semiconductor solution by dissolving PCBM in 1,2-dichlorobenzene to achieve a concentration of 20 mg/mL. This mixture was thoroughly agitated at  $60^\circ\text{C}$  for 30 minutes to ensure complete dissolution and homogeneity. For the device structure, we utilized both patterned and unpatterned ITO substrates, serving as source-drain and gate contacts, respectively. The UV-curable NOA65 monomer was selected as the adhesive material for its optimal optical and mechanical properties.

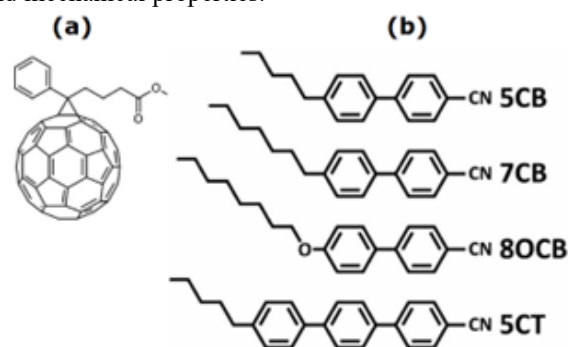


**Figure 1.** The chemical structure of a) PCBM b) E7 LC.

The OFET cell assembly began with the precise positioning of the ITO substrates, followed by the UV-curing process of NOA65 using 390 nm wavelength radiation. A crucial structural element was the incorporation of a polyimide film spacer (approximately 10  $\mu\text{m}$  thickness), which precisely defined the device's active and insulator layer dimensions. The composite mixture was prepared by combining equal volumes of E7 and the prepared PCBM solution, followed by a 30-minute sonication treatment to achieve uniform

dispersion throughout the medium. The final stage of fabrication involved the careful injection of the PCBM/E7 composite into the prepared cell structure. This process was conducted at an elevated temperature of 120°C, utilizing the capillary filling method. This approach was specifically chosen to minimize exposure to environmental contaminants such as moisture and oxygen, which could potentially compromise device performance. Upon successful filling, the injection ports were thoroughly sealed with epoxy adhesive, ensuring complete isolation from ambient conditions and preventing any potential leakage of the composite material.

### 2.1.1. Impedance Measurements

The electrical and dielectric properties, polarization, and relaxation mechanisms of the fabricated cell were evaluated using the Keithley 2400 SMU&GW Instek 8105 LCR electrical impedance measurement system, which communicates with a computer via an IEEE 488 card. The entire measurement is shown in scheme 1.



**Scheme 1.** The conducted impedance measurements.

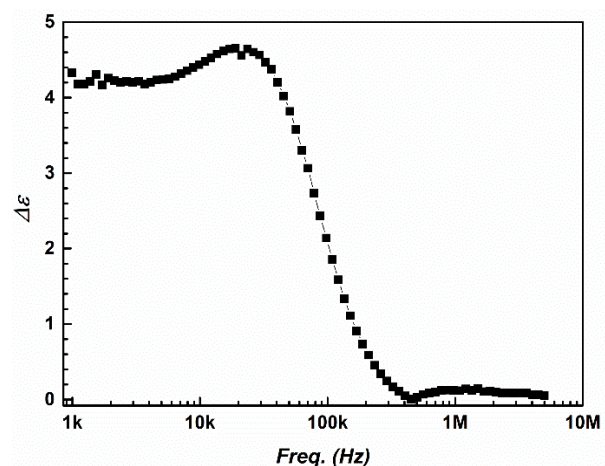
## 3. Results and Discussion

Figure 2 presents the frequency-dependent dielectric anisotropy ( $\Delta\epsilon$ ) which was measured between +6.0 V and 0.0 V of the PCBM/E7 composite by employing equation (1) [26].

$$\Delta\epsilon = \epsilon_{||} - \epsilon_{\perp} \quad (1)$$

Where  $\epsilon_{||}$  denotes the parallel and  $\epsilon_{\perp}$  is the perpendicular part of the dielectric constant. The real and imaginary parts of dielectric constant are  $\epsilon' = C/C_0$  and  $\epsilon'' = G/\omega C_0$ , respectively, here  $C$  denoted the capacitance,  $G/\omega$  illustrated the conductance, and  $C_0$  declares the capacitance of free space. Moreover  $C_0 = \epsilon_0 A/d$ ,  $\epsilon_0$ ,  $A$ , and  $d$  were vacuum permittivity ( $\epsilon_0 = 8.85 \times 10^{-14}$  F/cm), active contact area, and thickness of sample, respectively. To determine the dielectric anisotropy value of the PCBM/E7 investigated, the capacitance of the liquid crystal cell was measured as a function of applied voltage. The dielectric anisotropy was calculated as the difference between the permittivities measured parallel and perpendicular to the alignment of the liquid crystal molecules. This parameter is critical in understanding the

orientational ordering and alignment behavior of the liquid crystal molecules in the presence of an external field, which directly impacts the composite's optoelectronic properties. Based on the obtained results at lower frequencies (below approximately 10 kHz),  $\Delta\epsilon$  exhibited relatively minor variation, with values remaining negative and close to 5 suggesting that in this frequency range, the dielectric response is predominantly controlled by the relaxation processes associated with the liquid crystal E7, where the orientation of the dipoles does not readily follow the applied field due to the slow response time of the liquid crystals. Meanwhile as the frequency increases beyond 1 kHz,  $\Delta\epsilon$  undergoes a marked increase, with a steep rise observed between 1 kHz and 1 MHz. This can be attributed to the onset of a relaxation process, likely the result of reorientation of the liquid crystal molecules aligning with the applied electric field [27]. Interestingly the sharp rise in  $\Delta\epsilon$  indicates that the composite material exhibits strong dielectric anisotropy in this frequency range, with the molecular alignment becoming more pronounced. At higher frequencies (above 1 MHz),  $\Delta\epsilon$  plateaus, approaching zero. This behavior is typical for dielectric relaxation, where the response of the dipoles in the liquid crystal becomes outpaced by the rapidly alternating electric field. At these frequencies, the dipoles cannot reorient fast enough to contribute to the dielectric anisotropy, and the response becomes frequency-independent. The overall shape of the dielectric anisotropy curve indicated the presence of a clear dielectric relaxation process, which is essential for tuning the composite material's dielectric properties for optoelectronic applications. The observed dielectric anisotropy suggests that the PCBM/E7 composite is well-suited for devices where controlled molecular alignment and dielectric tuning are required, such as in liquid crystal displays (LCDs), photonic devices, and other optoelectronic applications.



**Figure 2.** The obtained dielectric anisotropy plot.

On the other hand, in order to gain deeper understanding of critical insights into the conduction mechanisms within the cell, as well as the impact of applied voltage on the material's conductive properties, the AC electrical conductivity ( $\sigma_{ac}$ ) of the fabricated special cell as a

function of frequency for different applied DC bias voltages ranging from  $-6.0$  V to  $6.0$  V was evaluated and illustrated in figure 3. The electrical conductivity was obtained by employing equation (2) as below [28]:

$$\sigma_{ac} = \varepsilon_0 \varepsilon'' \omega \quad (2)$$

Where  $\sigma_{ac}$  represents the electrical conductivity, and  $\omega$  represents the angular frequency ( $2\pi f$ ). Based on the obtained results at low frequencies (below approximately 10 kHz),  $\sigma_{ac}$  was found to remain relatively constant across all applied voltages, with minimal variation in conductivity. This plateau in conductivity is typical in materials where the conduction mechanism at low frequencies is dominated by localized charge carriers, such as ionic or dipole relaxation processes. The near-zero conductivity in this range suggests that the charge carriers are not sufficiently mobile to contribute to significant AC conductivity at low frequencies, which is common in systems where carrier hopping or dipole orientation under an electric field plays a significant role. As the frequency increases beyond 10 kHz, a sharp rise in conductivity was observed for all voltages. This increase is indicative of a frequency-dependent conductivity mechanism, such as hopping or tunneling of charge carriers between localized states. The observed increase in  $\sigma_{ac}$  as the frequency reaches the MHz range suggests that the charge carriers are gaining sufficient energy to overcome potential barriers, leading to enhanced mobility and higher conductivity [29]. Notably, the applied bias voltage has a clear influence on the AC conductivity, as evidenced by the separation of the conductivity curves at higher frequencies. At higher voltages, particularly at  $6.0$  V and  $4.5$  V, the  $\sigma_{ac}$  values at frequencies above 100 kHz were significantly higher compared to those at lower voltages, such as  $-6.0$  V and  $-4.5$  V. This behavior suggests that the applied voltage enhances the mobility of charge carriers of the fabricated special cell, possibly by reducing the potential barriers for conduction or inducing alignment of charge carriers, thereby increasing the overall conductivity.

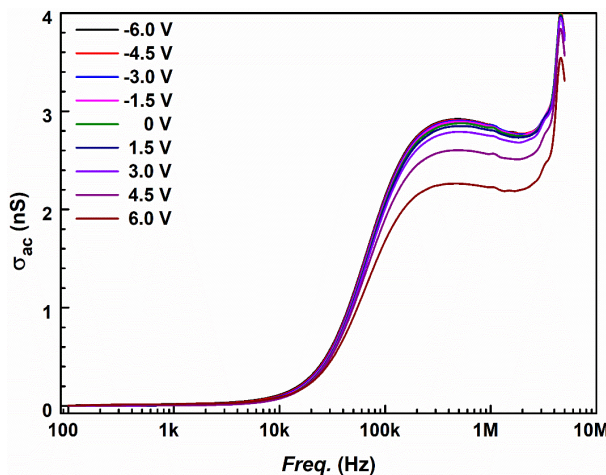


Figure 3. ac electrical conductivity of the fabricated cell

The divergence in  $\sigma_{ac}$  with increasing voltage at higher frequencies highlights the sensitivity of the fabricated device's conductive properties to external electric fields. The increased conductivity at higher voltages is particularly important for applications where tunable electrical properties are desirable, such as in optoelectronic devices, sensors, and capacitive systems. The enhanced conductivity at higher frequencies and voltages suggests that the fabricated special cell can be engineered to operate in high-frequency environments, where rapid charge carrier movement is essential [28].

Figure 4-a presents the frequency dependence of the real part of the electrical modulus ( $M'$ ) for the fabricated special cell under different applied bias voltages ranging from  $-6.0$  V to  $6.0$  V by employing equation (3) as below:

$$M'(\omega) = \frac{\varepsilon'}{\varepsilon'^2 + \varepsilon''^2} \quad \text{and} \quad M''(\omega) = \frac{\varepsilon''}{\varepsilon'^2 + \varepsilon''^2} \quad (3)$$

Where  $M'$ ,  $M''$  represents the real and the imaginary part of electrical modulus respectively. The real part of the electrical modulus provides insight into the relaxation dynamics and distribution of relaxation times within the material, as well as the degree of conductivity and polarization response of the studied system. At low frequencies (below approximately 10 kHz),  $M'$  were remained relatively constant for all applied voltages, with values ranging from 1000 to 10000. The low values of  $M'$  in this region suggest that the device exhibits significant capacitive behavior, with a high contribution from electrode polarization or space charge effects. This implies that the material has a low electrical modulus, which corresponds to a higher dielectric constant, meaning that the system stores more energy in the form of polarization at lower frequencies. As the frequency increases beyond 10 kHz,  $M'$  showed a gradual increase followed by a distinct peak near 1 MHz for all applied voltages. This rise in  $M'$  with frequency reflected the onset of dielectric relaxation, where the dipoles or charge carriers begin to respond to the applied AC field but with increasing difficulty as the frequency becomes higher. The appearance of a peak in  $M'$  around 1 MHz is characteristic of the device's dielectric relaxation process, where the bulk polarization of the material starts to lag behind the rapidly changing field, resulting in a reduction of the material's ability to store charge. Notably, at higher frequencies (above 1 MHz),  $M'$  shows a significant spike for all voltages, with the magnitude of the modulus increasing with the applied voltage. This behavior indicates that the relaxation time of the charge carriers shortens at higher frequencies, leading to an increased response in the real part of the modulus. The higher  $M'$  values at elevated frequencies suggest that the material becomes more conductive and less capable of storing charge, as the applied AC field is too rapid for significant polarization to occur. The effect of the applied voltage is apparent in the divergence of the modulus curves at higher frequencies. Higher applied voltages,



particularly 6.0 V and 4.5 V, lead to a more pronounced increase in  $M'$ , suggesting that the external field enhances the relaxation process and the movement of charge carriers, which indicates that the relaxation dynamics and conductivity of the material are sensitive to the applied voltage, with higher voltages inducing more rapid polarization and charge carrier mobility. On the other hand, figure 4-b presents the frequency dependence of the imaginary part of the electrical modulus ( $M''$ ) for the fabricated special cell under varying applied voltages, ranging from -6.0 V to 6.0V. The imaginary part of the modulus is closely related to the energy dissipation within the material and reflects the degree of relaxation of the polarization processes in the system. Based on the obtained results, at low frequencies (below approximately 10 kHz),  $M''$  exhibits relatively low values for all applied voltages, typically under 1,000. This region indicates that at low frequencies, the material displays minimal relaxation and dissipative effects. The polarization aligns relatively easily with the applied field, and the stored energy is primarily in the form of reversible polarization, with little energy loss due to dielectric relaxation. As the frequency increases beyond 10 kHz,  $M''$  shows a clear increase, eventually reaching a broad peak around 1 MHz for all voltages. This peak represents the relaxation process, where the dipoles in the material can no longer follow the rapidly changing electric field, leading to energy dissipation. The presence of this peak is characteristic of dielectric materials that exhibit a relaxation time, and the frequency at which this peak occurs provides information on the relaxation dynamics of the system. The effect of the applied voltage is particularly evident in the lower frequency region, where the magnitude of  $M''$  diverges for different voltages. Higher voltages, such as -6.0 V and 6.0 V, result in slightly larger values of  $M''$ , suggesting that increasing the applied voltage enhances the polarization response and energy dissipation within the material. This indicates that the polarization dynamics are sensitive to the external electric field, with higher fields inducing more significant dielectric relaxation effects. At high frequencies (beyond 1 MHz), the modulus decreases sharply, indicating that the dipoles or charge carriers are unable to respond to the fast-alternating field. In this region,  $M''$  reaches a plateau, where the material transitions to a purely conductive state with minimal energy storage or dissipation in the form of polarization. This high-frequency behavior is typical of materials that exhibit conductive loss rather than dielectric relaxation at very high frequencies. The imaginary modulus curves for different voltages converge at high frequencies, suggesting that the relaxation dynamics are largely voltage-independent in this regime. This implies that while the applied field influences the polarization and relaxation behavior at lower frequencies, at higher frequencies, the system behaves in a more uniform manner across the voltage range. The physical mechanism by which electrical charge conduction within the cell is depicted is given in Figure 5.

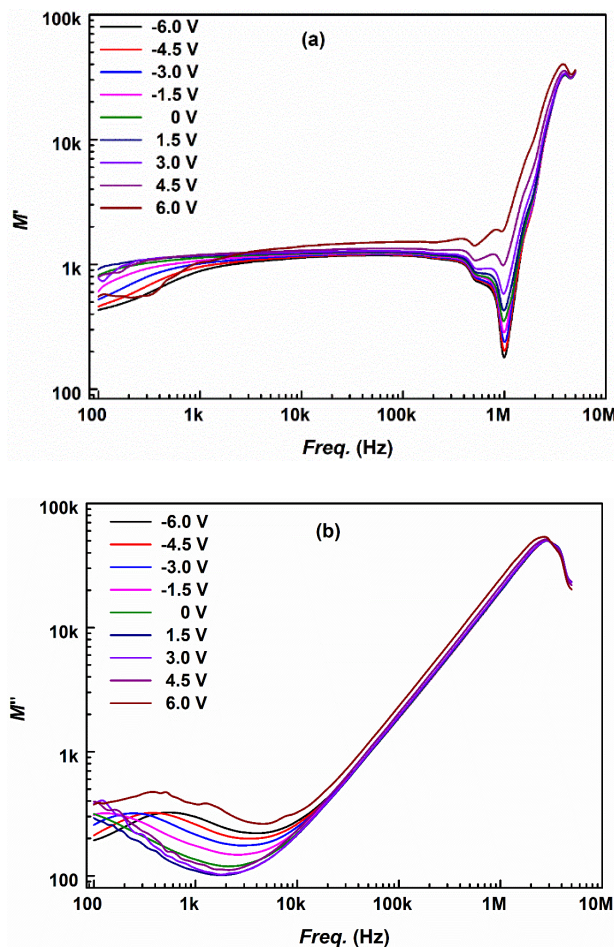


Figure 4. a) the real b) imaginary part of the electrical modulus of fabricated cell.

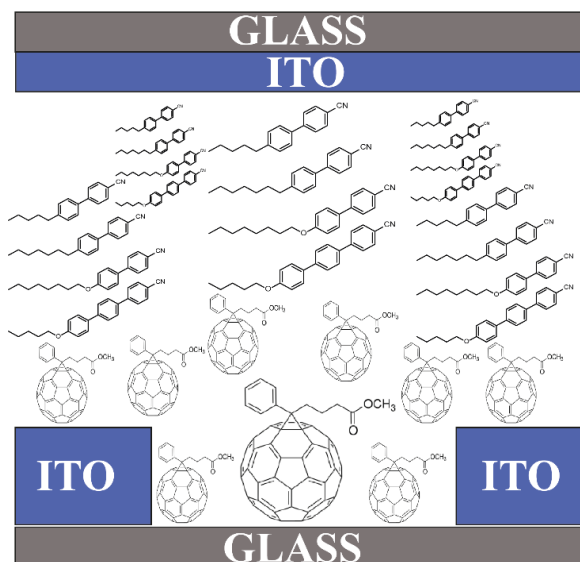


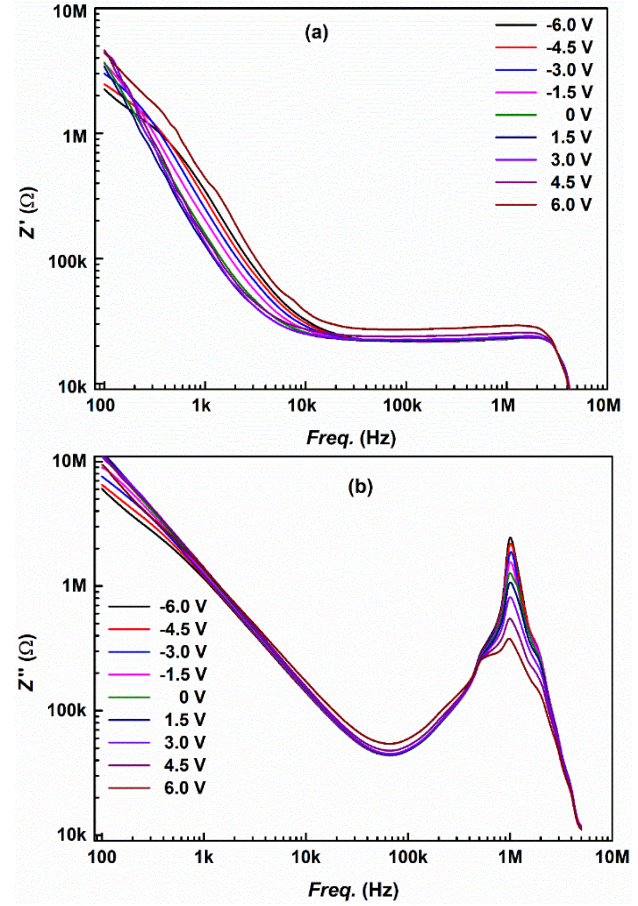
Figure 5. Real time electrical charge transfer mechanism of the fabricated cell.

Figure 6-a. shows the variation of the real part of impedance ( $Z'$ ) versus frequency for the fabricated device under different applied gate voltages ( $V_{GS}$ ) ranging from -6.0 V to +6.0 V by employing equation (4):



$$Z' = \frac{\epsilon''}{\omega C_0 [\epsilon'^2 + \epsilon''^2]} \text{ and } Z'' = \frac{\epsilon'}{\omega C_0 [\epsilon'^2 + \epsilon''^2]} \quad (4)$$

Where  $Z'$ ,  $Z''$  represents the real and imaginary part of impedance which after all can be obtained from the  $\epsilon'$  and  $\epsilon''$  values for each frequency. Based on the obtained results, the impedance spectrum exhibited three distinct regions: Low-frequency region (100 Hz - 10 kHz):  $Z'$  decreases rapidly with increasing frequency, indicating a strong frequency dependence of the device's resistive behavior. Mid-frequency region (10 kHz - 1 MHz):  $Z'$  plateaus, suggesting a relatively stable resistive component in this frequency range. High-frequency region ( $> 1$  MHz): A sharp drop in  $Z'$  was observed, likely due to the device's capacitive effects becoming dominant. The applied gate voltage influences the impedance response, particularly in the low-frequency region, where higher positive and negative  $V_{GS}$  values result in slightly increased  $Z'$ . This behavior suggests that the gate voltage modulates the charge transport mechanisms within the device, affecting its overall impedance characteristics. The observed trends provide valuable insights into the frequency-dependent electrical properties of the fabricated device and the impact of gate voltage on charge dynamics within the device structure. Meanwhile figure 6-b illustrates the frequency dependence of the imaginary part of impedance ( $Z''$ ) for the special cell at various gate voltages ( $V_{GS}$ ) from -6.0 V to +6.0 V was found to reveal several key features: Low-frequency region (100 Hz - 10 kHz):  $Z''$  decreases linearly with increasing frequency, indicating a dominant capacitive behavior. For the Mid-frequency region (10 kHz - 100 kHz): A minimum in  $Z''$  was observed, suggesting a transition in the device's electrical response. Lastly, under the High-frequency region (100 kHz - 10 MHz): A prominent relaxation peak appears, with its maximum around 1-2 MHz. This peak signifies a relaxation process, likely associated with interfacial polarization or charge carrier dynamics within the device. The applied gate voltage influences the relaxation peak intensity, with higher positive  $V_{GS}$  values resulting in lower peak magnitudes. This voltage dependence implies that the gate bias modulates the relaxation processes, possibly by altering the charge distribution or molecular alignment in the LC-PCBM composite. The observed  $Z''$  spectrum provided valuable insights into the capacitive nature and relaxation mechanisms of the LC-PCBM composite cell, complementing the real impedance data and offering a more complete picture of the device's complex electrical behavior.



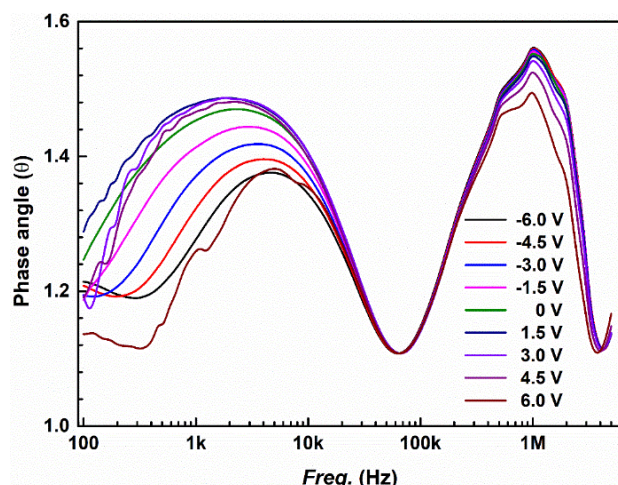
**Figure 6.** a) The variation of real part b) imaginary part of impedance versus frequency of fabricated cell

Figure 7 illustrates the phase angle's frequency dependence for the LC-PCBM special cell under various gate voltages ( $V_{GS}$ ) from -6.0 V to +6.0 V by employing the equation (5):

$$\tan \theta = Z''/Z' \quad (5)$$

The spectrum reveals intricate electrical behavior with multiple relaxation processes: In the low-frequency domain (100 Hz - 10 kHz), the phase angle rises with frequency, peaking around 5-10 kHz, indicating a shift from resistive to capacitive characteristics. The mid-frequency range (10 kHz - 100 kHz) shows a sharp phase angle decline, suggesting a return to more resistive behavior. At high frequencies (100 kHz - 10 MHz), a second, more prominent maximum emerges near 1 MHz before rapidly decreasing, likely signifying a distinct relaxation process within the device. The applied gate voltage markedly affects the phase angle response, especially in low and high-frequency regions. As  $V_{GS}$  shifts from negative to positive, the first phase angle peak (5-10 kHz) diminishes, while the second peak (1 MHz) remains relatively stable. This voltage-dependent behavior suggests that gate bias modulates the device's resistive and capacitive components, possibly through altering charge carrier dynamics or LC-PCBM composite molecular arrangement. The observation of two distinct

phase angle maxima indicates multiple relaxation mechanisms at different timescales. These may stem from interfacial polarization, charge trapping/detrapping, or molecular reorientation within the liquid crystal matrix. These insights into the LC-PCBM's complex impedance characteristics highlight its potential for gate voltage-tunable electrical properties.



**Figure 7.** Phase angle of the fabricated special cell

## Conclusion

In this study, we have thoroughly investigated the dielectric anisotropy and electrical modulus-impedance properties of a PCBM/E7 composite medium for enhanced optoelectronic applications. The dielectric anisotropy measurements revealed that at lower frequencies (below 10 kHz),  $\Delta\epsilon$  exhibited relatively minor variation, with values remaining negative and close to  $-5 \times 10^{-5}$ . A marked increase in  $\Delta\epsilon$  was observed between 10 kHz and 1 MHz, followed by a plateau approaching zero at higher frequencies, indicating well-defined dielectric relaxation processes. The AC conductivity analysis demonstrated frequency and voltage-dependent behavior, with significant enhancement at frequencies above 100 kHz, particularly at higher applied voltages (6.0 V and 4.5 V). The electrical modulus studies showed distinct relaxation dynamics, with the real part ( $M'$ ) exhibiting a characteristic peak near 1 MHz and significant voltage dependence at higher frequencies. The imaginary part ( $M''$ ) revealed a broad relaxation peak around 1 MHz, indicating complex polarization processes within the material. Impedance spectroscopy identified three distinct frequency regions in  $Z'$  and  $Z''$ , with multiple relaxation processes evidenced by dual-phase angle maxima at 5-10 kHz and 1 MHz. The findings show that PCBM/E7 composite exhibits complex charge transport and voltage-tunable properties, making it a promising candidate for advanced optoelectronic applications. The observed voltage-dependent behavior and multiple relaxation processes suggest potential applications in display technologies and electronic devices where precise control of electrical properties is essential.

## Ethics

There are no ethical issues after the publication of this manuscript.

## References

- [1]. Judele, R., Laschat, S., Baro, A., Nimtz, M. 2006. Gallic esters of 4,5-dinitrocatechol as potential building blocks for thermotropic liquid crystals. *Tetrahedron*; 62(41): 9681–9687.
- [2]. Chavda, V.P., Shah, K.N., Soni, S., Tripathi, M., Bhargava, S., Thakur, M., Parikh, P., Vora, L.K., Thakor, P., Makwana, M., Kapadia, N. 2023. Lyotropic liquid crystalline phases: Drug delivery and biomedical applications. *International Journal of Pharmaceutics*; 647: 123546.
- [3]. Takikawa, Y., Kaneko, K., Odani, S., Ikemura, T., Iwata, M. 2020. Dielectric anisotropy in PCPB/MBBA mixtures showing the dual frequency characteristic. *Japanese Journal of Applied Physics*; 59(SD): SDD05.
- [4]. Sasani Ghamsari, M., Carlescu, I. (Eds.). 2020. *Liquid Crystals and Display Technology*. IntechOpen.
- [5]. Kamanina, N.V., Serov, S.V., Savinov, V.P., Uskoković, D.P. 2005. Self-organization and dynamic characteristics study of nanostructured liquid crystal compounds. *Solid State Phenomena*; 106: 145–148.
- [6]. Khoo, I.C., Chen, C.W., Ho, T.J. 2016. Observation of photorefractive effects in blue-phase liquid crystal containing fullerene-C<sub>60</sub>. *Optics Letters*; 41(1): 123.
- [7]. Kamanina, N.V., Serov, S.V., Savinov, V.P., Uskoković, D.P. 2010. Photorefractive and photoconductive features of the nanostructured materials. *International Journal of Modern Physics B*; 24(06n07): 695–702.
- [8]. Zhang, Y., Yao, F., Pei, Y., Sun, X. 2009. High-diffraction-efficiency holographic gratings in C60-doped nematics. *Applied Optics*; 48(33): 6506–6510.
- [9]. Okutan, M., San, S.E., Basaran, E., Yakuphanoglu, F. 2005. Determination of phase transition from nematic to isotropic state in carbon nano-balls doped nematic liquid crystals by electrical conductivity-dielectric measurements. *Physics Letters A*; 339(6): 461–465.
- [10]. Ibragimov, T.D. 2021. Effect of fullerenes C60 on dielectric relaxation, electric conductivity, and electro-optic properties of 4-cyano-4'-pentylbiphenyl. *Fullerenes, Nanotubes and Carbon Nanostructures*; 29(6): 457–463.
- [11]. Ibragimov, T.D. 2021. Influence of fullerenes C60 and single-walled carbon nanotubes on the Carr-Helfrich effect in nematic liquid crystal. *Optik*; 237: 166768.
- [12]. Lee, W., Wang, C.Y., Shih, Y.C. 2004. Effects of carbon nanosolids on the electro-optical properties of a twisted nematic liquid-crystal host. *Applied Physics Letters*; 85(4): 513–515.
- [13]. Okutan, M., San, S.E., Köysal, O., Şentürk, E. 2010. The electrical properties of a fullerene and C.I. Acid Red 2 (methyl red) doped E7 nematic liquid crystal. *Dyes and Pigments*; 84(3): 209–212.
- [14]. Ibragimov, T.D., Imamaliyev, A.R., Ganizade, G.F. 2020. The threshold voltage, dielectric and conductivity properties of C60-doped smectic A liquid crystal. *Fullerenes, Nanotubes and Carbon Nanostructures*; 28(6): 509–514.

- [15]. Demir, A., Musatat, A.B. 2024. Evaluation of industrial Poly(tert-butyl acrylate) insulated A p-channel organic field-effect transistor (PtBA-p-OFET). *Düzce Üniversitesi Bilim ve Teknoloji Dergisi*; 12(3): 1762–1770.
- [16]. Sheraw, C.D., Zhou, L., Huang, J.R., Gleskova, H., Wagner, S., Jackson, T.N. 2002. Organic thin-film transistor-driven polymer-dispersed liquid crystal displays on flexible polymeric substrates. *Applied Physics Letters*; 80(6): 1088–1090.
- [17]. Rogers, J.A., Bao, Z., Makhija, A., Feng, Y., Zhang, Y., Mahajan, A., Veroff, R., Jones, T., MacLean, J., Schlittler, R., Whitesides, G.M. 2001. Paper-like electronic displays: Large-area rubber-stamped plastic sheets of electronics and microencapsulated electrophoretic inks. *Proceedings of the National Academy of Sciences*; 98(9): 4835–4840.
- [18]. Musatat, A.B., Atahan, A., Aksu, M., Zengin, M. 2022. Employing of 2-Acetylpyridine based chalcone as  $Hg^{2+}$  sensing material: Experimental and theoretical examination. *Düzce University Journal of Science and Technology Research*; 10(4): 2133–2143.
- [19]. Mas-Torrent, M., Rovira, C. 2011. Role of molecular order and solid-state structure in organic field-effect transistors. *Chemical Reviews*; 111(8): 4833–4856.
- [20]. Walser, M.P., Kalb, W.L., Mathis, T., Batlogg, B. 2009. Low-voltage organic transistors and inverters with ultrathin fluoropolymer gate dielectric. *Applied Physics Letters*; 95(23): 233301.
- [21]. Fang, X., Wei, Z., Qi, L., Chen, J., Wang, C., Ge, L., Yan, F. 2021. Patterning liquid crystalline organic semiconductors via inkjet printing for high-performance transistor arrays and circuits. *Advanced Functional Materials*; 31(21): 2100237.
- [22]. Gencel, O., Musatat, A.B., Demir, A., Tozluoğlu, A., Tutuş, A., Kılı, A., Fidan, H., Çavuş, K.F. Transforming industrial byproduct to eco-friendly functional material: Ground-granulated blast furnace slag reinforced paper for renewable energy storage. *Science of the Total Environment*; 176616.
- [23]. Kip, Ş., Gegin, K., Demir, A., Köysal, O., Öztürk, S., Kösemen, A. 2023. The novel n-channel liquid crystal organic field effect transistor (LC-n-OFET): A promising technology for low-power electronics. *Organic Electronics*; 106965.
- [24]. Katariya-Jain, A., Deshmukh, R.R. 2022. Effects of dye doping on electro-optical, thermo-electro-optical, and dielectric properties of polymer dispersed liquid crystal films. *Journal of Physics and Chemistry of Solids*; 160: 110363.
- [25]. Mi, X.D., Yang, D.K. 1998. Capillary filling of nematic liquid crystals. *Physical Review E*; 58(2): 1992–2000.
- [26]. Lueder, E. 2010. *Liquid Crystal Displays: Addressing Schemes and Electro-Optical Effects*. Wiley.
- [27]. Kocakulah, G. 2023. The role of rubrene concentration on dielectric parameters of nematic liquid crystal. *Hittite Journal of Science and Engineering*; 10(3): 193–199.
- [28]. Subaşı, A., Emiroğlu, M., Demir, A. 2023. Polarization and relaxation mechanisms in glass fiber-reinforced LED-cured polyester composites incorporating graphene nanotubes. *Materials Science and Engineering B*; 295: 116614.
- [29]. Demir, A., Köysal, O. 2016. Investigation of photo-induced change of electro-optical performance in a liquid crystal-organic field effect transistor (LC-OFET). *Philosophical Magazine*; 96(22): 2362–2371.



## A Morphological, Anatomical and Karyological Study on *Hieracium pannosum* BOISS. (Asteraceae)

Hakan Sepet<sup>1\*</sup> , Bahattin Bozdağ<sup>2</sup>  Canan Özdemir<sup>3</sup> 

<sup>1\*</sup> Kırşehir Ahi Evran University, Faculty of Engineering and Architecture,  
Department of Environmental Engineering, Kırşehir, Türkiye

<sup>2</sup> Menemen Anatolian High School Menemen-İzmir, Türkiye

<sup>3</sup> Manisa Celal Bayar University, Faculty of Arts and Sciences, Department of Biology, Manisa, Türkiye

\* [hakansepet@gmail.com](mailto:hakansepet@gmail.com)

\* Orcid No: 0000-0002-5841-9969

Received: 11 October, 2024

Accepted: 9 December, 2024

DOI: 10.18466/cbayarfbe.1565400

### Abstract

In this study *Hieracium pannosum* BOISS. morphological, anatomical and karyological features of the species were investigated. The samples were collected from Manisa Spil Mountain. The findings were compared with previous studies. We observed some changes in the morphological measurements of the species examined in the flora of Türkiye. In the anatomical studies, root stem and leaf characteristics of the species were determined. The body of the plant has a rounded shape in cross-section and contains 5-15 ordinary cortex layers. The body is self-parenchymatic. Palisate and sponge cells are similar in leaf mesophyll. The chromosome number of the species was determined as  $2n = 27$ . Also, karyograms and idiograms were made.

**Keywords:** Anatomy, *Hieracium pannosum*, Karyology, Morphology.

### 1. Introduction

The Asteraceae family, one of the richest families on earth, is the second largest family in the Turkish Flora with 1156 species, and the geographical origin of this family is accepted as South America in phylogenetic terms [1-2]. *Hieracium* L. is in the Lactuceae tribe of the Asteraceae family and has more than 1000 species [3]. It is represented in Turkey with about 102 taxa [2-4]. This genus is distributed in mountainous areas all over the world [5]. *Hieracium* ssp. is found among the plants found in the pastures of Europe and North America [6-11]. *Hieracium* taxon has a wide variety of habitats. This genus has different taxonomic characters used in the classification of apomictic taxa. Due to the intense hybridization in the *Hieracium* genus, many difficulties are encountered in taxonomic classification [12-14].

In this study, the chromosome numbers of 8 *Hieracium* species collected from Turkey were studied. Different chromosome numbers ranging from 18 to 36 were determined for the species examined [15].

There is no anatomical and morphological study on the species *Hieracium pannosum*. The aim of this study is to determine the morphological, anatomical and karyological features of these species and contribute to their introduction.

### 2. Material and Method

#### 2.1. Material

The plant samples in the study were collected from the following location where they naturally spread in Turkey.

B1 Manisa, Spil Mountain, At Alanı Location, 1520 m, 18.06.2012, Bozdağ 055 (Figure 1).

Some of the plant samples obtained in the field studies were dried using standard herbarium techniques to be used in morphological studies. The dried plant samples are currently stored in the Celal Bayar University herbarium. Species identifications of the studied samples were made using fresh and dry samples using the 5th volume of Davis (1975)'s "Flora of Turkey".

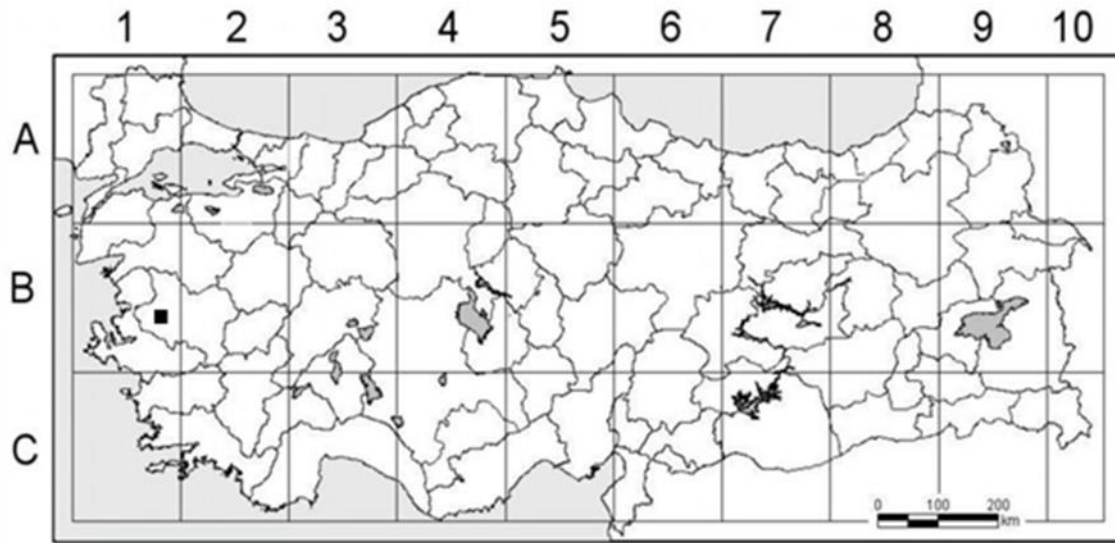


**Figure 1.** The Region Where the Species Examined Was Collected (Manisa, Spil Mountain)

## 2.2. Method

The parts taken from the roots, stems and leaves of the samples were stored in 70% alcohol. These samples were first passed through alcohol series in order. Then, the sections were taken from the paraffin blocks prepared with the parts taken from the roots, stems and leaves of this species for the studies [16] and these sections were stained with safranin and fast green dyes. Photographs were taken from the sections using a Leica DM3000 motorized microscope. The findings obtained are shown in figures and tables. The matured large seeds selected for karyological studies were left to germinate in petri dishes. 1-1.5 cm were cut from the root tips of the germinated seeds and exposed to the pretreatment agent ( $\alpha$ -monobromonaphtalene) for 16 hours. The root tips removed from the pretreatment agent were hydrolyzed in 1 N HCl at 60 °C for 3-6 minutes. The hydrolyzed root tips were stained in Feulgen dye for 1.5 hours. After the stained root tips were washed several times with tap water, samples prepared with the crushing preparation method were examined for chromosome examination [17]. Photographs were taken from these preparations with a Leica DM3000 motorized microscope. The chromosome samples obtained from the photographs were named according to the method developed by Levan et al. (1964) [18].

## 3. Findings

### 3.1. Morphological Findings

The stem can grow up to 15-60 cm. The plant carries numerous stellate and long covering hairs. The leaves are 5-8(-12) in size, 40-200x20-55 mm. The leaves are denser in the lower part of the stem and can sometimes form a false rosette structure. The leaves are oblanceolate-oblong or obovate, usually obtuse, sometimes mucronate. They have entire or few small toothed structures. The leaves narrow towards the base and are attached to the stem more or less amplexally. The leaves are lanceolate with long plumose types. Capitula are 1-4 in number.

Peduncles extend up to 30 cm. They have 1-3 linear bracts. They have dense stellate and numerous long plumose hairs. The involucre is 13-20 mm in diameter. Phyllaries are narrowly linear-lanceolate, with a more or less acute apex and numerous stellate hairs. Phyllaries have small scattered yellowish glandular hairs, dense long plumose hairs. Ligules are globrous. Styles are yellow. Achenes are yellowish-brown and 3.5-4.5 mm in size. Flowering occurs in 6-9 months. It can usually be found among calcareous rocks, sometimes in stony areas or in open areas of forests. Its distribution is between 1000-2700 m (Figure 2).





**Figure 2.** A view from the natural habitat of the *H. pannosum* species.

### 3.2. Anatomical Findings

#### 3.2.1 Root

At the outermost part of the root cross-section, there is a peridermis layer with fragmented cells and a cortex parenchyma consisting of 15-25 cell rows underneath. While the cell boundaries of these cells are clear in the young root cross-section, their walls are fragmented in the old root cross-section. In the young root, the endodermis layer immediately covering the vascular bundles is clear. In the root cross-section, the phloem cells have lost their integrity because their walls are fragmented. In the vascular tissue located in the central cylinder, the phloem layer covers a very small area. In contrast, xylem elements fill almost the entire center. In the old root of the plant, cambium cells can be seen here and there between the phloem and xylem elements (Figure 3, Table 1).

#### 3.2.2 Stem

On the outermost part of the cross-section taken from the stem, there is a thin cuticle layer covered with a single row of epidermis cells, the widths of which are larger than their lengths. Just below the epidermis layer, there is a cortex parenchyma with cells that cover a very wide area and are larger than their lengths. In the vascular bundles, phloem cells are covered by

sclerenchyma cells with thickened walls. Phloem cells cover a narrow area and their walls are fragmented. In the perennial stem, 1-2 rows of cambium cells can be distinguished between the vascular bundles. In the cross-section of the stem, the pith region covers a very wide area. The cells here are round-shaped and their diameters increase as they approach the center (Figure 4, Table 1).

#### 3.2.3 Leaf

In the cross-section taken from the leaf, the cuticle width on the abaxial side is wider than on the adaxial side. There are two rows of epidermis cells on both sides of the leaf, the widths of which are larger than their lengths. The width and length of adaxial epidermis cells are larger than abaxial epidermis cells. There are stomata cells and dense covering hairs arranged at certain intervals on both surfaces of the leaf. The cells forming the mesophyll layer have shapes close to round. In the leaf mesophyll layer, the cells forming the palisade parenchyma and the cells forming the sponge parenchyma cannot be easily distinguished from each other. The width and length of epidermis cells are often larger than the dimensions of the cells forming the mesophyll layer. Sclerenchyma cells cover the phloem cells in the vascular bundles (Figure 5, Table 1).

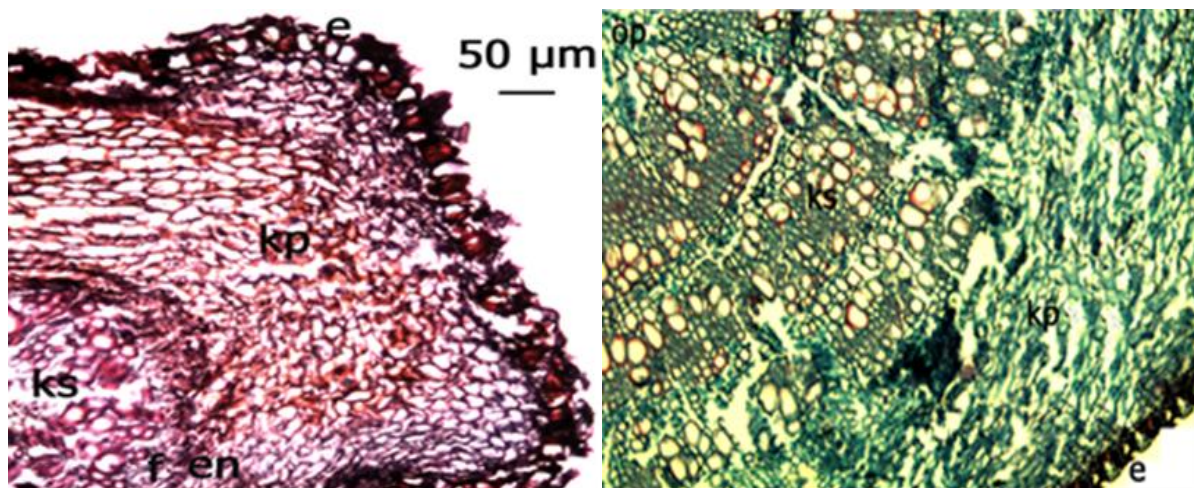


**Figure 3.** Anatomical sections of *H. pannosum* species A- young root, B- old root e. Epidermis end. Endodermis end. Peridermis end. Cortex parenchyma end. Xylem end. Sclerenchyma cells.

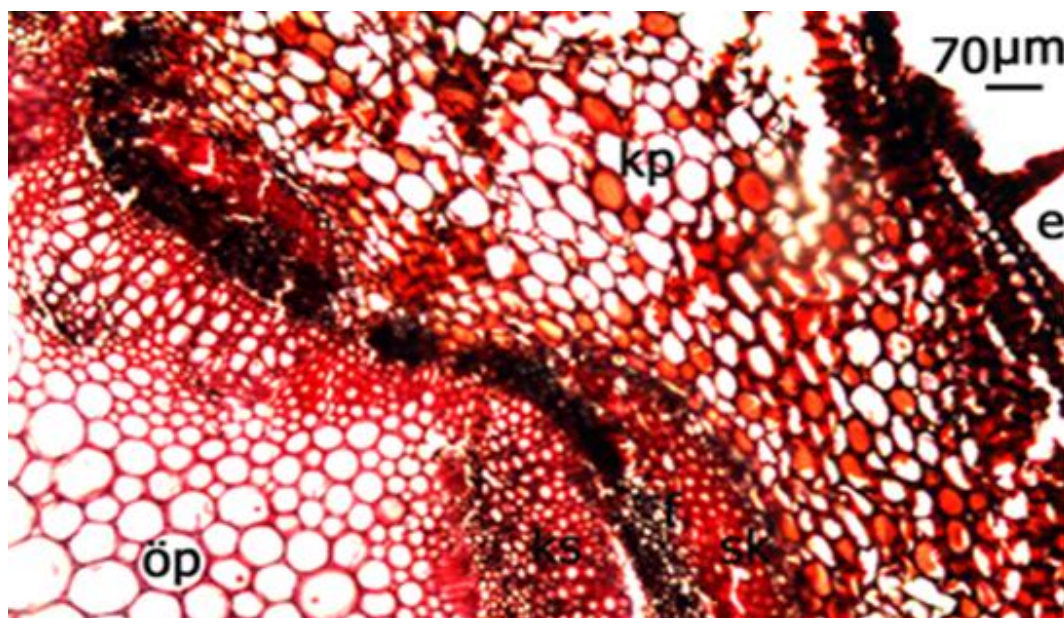


**Figure 4.** *H. pannosum* Stem cross-section, e. Epidermis, k. pith parenchyma, kp. Cortex parenchyma, sk. Sclerenchyma cells, f. Phloem, ks. Xylem.



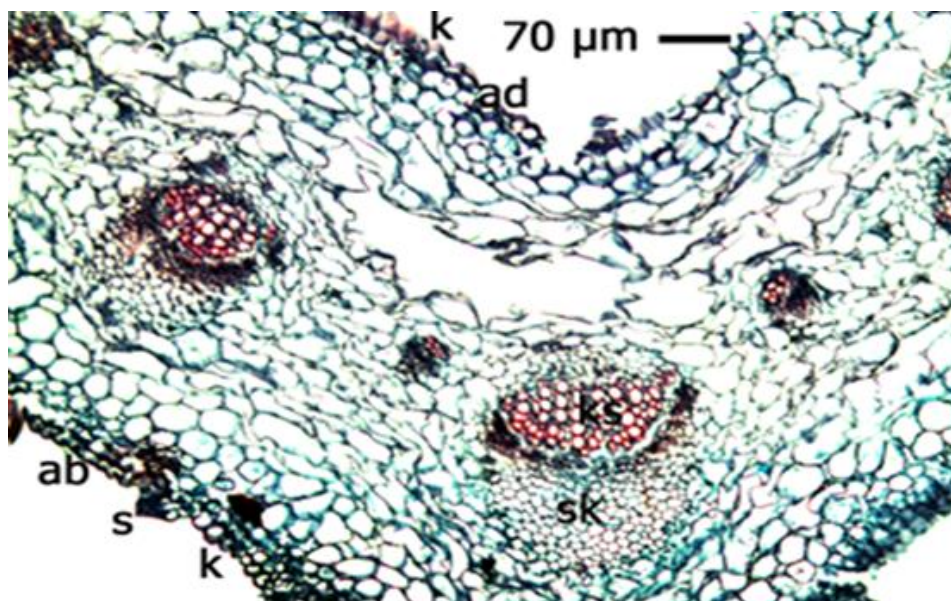


**Figure 5.** Leaf cross-section k. Cuticle, s. Stoma, ad. Adaxial epidermis, ab. Abaxial epidermis e. Epidermis, kiss. Pith parenchyma, ks. Xylem.

**Table 1.** Anatomical measurements of various parts of the species *H. Pannosum*

	width				height			
	Min	-	Max	Average	Min	-	Max	Average
	(µm)		(µm)		(µm)		(µm)	
<b>Root</b>								
Epidermis	12.25	-	40.00	24.13	16.25	-	30	22.63
Cortex parenchyma	30.00	-	47.50	37.25	11.25	-	22.50	16.63
Trachea (diameter)	15.00	-	40.00	28.50				
<b>Stem</b>								
Cuticle					2.50	-	6.25	3.50
Epidermis	10.00	-	20.00	15.88	11.25	-	22.50	17.75
Cortex parenchyma	25.00	-	62.50	40.25	15.00	-	43.75	30.75
Trachea (diameter)	12.50	-	30.00	21.00				
Spongy parenchyma	27.50	-	125.00	64.50				
<b>Leaf</b>								
Adaxial cuticle					1.25	-	5.00	2.94
Adaxial epidermis	16.25	-	32.50	21.88	15.00	-	25.00	20.50
Mesophyll cells	25.00	-	67.50	34.50	22.50	-	52.50	43.38
Trachea (diameter)	10.25	-	24.75	19.63				
Bundle sheath cells (diameter)	10.00	-	25.00	18.63				
Abaxial epidermis	12.50	-	21.25	18.13	12.50	-	22.50	15.38
Abaxial cuticle					1.88	-	5.00	3.25

S.D\*. Standard deviation

### 3.3.Kariological Findings

**Table 2.** Measurements of mitotic metaphase chromosomes of *H. pannosum* species.

Chromosome no	Total chromosome length (C) $\mu\text{m}$	Long arm length (L) $\mu\text{m}$	Short arm length (S) $\mu\text{m}$	Arm ratio R: L/S	Centromeric index I: (S/C). 100 $\mu\text{m}$	Centromeric position S.D	Satellite
1	8.79	5.08	3.71	1.37	42.20	m	-
2	8.14	5.17	2.97	1.74	36.48	sm	-
3	7.86	4.90	2.96	1.65	37.66	m	-
4	7.68	4.62	3.06	1.51	39.84	m	-
5	7.12	4.80	2.32	2.06	32.58	sm	-
6	7.02	4.60	2.42	1.90	34.47	sm	-
7	6.94	4.24	2.70	1.57	38.90	m	-
8	6.48	4.44	2.04	2.17	31.48	sm	-
9	6.48	4.16	2.32	1.79	35.80	sm	-
10	6.48	3.88	2.60	1.49	40.12	m	-
11	6.22	4.07	2.15	1.89	34.56	sm	-
12	6.02	3.70	2.32	1.59	38.53	m	-
13	5.85	3.51	2.34	1.50	40.00	m	-
14	5.85	3.51	2.34	1.50	40.00	m	-
15	5.28	3.50	1.78	1.96	33.71	sm	-
16	5.28	3.43	1.85	1.85	35.03	sm	-
17	5.18	3.24	1.94	1.67	37.45	m	-
18	4.90	2.96	1.94	1.52	39.59	m	-
19	4.90	2.22	1.35	1.64	27.55	m	1.33
20	4.81	2.96	1.85	1.60	38.46	m	-
21	4.81	2.13	1.39	1.53	28.89	m	1.29
22	4.72	3.05	1.67	1.82	35.38	sm	-
23	4.63	2.77	1.86	1.49	40.17	m	-
24	4.35	2.59	1.76	1.47	40.46	m	-
25	4.26	2.59	1.67	1.55	39.20	m	-
26	4.16	2.59	1.57	1.65	37.74	m	-
27	3.79	2.31	1.48	1.56	39.05	m	-

The chromosome number of the species was determined as  $2n=3x=27$ . In the karyotype analysis, submedian centromeres were determined in 9 chromosomes and median centromeres in 18 chromosomes. Satellites were observed in the 19th and 21st chromosomes. When the chromosomes of the species were examined, the largest

chromosome was  $8.79 \mu\text{m}$  and the smallest chromosome was  $3.79 \mu\text{m}$ . The longest arm was  $5.17 \mu\text{m}$  and the shortest arm was  $1.35 \mu\text{m}$ . The total chromosome length was  $158 \mu\text{m}$ . (Table 2, Figure 6, Figure 7)

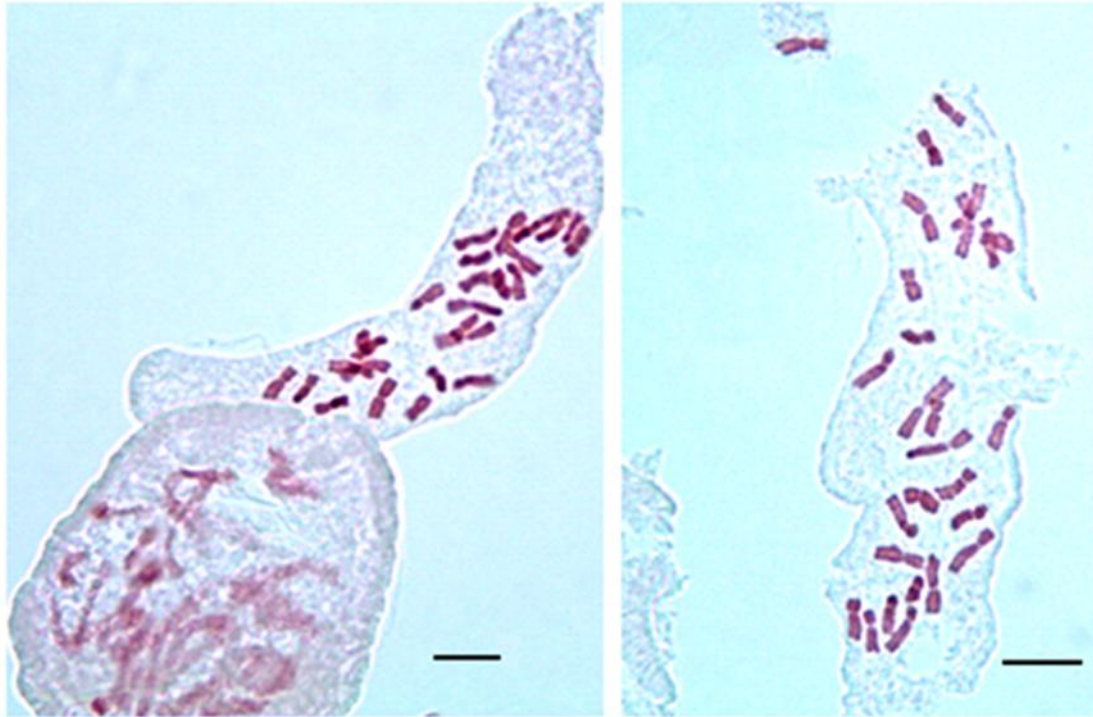


**Figure 6.** Somatic metaphase image of *H. pannosum* species (Scale  $10\mu\text{m}$ )



**Figure 7.** Idiogram of *H. pannosum* species



#### 4. Discussion and Conclusion

In this study, the anatomical, morphological and karyological structure of the *H. pannosum* species, which is included in the Asteraceae family, was examined and it was aimed to contribute to the introduction of the species.

There are dense covering hairs on the above-ground parts of the species. The phyllaries in the capitulum are in 4-7 rows and are arranged in an imbricate manner. The tips of the ligular flowers are indented and protruding in a sawtooth-like manner. The leaves are located at the base in the form of a rosette in most samples. The flower stalk also serves as a stem.

In anatomical examinations, the cortex parenchyma covers a very large area in the root of the species. Typical radial conduction tissue is evident in the young root. In the old root, xylem is evident in the conduction tissue and endodermis cells have disappeared. There is a wide pith region in the stem and the walls of the cells are thin and their diameters increase as they approach the conduction bundles. When old stems are examined, it is seen that xylem elements occupy a large space in the vascular bundles, phloem elements remain in a narrow area, and they are covered by sclerenchyma cells with thickened walls. It has been observed that the vascular bundles in the main vein of the leaves are larger. As we approach the leaf tips, it is seen that the vascular bundles are arranged at certain intervals. The length of the cuticle layer on the abaxial side of the leaf is larger than on the adaxial side. The width and length of the adaxial epidermis cells are larger than the width and length of the epidermis cells on the abaxial side. The distinction between palisade parenchyma and sponge parenchyma in the mesophyll layer is not clear. Mesophyll cells are generally round in shape.

The chromosome basic number in *Hieracium* species was determined as  $n = 9$ . There is also a lot of polyploidy in these species [15,19-20].

A study published in 2011 gave the chromosome numbers of *Hieracium* and *Pilosella* species distributed in Southeastern and Central Europe. In this study, the chromosome number of *H. pannosum* was determined as  $2n=3x=27$  [21].

A study published in 2010 examined the *Hieracium renatae* species and stated that these species can live especially at altitudes of 2400-2520 m [22]. Materials belonging to the *H. pannosum* species were collected from an altitude of approximately 1250 m.

In a study conducted in Pakistan in 2009, it was stated that *Hieracium bichlorophyllum* (Druce & Zahn) Pugsley, *Hieracium diaphanoides* Lindeb., *Hieracium*

*umbellatum* L., *Hieracium virosum* Pallas and *Hieracium vulgatum* Fr. species have dense hairy stems and bifacial leaves [6]. The *H. pannosum* species examined in this study also has dense hairy stems and leaves. The distinction between palisade parenchyma and sponge parenchyma in the leaves of the species is not clear. *H. pannosum* species has morphological, anatomical and karyological similarities to other *Hieracium* species. It is thought that morphological, anatomical and karyological studies will help in the scientific recognition of this species.

#### References

- [1].Bremer, K. 1994. Asteraceae: Cladistics & Classification. *Timber Press, Oregon*. USA 10 (2):295-304
- [2].Davis, P.H. 1975. Flora of Turkey and the East Aegean Islands. *Edinburgh Univ. Press*, Edinburgh, Vol. 5.
- [3].Petrović SD, Gorunoviā MS, Wray V, Merfort I. 1999. A taraxasterol derivative and phenolic compounds from *Hieracium gymnocephalum*. *Phytochemistry*. 50 (2): 293-296.
- [4].Ekim, T. Koyuncu, M. Vural, M. Duman, H. Aytaç, Z. Adıgüzel, N. 2000. Türkiye Bitkileri Kırmızı Kitabı (Red Data Book of Turkish Plants). *Türkiye tabiatını Koruma derneği*, Ankara.
- [5]. Gottschlich G (1996) Tolpis/Hieracium. In: Sebald O, Seybold S, Philippi G & Wörz A (Hrsg.): Die Farn- und Blütenpflanzen Baden-Württembergs. Band 6: Spezieller Teil (Spermatophyta, Unterklasse Asteridae) Valerianaceae bis Asteraceae, pp 300-302, 393-535. *Eugen Ulmer*, Stuttgart
- [6].Qureshi, S.J. Khan, M.A. Arshad, M. Rashid, A. Ahmad, M. and Zafar, M. 2009. Morphological, palynological, and anatomical investigations of *Hieracium* L. (Lactuceae, Asteraceae) in Pakistan. *Métodos en Ecología y Sistemática* Vol. 4(3): 1-22
- [7].Hunter, G.G. 1991. Distribution of hawkweeds (*Hieracium* spp.) in the South Island, indicating problem status. Review. *Journal of the N.Z. Mountain Lands Institute* 48: 21- 31.
- [8].Rose, A.B. Basher, L.R. Wiser, S.K. Platt, K.H. Lynn, I.H. 1998. Factors predisposing short-tussock grasslands to *Hieracium* invasion in Marlborough, New Zealand. *NZ J Ecol.* 22 (2): 121-140.
- [9].Birdsall, J. and Quimby, P.C. 1996. Hawkweeds. In: Rees, N. et al. (Eds.), Biological Control of Weeds in the West. Western Society of Weed Science in Cooperation with USDA Agricultural Research Service. *Montana Department of Agriculture and Montana State University*, Bozeman.
- [10].Fernald, M.L. 1950. Gray's Manual of Botany. A Handbook of the Flowering Plants and Ferns of the Central and Northeastern United States and Adjacent Canada, Eighth (Centennial) Edition Illustrated, *American Book Company*, New York.
- [11].Wilson, L.M. Callihan, R.H. 1999. Meadow and orange hawkweed. In: Sheley, R.L., Petroff, J.K. (eds.), Biology and Management of Noxious Rangeland Weeds. *Oregon State University Press*. Corvallis, 238-248.
- [12].Gustaffson, A. 1946., 1947. Apomixis in higher plants I-III. *Acta Univ. Lund*. N.S. 42 (3): 1-67; 43 (2): 69-179; 43 (12):181-371
- [13].Merxmüller, H. 1975. Diploide Hieracien. *Anales Inst. Bot. Cavanilles* 32 (2): 189-196.
- [14].Asker, S.E. and Jerling, L. 1992. Apomixis in plants. *CRC Press, Boca Raton, etc.*

- [15].Hayirlioglu-Ayaz, S. and İnceer, H. 2004. Chromosome Numbers Of Some Species Of The Genus *Hieracium* S.STR. (Asteraceae) From Turkey. *Folia Geobotanica* 39 (3): 319-325
- [16].Algan, G. 1981. Microtechnics for the Plant Tissues. *Publication of Fırat Univ. Science & Art Faculty, Number 1*, İstanbul
- [17].Elçi, Ş. 1994. Sitogenetikte Araştırma Yöntemleri ve Gözlemler. 100. Yıl Üniversitesi Yayınları. No: 18 *Fen Edebiyat Fak. Yayın* No: 16. Van.
- [18].Levan, A. Fredga, M. and Sandberg, A. 1964. Nomenclature for centromeric position on chromosomes *Hereditas*, 52 (2): 201-220.
- [19].Chrtek, jun J., Mrfız P., Zahradnicek, J., Mateo, G. and Szelag, Z. 2007. Chromosome Numbers and DNA Ploidy Levels Of Selected Species Of *Hieracium* S.Str. (Asteraceae") *Folia Geobotanica* 42 (4): 411-430
- [20].Niketic, M. Vladimirov, V. and Mraz, P. 2006. Chromosome numbers and taxonomic-chorological notes on selected species of *Hieracium* s.str. (Asteraceae) from Montenegro. *Phytol. Balc.* 12 (1): 85-97
- [21].Ilnicki, T., & Szelag, Z. (2011). Chromosome numbers in *Hieracium* and *Pilosella* (Asteraceae) from central and southeastern Europe. *Acta Biologica Cracoviensia. Series Botanica*, 53(1).
- [22].Zbigniew, S. 2010. *Hieracia balcanica* V.A new diploid species in *Hieracium* sect. *Naegeliania* (Asteraceae) from Macedonia. *Ann. Bot. Fennici* 47 (4): 315-319

# A New Distribution Area of the Endangered Endemic *Linum vuralianum* (Linaceae) in Türkiye

Dilek Oskay<sup>1\*</sup> 

<sup>1\*</sup>Manisa Celal Bayar University, Faculty of Engineering and Natural Sciences, Department of Biology, Section of Botany, Manisa, Türkiye

\* [dilek.oskay@cbu.edu.tr](mailto:dilek.oskay@cbu.edu.tr)

\* Orcid No: 0000-0002-5318-4750

Received: 14 October, 2024

Accepted: 25 December, 2024

DOI: 10.18466/cbayarfbe.1567122

## Abstract

*Linum vuralianum* Yılmaz & Kaynak (Linaceae) is an endemic species described in 2008, known from only two localities (Emet-Kütahya and Pelitözü-Bilecik) in Türkiye. According to the distribution area and population data, the threat category of the IUCN has been recommended as “EN” by the authors of the species. It has been determined that the species has a new distribution area in Çamlıca Mountain, Soma-Manisa with this study. It has been determined that *Linum vuralianum* is distributed in open forest places at about 1000 m altitude on the north-western view of Çamlıca Mountain. According to the observations made during the field study, it was concluded that the threat category of the species should be protected in the same way.

**Keywords:** Distribution, Endemic, *Linum vuralianum*, Manisa, Türkiye

## 1. Introduction

*Linum* is a large genus containing about 200 species worldwide belonging to the family Linaceae. The genus *Linum* is distributed in the Mediterranean basin, the southwest and north of America, and the temperate and subtropical regions of Asia [1]. The main distribution area of the genus *Linum* is the North American continent, the Balkan Peninsula and Anatolia [2, 3].

The first revision of *Linum* species in Türkiye and the East Aegean Islands was made by Davis who recognised 49 taxa [4]. Since then with the new taxa identified, added as a new record to the flora and with new combination the *Linum* taxa in Türkiye has been reached to 55, 26 of which are endemic [4-14].

The fact that 75 species in the Mediterranean basin represent the genus *Linum* [15] that the number of taxa in Anatolia has reached 55 with the newly added species and that the endemism rate (47%) is high [14] indicates that Anatolia may be one of the gene centres of this genus.

With many taxonomic studies conducted in our country in recent years, new data have begun to be obtained regarding the situation of endemic and rare taxa in nature [16-25].

In studies conducted on species whose new distribution areas have been identified, their descriptions are renewed, maps showing the distribution areas of taxa are updated, and existing danger categories are re-evaluated according to the new observations obtained.

With this study, it has been revealed that the endemic *Linum vuralianum* Yılmaz & Kaynak, known from only two localities in Türkiye, has a new distribution area [9].

## 2. Materials and Methods

It has been collected *Linum* samples while conducting fieldwork in Çamlıca Mountain in June 2024 (39°03'55.64"N 27°33'38.46"E).

The specimens were checked against the Flora of Turkey [4], taxonomical investigations of *Linum* species in Türkiye [26-30] and the latest identified new *Linum* taxa.

As a result of the examinations, it was understood that the collected species was *Linum vuralianum* Yılmaz & Kaynak, an endemic species that was identified in 2008 and is known only from two localities (Kütahya-Emet and Bilecik-Pelitözü) in Türkiye.



The description of the species is given based on measurements made on samples collected from its new distribution area. Then, photographs of the species taken during field studies and a map showing the current distribution have been added.

The assessment regarding the IUCN threat category was made by taking into consideration the number of individuals in the new distribution area of *L. vuralianum* and its situation in its natural environment during field studies [31].

### 3. Results

#### 3.1. Description

Plants annual or biennial (Figure 1). Flowering stems erect, 15–66 cm, with scabrid ridges and persistent basal rosettes. Rosette leaves dense, spatulate, petiolate, 15–30 x 6–10 mm. Lower cauline leaves narrowly oblanceolate-spathulate, acute 15–60 x 6–13 mm, Uppermost cauline leaves narrowly oblanceolate or linear, acute, 17–55 x 2.5–10 mm, one- (to three-) nerved, with stipular glands at base.



**Figure 1.** Habit of *Linum vuralianum*.

Inflorescence many flowered. Flowers heterostylous. Sepals lanceolate or narrowly ovate, acuminate, 10–12 x 2–2.5 mm, keeled, with narrow membranous glandular ciliate margins. Petals yellow, obovate, 17–26 x 5–8 mm, acute or obtuse (Figure 2). Filament equal, 5–11 mm,

united at base into a short tube, 1 mm; anthers, oblong, 3 mm; staminode, 1 mm. Styles in short-styled flowers c. 4 mm in long-styled flowers c. 7 mm and united in the middle, stigma linear. Capsule spherical, 3–5 mm, seeds oblong, 3–3.5 x 1.5–2 mm, brown.





**Figure 2.** *Linum vuralianum* in population of Çamlıca Mountain (Soma/Manisa).

### 3.2. Flowering, Habitat and Distribution

It grows in the open places forest of *Pinus nigra* at an altitude of 700–1050 m, on the north-western view of Çamlıca Mountain.

Flowering is in June. It is distributed in a limited area at Çamlıca Mountain approximately a total number of 200 individuals but the population density is in good condition.

### 3.3. Conservation status

According to the distribution area and population data (two different localities, a distribution area of 5000 km<sup>2</sup>

and about a total of 300 individuals in two populations), the threat category of the IUCN has been recommended as “EN” (criterion B1a) by the authors of the species [9].

It has been determined that the species has a new distribution area in Çamlıca Mountain, Manisa-Soma district with this study (Figure 3). Although the distribution area of the taxon has expanded with the discovery of a new distribution area for *L. vuralianum*, the number of individuals in the population and when the previous data are evaluated together, it was concluded that the threat category of the species should be protected in the same way.

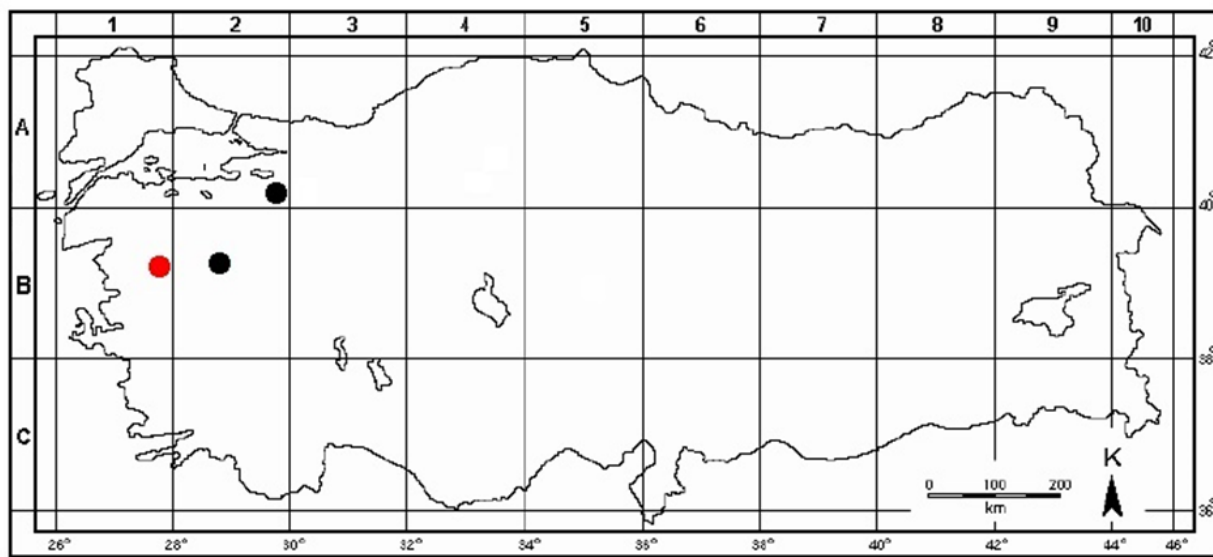


**Figure 3.** Current distribution map of *Linum vuralianum* (●); New distribution area (Manisa-Soma), (●); Other known distribution areas (Kütahya-Emet and Bilecik-Yenişehir, respectively).

### 4. Discussion

*Linum* is represented by five sections in Türkiye. *L. vuralianum* is an annual or biennial taxon in the *Linum* section *Syllinum* [32]. The others, except one (*Linum nodiflorum* L.), are perennials.

*Linum* section *Syllinum* is characterized by having keeled or striated stems (keels smooth or papillose hairy), leaves usually having stipules at the base, and petals being yellow or rarely white and fused at the base.

Some taxa such as *L. vuralianum*, carry rosette leaves at the base of their flowering stems. The flowers are mostly heterostylous. Sepals are distinctly veined, keeled, membranous and glabrous. Sepals are longer than capsules.

Section *Syllinum*, is rich in terms of the number of endemic taxa for Türkiye, together with the newly added

taxa (17 out of 22 taxa are endemic) [6, 8, 14, 26]. Almost all of the endemic taxa are narrowly distributed, endangered or vulnerable species [26].

Therefore, it is very pleasing to find a new distribution area for any species that is endangered and has localized distribution areas.

When we compare morphological measurements of characters in different populations, it can be said that there are slightly larger individuals in the Manisa population (Table 1.).

According to morphological measurements, the fact that individuals in the Çamlıca population are slightly larger is probably due to environmental factors.

Considering the common parameters such as the lack of long distances between their distribution areas, their closeness in terms of latitude, and their presence at



similar elevations, it is thought that the determining factor may be soil. The accuracy of this inference will of course be possible by comparing soil samples taken from the distribution areas of different populations.

**Table 1.** Comparison of morphological measurements of characters in different populations.

<i>Linum vuralianum</i>	Kütahya and Bilecik Populations (Yılmaz & Kaynak 2008)	Manisa Population (In this study)
<b>Plant height</b>	15–60 cm	15–66 cm
<b>Basal leaves</b>	15–30 × 6–10 mm	15–45 × 6–14 mm
<b>Lower cauline leaves</b>	20–45 × 3–6 mm	15–70 × 6–13 mm
<b>Uppermost cauline leaves</b>	15–35 × 2–6 mm	17–55 × 2.5–10 mm
<b>Sepals</b>	7–10 × 2–2.5 mm	7–12 × 2–2.5 mm
<b>Petals</b>	18–22 × 8–11 mm	17–26 × 5–8 mm
<b>Capsule</b>	3–5 mm	4–5 mm
<b>Seeds</b>	2.5– 3 × 1–1.5 mm	3–3.5 × 1.5–2 mm

## 5. Conclusion

The discovery of a new distribution area of the endangered endemic species is a pleasant event. When looking at studies on the flora of any province in Türkiye, it is exciting how many new areas there are to be discovered. It is clear that in the long term, a large information pool will be formed where the complete flora of Türkiye and the distribution of taxa are supported by more data.

Studies on the newly discovered distribution areas of taxa are quite necessary and valuable from this perspective.

## Ethics

There are no ethical issues after the publication of this manuscript.

## References

- [1]. Mabberley, DJ. The plant book: a portable dictionary of the higher plants; Cambridge University Press: Cambridge, United Kingdom, 2002; pp 858.
- [2]. Davis, PH. 1957. Materials for a flora of Turkey: II. *Linum* Linn. *Notes Royal Botanic Garden Edinburgh*; 22: 135-161.
- [3]. Robertson, KR. 1971. The Linaceae in the Southeastern United States. *Journal of the Arnold Arboretum*; 52: 649-665.
- [4]. Davis, PH. *Linum* L. In: Davis PH (ed) Flora of Turkey and the East Aegean Islands, Vol. 2. Edinburgh University Press, Edinburgh, 1967, pp 425–450.
- [5]. Güner, A, Vural, M, Duman, H, Dönmez, A, Şağban, H. 1996. The Flora of the Köyceğiz-Dalyan specially protected area (Muğla-Turkey). *Doğa Türk Biyoloji Dergisi*; 20: 329-371.
- [6]. Yılmaz, Ö, Kaynak, G, Vural, M. 2003. A new taxon of *Linum* (Linaceae) from Northwest Anatolia, Turkey. *Annales Botanici Fennici*; 40: 147–150.
- [7]. Yılmaz, Ö, Kaynak, G. 2006a. *Linum hirsutum* subsp. *platyphyllum* stat. nova (Linaceae). *Annales Botanici Fennici*; 43(1): 62-63.
- [8]. Yılmaz, Ö, Kaynak, G. 2006b. New combination in *Linum* sect. *Syllinum* (Linaceae). *Annales Botanici Fennici*; 43(1): 77-79.
- [9]. Yılmaz, Ö, Kaynak, AG. 2008a. A new species of *Linum* (Linaceae) from west Anatolia, Turkey. *Botanical Journal of The Linnean Society*; 156, 459–462.
- [10]. Yılmaz, Ö, Kaynak, G. 2010. A new taxon of *Linum* (Linaceae) from Southwest Anatolia, Turkey. *Novon: A Journal for Botanical Nomenclature*; 20(4): 507-511.
- [11]. Yılmaz, Ö. 2010. *Linum kaynakiae* sp. nov. (sect. *Syllinum*, Linaceae) from Turkey. *Nordic Journal of Botany*; 28(5): 605-612.
- [12]. Tugay, O, Bağcı, Y, Uysal, T. 2010. *Linum ertugrui* (Linaceae), a new species from Central Anatolia, Turkey. *Annales Botanici Fennici*; 47(2): 135-138.
- [13]. Yılmaz, Ö. 2018. *Linum ayliniae* (Linaceae), a new species from West Anatolia, Turkey. *Novon: A Journal for Botanical Nomenclature*; 26: 174-179.
- [14]. Tugay, O, Ulukuş, D. 2019. *Linum aksehirense* (sect. *Dasylinum*, Linaceae), a new species from Central Anatolia (Turkey). *PhytoKeys*; 136: 23-34.
- [15]. Greuter, W, Burdet, HM, Long, G. Med-Checklist 4, Dicotyledones (Lauraceae-Rhamnaceae). Organization for the Phyto-Taxonomic Investigation of the Mediterranean Area (OPTIMA). Geneva, 1989; pp 357.
- [16]. Sönmez, S. 2000. Sarı Çiçekli Orman gülünün (*Rhododendron luteum*) Batı Anadolu'da (Balıkesir-Burhaniye) yeni bir yayılış alanı. *Balıkesir Üniversitesi Sosyal Bilimler Enstitüsü Dergisi*; 3(4): 42-52.
- [17]. Özusu, E, Öztekin, M. 2008. A new localization for *Teucrium paederotoides* Boiss. et. Hausskn. (Lamiaceae). *Biodicon*; 1(2): 86-90.

- [18]. Ok, T, Aşar, MD. 2009. New distribution areas of Kadıncık shrub *Flueggea Anatolia* Gemici determined in the Andırın region, Kahramanmaraş/Turkey. *Biological Diversity and Conservation*; 2(1): 65-70.
- [19]. Senol, SG, Yildirim, H. 2010. A new distribution area of *Asperula daphneola* (Rubiaceae) in Western Turkey and its new recommended IUCN threat category. *Biological Diversity and Conservation*; 3(2): 123-127.
- [20]. Yıldırım, H, Şenol, SG. 2010. A new distribution area of *Scorzonera argyria* Boiss.(Asteraceae) and contribution of its morphological characters. *Biological Diversity and Conservation*; 3(3): 6-9.
- [21]. Aydınöz, D., Çoban, A., & Tunç, H. Tüylü Meşe'nin (*Quercus pubescens*) Türkiye'de yeni bir yayılış alanı: Elmalı Dağı (Kayseri). *Doğu Coğrafya Dergisi*; 22(37): 83-98.
- [22]. Güzel, ME, Gültepe, M, Coşkunçelebi, K, Makbul, S. 2019. Endemik *Lactuca boissieri* Rouy (Kocamarul) için yeni ve muhtemel yayılış alanları. *Bağbahçe Bilim Dergisi*; 6(2): 25-31.
- [23]. Yılmaz, Ö, Yılmaz, A, Kaynak, G. 2019. Yerel endemik *Erodium somanum* H. Peşmen (Geraniaceae) için Kadriye (Bursa) çevresinden yeni bir yayılış alanı. *Eskişehir Teknik Üniversitesi Bilim ve Teknoloji Dergisi C- Yaşam Bilimleri ve Biyoteknoloji*; 8(1): 1-5.
- [24]. Semiz, G, Yılmaz, Ö. 2020. Türkiye'de nadir yayılışı olan *Linum punctatum* Presl subsp. *pyncophyllum* (Boiss. & Heldr.) Gustavsson (Benliketen) için yeni bir yayılış alanı. *Bağbahçe Bilim Dergisi*; 7(2): 29-33.
- [25]. Akbaş, K, Topçuoğlu, B, Yildirim, H. 2021. Two new distribution areas at amazing altitudes for *Sternbergia candida* which is locally endemic at subalpine zone in Turkey and its updated IUCN category. *Acta Biologica Turcica*; 34(4), 169-176.
- [26]. Yılmaz, Ö. 2009. Türkiye'deki *Linum* L. (Linaceae) Türleri Üzerinde Taksonomik Araştırmalar. Doktora tezi. T.C. Uludağ Üniversitesi Fen Bilimleri Enstitüsü, Biyoloji Anabilim Dalı. Bursa.
- [27]. Özhatay, E. *Linum* L. In: Güner, A, Özhatay, N, Ekim, T, Baser, KHC, (eds) *Flora of Turkey and the East Aegean Islands*, Vol. 11 (Supplement). Edinburgh University Press, Edinburgh, 2000, pp 73.
- [28]. Yılmaz, Ö, Kaynak, G. 2008b. The check-list and chorology of the *Linum* L. (Linaceae) taxa in the flora of Turkey. *Journal of Biological and Environmental Sciences*; 2(5): 35-43.
- [29]. Yılmaz, Ö, Kaynak, G. 2008c. New combination in *Linum* sect. *Dasylinum* (Linaceae). *Journal of Biological and Environmental Sciences*; 2(4): 5-9.
- [30]. Güner, A, Aslan, S, Ekim, T, Vural, M, Babaç, MT. Türkiye Bitkileri Listesi (Damarlı Bitkiler). Nezahat Gökyiğit Bahçesi ve Flora Araştırmaları Derneği Yayını, İstanbul, 2012.
- [31]. IUCN (2022) Guidelines for using the IUCN Red List Categories and Criteria. Version 15.1, July 2022. <https://www.iucnredlist.org/resources/redlistguidelines> (accessed 06 August 2024).
- [32]. Grisebach, AHR. *Spicilegium Florae Rumelicae et Bithynicae Exhibens Synopsis Plantarum quas in aest* (Vol. 1). Vieweg & Son, Brunsvigae, 1843, 407.



## Anderson Type Polyoxometalates Containing Vitamin B<sub>1</sub>

Hülya Avcı Özbek<sup>1\*</sup> 

<sup>1\*</sup> Department of Chemistry, Faculty of Engineering and Natural Sciences, Manisa Celal Bayar University, Manisa, Türkiye

\* [hulya.avci@cbu.edu.tr](mailto:hulya.avci@cbu.edu.tr)

\* Orcid No: 0000-0003-1508-2558

Received: 22 October, 2024

Accepted: 12 May, 2025

DOI: 10.18466/cbayarfbe.1570842

### Abstract

The novel vitamin B<sub>1</sub>-substituted polyoxomolybdates (C<sub>12</sub>H<sub>17</sub>N<sub>4</sub>OS)<sub>3</sub>[Co(III)Mo<sub>6</sub>O<sub>24</sub>H<sub>6</sub>]·7H<sub>2</sub>O (**1**) and (C<sub>12</sub>H<sub>17</sub>N<sub>4</sub>OS)<sub>4</sub>[Ni(II)Mo<sub>6</sub>O<sub>24</sub>H<sub>6</sub>]·7H<sub>2</sub>O (**2**) have been synthesized using (NH<sub>4</sub>)<sub>3</sub>[Co(III)Mo<sub>6</sub>O<sub>24</sub>H<sub>6</sub>]·7H<sub>2</sub>O and (NH<sub>4</sub>)<sub>4</sub>[Ni(II)Mo<sub>6</sub>O<sub>24</sub>H<sub>6</sub>]·7H<sub>2</sub>O respectively as a precursor for the in situ formation of the counter ion vitamin B<sub>1</sub> (C<sub>12</sub>H<sub>17</sub>N<sub>4</sub>OS)<sup>+</sup>. These compounds have been thoroughly characterized in the solid state FT-IR spectroscopy, powder X-ray diffraction (PXRD), TGA and elemental analysis.

**Keywords:** Cobalt, Molybdenum, Nickel, Polyoxometalate, Thiamine Hydrochloride, Vitamin B<sub>1</sub>

### 1. Introduction

Polyoxometalates (POMs) are a broad class of anionic clusters composed of high oxidation state metal ions linked by oxygen atoms in a variety of structures that can be divided into two main categories: isopolyanion and heteropolyanion. An isopolyanion consists of a single element bridged by oxygen atoms. A heteropolyanion incorporates functional heteroatoms (e.g., rare earths, transition metals and noble metals) to make the design of advanced functional materials more accessible and rational. Depending on their size, charge and composition, POM frameworks exhibit numerous different properties, opening up potential applications in diverse research areas, including catalysis, materials science, biological chemistry, photophysics, energy and medicine [1-15].

Within the POM family, transition metal substituted polyoxometalates are the largest group and the activities of these compounds are also widely studied in biological studies. For example, Golubeva and Ostroushko emphasised those containing vitamin B<sub>1</sub> in their POM studies with their groups [16-17]. In addition the interesting biological properties of Anderson-type POMs and their use in medicine have attracted the attention of scientists. Mahvash et al., reported the synthesis and characterization of Anderson type POMs and investigated their effects against breast cancer [18]. In the study of Ramezani-Aliakbari and co-workers, the effects of newly synthesised Anderson type POMs against breast

cancer were investigated [19-20]. Considering these data, it is important to investigate the interaction between POMs and drugs. Therefore in this study, vitamin B<sub>1</sub> (thiamine hydrochloride) was chosen as a model drug and two new Anderson type POMs (C<sub>12</sub>H<sub>17</sub>N<sub>4</sub>OS)<sub>3</sub>[Co(III)Mo<sub>6</sub>O<sub>24</sub>H<sub>6</sub>]·7H<sub>2</sub>O (**1**) and (C<sub>12</sub>H<sub>17</sub>N<sub>4</sub>OS)<sub>4</sub>[Ni(II)Mo<sub>6</sub>O<sub>24</sub>H<sub>6</sub>]·7H<sub>2</sub>O (**2**) were synthesized and characterized. The limited number of studies on species containing vitamin B<sub>1</sub> in Anderson type POMs enhances the significance of this study.

### 2. Materials and Methods

All chemicals used were obtained from Aldrich and used without any purification. (NH<sub>4</sub>)<sub>3</sub>[Co(III)Mo<sub>6</sub>O<sub>24</sub>H<sub>6</sub>]·7H<sub>2</sub>O and (NH<sub>4</sub>)<sub>4</sub>[Ni(II)Mo<sub>6</sub>O<sub>24</sub>H<sub>6</sub>]·7H<sub>2</sub>O were synthesized as described in a previous report [21]. C, H, N and S elemental analyses were obtained on a LECO-932 CHNS elemental analyser. Ni, Mo and Co were determined by ICP-MS Agilent Technology 7700. The FT-IR spectra were measured by a Perkin Elmer LR 64912 C spectrometer in the range 400-4000 cm<sup>-1</sup> with KBr pellet. Thermal gravimetric analysis (TGA) was recorded on a Hitachi Exstar TG/DTA 7300 in flowing N<sub>2</sub> with a heating rate of 50.0 mL min<sup>-1</sup> 10 °C/min at 25 and 1000 °C. PXRD spectra was recorded on a PANalytical X-Pert3 Powder.

## 2.1. Synthesis of Compounds

### 2.1.1. $(C_{12}H_{17}N_4OS)_3[Co(III)Mo_6O_{24}H_6] \cdot 7H_2O$ (1)

The solutions required for the reaction were prepared separately. **Solution 1:**  $(NH_4)_3[Co(III)Mo_6O_{24}H_6] \cdot 7H_2O$  was (200 mg, 0.16 mmol) was dissolved in 10 mL  $H_2O$  under stirring. **Solution 2:** Thiamine hydrochloride (excess) was dissolved in 5 mL  $H_2O$ . Afterwards the two solutions were mixed and stirred. The resulting mixture was kept at 80 °C for 24 hours and filtered. The brown product was washed with ethanol and water and dried at 60 °C. Yield: 485 mg, 25%. FT-IR data ( $cm^{-1}$ ): 441 (s), 507 (m), 524 (s), 570 (m), 641 (m), 660 (m), 691 (m), 722 (m), 794 (m), 871 (m), 897 (m), 953 (m), 1046 (m), 1072 (m), 1108 (m), 1169 (m), 1186(s), 1224 (m), 1381 (m), 1421 (m), 1434(m), 1480 (m), 1530 (m), 1616 (m), 1656 (m), 1732 (m), 3044 (m), 3419 (m), 3490 (m). Anal. Calcd. (%) for  $C_{36}H_{71}N_{12}S_3CoMo_6O_{34}$  (1946.77 g/mol): C, 22.21; H, 3.68; N, 8.63; S, 4.94; Mo, 29.57; Co, 3.03. Found (%): C, 20.84; H, 3.00; N, 7.54; S, 5.24; Mo, 30.75; Co, 3.22. TGA (loss of 7  $H_2O$ ): calcd. 6.48%. found 6.55%; (loss of 3  $(C_{12}H_{17}N_4OS)^+$ ): calcd. 40.89%, found 40.95%.

### 2.1.2. $(C_{12}H_{17}N_4OS)_4[Ni(II)Mo_6O_{24}H_6] \cdot 7H_2O$ (2)

The solutions required for the reaction were prepared separately. **Solution 1:**  $(NH_4)_4[Ni(II)Mo_6O_{24}H_6] \cdot 7H_2O$  was (200 mg, 0.15 mmol) was dissolved in 10 mL  $H_2O$  under stirring. **Solution 2:** Thiamine hydrochloride (excess) was dissolved in 5 mL  $H_2O$ . Afterwards the two

solutions were mixed and stirred. The resulting mixture was kept at 80 °C for 24 hours and filtered. The green product was washed with ethanol and water and dried at 60 °C. Yield: 485 mg, 25%. FT-IR data ( $cm^{-1}$ ): 469 (s), 507 (m), 522 (s), 568 (m), 641 (m), 663 (m), 705 (m), 750 (m), 786 (m), 873 (m), 895 (m), 989 (m), 1024 (m), 1044 (m), 1075 (m), 1088 (m), 1112 (m), 1169 (m), 1184 (m), 1224 (m), 1281 (m), 1482 (m), 1526 (m), 1657 (m), 1732 (m), 2074 (m), 3035 (m), 3428 (m), 3503 (m). Anal. Calcd. (%) for  $C_{48}H_{88}N_{16}S_4NiMo_6O_{35}$  (2211.89 g/mol): C, 26.06; H, 4.01; N, 10.13; S, 5.80; Mo, 26.02; Ni, 2.65. Found (%): C, 25.93; H, 3.75; N, 9.82; S, 5.02; Mo, 26.27; Co, 2.37. TGA (loss of 7  $H_2O$ ): calcd. 5.70%. found 5.59%; (loss of 4  $(C_{12}H_{17}N_4OS)^+$ ): calcd. 47.98%, found 47.93%.

## 3. Results and Discussion

Compounds **1** and **2** were synthesized by reacting of  $(NH_4)_3[Co(III)Mo_6O_{24}H_6] \cdot 7H_2O$  and  $(NH_4)_4[Ni(II)Mo_6O_{24}H_6] \cdot 7H_2O$  with thiamine hydrochloride in an aqueous medium (Figure 1). The experimentally obtained spectroscopic data (ICP-MS, TGA and FT-IR) and elemental analyses results (Table 1) support the formulations of **1** and **2** as  $(C_{12}H_{17}N_4OS)_3[Co(III)Mo_6O_{24}H_6] \cdot 7H_2O$  (**1**) and  $(C_{12}H_{17}N_4OS)_4[Ni(II)Mo_6O_{24}H_6] \cdot 7H_2O$  (**2**).

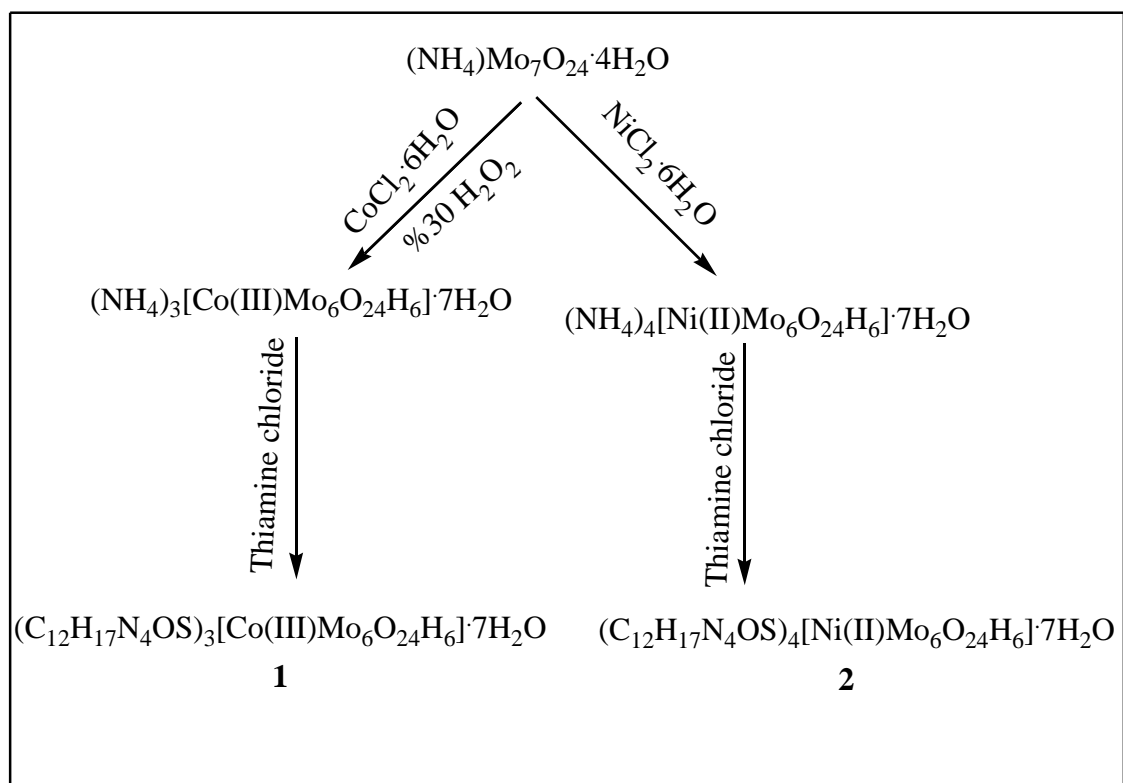


**Figure 1. Synthesis of 1-2**

**Table 1.** Elemental and ICP-MS values of **1** and **2**

Compounds	M.W.	Elemental and ICP-MS						
		C	H	N	S	Mo	Co	Ni
		C/E	C/E	C/E	C/E	C/E	C/E	C/E
<b>1</b>	1946.77	22.01/20.84	3.68/3.00	8.63/7.54	4.94/5.24	29.57/30.75	3.03/3.22	-
<b>2</b>	2211.89	26.06/25.93	4.01/3.75	10.13/9.82	5.80/5.02	26.02/26.27	-	2.65/2.37

M.W.: Molecular Weight, C: Calculated, E: Experimental

In the FT-IR spectrum of POMs, the region between 1000 and 400  $\text{cm}^{-1}$  is characterised as the fingerprint region. The vibrations in this region can be attributed to the M=O and M-O-M (M = Co, Ni, Mo) stretching vibrations of the Anderson type POM cluster [22-24]. The characteristic bands of  $\nu(\text{M=O})$  (M= Co, Ni, Mo) vibrations are observed at 952 and 989  $\text{cm}^{-1}$  for **1** and **2** respectively (Figure 2 and 3). The peaks in the region from 469 to 953  $\text{cm}^{-1}$  correspond to the antisymmetric and symmetric deformation vibrations of the M-O-M (M= Co, Ni, Mo). The FT-IR spectrum also shows stretching vibrations related to vitamin B<sub>1</sub> [17]. The selected bands of vitamin B<sub>1</sub> are at 3490 (OH); 3419 (N-H in  $\text{NH}_2$ ); 3044 (C-H in  $\text{CH}_3$ ); 1656 (NH in  $\text{NH}_2$ ); 1616, 1530, 1480; 1434 (CH in  $\text{CH}_2\text{-CH}_2$ ); 1046 (C-O)  $\text{cm}^{-1}$  for **1**, 3503 (OH); 3428 (N-H in  $\text{NH}_2$ ); 3035 (C-H in  $\text{CH}_3$ ); 1657 (NH in  $\text{NH}_2$ ); 1526, 1482 (CH in  $\text{CH}_2\text{-CH}_2$ ); 1044 (C-O)  $\text{cm}^{-1}$  for **2**. The broad bands at 3400-3500  $\text{cm}^{-1}$  are due to  $\nu(\text{O-H})$  stretching vibrations.

TGA results of **1** (Figure 4) exhibits that 6.55% weight loss between 65-233  $^{\circ}\text{C}$  can be assigned to approximately seven water molecules in the crystal lattice. The 40.95% weight loss between between 234-820  $^{\circ}\text{C}$ , is assigned to the removal of three thiamine cations. The TGA data for **2** (Figure 4) shows the two weight-loss steps between 25  $^{\circ}\text{C}$  and 1000  $^{\circ}\text{C}$  too. The 5.59% weight loss of **2** is due to the loss of lattice water in the temperature range of 49-169  $^{\circ}\text{C}$ . The 47.93% weight loss between 170-813  $^{\circ}\text{C}$  is assigned to the removal of four thiamine cations. The cluster is stable up to 1000  $^{\circ}\text{C}$ .

PXRD diagrams are given in Figure 5. The products were found to be amorphous because they precipitated in the form of powder rather than crystalline structure.

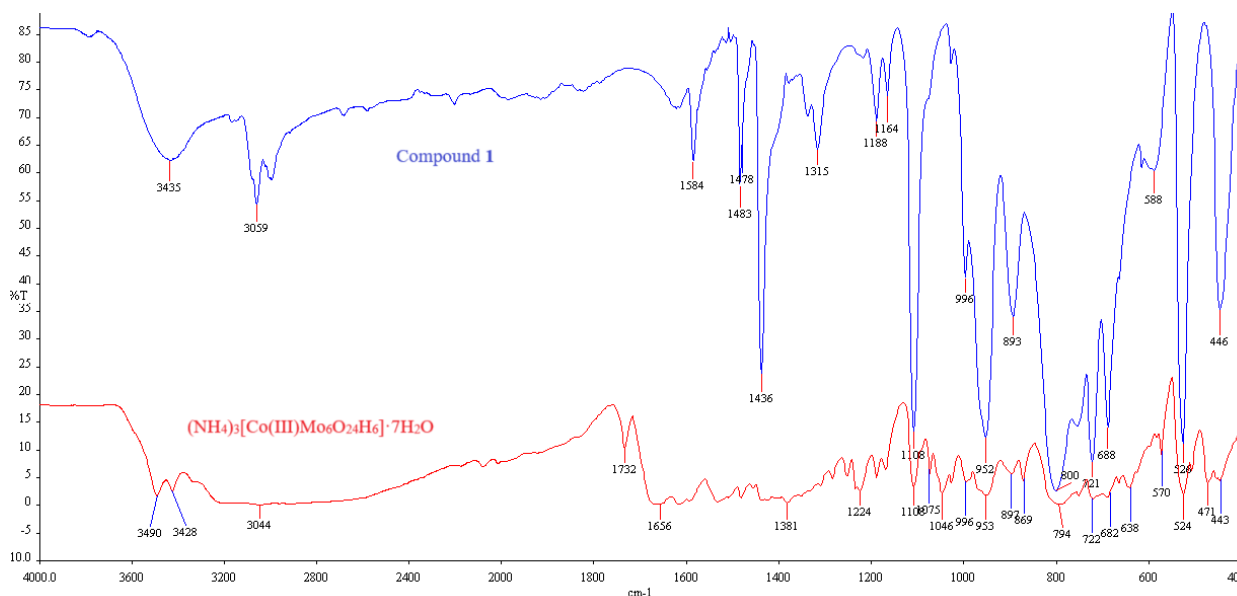


**Figure 2.** FT-IR spectrum of **1** and  $(\text{NH}_4)_3[\text{Co(III)Mo}_6\text{O}_{24}\text{H}_6] \cdot 7\text{H}_2\text{O}$

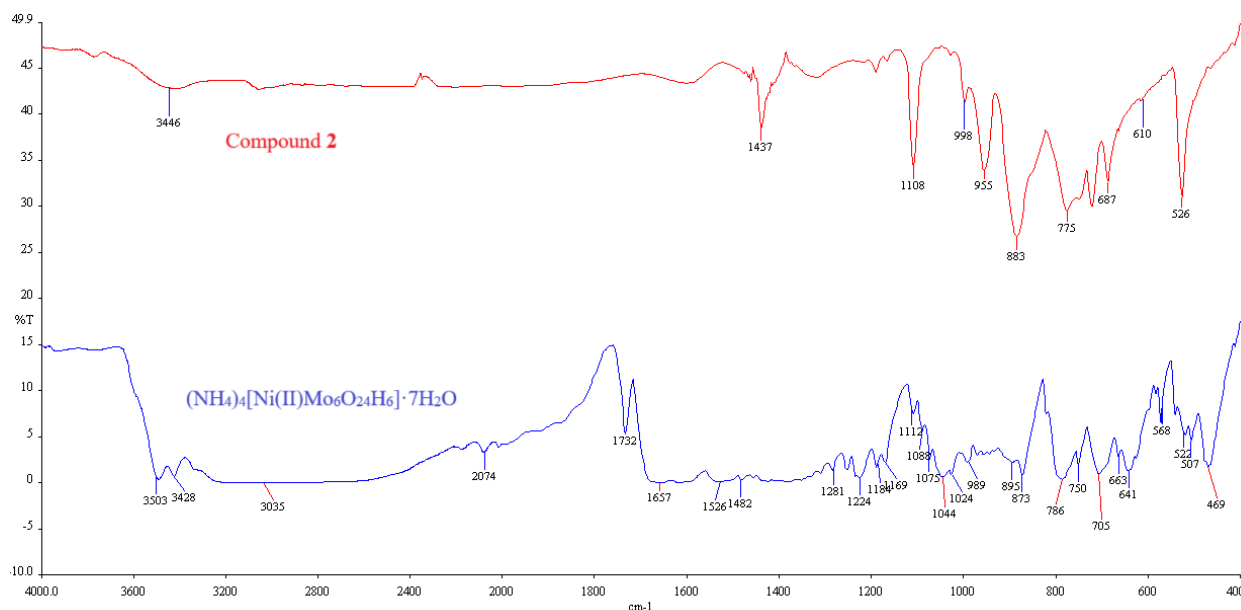


Figure 3. FT-IR spectrum of **2** and  $(\text{NH}_4)_4[\text{Ni}(\text{II})\text{Mo}_6\text{O}_{24}\text{H}_6] \cdot 7\text{H}_2\text{O}$

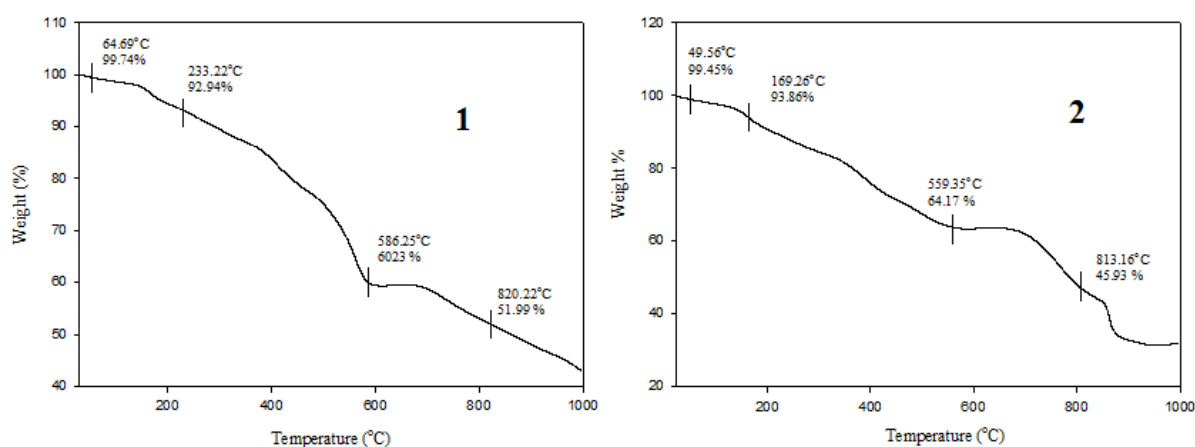


Figure 4. TGA spectrum of **1** and **2**

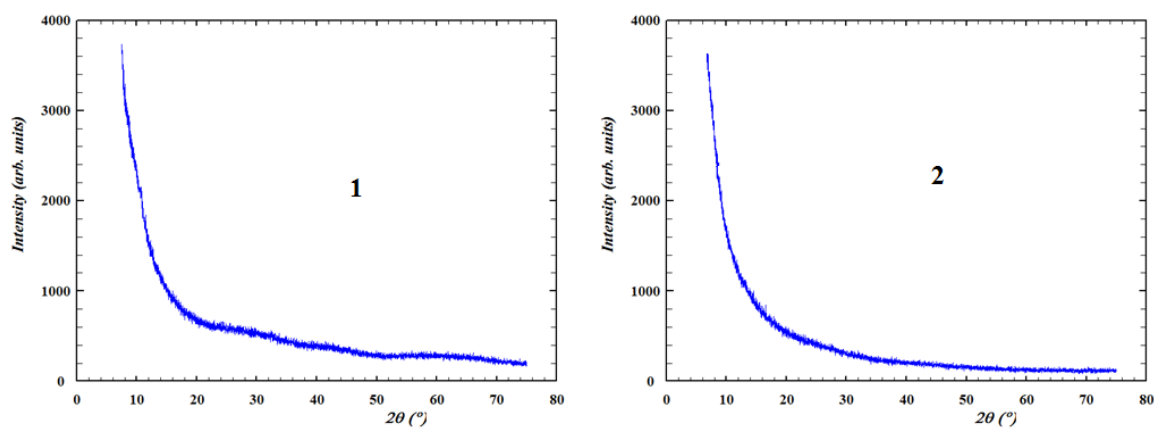


Figure 5. PXRD spectrum of **1** and **2**



#### 4. Conclusion

In conclusion, the synthesis and characterisation of Anderson-type POMs  $((C_{12}H_{17}N_4OS)_3[Co(III)Mo_6O_{24}H_6] \cdot 7H_2O$  (1) and  $(C_{12}H_{17}N_4OS)_4[Ni(II)Mo_6O_{24}H_6] \cdot 7H_2O$  (2)) containing a biologically active moiety (vitamin B<sub>1</sub>) were achieved in this study. Due to the limited number of studies in the literature with POM compounds containing vitamin B<sub>1</sub>, this study may open new perspectives for the preparation of new Anderson-type POM archetypes.

#### Ethics

There are no ethical issues after the publication of this manuscript.

#### References

- [1]. Wang, SS, Yang, GY. 2015. Recent advances in polyoxometalate-catalyzed reactions. *Chemical Reviews*; 115: 4893-4962.
- [2]. Kastner, K, Kibler, AJ, Karjalainen, E, Fernandes, JA, Sans, V, Newton, GN. 2017. Redox-active organic-inorganic hybrid polyoxometalate micelles. *Journal of Materials Chemistry A*; 5:11577-11581.
- [3]. Bijelic, A, Aureliano, M, Rompel, A. 2018. The antibacterial activity of polyoxometalates: structures, antibiotic effects and future perspectives. *Chemical Communications*; 54:1153-1169.
- [4]. Bijelic, A, Aureliano, M, Rompel, A. 2019. Polyoxometalates as potential next-generation metallodrugs in the combat against cancer. *Angewandte Chemie International Edition*; 58:2980-2999
- [5]. Avcı Özbek, H, Kopar, E, Demirhan, F. 2021. Synthesis, structure, and antimicrobial properties of mixed-metal organometallic polyoxometalates.  $[Cp^*_2M_5VO_{17}]^-$  (M=Mo, W). *Journal of Coordination Chemistry*; 74:1794-1809.
- [6]. Avcı Özbek, H. 2023. V-substituted lindqvist-type polyoxometalates: preparation, structural characterization and antibacterial activity. *Chemical Papers*; 77:5663-5669.
- [7]. Avcı Özbek, H. 2023. Synthesis and characterization of Anderson-Evans type polyoxometalates, antibacterial properties. *Turkish Journal of Chemistry*; 47(4): 742-748.
- [8]. Avcı Özbek, H. 2024. Molybdenum-Vanadium Oxide Clusters: Syntheses, Structures and Antibacterial Properties. *Journal of the Institute of Science and Technology*; 14 (1):356-362.
- [9]. Wang, YJ, Chen, WL, Chen, L, Zheng, XT, Xu, SS, Wang, EB. 2017. Sandwich-type silicotungstate modified TiO<sub>2</sub> microspheres for enhancing light harvesting and reducing electron recombination in dye-sensitized solar cells. *Inorganic. Chemistry Frontiers*; 4:559-565.
- [10]. Yang, HK, Cheng, YX, Su, MM, Xiao, Y, Hu, MB, Wang, W, Wang, Q. 2013. Polyoxometalate-biomolecule conjugates: a new approach to create hybrid drugs for cancer therapeutics. *Bioorganic & Medicinal Chemistry Letters*; 23:1462-1466.
- [11]. Song, F, Wang, T. 2022. Application of Polyoxometalates in Chemiresistive Gas Sensors: A Review. *ACS Sensors*; 7(12) 3634-3643.
- [12]. Xing, C, Ma, M, Chang, J, Ji, Z, Wang, P, Sun, L, Li, S, Li, M. 2023. Polyoxometalate anchored zinc oxide nanocomposite as a highly effective photocatalyst and bactericide for wastewater decontamination. *Chemical Engineering Journal*; 464:142632.
- [13]. Zhao, M., Fang, Y, Ma, L, Zhu, X, Jiang, L, Li, M., Han, Q. 2020. Synthesis, characterization and in vitro antibacterial mechanism study of two Keggin-type polyoxometalates. *Journal of Inorganic Biochemistry*; 210:111131.
- [14]. Çetindere, S. 2023. Polyoxometalate-based boron dipyrromethene (BODIPY) conjugates: syntheses, characterization and photophysical properties. *Journal of the Iranian Chemical Society*; 20:3069-3077.
- [15]. Çetindere, S, Ardiç Alidağı, H, Anjass, M. 2023. Two novel Anderson-type polyoxometalate based MnIII complexes constructed from pyrene derivatives: Synthesis, photophysical, and electrochemical properties. *Inorganica Chimica Acta*; 545: 121280.
- [16]. Golubeva, OY, Pavlova, SV. 2014. Adsorption of Thiamine Hydrochloride (Vitamin B<sub>1</sub>) by Synthetic Layered Silicates with a Montmorillonite Structure. *Glass Physics and Chemistry*; 40(3):375-379.
- [17]. Ostroushko, A, Gagarin, I, Tonkushina, M, Grzhegorzhevskii, K, Russkikh, O. 2018. Association of Spherical Porous Nanocluster Keplerate-Type Polyoxometalate Mo<sub>72</sub>Fe<sub>30</sub> with Biologically Active Substances. *Journal of Cluster Science*; 29:111-120.
- [18]. Mahvash, S, Zavareh, VA, Taymouri, S, Mirian, M, Ramezani-Aliakbari, M, Dousti, F, Rostami, M. 2023. Anderson-type manganese polyoxomolybdate hybrid nanocomposite for boosting drug delivery against breast cancer. *Journal of Drug Delivery Science and Technology*; 87:104778.
- [19]. Ramezani-Aliakbari, M, Varshosaz, J, Sadeghi-aliabadi, H, Hassanzadeh, F, Rostami, M. 2021. Biotin-Targeted Nanomicellar Formulation of an Anderson-Type Polyoxomolybdate: Synthesis and In Vitro Cytotoxicity Evaluations. *Langmuir*; 37:6475-6489.
- [20]. Ramezani-Aliakbari, M, Varshosaz, J, Mirian, M, Khodarahmi, G, Rostami, M. 2022. pH-responsive glucosamine anchored polydopamine coated mesoporous silica nanoparticles for delivery of Anderson-type polyoxomolybdate in breast cancer. *Journal of Microencapsulation*; 39(5): 433-451.
- [21]. Nomiya, K, Takahashi, T, Shirai, T, Miwa, M. 1987. Anderson-type heteropolyanions of molybdenum(VI) and tungsten(VI). *Polyhedron*; 6(2):213-218.
- [22]. Tewari, S, Adnan, M, Balendra, Kumar, V, Jangra, G, Prakash GV, Ramanan, A. 2019. Photoluminescence properties of two closely related isostructural series based on Anderson-Evans cluster coordinated with lanthanides  $[Ln(H_2O)_7\{X(OH)_6Mo_6O_{18}\}] \cdot yH_2O$ , X = Al, Cr. *Frontiers in Chemistry*; 6 (631):1-19.
- [23]. Thabet, S, Ayed, D, Haddad, A. 2013. Novel organic-inorganic hybrid with Anderson type polyanions as building blocks:  $(C_6H_{10}N_3O_2)_2Na(H_2O)_2[Al(OH)_6Mo_6O_{18}] \cdot 6H_2O$ . *Materials Research Bulletin*. 47:3791-3796.
- [24]. Avcı Özbek, H. 2023. Synthesis and Characterization of New Anderson-Type Polyoxometalates:  $[M((1,10\text{-phen})(OH)_x)_3(Cr(OH)_6Mo_6O_{18})] \cdot 16H_2O$  (M= Cr, Mn, Co, Ni, Cu; x= 1, 2). *Journal of the Turkish Chemical Society Section A: Chemistry*; 1 (2): 315-324.

# Oxidation of Benzyl Alcohols by Monomeric Iron Phthalocyanine Complexes: Substituents' Effect on Their Catalytic Performance

Zeynel Şahin<sup>1\*</sup> 

<sup>1\*</sup> Marmara University, Faculty of Technology, Department of Metallurgical and Materials Engineering, Istanbul, Türkiye

\* [zeynel.sahin@marmara.edu.tr](mailto:zeynel.sahin@marmara.edu.tr)

\*Orcid No: 0000-0002-7719-7652

Received: 21 October, 2024

Accepted: 20 January, 2025

DOI: 10.18466/cbayarfbe.1570991

## Abstract

Iron phthalocyanines tetra substituted with either electron-donating *n*-hexyloxy or electron-withdrawing *n*-hexylsulfonyl substituents were prepared and tested as oxidation catalysts for benzyl alcohol, 4-bromobenzyl alcohol, 4-methylbenzyl alcohol and 4-*tert*-butylbenzyl alcohol. Oxidation reactions were performed at room temperature in acetonitrile, acetone, ethanol, toluene, and the best result was obtained in acetonitrile. Oxidation of alcohols using *tert*-butyl hydroperoxide as an oxidant in the presence of these iron(II) phthalocyanines resulted in the production of corresponding benzaldehyde and benzoic acid. When comparing the substituent effect, the hexylsulfonyl electron-withdrawing substituted phthalocyanine complex exhibited better catalytic performance in acetonitrile for all benzylic alcohol derivatives. It showed that electron-withdrawing substituted iron(II) phthalocyanine tends to produce benzaldehydes, while electron-donating substituted iron(II) phthalocyanine produced benzoic acid. This kind of catalytic system is suitable for the oxidation of benzylic alcohols to produce benzaldehyde and benzoic acid derivatives.

**Keywords:** Oxidation, Benzyl alcohol, Iron phthalocyanine, Catalyst

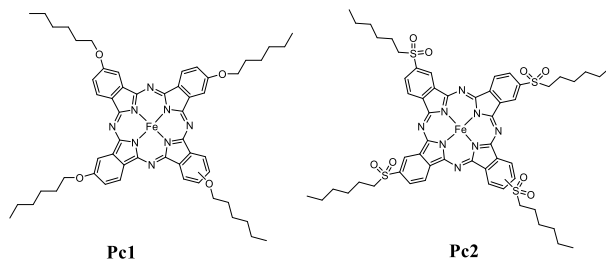
## 1. Introduction

Oxidation reactions are amongst the most important in synthetic chemistry and offer a significant methodology for the modification of chemical substances [1]. Numerous oxidation reactions have been employed for the improvement in organic synthesis and industrial applications. Aldehydes and other carbonyl group compounds are very important organic intermediates in the production of medicine, fragrance, flavors and dyes [2]. Therefore, the selective oxidation of alcohols by transition metal catalysts and various catalytic systems have been broadly studied and to obtain the corresponding carbonyl compound to alcohol is a main goal [3]. Iron is a versatile metal center, cheap, nontoxic and possesses several stable oxidation states which makes it interesting for chemical applications [4]. So many iron compounds, such as iron(III) nitrate [5], iron(III) dodecyl sulfonate [6], and iron(III) tosylate [7] have been used as catalysts for the oxidation of alcohols into corresponding carbonyl compounds. Phthalocyanine complexes (Pcs) are aromatic compounds that have excellent properties such as thermal, chemical and light stability. The chemical and electronic structure of these molecules can be tailored by either metal insertion or

covalent peripheral and non-peripheral substitutions [8]. Metal phthalocyanines (MPcs) have been used in many areas, including commercial pigments [9], photodynamic therapy [10], gas sensing materials [11, 12], information storage, computer disk writing, and catalysis [13]. MPcs complexes are structurally similar to porphyrin complexes that perform aerobic oxidation, reduction and transport of dioxygen destruction of peroxide in nature. Pcs are amongst the preferred catalysts because of their similar structural analogy with porphyrin and their possible preparation on a large scale as well as their chemical and thermal stability [14]. MPcs are most important compounds for catalytic oxidation reactions, which have been used for the oxidation of epoxidation of alkenes [15], olefins, aromatic, benzylic, and so many other complexes [16]. Different types of monomeric iron phthalocyanine were used in alcohol oxidation reactions and some substituent effect on the conversion, yield and selectivity has been investigated [17].

To further investigate these effects, two different MPcs substituted with hexyloxy electron-donating and hexylsulfonyl electron-withdrawing groups were used (**Scheme 1**) and their catalytic activities were examined. Linear hexyl groups were selected to enhance solubility

in organic solvents. Oxidation of benzyl alcohol was selected as a model oxidation reaction.



**Scheme 1:** Molecular structure of iron (II) tetra-(hexyloxy)phthalocyanine (**Pc1**) and iron (II) tetra-(hexylsulfonyl)phthalocyanine (**Pc2**).

## 2. Materials and Methods

Iron (II) tetra-(hexyloxy)phthalocyanine (**Pc1**) and iron (II) tetra-(hexylsulfonyl)phthalocyanine (**Pc2**) were

prepared according to literature methods [18, 19]. Benzyl alcohol, 4-bromobenzyl alcohol, 4-methylbenzyl alcohol, 4-*tert*-butylbenzyl alcohol, ethanol, acetone, toluene, acetonitrile and *tert*-butyl hydroperoxide (TBHP, 70% in water) were purchased from Aldrich and used as received. All oxidation reactions were performed under ambient conditions. The oxidation products were monitored by an Agilent Technologies 7820A GC system.

### 2.1. General procedure for oxidation of alcohols

Oxidation reactions were performed in 10 mL flasks. Alcohol (0.125 mmol, 1 eqv.) and catalyst (2.5 µmol, 0.02 eqv.) were stirred in solvent (4 mL). After the solution became homogeneous, the reaction was initiated by adding 70 % TBHP solution (12.5 mmol, 100 eqv.). The oxidation reactions were carried out at room temperature and under air for 1 hour. The oxidation product yields were determined by GC.

The calculation of conversion and selectivity were defined according to the following equations:

$$\text{Conversion (\%)} = 100 - \frac{\text{Peak area of alcohol}}{\text{Peak area of (alcohol+all products)}} \times 100 \quad (1)$$

Equation (1). Conversion calculation

$$\text{Selectivity to BzA (\%)} = 100 - \frac{\text{Peak area of benzaldehyhde}}{\text{Peak area of all products}} \times 100 \quad (2)$$

Equation (2). Selectivity to BzA calculation.

$$\text{Selectivity to BA (\%)} = 100 - \frac{\text{Peak area of benzoic acid}}{\text{Peak area of all products}} \times 100 \quad (3)$$

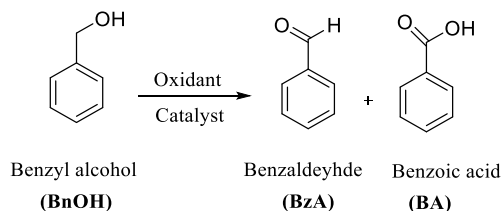
Equation (3). Selectivity to BA calculation.

## 3. Results and Discussion

### 3.1. Optimization of oxidation reaction conditions

Optimum reaction conditions (substrate/catalyst ratio, reaction temperature and use of the TBHP as an oxidant) were adjusted to our previous works with *N*-bridged diiron phthalocyanines bearing eight *t*-butyl groups that highly provide solubility in organic solvents used as oxidation catalysts [20]. Since monomeric and dimeric phthalocyanines have different chemical structures, the solubility of these complexes could be different and affect conversion in oxidation reactions. To find first the solvent effect, oxidation reactions were performed in ethanol, toluene, acetone and acetonitrile at room temperature for one hour. Oxidation of benzyl alcohol (**BnOH**) was selected as a model reaction by using **Pc2**.

Products were identified using gas chromatography (GC) by comparison with corresponding standard compounds. As seen in **Fig. 1**, two product formations were clearly observed on GC spectra. These products are benzaldehyde (**BzA**) and benzoic acid (**BA**) (**Scheme 2**).



**Scheme 2.** Catalytic oxidation products of benzyl alcohol, catalyzed by **Pc2**.

As seen in GC spectra (**Fig.1**), conversion of **BnOH** to **BzA** and **BA** were observed in all solvents. As a depicted in **Fig.2**, highest conversion (100%) was observed in

acetonitrile and a slightly lower conversion (84%) was obtained in acetone. In terms of product selectivity, **BzA** formation was predominant in ethanol (65%) and toluene (61%), while reaction performed in acetone (79%) and acetonitrile (54%) induced the formation of **BA** as a main product. The reaction in acetonitrile supported poorly one product formation that was 46 % **BzA** and 54 % **BA**, nonetheless it was most effective solvent in terms of **BnOH** conversion.

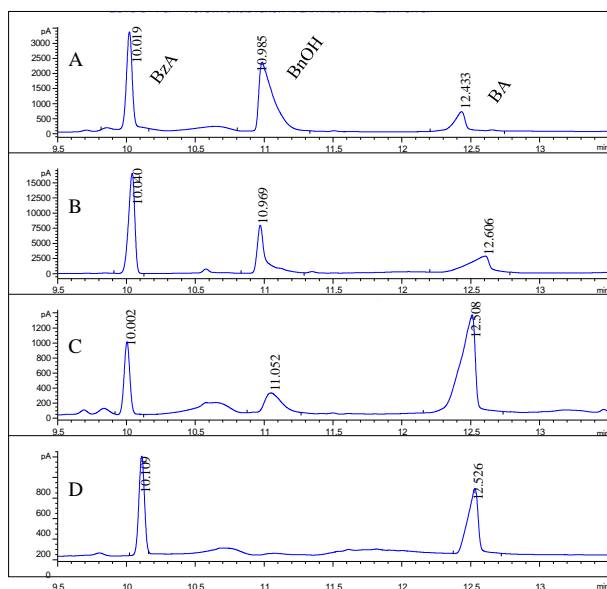


**Figure 1:** Solvent effect on the conversion of benzyl alcohol in ethanol A, toluene B, acetone C and acetonitrile D, catalyzed by **Pc2**.

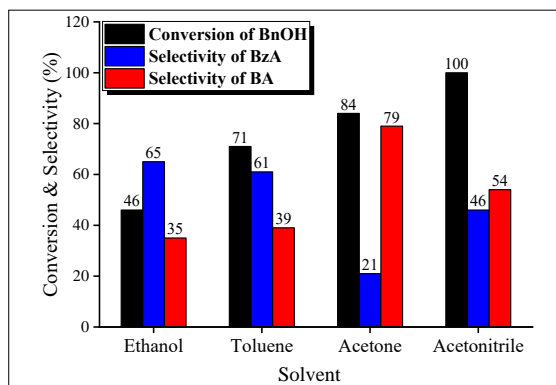


**Figure 2:** Solvent effect on the selectivity of benzyl alcohol, catalyzed by phthalocyanine **Pc2**.

### 3.2. Oxidation of alcohols with **Pc1** and **Pc2**.

The catalytic performance of the phthalocyanines complexes were investigated with four different benzylic alcohols. As shown in **Fig.3**, the oxidation products all of the benzylic alcohols are corresponding benzaldehydes and benzoic acids. The catalytic activity of the  $\text{SO}_2\text{R}$  electron-withdrawing groups substituted iron phthalocyanine **Pc2** was higher than OR electron-

donating groups substituted iron phthalocyanine **Pc1** in the oxidation of all alcohols. In terms of the selectivity, **Pc2** exhibited better selectivity to benzaldehyde in acetonitrile. The performed benzyl alcohol oxidation here was compared with the reports on FePc derivatives catalyzed reactions regarding temperature, reaction time and conversion **Table 1**. It can be seen that in spite of good selectivity to benzaldehyde and with higher benzyl alcohol conversion previously studied FePc catalysts, they need slightly high reaction temperature and time [21-23]. Although chitosan aerogel FePc catalyst milder reaction conditions and had selectivity to benzaldehyde at 100%, it exhibited 40% benzyl alcohol conversion [24]. In the meantime, catalysts **Pc1** and **Pc2** exhibited high conversion of benzyl alcohol and its derivatives at room temperature. When the two catalysts were compared with each other, the **Pc2** exhibited the higher benzyl alcohol conversion than the **Pc1**.

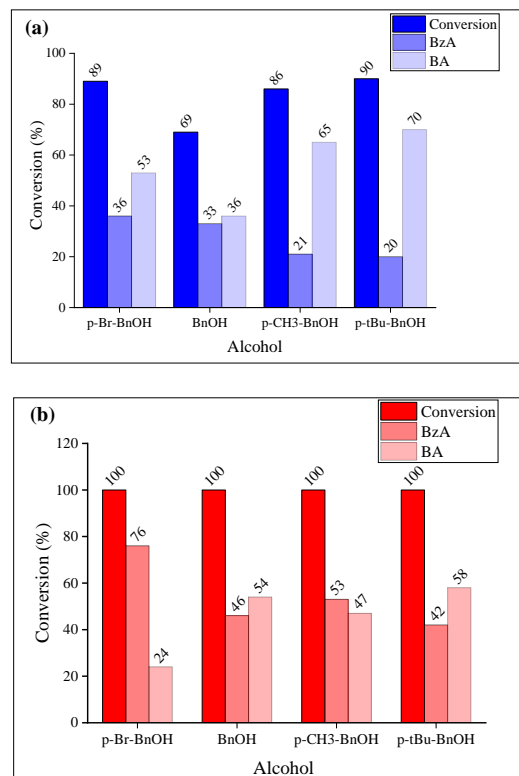


**Figure 3:** Oxidation of benzyl alcohols, catalyzed by **Pc1** (a) and **Pc2** (b).

### 3.3. Proposed catalytic mechanism

The catalytic activity of the phthalocyanine complexes depends on the iron atom at the macrocycle center that tends to produce radical intermediates with TBHP [23]. A possible mechanism of these oxidation reactions is based on progress on the radical intermediates as shown in **Scheme 3**. Firstly, the reaction is initiated interaction between the iron atom in the phthalocyanine cavity and *tert*-butyl hydroperoxide can give rise to active a higher state Fe(III)Pc-OH and *tert*-butoxy radical species [24].

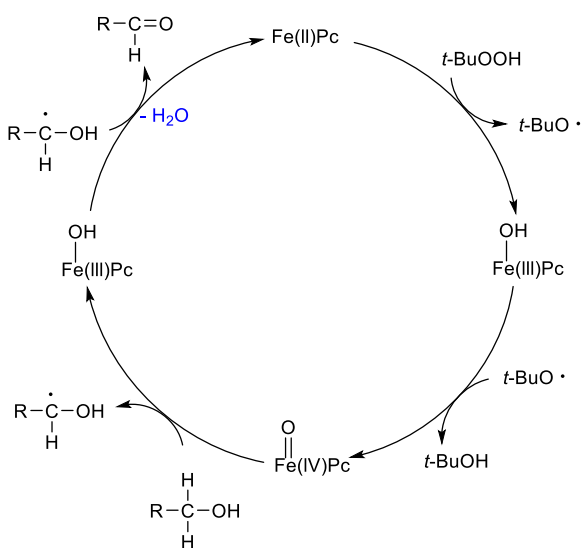


Then, Fe(III)Pc-OH can be activated by the reaction with *tert*-butoxy radical to which can produce further a higher state of active Fe(IV)Pc=O complex. In the next step, Fe(IV)Pc=O can absorb a radical hydrogen from alcohol

and come back to Fe(III)Pc-OH state. Complex Fe(III)Pc-OH can take a hydrogen from radical benzaldehyde intermediate and benzaldehyde formation can occur in the last step [14, 20].

**Table 1.** Comparison of catalyst performance of previously reported some FePc catalysts for BA oxidation.

Catalyst	Oxidant	Rxn temp. (°C)	Rxn time (h)	Conversion (%)	Ref
Tetra-substituted FePc	TBHP	70	3	94	[21]
Polyfluoro substituted FePc	TBHP	50	3	89	[22]
Fluoro substituted FePc	TBHP	90	3	90	[22, 23]
Chitosan aerogel FePc	H <sub>2</sub> O <sub>2</sub>	25	24	40	[14, 24]
Pc1	TBHP	25	1	69	
Pc2	TBHP	25	1	100	



**Scheme 3.** The proposed mechanism for the oxidation of alcohols by TBHP in the presence of iron phthalocyanine catalyst.

#### 4. Conclusion

Sulfonyl substituted **Pc2** was selected for the model reaction and tested for alcohol oxidation reactions in four different solvents. Among these solvents, acetonitrile was shown to be most adequate for alcohol oxidation reactions. The catalytic activities of **Pc1** and **Pc2** were then tested for oxidation of benzylic alcohols in acetonitrile. The oxidation products of both iron phthalocyanine catalysts were benzaldehyde and benzoic acid as expected. Compared to the substituent effect of phthalocyanine complexes, **Pc2** containing electron-withdrawing groups showed better catalytic performance than **Pc1** containing electron-donating groups in all benzylic alcohol derivatives. In general, phthalocyanine complexes are useable catalysts for benzyl alcohol oxidation because of their room temperature condition,

good substrate conversion and easily obtainable materials.

#### Author's Contribution

**Zeynel Şahin:** Drafted and wrote the manuscript, performed the experiment and result analysis.

#### Ethics


There are no ethical issues after the publication of this manuscript.

#### Reference

- [1]. Mamedov, E, Corberán, VC. 1995. Oxidative dehydrogenation of lower alkanes on vanadium oxide-based catalysts. The present state of the art and outlooks. *Applied Catalysis A: General*; 127(1-2): 1-40.
- [2]. Ahmad, JU, Räisänen, MT, Leskelä, M, Repo, T. 2012. Copper catalyzed oxidation of benzylic alcohols in water with H<sub>2</sub>O<sub>2</sub>. *Applied Catalysis A: General*; 411: 180-7.
- [3]. Kheirjou, S, Kheirjou, R, Rezayan, AH, Shakourian-Fard, M, Hashemi, MM. 2016. Selective aqueous oxidation of alcohols catalyzed by copper (II) phthalocyanine nanoparticles. *Comptes Rendus Chimie*; 19(3): 314-9.
- [4]. Stanje, B, Traar, P, Schachner, J, Belaj, F, Mösch-Zanetti, N. 2018. Iron catalyzed oxidation of benzylic alcohols to benzoic acids. *Dalton Transactions*; 47(18): 6412-20.
- [5]. Namboodiri, VV, Polshettiwar, V, Varma, RS. 2007. Expedient oxidation of alcohols to carbonyl compounds using iron (III) nitrate. *Tetrahedron Letters*; 48(50): 8839-42.
- [6]. Yu, Y, Lu, B, Wang, X, Zhao, J, Wang, X, Cai, Q. 2010. Highly selective oxidation of benzyl alcohol to benzaldehyde with hydrogen peroxide by biphasic catalysis. *Chemical Engineering Journal*; 162(2): 738-42.
- [7]. Zhao, Y, Yu, C, Wu, S, Zhang, W, Xue, W, Zeng, Z. 2018. Synthesis of benzaldehyde and benzoic acid by selective oxidation of benzyl alcohol with iron (III) tosylate and hydrogen peroxide: a solvent-controlled reaction. *Catalysis Letters*; 148: 3082-92.

- [8]. Li, Z, Xu, S, Chen, Z, Zhang, F. 2014. Photophysical and nonlinear optical properties of an azobenzene substituted zinc phthalocyanine. *Optik*; 125(15): 3833-6.
- [9]. Dahlen, MA. 1939. The phthalocyanines a new class of synthetic pigments and dyes. *Industrial & Engineering Chemistry*; 31(7): 839-47.
- [10]. Lo, P-C, Rodríguez-Morgade, MS, Pandey, RK, Ng, DK, Torres, T, Dumoulin, F. 2020. The unique features and promises of phthalocyanines as advanced photosensitisers for photodynamic therapy of cancer. *Chemical Society Reviews*; 49(4): 1041-56.
- [11]. Şahin, Z, Meunier-Prest, R, Dumoulin, F, Kumar, A, İsci, Ü, Bouvet, M. 2021. Tuning of organic heterojunction conductivity by the substituents' electronic effects in phthalocyanines for ambipolar gas sensors. *Sensors and Actuators B: Chemical*; 332: 129505.
- [12]. Sahin, Z, Meunier-Prest, R, Dumoulin, F, İsci, U, Bouvet, M. 2020. Alkylthio-tetrasubstituted  $\mu$ -nitrido diiron phthalocyanines: spectroelectrochemistry, electrical properties, and heterojunctions for ammonia sensing. *Inorganic Chemistry*; 59(2): 1057-67.
- [13]. Qiu, S, Li, Y, Xu, H, Liang, Q, Zhou, M, Rong, J, Li, Z, Xu, S. 2022. Efficient catalytic oxidation of benzyl alcohol by tetrasubstituted cobalt phthalocyanine-MWCNTs composites. *Solid State Sciences*; 129: 106905.
- [14]. Sorokin, AB. 2013. Phthalocyanine metal complexes in catalysis. *Chemical reviews*; 113(10): 8152-91.
- [15]. Safari, N, Bahadoran, F. 2001. Cytochrome P-450 model reactions: a kinetic study of epoxidation of alkenes by iron phthalocyanine. *Journal of Molecular Catalysis A: Chemical*; 171(1-2): 115-21.
- [16]. Sorokin, A, Kudrik, E. 2011. Phthalocyanine metal complexes: versatile catalysts for selective oxidation and bleaching. *Catalysis Today*; 159(1): 37-46.
- [17]. Yüceel, Ç, Şahin, Z, İsci, Ü. 2022. Substituent effect on iron phthalocyanines as cyclohexene oxidation catalysts. *Journal of Porphyrins and Phthalocyanines*; 26(06n07): 452-7.
- [18]. Ravikanth, M, Achim, C, Tyhonas, JS, Münck, E, Lindsey, JS. 1997. Investigation of phthalocyanine catalysts for the aerobic synthesis of meso-substituted porphyrins. *Journal of Porphyrins and Phthalocyanines*; 1(04): 385-94.
- [19]. İsci, Ü, Afanasiev, P, Millet, J-MM, Kudrik, EV, Ahsen, V, Sorokin, AB. 2009. Preparation and characterization of  $\mu$ -nitrido diiron phthalocyanines with electron-withdrawing substituents: application for catalytic aromatic oxidation. *Dalton Transactions*; (36): 7410-20.
- [20]. Şahin, Z, Yüceel, Ç, Yıldız, DB, Dede, Y, Dumoulin, F, İsci, Ü. 2024. Phthalocyanine vs porphyrin: Experimental and theoretical comparison of the catalytic activity of N-bridged diiron tetrapyrrolic complexes for alcohols oxidation. *Molecular Catalysis*; 559: 113986.
- [21]. Cakır, V, Saka, ET, Bıyıklıoğlu, Z, Kantekin, H. 2014. Highly selective oxidation of benzyl alcohol catalyzed by new peripherally tetra-substituted Fe (II) and Co (II) phthalocyanines. *Synthetic metals*; 197: 233-9.
- [22]. Aktaş, A, Acar, I, Saka, ET, Bıyıklıoğlu, Z. 2016. Synthesis of polyfluoro substituted Co (II), Fe (II) phthalocyanines and their usage as catalysts for aerobic oxidation of benzyl alcohol. *Journal of Organometallic Chemistry*; 815: 1-7.
- [23]. Aktaş, A, Acar, I, Saka, ET, Bıyıklıoğlu, Z, Kantekin, H. 2016. Fluoro functional groups substituted cobalt (II), iron (II) phthalocyanines and their catalytic properties on benzyl alcohol oxidation. *Journal of Inclusion Phenomena and Macrocyclic Chemistry*; 86: 183-90.
- [24]. Azimi, F, Poursattar Marjani, A, Keshipour, S. 2021. Fe (II)-phthalocyanine supported on chitosan aerogel as a catalyst for oxidation of alcohols and alkyl arenes. *Scientific Reports*; 11(1): 23769.

## Evaluation of the Altmetric Attention Score of Recent Hazard Food-Marker: Advanced Glycation End Products

Büşra Yusufoglu<sup>1\*</sup> 

<sup>1\*</sup> Department of Chemistry, Science and Letter Faculty İstanbul Technical University Ayazağa, Sarıyer, 34467, İstanbul, Türkiye

\*[yusufoglu@itu.edu.tr](mailto:yusufoglu@itu.edu.tr)

\*Orcid No: 0000-0002-9158-9732

Received: 6 November 2024

Accepted: 10 January 2025

DOI: 10.18466/cbayarfbe.1580554

### Abstract

Recent trends in dietary habits have led to increased oxidative stress, heightened inflammatory responses and an increased incidence of chronic disease. With the increasing consumption of processed foods, advanced glycation end products (AGEs) have gained attention as significant "hazard food markers" associated with diets high in sugar and fat. AGEs can originate internally in the body or externally from sources such as food and smoking. This study examines the Altmetric Attention Score (AAS) to assess the online visibility and impact of recent research on AGEs. By conducting systematic searches of scientific databases and analyzing data from the Altmetric platform, the study evaluates the AAS and related online engagement metrics. The results show that AGEs-related articles receive varying levels of online attention, with notable interactions on social media, news platforms and forums. Moreover, keyword co-occurrence analysis revealed three dominant thematic areas in AGEs-related research, including dietary sources, oxidative stress mechanisms, and food processing-induced formation. This research highlights how factors such as publication venue, article type and topic relevance influence AAS, highlighting its importance in understanding the digital impact of food safety research.

**Keywords:** Altmetric Attention Score, AGEs, Food Processing, Food Safety

### 1. Introduction

The concept of food safety refers to the process of preventing some chemically and physically hazardous substances from entering the food supply chain at any stage, starting with the production of food, and continuing until its storage and consumption [1]. Studies on food safety behaviors of socio-demographic factors and information sources investigate consumers' knowledge levels, attitudes towards food safety and actual practices. Study findings highlighted the need to inform policymakers about effective food safety information dissemination methods [2]. In these stages, processing of food is one of the most basic issues and it creates some health risks for public health by affecting the nutritional elements of the food and causing the formation of some chemical molecules [3].

Ultra-processed foods are found to be more energy-dense and contain higher amounts of sugar, fat, and sodium than less processed foods, and consuming these foods has been shown to have potential health effects [4].

Advanced glycation end products (AGEs), one of the non-enzymatic reactions that occur in foods, are formed as a result of food processing and are one of the most important food safety and public health problems [5, 6]. AGEs are formed endogenously during normal metabolism but can also be introduced exogenously through diet, particularly by consuming foods processed at high temperatures [6]. To shed on light details of AGEs, it should get to their different molecular types such as early, intermediate and advanced phases. All phases are responsible basic reactive AGEs formations including N $\epsilon$ -(carboxymethyl)lysine, N $\epsilon$ -(carboxyethyl) lysine (CEL), methylglyoxal (MGO), glyoxal (GO), pentosidine etc. [7]. These complex molecules formed through the non-enzymatic reaction of reducing sugars with proteins, lipids, or nucleic acids. They play a significant role in the aging process and the development of various diseases, including diabetes, cardiovascular diseases, and neurodegenerative diseases as hazards food markers [8]. AGEs content in food, highlighting the relationship between frying conditions, moisture content, oil absorption and AGEs formation [9]. Peng et al., 2023 have investigated the inhibitory effects of blueberry

anthocyanins extract (BAE) on the formation of AGEs and their consequent inflammation in cells. It demonstrates BAE's capability to attenuate AGEs formation and AGEs-induced inflammatory responses, showcasing its potential as a natural inhibitor for AGEs and chronic inflammation caused by AGEs [10]. Si et al., (2024) have presented a comprehensive analysis of the association between the consumption of AGEs from various food sources and the risks of for all-reasons, cardiovascular disease (CVD), and cancer mortality. Utilizing data from a large national cohort, the study assesses AGEs intake through dietary questionnaires and investigates its correlation with mortality risks. The findings highlight the significance of dietary AGEs consumption about CVD and cancer mortality, offering insight into the impact of diet on long-term health outcomes [11]. Sourris et al. (2024) have delved into the impact of glucagon-like peptide-1 receptor (GLP-1R) signaling on diabetic kidney disease, focusing on its role in mitigating receptor for advanced glycation end products (RAGE)-induced inflammation. It presents findings from studies on mice, revealing that GLP-1R signaling is crucial for kidney health, and its deficiency can lead to kidney damage, which is exacerbated by diabetes. The study also demonstrates the therapeutic potential of the GLP-1R agonist liraglutide in reducing kidney injury by modulating RAGE expression and promoting anti-inflammatory responses [12]. Takeuchi et al., (2024) have explored the connection between the habitual overconsumption of sugars and the onset of lifestyle-related diseases (LSRD), focusing on the role of toxic advanced glycation end-products (TAGE) derived from glyceraldehyde. It discusses the formation and characteristics of these AGEs, their potential cytotoxic effects, and the relevance of TAGE as biomarkers for early diagnosis and monitoring of LSRD. The study underscores the importance of understanding AGEs structures and their varying toxicity to address and mitigate the health risks associated with high sugar consumption and LSRD [13]. AGEs are responsible some disease categories such as metabolic disorders (obesity and insulin resistance etc.), cardiovascular diseases, renal diseases, neurological disorders (Alzheimer's and Parkinson's disease etc.), cancer (breast, colorectal, pancreatic etc.), skin disorders (aging and wrinkles) [14].

Altmetric attention scores (AAS) are updated in real-time, allowing researchers, publishers, and institutions to see the immediate impact of their work. On the other hand, altmetric has captured the diverse ways research impacts society by tracking mentions across different platforms, offering a more comprehensive view of an article's reach than citations alone. AAS reflects how research is discussed and disseminated among the public, not just within academic circles [15-16].

The Altmetric Attention Score is a quantitative measure of the attention that a scholarly article or academic

research output receives. It aggregates data from various sources, including social media, news media, policy documents, blogs, and online reference managers, among others, to gauge the broader impact and dissemination of research beyond traditional citation metrics. Used alongside traditional citation metrics, Altmetric offers a more nuanced and complete picture of research impact, enriching the evaluation of academic outputs. Altmetric Attention Score provides a multi-dimensional view of the impact and dissemination of research, capturing the immediate and diverse ways in which scholarly work engages with the wider world [15-16].

Advantages of the AAS including various aspects are assessing the impact of scholarly work, great sources for researchers, librarians, and academics, public engagement, discuss the integration of altmetrics into academic evaluation processes, discuss the role of social media. This social media perspective has present new perspective for scientists how to promote their research for maximum impact on public. In this context, the study aims to raise public awareness and reveal the effects of scientific studies on social media.

## 2. Materials and Methods

A bibliometric analysis was conducted using Web of Science (WoS) platform (<https://www.webofscience.com>) through a topic-based search method related to advanced glycation end products (AGEs). The search was performed on June 17, 2024, using the query TS=("advanced glycation end products") AND TS=("food" OR "diet" OR "nutrition"). Then, publications were filtered to peer-reviewed articles, review articles, and proceedings papers published from 1992 to 2025. As a result, a total of 1766 publications were obtained for analysis. The data was extracted in plain text format with full records and cited references and analysed using VOSviewer software (v1.6.20). A keyword co-occurrence analysis was carried out through the full counting method, and 477 keywords were included in the map after use of minimum occurrence threshold on the data. Figure 1 shows a summary of the data collection.



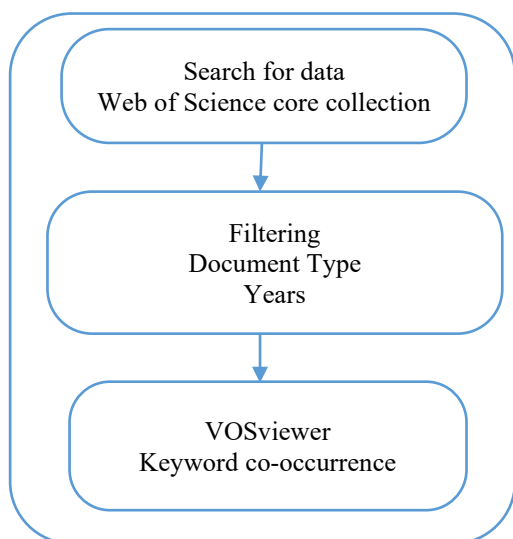


**Figure 1.** Overview of the bibliometric analysis process using VOSviewer

Moreover, the information for this bibliometric citation analysis was collected using the Web of Science (WoS) Core Collection database and PubMed. To find relevant articles in the WoS database, we have searched for the term "Advanced Glycation End Products." From a total of 17.630 articles, we have investigated the first 100 research, review and proceeding book studies (T100) that received the highest number of citations. For additional details on the study, we also consulted PubMed. To gather Altmetric attention scores (AASs), we downloaded the "Altmetric" tool from the Altmetric.com website. The AAS is determined by an algorithm that calculates a weighted total of all the attention a research piece gets. We explored the relationship between the total number of citations and Altmetric scores.

### 3. Results and Discussion

Based on the network visualisation created by VOSviewer, 477 keywords formed a clustered structure reflecting different but interconnected research areas. The map given in Figure 2 consists of three main thematic clusters. The green cluster in the center includes keywords such as Maillard reaction, protein glycation, dietary AGEs, diabetes, and hyperglycemia. In this cluster, dietary and physiological terms are prominent, and it is seen that the majority of the literature examines how AGEs are formed, absorbed, and metabolically processed.

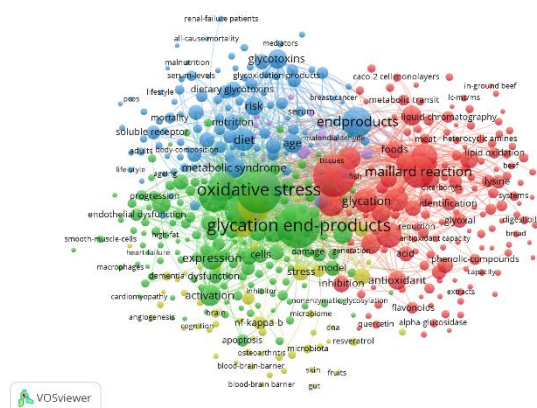


**Figure 2.** Keyword co-occurrence network map of AGEs-related publications in the field of food and nutrition (1992–2025).

Another cluster group, the blue cluster, is seen to include concepts such as inflammation, endothelial dysfunction, renal failure, and diabetes mellitus, as well as the concept of oxidative stress as the main character. This group emphasises the pathophysiological mechanisms linking AGEs to the development of chronic diseases. Due to the frequency of vascular and renal complication terms observed in clinical terms, it shows that the biomedical consequences of AGE accumulation are emphasised in studies.

Finally, the red cluster showed a focus on food processing topics, including keywords such as thermal processing, grilled meat, advanced food technologies, and analytical methods. This cluster indicated the technological dimension of AGEs research, which is related to the formation of harmful AGEs during food processing methods and the methods developed for their measurement and reduction.

The connections between these clusters emphasise the interdisciplinary nature of AGEs research, bridging food chemistry, nutritional sciences, and biomedical research. The distribution of keywords also reflects the increasing emphasis on areas such as studies on AGE-mediated cellular damage, dietary changes, and the effects of food processing

To investigate the novel aspects of the top 100 (T100) most cited scientific research papers in academia, 100 most discussed research papers were selected on social media platforms about AGEs from 1993 to 2014 and they were compared in terms of bibliometrics in web of science and in terms of social media impact in altmetric.com. All articles are published in English. We found the average citation of the top 100 articles to be  $444.46 \pm 270$  (242–1898). According to Table 1, the average altmetric value of T100 is  $29.22 \pm 135$  (0–1335). The list of 100 articles is ranked by the number of

citations. All articles were published in English. One of the scientific papers that received the most cited "Advanced glycation end-products: a review" scientific paper named was published by Rajesh Sing et al. 2001 and received 1.898 citations. AGEs studies carried out in the Australia and United States of America made up the first three publications with more than 3000 citations, as you can see in Table 1. The article with the highest Altmetric value is the 7th article with the highest citation value. When T100 articles are examined according to the distribution of research areas, "Advanced Glycation End Products" constitute the subject. When T100 articles are examined according to the distribution of document type, most articles were published as research articles and review articles (n:100).

As a result of social media platforms mentioned in various including Patents (980), facebook page (135), news outlets (140), blogs (33), Twitter (999), wikipedia pages (58), youtube creators (86), policy source (2), redditors (3), Research Highlight Platform (2), Mendeley (270) respectively.

Twitter geographical and demographic breakdown datas were collected from the profiles of Twitter users who shared these scientific papers and were categorized as the number of shares on Twitter. Our results demonstrate that the United States of America (USA) (61) is the country where most of the social media posts have been done in the world. USA is followed by the Japan (17) and Germany (15). In the top 45 journals that published T100 articles, one or more scientific publications were published.

Most articles published in Journal of Biological Chemistry, the number of articles published was 17. The

majority of the articles were published in Journal of Biological Chemistry and Journal of Clinical Investigation, with 17 and 9 articles published, respectively. The average H-index of 45 journals with two or more AGEs publications are  $265,59 \pm 168.13$ . When we compared our results in Table 2 in terms of quartile (Q) scores of the journals, 37 of them were in Q1, 4 of them were in Q2, 3 of them were in Q3, and 1 of them was in Q4. In the list of countries where T100 articles are published most, with USA (61) dominates in the first place, followed by Japan (17) and Germany (15) (Figure 2). Twenty-five universities with 3 or more publications were included in the list of universities with the highest number of T100 articles. The universities where the most articles were published were Columbia University (USA, 23), University of South Carolina Columbia (USA, 10), University of South Carolina System (USA, 10), and Baker Heart and Diabetes (USA,7) (Figure 3). We found that the most prominent authors in T100 articles were Shoichi Yamagishi with 3 publications, Josephine M. Forbes, Jaime Uribarri and Helen Vlassara with 2 publications.

A study has examined the ketogenic diet's impact and popularity, particularly focusing on altmetric analysis, which gauges the digital attention and engagement research receives on various platforms. The study contrasts the top 100 most-cited research papers with the top 100 most-discussed research papers on social media platforms, evaluating the correlation between traditional biblio-metric analyses and altmetric scores. The study underscores the importance of both bibliometric and altmetric assessments in comprehending the reach and impact of scientific research in the field of the ketogenic diet [16].

**Table 1:** Details of T100 scientific paper in terms of other metrics

Rank	Title	Year	First Author	TC	AC	AS
1	Advanced glycation end-products: a review	2001	Rajesh Sing	1,898	79.08	58
2	Advanced glycation end products: sparking the development of diabetic vascular injury	2006	Alison Goldin	1,635	86.05	79
3	Enhanced cellular oxidant stress by the interaction of advanced glycation end products with their receptors/binding proteins	1994	Shi Du Yan	1,084	34.97	11
4	Understanding RAGE, the receptor for advanced glycation end products	2005	Angelika Bierhaus	1,000	50	11
5	RAGE is a Cellular Binding Site for Amphoterin-Mediation of neurite outgrowth and co-expression of rage and amphoterin in the developing nervous system	1995	Osamu Hori	991	33.03	9
6	Advanced Glycation End Products and Diabetic Complications	2014	Varun P. Singh	879	79.91	67
7	Advanced Glycation End Products in Foods and a Practical Guide to Their Reduction in the Diet	2010	Jaime Uribarri	818	54.53	1335
8	Role of advanced glycation end products in cellular signaling	2014	Christiane Ott	764	69.45	13
9	CML Adducts of Proteins Are Ligands for Receptor for AGEs That Activate Cell Signaling Pathways and Modulate Gene Expression	1999	T. Kislinger	763	29.35	6
10	The role of advanced glycation end products in progression and complications of diabetes	2008	Su-Yen Goh	761	44.76	3
11	Advanced glycation end products contribute to amyloidosis in Alzheimer disease	1994	Michael P. Vitek	741	23.9	8
12	Advanced glycation end products and vascular inflammation: implications for accelerated atherosclerosis in diabetes	2004	Giuseppina Basta	728	34.67	51
13	The Advanced Glycation End Product, Ne -(Carboxymethyl)lysine, Is a Product of both Lipid Peroxidation and Glycoxidation Reactions	1996	Min-Xin Fu	701	24.17	40
14	Advanced Glycation End Products and Oxidative Stress in Type 2 Diabetes Mellitus	2015	Kerstin Nowotny	685	68.5	165

15	Survey of the Distribution of a Newly Characterized Receptor for Advanced Glycation End Products in Tissues	1993	Jerold Brett	682	21.31	4
16	Activation of the receptor for AGEs triggers a p21(ras)-dependent mitogen-activated protein kinase pathway regulated by oxidant stress	1997	Harry M. Lander	649	23.18	12
17	Activation of receptor for AGEs - A mechanism for chronic vascular dysfunction in diabetic vasculopathy and atherosclerosis	1999	Ann Marie Schmidt	643	24.73	10
18	Effect of collagen turnover on the accumulation of advanced glycation end products	2000	Nicole Verzijl	641	25.64	58
19	Advanced glycation end products and RAGE: a common thread in aging, diabetes, neurodegeneration, and inflammation	2005	Ravichandran R.	613	30.65	19
20	Novel splice variants of the receptor for AGEs expressed in human vascular endothelial cells and pericytes, and their putative roles in diabetes-induced vascular injury	2003	Hideto Yonekura	607	27.59	9
21	The biology of the receptor for advanced glycation end products and its ligands	2000	Ann Marie Schmidt	591	23.64	9
22	Improved arterial compliance by a novel advanced glycation end-product crosslink breaker	2001	David A. Kass	562	23.42	3
23	RAGE-mediated neurite outgrowth and activation of NF- $\kappa$ B require the cytoplasmic domain of the receptor but different downstream signaling pathways	1999	Henri J. Huttunen	548	21.08	6
24	Cellular receptors for AGEs. Implications for induction of oxidant stress and cellular dysfunction in the pathogenesis of vascular lesions	1994	Ann Marie Schmidt	541	17.45	51
25	Diastolic stiffness of the failing diabetic heart: importance of fibrosis, advanced glycation end products, and myocyte resting tension	2008	Loek van Heerebeek	539	31.71	4
26	Coregulation of Neurite Outgrowth and Cell Survival by Amphotericin and S100 Proteins through RAGE Activation	200	Henri J. Huttunen	502	20.08	6
27	Receptor-mediated endothelial cell dysfunction in diabetic vasculopathy-Soluble receptor for AGEs blocks hyperpermeability in diabetic rats	1996	Jean-luc Wautier	473	16.31	9
28	AGEs activate endothelium through signal-transduction receptor RAGE- A mechanism for amplification of inflammatory responses	2002	Giuseppina Basta	454	19.74	7
29	N-epsilon-(Carboxymethyl)lysine Is a Dominant Advanced Glycation End Product (AGEs) Antigen in Tissue Proteins	1995	Sharanya Reddy	449	14.97	9
30	Convergence and amplification of TLR and receptor for RAGE signaling pathways via high mobility group B1 (HMGB1)	2008	Judy R. van Beijnum	436	25.65	4
31	Receptor for advanced glycation end products (RAGE) regulates sepsis but not the adaptive immune response	2004	Birgit Liliensiek	434	20.67	10
32	Characterization and functional analysis of the promoter of RAGE, the receptor for advanced glycation end products	1997	Jianfeng Li	431	15.39	7
33	Modification of low density lipoprotein by advanced glycation end products contributes to the dyslipidemia of diabetes and renal insufficiency.	1994	Rick Bucala	429	13.84	7
34	Release of high mobility group box 1 by dendritic cells controls T cell activation via the receptor for advanced glycation end products	2005	Ingrid E. Dumitriu	428	21.4	10
35	Advanced glycation end products induce glomerular sclerosis and albuminuria in normal rats.	1994	Helen Vlassara	407	13.19	6
36	Advanced Glycation End Products (AGE) and Diabetes: Cause, Effect, or Both?	2014	Helen Vlassara	395	35.91	25
37	Carboxymethyllysine Protein Adduct Is a Major Immunological Epitope in Proteins Modified with AGEs of the Maillard Reaction	1996	Kazuyoshi Ikeda	394	13.59	12
38	Beta 2-Microglobulin modified with advanced glycation end products is a major component of hemodialysis-associated amyloidosis.	1993	Toshio Miyata	394	12.31	6
39	Expression of advanced glycation end products and their cellular receptor RAGE in diabetic nephropathy and nondiabetic renal disease	2000	Nozomu Tanji	389	15.56	6
40	Hyperglycemia-Induced Reactive Oxygen Species Increase Expression of the Receptor for Advanced Glycation End Products (RAGE) and RAGE Ligands	2010	Dachun Yao	383	25.53	3
41	RAGE is induced by the glycation products themselves and TNF- $\alpha$ through nuclear Factor- $\kappa$ B, and by 17 $\beta$ -estradiol through Sp-1 in human vascular endothelial cells	2000	Nobushige Tanaka	376	15.04	7
42	Cellular signalling of the receptor for advanced glycation end products (RAGE)	2013	Jianling Xie	371	30.92	3
43	Advanced glycation end products cause epithelial-myofibroblast transdifferentiation via the RAGE	2001	Matthew D. Oldfield	368	15.33	6
44	Advanced glycation end-products and advanced oxidation protein products in patients with diabetes mellitus	2002	Marta Kalousova	358	15.57	0
45	Receptor for advanced glycation end-products is a marker of type I cell injury in acute lung injury	2006	Tokujiro Uchida	357	18.79	6
46	Advanced glycation end products Key players in skin aging?	2012	Paraskevi Gkogkolou	354	27.23	165
47	Randomized trial of an inhibitor of formation of advanced glycation end products in diabetic nephropathy	2004	W. Kline Bolton	353	16.81	3
48	A breaker of advanced glycation end products attenuates diabetes-induced myocardial structural changes	2003	Riccardo Candido	352	16	3



49	Crosslinking by AGEs increases the stiffness of the collagen network in human articular cartilage - A possible mechanism through which age is a risk factor for osteoarthritis	2002	Nicole Verzijl	346	15.04	8
50	Advanced glycation end products increase retinal vascular endothelial growth factor expression	1998	Ming Lu	343	12.7	6
51	Mechanisms of disease: advanced glycation end-products and their receptor in inflammation and diabetes complications	2008	Shi Fang Yan	342	20.12	0
52	Breakers of advanced glycation end products restore large artery properties in experimental diabetes	1998	Bruce H. R.	341	12.63	10
53	Receptor for advanced glycation end products (RAGE) deficiency attenuates the development of atherosclerosis in diabetes	2008	Aino Soro-Paavonen	340	20	0
54	Involvement of beta 2-microglobulin modified with advanced glycation end products in the pathogenesis of hemodialysis-associated amyloidosis. Induction of human monocyte chemotaxis and macrophage secretion of tumor necrosis factor-alpha and interleukin-1	1994	Toshio Miyata	339	10.94	3
55	Blockade of receptor for advanced glycation end-products restores effective wound healing in diabetic mice	2001	Mouza T. Goova	338	14.08	3
56	Does Accumulation of Advanced Glycation End Products Contribute to the Aging Phenotype?	2010	Richard D. Semba	336	22.4	46
57	Advanced Glycation End Products in Alzheimer's Disease and Other Neurodegenerative Diseases	1998	Nobuyuki Sasaki	331	12.26	30
58	Identification of Galectin-3 As High-Affinity Binding Protein for AGEs: A New Member of the AGE-Receptor Complex	1995	Helen Vlassara	331	11.03	7
59	Advanced Glycation End Product-Induced Activation of NF- $\kappa$ B is Suppressed by $\alpha$ -Lipoic Acid in Cultured Endothelial Cells	1997	Angelika Bierhaus	330	11.79	4
60	Implication of an increased oxidative stress in the formation of advanced glycation end products in patients with end-stage renal failure	1997	Toshio Miyata	330	11.79	3
61	Plasma Levels of Soluble Receptor for Advanced Glycation End Products and Coronary Artery Disease in Nondiabetic Men	2005	Colomba Falcone	328	16.4	9
62	Diet-derived advanced glycation end products are major contributors to the body's AGE pool and induce inflammation in healthy subjects	2005	Jaime Uribarri	327	16.35	26
63	AGEs on the surface of diabetic erythrocytes bind to the vessel wall via a specific receptor inducing oxidant stress in the vasculature: a link between surface-associated AGEs and diabetic complications.	1994	Jean-luc Wautier	324	10.45	16
64	The Role of Advanced Glycation End Products in Aging and Metabolic Diseases: Bridging Association and Causality	2018	Jyotiska Chaudhuri	315	45	101
65	The myeloperoxidase system of human phagocytes generates CML on proteins: a mechanism for producing AGEs at sites of inflammation	1999	Melissa Anderson	314	12.08	9
66	Prevention of Diabetic Vascular Dysfunction by Guanidines: Inhibition of Nitric Oxide Synthase Versus AGEs-Formation	1993	Ronald G. Tilton	308	9.63	0
67	Skin Autofluorescence, a Measure of Cumulative Metabolic Stress and AGEs, Predicts Mortality in Hemodialysis Patients	2005	Robbert Meerwaldt	301	15.05	11
68	Advanced glycation end products and the kidney	2005	Jürgen Bohlender	297	14.85	1
69	AGEs-induced Apoptosis and Overexpression of VEGF and Monocyte Chemoattractant Protein-1 in Human-cultured Mesangial Cells	2002	Sho-ichi Yamagishi	295	12.83	0
70	Immunochemical approach to characterize AGEs of the Maillard reaction: Evidence for the presence of a common structure	1991	Seikoh Horiuchi	287	8.44	6
71	Advanced Glycation end Products, Oxidative Stress and Diabetic Nephropathy	2010	Sho-ichi Yamagishi	286	19.07	0
72	Determination of Advanced Glycation End Products in Serum by Fluorescence Spectroscopy and Competitive ELISA	1997	Gerald Münch	286	10.21	0
73	Advanced glycation end products-driven angiogenesis <i>in vitro</i>	1997	Sho-ichi Yamagishi	286	10.21	3
74	Advanced glycation end products up-regulate gene expression found in diabetic glomerular-disease	1994	Chih-Wei Yang	281	9.06	6
75	Inhibition of NADPH Oxidase Prevents AGEs-Mediated Damage in Diabetic Nephropathy Through a PKC- $\alpha$ -Dependent Pathway	2008	Vicki Thallas-Bonke	278	16.35	0
76	Role of the Maillard reaction in aging of tissue proteins- AGEs-dependent increase in imidazolium cross-links in human lens proteins	1998	Elisabeth B. Frye	278	10.3	4
77	Collagen, cross-linking, and advanced glycation end products in aging human skeletal muscle	2007	Jacob M. Haus	276	15.33	8
78	rAGEs has a central role in vessel wall interactions and gene activation in response to circulating AGE proteins	1994	Ann Marie Schmidt	276	8.9	9
79	Immunohistochemical and ultrastructural detection of AGEs in atherosclerotic lesions of human aorta with a novel specific monoclonal antibody	1995	Shuichi Kume	275	9.17	0
80	Expression of receptors for RAGE is closely associated with the invasive and metastatic activity of gastric cancer	2002	Hiroki Kuniyasu	273	11.87	1
81	Advanced glycation end products (AGEs) co-localize with AGE receptors in the retinal vasculature of diabetic and of AGE-infused rats	1997	Alan Stitt	272	9.71	0
82	Chelating activity of advanced glycation end-product inhibitors	2001	David L. Price	271	11.29	4
83	RAGE is a central mediator of the interaction of AGE-beta2microglobulin with human mononuclear phagocytes via an oxidant-sensitive pathway. Implications for the pathogenesis of dialysis-related amyloidosis.	1996	Toshio Miyata	271	9.34	9



84	Oxidative stress and advanced lipoxidation and glycation end products (ALEs and AGEs) in aging and age-related diseases	2019	N.Moldogazie	266	44.33	17
85	Advanced glycation end product interventions reduce diabetes-accelerated atherosclerosis	2004	Josephine M. Forbes	266	12.67	1
86	Restriction of dietary glycotoxins reduces excessive advanced glycation end products in renal failure patients	2003	Jaime Uribarri	263	11.95	12
87	Dietary advanced glycation end products and aging	2010	C.L. Contreras	261	17.4	101
88	Role of advanced glycation end products in diabetic nephropathy	2003	Josephine M. Forbes	259	11.77	0
89	Advanced glycation end-products and the progress of diabetic vascular complications	2004	Vladimir Jakuš	258	12.29	3
90	Advanced glycation end products stimulate osteoblast apoptosis via the MAP kinase and cytosolic apoptotic pathways	2007	Mani Alikhani	255	14.17	0
91	RAGE sustains autophagy and limits apoptosis, promoting pancreatic tumor cell survival	2010	Rui Kang	252	16.8	4
92	Angiotensin II Receptor Antagonists and Angiotensin-Converting Enzyme Inhibitors Lower <i>in vitro</i> the Formation of AGEs Biochemical Mechanisms	2002	Toshio Miyata	251	10.91	9
93	Advanced glycation end products: A nephrologist's perspective	2000	Dominic Raj	251	10.04	3
94	In Vitro Kinetic Studies of Formation of Antigenic Advanced Glycation End Products (AGEs)	1997	A. Ashley Booth	249	8.89	9
95	Immunochemical evidence for the presence of advanced glycation end products in human lens proteins and its positive correlation with aging	1992	Noire Araki	249	7.55	0
96	Restriction of advanced glycation end products improves insulin resistance in human type 2 diabetes: potential role of AGER1 and SIRT1	2011	Jaime Uribarri	248	17.71	21
97	RAGE-binding COOH-terminal motif of amphoterin inhibits invasive migration and metastasis	2002	Henri J. Huttunen	248	10.78	0
98	Regulation of human mononuclear phagocyte migration by cell surface-binding proteins for advanced glycation end products.	1993	Ann Marie Schmidt	246	7.69	8
99	Role of advanced glycation end products in cardiovascular disease	2012	Zeinab Hegab	242	18.62	24
100	Reduction of the accumulation of advanced glycation end products by ACE inhibition in experimental diabetic nephropathy	2002	Josephine M. Forbes	242	10.52	6

TC:Total Citation, AC:Avarage Citation, AS:Altmetric Score

A study has focused on social attention of the relationship between oxidative stress and cancer in terms of AAS. They have used altmetric scores to gauge the impact of these articles on social media and other digital platforms. The study is pioneering in evaluating how cancer and oxidative stress research resonates in the digital space, emphasizing the increasing importance of online social media in academic and public domains [15]. Araujo and his colleagues have shown that a systematic review analyzing how different variables of published articles and journals relate to altmetric scores, which reflect the online media attention garnered by scientific articles. The study identifies key factors like citation counts, journal impact factor, and open access status as influential for altmetric scores, providing insights into the dynamics between scholarly impact and social media presence [17]. Baspakova et al. (2024) have carried out a comprehensive bibliometric analysis, exploring the intricate relationship between ultra-processed foods and gut microbiota. It identifies key research articles, analyzes publication and citation trends, and assesses the global research. The study underscores the escalating concern regarding ultra-processed foods and their potential adverse effects on human health, particularly on the gut microbiota [18]. Alkan et al. (2023) have investigated the relationship between dietary and serum AGEs and serum inflammatory and oxidative stress biomarkers in breast cancer patients. The study assesses the correlation of dietary carboxymethyl lysine (dCML) intake and serum levels of CML with inflammation and oxidative stress markers, considering the treatment phase and human epidermal growth factor receptor-2 (HER2) status [19]. Yu et al. (2021) have discussed a

comprehensive analysis of AGEs in peanuts during the roasting process. It emphasizes the relationship between roasting conditions (temperature and time) and the formation of harmful compounds like AGEs. The study provides a detailed correlation analysis among these compounds, revealing a significant increase in AGEs with the roasting temperature and duration. This research highlights the importance of monitoring and controlling the levels of AGEs in thermally processed foods to ensure food safety [20]. CML, a biomarker of AGEs, is a focal point in food safety due to its potential health implications. Golchinfar et al. have provided a comprehensive overview of the formation, perception, and biological consequences of CML in food and the human body, highlighting the significance of chemical analysis in understanding and mitigating the risks associated with dietary AGEs [21]. Brzezowska et al., 2023 have presented a comparative study on the antioxidant, antiglycation, and chemoprotective potential of beetroot juice powder formulations with functional carriers. It explores the effect of fermentation and carrier type on the quality of freeze and spray-dried powders derived from beetroot juice, assessing their physicochemical, biological properties, and implications for health. The research highlights the relevance of processing methods and the choice of carriers in enhancing the functional properties of beetroot juice powders [22]. Gutierrez Mariscal et al. (2024) have studied the effects of dietary intervention on kidney function in patients with type 2 diabetes and coronary heart disease, focusing on the reduction of circulating methylglyoxal levels and the modulation of AGEs metabolism. It compares the impact of a Mediterranean

diet to a low-fat diet over a five-year period, observing that the Mediterranean diet is linked to a preservation of kidney function, especially in patients with mildly decreased estimated glomerular filtration rate. The study emphasizes the potential benefits of dietary modification in managing AGE-related health issues [23]. Henney et al., (2024) have conducted a systematic review and meta-analysis to explore the association between ultra-processed food intake and dementia risk. It highlights a statistically significant association between high intake of ultra-processed foods and increased dementia risk, underlining the importance of dietary quality in cognitive health and dementia prevention [24]. Huang et al. (2022) have evaluated the formation of AGEs, specifically N-carboxymethyl-lysine (CML), in broiler muscle during postmortem aging and storage. It compares the CML content in white and yellow feather broilers, examining the impact of storage and aging on CML formation. The study also assesses the effect of boiling on CML levels, providing insights into how different types of broiler meat and processing methods influence AGEs formation [25]. Liu et al. (2024) have carried out the role of the Maillard reaction and lipid oxidation in forming AGEs in batter-coated meat products during frying. The study assesses the impact of frying temperature and time on AGE formation, revealing that higher temperatures and longer durations increase AGE levels. It emphasizes the importance of controlling frying conditions to manage a cohort study explores the dietary patterns during pregnancy, particularly focusing on the increased intake of ultra-processed foods (UPF). It examines the association between this dietary shift and various factors like age, education, and lifestyle

behaviors. The study provides insights into how these changes impact maternal and fetal health and highlights the need for targeted public health policies to promote healthier eating habits during pregnancy [26]. A comparison study is related to evaluation of the effect of phenylpropanoids on the binding of heparin to human serum albumin and glycosylated human serum albumin concerning anticoagulant activity. They examine the interaction between phenylpropanoids (caffeic acid, cinnamic acid and p-coumaric acid) and human serum albumin (HSA)/glycosylated human serum albumin (gHSA). It focuses on the implications for anticoagulant activity, particularly in the context of diabetes-related complications. The study utilizes spectroscopic techniques and molecular docking to understand the binding interactions, aiming to contribute to the development of more effective molecules for treating protein conformational diseases [27].

The study utilizes spectroscopic techniques and molecular docking to understand the binding interactions, aiming to contribute to the development of more effective molecules for treating protein conformational diseases [27]. One of the recent investigates the impact of plant extracts on reducing the formation of harmful AGEs in meatballs during cooking. It particularly focuses on the CML levels and explores the phytochemical and bioactivity properties of the extracts. The study provided detailed methodologies on the preparation of meatball samples, cooking, and analysis, aiming to contribute to healthier food processing practices [28].

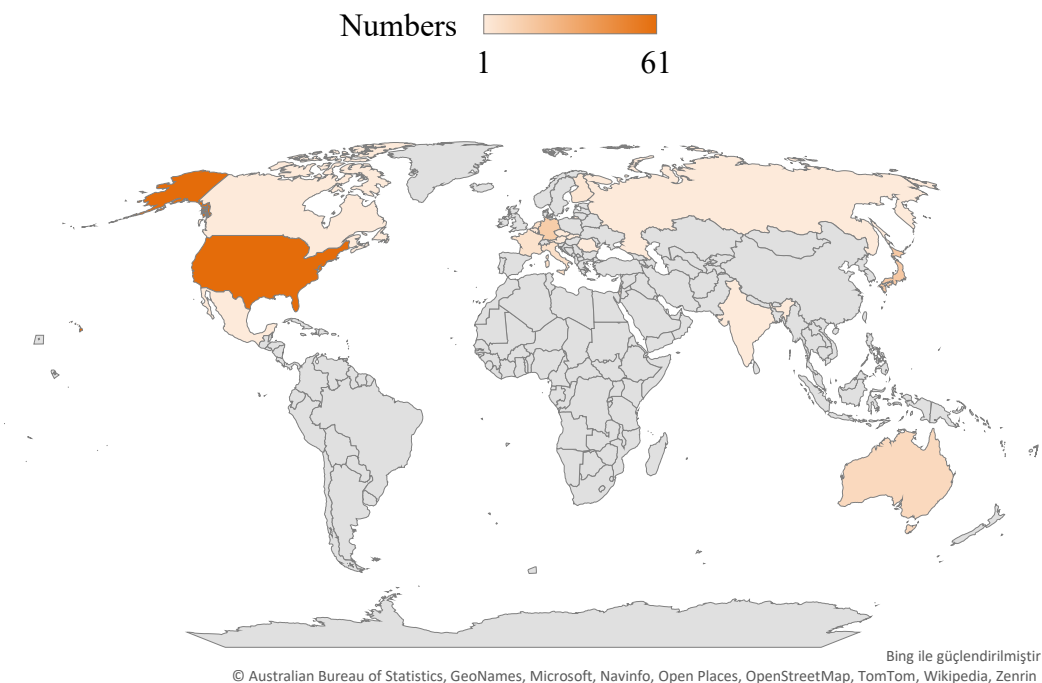


**Figure 2.** Sources of scientific papers from different various countries (T100, WOS).

**Table 2.** Journals with top-100 articles, ranked according to the citations

Journal name	Number of articles	IF*	Q category**	H index**
Journal of Biological Chemistry	17	***	Q1	544
Journal of Clinical Investigation	9	15.9	Q1	527
Diabetes	7	7.7	Q1	359
Proceedings of The National Academy of Sciences of The United States of America	7	11.1	Q1	838
American Journal of Pathology	5	6	Q1	297
Journal of The American Society of Nephrology	5	13.6	Q1	306
Circulation	4	37.8	Q1	654
Biochemistry	2	2.9	Q1	269
Circulation Research	2	20.1	Q1	369
Oxidative Medicine and Cellular Longevity	2	7.310	Q1	134
Physiological Research	2	2.103	Q3	77
Arteriosclerosis, Thrombosis, and Vascular Biology	2	8.7	Q1	287
American Journal of Kidney Diseases	1	13.2	Q1	231
American Journal of Nephrology	1	13.6	Q1	306
American Journal of Physiology Renal Physiology	1	4.2	Q1	184
American Journal of Respiratory and Critical Care Medicine	1	24.7	Q1	404
Angiogenesis	1	9.8	Q1	98
Annals of The New York Academy of Sciences	1	5.2	Q1	274
Journal of Molecular Medicine- JMM	1	4.7	Q1	152
Korean Journal of Physiology & Pharmacology	1	2.0	Q4	37
Redox Biology	1	11.4	Q1	120
Journal of Clinical Endocrinology & Metabolism	1	5.8	Q1	378
Biomolecules	1	5.5	Q2	89
Biochemical Journal	1	4.1	Q2	282
Journal of Immunology	1	5.426	Q1	401
Molecular Medicine	1	5.7	Q1	128
Kidney International	1	19.6	Q1	304
Cell Metabolism	1	29	Q1	318
Arthritis and Rheumatism	1	13	Q1	353
European Journal of Clinical Chemistry and Clinical Biochemistry	1	6.8	Q1	115
Journal of Applied Physiology	1	3.3	Q2	251
The Journal of Pathology: a Journal of the Pathological Society of Great Britain and Ireland	1	2.43	Q1	210
Nutrients	1	5.9	Q1	178
Bone	1	4.1	Q1	217
Cell Death and Differentiation	1	12.4	Q1	243
Diabetes Care	1	16.2	Q1	399
Cancer Research	1	11.2	Q1	483
World Journal of Cardiology	1	1.9	Q3	9
Current Diabetes Reports	1	4.2	Q1	94
Cellular Signalling	1	4.8	Q2	163
Dermato- Endocrinology	1	0.043	Q3	45
Nature Clinical Practice Endocrinology & Metabolism	1	40.5	Q1	187
Journal of Gerontology Series A Biology Sciences and Medical Sciences	1	5.1	Q1	210
Cardiovascular research	1	10.9	Q1	234
Redox Biology	1	11.4	Q1	120
Journal of Clinical Endocrinology & Metabolism	1	5.8	Q1	378
Biomolecules	1	5.5	Q2	89
Biochemical Journal	1	4.1	Q2	282
Journal of Immunology	1	5.426	Q1	401
Molecular Medicine	1	5.7	Q1	128
Kidney International	1	19.6	Q1	304
Cell Metabolism	1	29	Q1	318
Arthritis and Rheumatism	1	13	Q1	353
European Journal of Clinical Chemistry and Clinical Biochemistry	1	6.8	Q1	115
Journal of Applied Physiology	1	3.3	Q2	251
The Journal of Pathology: a Journal of the Pathological Society of Great Britain and Ireland	1	2.43	Q1	210
Nutrients	1	5.9	Q1	178
Bone	1	4.1	Q1	217
Cell Death and Differentiation	1	12.4	Q1	243
Diabetes Care	1	16.2	Q1	399
Cancer Research	1	11.2	Q1	483
World Journal of Cardiology	1	1.9	Q3	9
Current Diabetes Reports	1	4.2	Q1	94
Cellular Signalling	1	4.8	Q2	163
Dermato- Endocrinology	1	0.043	Q3	45
Nature Clinical Practice Endocrinology & Metabolism	1	40.5	Q1	187
Journal of Gerontology Series A Biology Sciences and Medical Sciences	1	5.1	Q1	210
Cardiovascular research	1	10.9	Q1	234

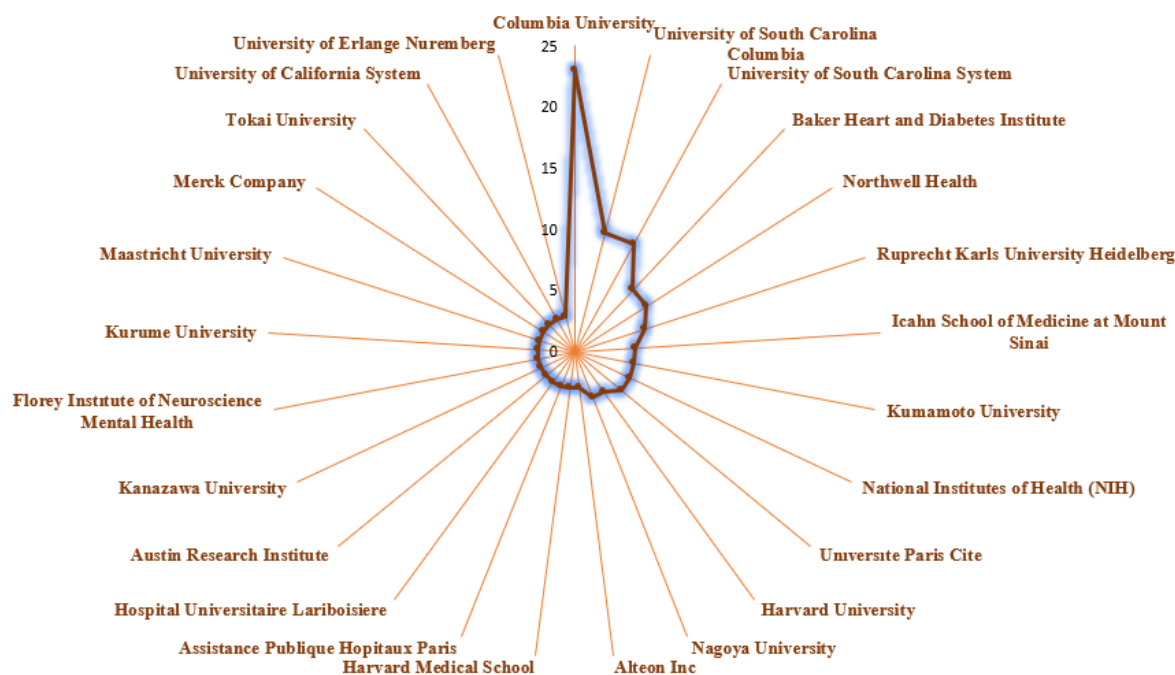


**Figure 3.** Some familiar institutions/universities of T100 most cited page

As Figure 4 has demonstrated, there is no correlation between altmetric scores and the number of citations. This may be because not all AGEs articles are shared on social media because they don't get enough attention from scientists and other researchers. In light of this, it would be preferable for any academic research on public health to be posted on social media platforms so that everyone is able to read it in order to enhance their knowledge and behaviors.

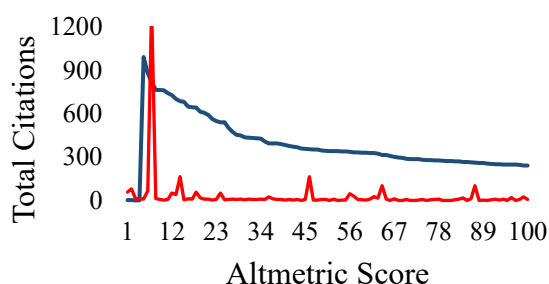


**Figure 4:** Graph of correlations TC-AS numbers

In recent years, the intersection of analytical and organic chemistry has emerged as a pivotal force in enhancing food preservation and safety. The focus has been on leveraging these scientific disciplines to innovate in areas such as advanced food packaging, precise detection methods for harmful substances, and the creation of ingredients that promote health. This multidisciplinary approach is not only addressing current industry challenges but is also setting a new standard for ensuring

the safety and quality of food products. With the backing of impactful research and a commitment to excellence, the field continues to evolve, offering promising solutions to some of the most pressing issues faced by the food industry today. Considering the significant impact of dietary habits on AGEs accumulation, the most fundamental intervention to limit AGEs intake would be to reduce endogenous AGEs formation. Another strategy is to adopt a diet rich in raw fruits and vegetables, reduce processed food intake, and use cooking methods that minimize the formation of AGEs. In addition, lifestyle changes such as physical activities and quitting smoking also play an important role in reducing AGEs accumulation. On the other hand, the formation and accumulation of AGEs play a critical role in aging and the pathogenesis of various chronic diseases. Although endogenous formation of AGEs is a natural part of metabolism, lifestyle and dietary choices significantly affect their levels in the body. Adopting a diet low in AGEs and making conscious lifestyle choices can potentially reduce the risk or slow the progression of diseases associated with AGEs. Further research to fully understand the complex mechanisms of the formation of AGEs and their precise role in disease pathology is important and offers a promising avenue for the development of targeted interventions. Recently, studies have emphasized the latest innovations in food packaging and safety, as well as the use of analytical methods during the detection of toxic molecules and to ensure food quality. In this context, emerging research topics such as the use of bioinformatics, biosensors and computational



chemistry in food science are also areas that need to be focused on.

The relationship between the AAS and research on AGEs involve how the scientific community and the public engage with and value this research. The AAS provides a quantitative measure of the attention a research article receives across various platforms, including social media, news outlets, blogs, and academic citations. AAS could show some crucial four points to scholar/researchers such as public engagement, research impact, academic interest, feedback loop. Research on AGEs that garners high Altmetric scores likely resonates with or is deemed relevant by a broader audience. This can include patients, healthcare providers, or individuals interested in aging, diabetes, and related health issues. High scores indicate that the research has been widely shared, discussed, or mentioned across various media. A high Altmetric score suggests that the research on AGEs has a significant impact on its field or on public awareness. This could influence funding decisions, policy-making, or further studies in the area of glycation and its implications for health and disease. Beyond public engagement, high scores can also reflect academic interest, indicating that the research is being cited in other scholarly works, discussed in academic circles, or presented at conferences. This level of interest can contribute to the development of new hypotheses, research projects, and collaborations. The attention measured by Altmetric can create a feedback loop, where increased visibility leads to more research, funding, and further public and academic interest in AGEs. This can accelerate advancements in understanding and potentially addressing the health impacts associated with AGEs. In summary, the relationship between the AASs and research on AGEs underscores the importance of disseminating scientific findings and engaging a wide audience. It highlights the relevance of research on AGEs to various stakeholders, from scientists to the general public, and its potential impact on health and disease understanding and management.

This study provides a comprehensive analysis of the social interactions surrounding a critical public health issue. The analysis of these interactions, using tools such as AAS, provides valuable insights into how academic research transcends traditional boundaries and impacts various professional, social and interdisciplinary contexts. The study highlights the potential of research to contribute to public discourse and its application in broader societal conversations, thus emphasizing the extended impact of academic knowledge. In addition, a high AAS can increase the visibility of research, potentially leading to more collaborations, funding opportunities and citations. This helps researchers understand and demonstrate the wider impact of their work. Such studies are a guide to the assessment of the social relevance and impact of research, and a basis for the design of future projects to better meet public needs and expectations. Such studies provide a guide to

assessing the level of social relevance and impact of the research. It also has the potential to become a research basis for the design of future projects to better meet public needs and expectations. In addition, these findings can inform strategies for more effective dissemination of research results to a broader public. In this context, the present study provides a detailed analysis of the biochemical pathways leading to the formation of AGEs, a topic of significant public health relevance. It also examines the major dietary sources of AGEs and the role of food processing in their accumulation. The study aims to highlight the importance of AGEs accumulation for both individual and societal health and to provide a basis for future research and public health interventions.

The article also examined bibliometric and altmetric analysis of research topics such as AGEs and the link between chemistry, biochemistry, food chemistry, clinical studies, and natural compounds. It also highlighted the importance of both traditional citation metrics and modern digital engagement metrics in understanding the reach and impact of scientific research in terms of the impact of ultra-processed foods.

#### 4. Conclusion

Food preservation and safety are paramount for public health. Recent strides in analytical and biochemistry studies have significantly bolstered our ability to maintain food quality and safety. This article synthesizes findings from four pivotal studies, highlighting the interplay between chemical analysis, food vendor practices, and the biological implications of foodborne compounds like AGEs. Exploration of the most-cited and most-discussed research articles in fields like the AGEs, highlighting the correlation between traditional bibliometric analyses and altmetric scores. The significance of social media and digital platforms in disseminating and discussing glycation and clinical research findings. This study provides a comprehensive overview of AGEs from previous to today, beginning of their formation, health implications, and possible interventions. Once the content of the provided documents is accessible, more specific details and citations can be incorporated to enrich the article with recent research findings and data. This encompasses a range of activities including proper agricultural practices, hygienic food processing, thorough testing for contaminants, and educating consumers about safe food handling. In the contemporary landscape of food science, the intersection of nutritional quality, food safety, and the impact of food processing techniques remains a critical area of research. The global dependency on processed foods, underscored by the burgeoning consumption of pre-packaged and thermally processed items, necessitates a profound understanding of their nutritional profiles and potential health implications. Moreover, the articles extend beyond the laboratory to encompass the realm of digital engagement and societal discourse, exploring the impact of scientific research in the digital age through bibliometric and altmetric analyses.

## 5. References

- [1]. Madilo, F. K., Kunadu, A. P.-H., Tano-Debrah.K. 2024. Challenges with food safety adoption: A review. *Journal of Food Safety*;44(1):e13099. <https://doi.org/10.1111/jfs.13099>
- [2]. Barnabas, B., Bavorova, M., Madaki, M. Y., Kaechele. H. 2024. Food safety knowledge, attitudes, and practices of food vendors participating in Nigeria's school feeding program. *Journal of Consumer Protection and Food Safety*; (19):1-14 <https://doi.org/10.1007/s00003-023-01476-3>
- [3]. Albuquerque, T. G., Bragotto, A. P. A., Costa. H. S. 2022. Processed Food: Nutrition, Safety, and Public Health. *International Journal of Environmental Research and Public Health*; 19(24): 16410. <https://doi.org/10.3390/ijerph192416410>
- [4]. Vale, C., Almeida, C., Azevedo, J., Padrao, P. 2024. Nutrient profile of packaged foods according to the degree of processing. *International Journal of Food Sciences and Nutrition*;75 (2), 148-158 <https://doi.org/10.1080/09637486.2023.2299771>
- [5]. Chattu V.K. 2015. Food safety as an integral part of Food Security: Addressing the governance issues and the critical role of climate change. *International Journal of Advanced Research*;3(12): 1472–1474.
- [6]. Yusufoglu, B., Karakuş, E., Yaman, M. (2022). Determining the amount and bioaccessibility of methylglyoxal and glyoxal in functional snack foods with herbal teas: effect of different herbal teas on  $\alpha$ -Dicarbonyls. *Food Science and Technology*; 42:e82621.
- [7]. Ravichandran, G., Lakshmanan, D. K., Raju, K., Elangovan, A., Nambirajan, G., Devanesan, A. A., Thilagar. S. 2019. Food advanced glycation end products as potential endocrine disruptors: An emerging threat to contemporary and future generation. *Environment International*; 123, 486–500. <https://doi.org/10.1016/j.envint.2018.12.032>
- [8]. Toydemir, S., Yusufoglu. B. 2024. Effect of Processed Foods on Advanced Glycation End Products: Cancer Cases. *ITU Journal of Food Science and Technology*; 2(1):9-18.
- [9]. Liu, Y., Liu, C., Huang, X., Li, M., Zhao, G., Sun, L., Deng. W. 2024. Exploring the role of Maillard reaction and lipid oxidation in the advanced glycation end products of batter-coated meat products during frying. *Food Research International*; 178;113901.
- [10]. Peng, J., Liang, G., Wen, W., Huang, W., Qiu, Y., Xiao, G., Wang. Q. 2024. Blueberry anthocyanins extract inhibits advanced glycation end-products (AGEs) production and AGEs-stimulated inflammation in RAW264.7 cells. *Journal of the Science of Food and Agriculture*;104(1):75–82. <https://doi.org/10.1002/jsfa.12893>
- [11]. Si, C., Liu, F., Peng, Y., Qiao, Y., Wang, P., Wang, X., Gong, J., Zhou, H., Zhang, M., Song. F. 2024. Association of total and different food-derived advanced glycation end-products with risks of all-cause and cause-specific mortality. *Food & Function*; 15(3), 1553-1561. <https://doi.org/10.1039/D3FO03945E>
- [12]. Sourris, K. C., Ding, Y., Maxwell, S. S., Al-Sharea, A., Kantharidis, P., Mohan, M., Rosado, C. J., Penfold, S. A., Haase, C., Xu, Y., Forbes, J. M., Crawford, S., Ramm, G., Harcourt, B. E., Jandeleit-Dahm, K., Advani, A., Murphy, A. J., Timmermann, D. B., Karihaloo, A., Coughlan. M.T. 2024. Glucagon-like peptide-1 receptor signaling modifies the extent of diabetic kidney disease through dampening the receptor for advanced glycation end products-induced inflammation. *Kidney International*;105(1): 132–149. <https://doi.org/10.1016/j.kint.2023.09.029>
- [13]. Takeuchi, M., Suzuki, H., Takeda, K., Sakai-Sakai. A. 2024. Toxic advanced glycation end-products (TAGE) are major structures of cytotoxic AGEs derived from glyceraldehyde. *Medical Hypotheses*; 183:111248. <https://doi.org/10.1016/j.mehy.2023.111248>
- [14]. Schalkwijk, C. G., Stehouwer, C. D. A. (2020). Methylglyoxal, a Highly Reactive Dicarbonyl Compound, in Diabetes, Its Vascular Complications, and Other Age-Related Diseases. *Physiological Reviews*; 100(1):407–461.<https://doi.org/10.1152/physrev.00001.2019>
- [15]. Vardar, G., Hanikoglu, F., Guney, T., Dokur, M., & Karadag, M. (2022). Evaluation of the Relationship between Cancer and Antioxidants from an Altmetric Perspective. *Eurasian Journal of Medicine and Oncology*; 6(1):128–139.
- [16]. Yusufoglu, B., Vardar, G., Kaya, G., Yalcin, H. 2023. A new approach to biochemistry: Bibliometric and altmetric analyses in the ketogenic diet. *Medicine Science International Medical Journal*;12(4):1145. <https://doi.org/10.5455/medscience.2023.07.108>
- [17]. Araujo, A. C., Vanin, A. A., Nascimento, D. P., Gonzalez, G. Z., Pena Costa. L.O. 2021. What are the variables associated with Altmetric scores? *Systematic Reviews*;10(1):193. <https://doi.org/10.1186/s13643-021-01735-0>
- [18]. Baspakova, A., Bazargaliyev, Y. S., Kaliyev, A. A., Mussin, N. M., Karimsakova, B., Akhmetova, S.Z., Tamadon. A. 2024. Bibliometric analysis of the impact of ultra-processed foods on the gut microbiota. *International Journal of Food Science and Technology*, 59(3), 1456-1465. <https://doi.org/10.1111/ijfs.16894>
- [19]. Alkan, Ş. B., Artaç, M., Aksoy, F., Belviranlı, M. M., Gürbilek, M., Çizmecioğlu, H. A., Rakıcıoğlu. N. 2023. Are dietary and serum advanced glycation end-products related to inflammation and oxidation biomarkers in breast cancer patients: A follow-up study. *Supportive Care in Cancer*;31(6):334. <https://doi.org/10.1007/s00520-023-07772-w>
- [20]. Yu, J., Yu, X., Shi, L., Liu. W. 2023. Comprehensive Analyses of Advanced Glycation end Products and Heterocyclic Amines in Peanuts during the Roasting Process. *Molecules*; 28(20):7012 <https://doi.org/10.3390/molecules28207012>
- [21]. Golchinfar, Z., Farshi, P., Mahmoudzadeh, M., Mohammadi, M., Tabibiazar, M., Smith. J.S. 2023. Last five years development in food safety perception of n-Carboxymethyl lysine. *Food Reviews International*;39(6):3225-3261.
- [22]. Brzezowska, J., Skrzypczak, K., Radzki, W., Turkiewicz, I. P., Ziaja-Softys, M., Bogucka-Kocka, A., Wojdyło, A., Michalska-Ciechanowska. A. 2023. Comparative study of antioxidant, antiglycation and chemoprotective potential of beetroot juice powder formulations with functional carriers. *Food Bioscience*; 55:103049.<https://doi.org/10.1016/j.fbio.2023.103049>
- [23]. Gutierrez-Mariscal, F. M., Podadera-Herreros, A., Alcalá-Díaz, J. F., Cardelo, M. P., Arenas-de Larriva, A. P., de la Cruz-Ares, S., Torres-Pena, J. D., Luque, R. M., Perez-Martinez, P., Delgado-Lista, J., Lopez-Miranda, J., Yubero-Serrano. E.M. 2024. Reduction of circulating methylglyoxal levels by a Mediterranean diet is associated with preserved kidney function in patients with type 2 diabetes and coronary heart disease: From the CORDIOPREV randomized controlled trial. *Diabetes & Metabolism*;50(1):101503. <https://doi.org/10.1016/j.diabet.2023.101503>
- [24]. Henney, A. E., Gillespie, C. S., Alam, U., Hydes, T. J., Mackay, C. E., Cuthbertson. D.J. 2024. High intake of ultra-processed food is associated with dementia in adults: A systematic review and meta-analysis of observational studies. *Journal of Neurology*;271(1):198–210. <https://doi.org/10.1007/s00415-023-12033-1>
- [25]. Huang, S., Dong, X., Zhang, Y., Chen, Y., Yu, Y., Huang, M., Zheng. Y. 2022. Formation of advanced glycation end products in raw and subsequently boiled broiler muscle: Biological variation and effects of postmortem ageing and storage. *Food Science and Human Wellness*;11(2):255–262. <https://doi.org/10.1016/j.fshw.2021.11.012>

- [26]. Fraga, A. C. S. A., Bastos, M. P., Theme-Filha, M.M. 2024. Increased consumption of ultra-processed foods during pregnancy is associated with sociodemographic, behavioral, and obstetric factors: A cohort study. *Nutrition Research*;121:28–38.  
<https://doi.org/10.1016/j.nutres.2023.10.006>
- [27]. Akbari, V., Ghobadi, S. (2024). Evaluation of the effect of phenylpropanoids on the binding of heparin to human serum albumin and glycosylated human serum albumin concerning anticoagulant activity: A comparison study. *International Journal of Biological Macromolecules*;257:128732.  
<https://doi.org/10.1016/j.ijbiomac.2023.128732>
- [28]. Aydemir, M. E., Arslan, A., Takim, K., Altun, S. K., Yilmaz, M. A., & Cakir, O. (2024). Inhibitory effect of *Paliurus spina-christi* Mill., *Celtis tournefortii* L. and *Nigella sativa* L. on N-ε-(Carboxymethyl) lysine in meatballs. *Meat Science*;207:109362.  
<https://doi.org/10.1016/j.meatsci.2023.109362>

# Effects of 2,2-Dichloroacetamide Additive on Perovskite Solar Cells Efficiency

Adem Mutlu<sup>1\*</sup> , Sevdie Başak Turgut<sup>1</sup> 

<sup>1</sup> Solar Energy Institute, Ege University, Izmir, Türkiye, 35100

\* [adem.mutlu@ege.edu.tr](mailto:adem.mutlu@ege.edu.tr)

\* Orcid No: 0000-0002-1696-4379

Received: 9 November, 2024

Accepted: 16 December, 2024

DOI: 10.18466/cbayarfbe.1582175

## Abstract

This study investigates the effect of adding 2,2-dichloroacetamide (DCA) to the anti-solvent process in perovskite film fabrication. The results show that DCA additive increases the apparent grain size of the perovskite, reduces crystal defects, and improves the optoelectronic properties of perovskite solar cells (PSCs). Triple-cation perovskite thin films modified with DCA exhibit a 16% improvement in device performance compared to the unmodified control cell, due to increased emission intensity, longer charge carrier lifetimes, and passivation of surface defects, resulting in reduced hysteresis. The use of DCA reduces charge carrier recombination losses in PSCs, leading to enhancements in fill factor (FF), short-circuit current density ( $J_{sc}$ ), and power conversion efficiency (PCE), increasing the PCE of the control cell from 12.6% to 14.6%. This research highlights the potential of molecular additives to optimize crystallization kinetics, facilitating the development of more efficient PSCs. The findings reveal that DCA additive plays a significant role in enhancing perovskite film quality. This strategy has the potential to improve the structural integrity and optoelectronic properties of perovskite layers, thereby enhancing the performance of solar cells.

**Keywords:** perovskite, solar cell, efficiency, crystallization, passivation, anti-solvent, additive

## 1. Introduction

Perovskite solar cells (PSCs) are widely recognized as a leading and rapidly developing technology in the field of renewable energy. The high production costs and efficiency limitations of traditional silicon-based solar cells have increased the demand for more cost-effective alternatives. On the other hand, PSCs have attracted considerable attention in the photovoltaic industry because of their low production costs, flexible manufacturing processes, and improving efficiency due to continuous research and development. Materials such as methylammonium lead iodide ( $\text{CH}_3\text{NH}_3\text{PbI}_3$ ) in perovskite solar cells are more effective at converting sunlight into electricity, thanks to their wide light absorption spectrum and high charge carrier mobility, thereby enhancing device performance [1-3]. Thanks to these key properties, the efficiency of PSCs has risen from 3.8% to 26.7% through various studies, bringing them close to competing with silicon-based cells [4]. However, one of the biggest challenges faced by perovskite solar cells is their environmental stability,

which is not yet sufficient for long-term use. The perovskite structure is prone to degradation when exposed to factors like thermal stability, moisture, and oxygen. This degradation reduces the material's performance over time and slows down the transition to commercial use [5,6]. The volatility of organic components in the perovskite structure and their sensitivity to environmental factors lead to structural degradation and the formation of unwanted by-products such as lead iodide ( $\text{PbI}_2$ ). Therefore, various strategies are being developed to improve the long-term stability of PSCs [7,8]. Changes in the perovskite structure and composition have been shown to enhance stability by achieving a more crystalline and homogeneous surface and creating larger grain boundaries, which in turn improve the material's stability [9]. One of the most common methods to address stability issues is modifying the chemical composition of the perovskite structure and optimizing the film morphology. For example, replacing methylammonium ( $\text{MA}^+$ ) ions with more stable cations such as cesium ( $\text{Cs}^+$ ) and formamidinium ( $\text{FA}^+$ ) reduces the degradation tendency of the structure and enhances the environmental stability of PSCs. This type of



structure, known as a triple-cation structure, forms the CsFAMA composition. Triple-cation structures offer higher stability and efficiency compared to single-cation ones, making PSCs more resistant to environmental factors. Additionally, using different halogens such as iodide (I<sup>-</sup>), bromine (Br<sup>-</sup>), and chlorine (Cl<sup>-</sup>) in the perovskite material helps broaden the light absorption spectrum and increase charge carrier mobility, enabling the production of more efficient devices. These modifications reduce crystal defects and minimize carrier losses by obtaining larger grain boundaries in the perovskite layer [10-12].

Various approaches have been developed to reduce crystal defects and prevent charge carrier recombination in perovskite films [13-15]. The use of additives is one such effective method. Additives that influence crystal growth and film morphology play a crucial role in obtaining more stable and efficient devices [16,17]. Studies by researchers such as Zhang and Snaith have demonstrated that certain additives can stabilize the structure and enhance the efficiency of PSCs. These additives passivate defects on the crystal surfaces, reducing carrier losses and improving device performance [18,19].

The production processes of perovskite thin films have a significant impact on solar cell performance. Solution-based techniques are commonly used in PSC fabrication, and these techniques directly affect the quality of the perovskite thin films. Solution-based methods like the anti-solvent technique are employed to optimize the crystallization rate and surface morphology of perovskite solutions. However, to achieve stable crystal structures and smooth morphology, the use of additional additives during the anti-solvent process is necessary. Additives incorporated into anti-solvents help regulate the crystallization process, leading to the formation of more stable and efficient structures [9,20,21].

In this study, we focused on incorporating 2,2-dichloroacetamide (DCA) additive into the anti-solvent to improve the crystallization process and surface morphology of perovskite films. By regulating the crystallization kinetics, DCA creates a structure in the film where perovskite crystallization is enhanced and defects are passivated, thereby minimizing carrier losses. The results of the analysis show that DCA directs crystal growth, leading to a smoother and homogeneous surface with higher crystallinity. As a result, the perovskite film's light absorption increases, charge carrier recombination decreases, and the overall optoelectronic performance of the device improves.

## 2. Materials and Methods

### 2.1. Materials

The lead iodide (PbI<sub>2</sub>, 99.99%) used in the study was obtained from Tokyo Chemical Industry (TCI). 2-

Propanol (HPLC, 99.9%), titanium isopropoxide (Ti[OCH(CH<sub>3</sub>)<sub>2</sub>]<sub>4</sub>, 97%), acetonitrile (anhydrous ACN, 99.8%), hydrochloric acid (HCl, 37%), chlorobenzene (anhydrous CB, 99.8%), cesium iodide (CsI, 99.999%), 4-tert-butylpyridine (4-tBP, 98.0%), and 2,2-dichloroacetamide (DCA) were obtained from Sigma-Aldrich. Fluorine-doped tin oxide glass (FTO) with a sheet resistance of 14 Ohm/sq and dimensions of 2.5x2.5 cm<sup>2</sup> were provided by OPVTECH (FTO22-15). Lead bromide (PbBr<sub>2</sub>, 99.999%), methylammonium bromide (MABr, >99.5%) and formamidinium iodide (FAI, >99.5%) were supplied by Lumtec. Spiro-OMeTAD was purchased from Borun. Anhydrous N,N-dimethylformamide (DMF, >99.5%) and bis(trifluoromethanesulfonyl) lithium salt (Li-TFSI, 99.0%) were provided by Acros, while dimethyl sulfoxide (DMSO, >99.7%) was obtained from Merck.

### 2.2. Characterization

Various experimental methods and devices were used for the characterization of photovoltaic devices. Electrical properties were determined through current density-voltage (J-V) measurements performed using a Keithley 2400 source meter under AM1.5G simulation, while morphological and structural properties were examined with an Ambios atomic force microscope (AFM) and a Panalytical X-ray diffractometer (XRD). Optical properties were analyzed by obtaining absorption spectra using a Perkin Elmer Lambda 950 UV-Vis spectrophotometer, and photoluminescence (PL) and time-resolved photoluminescence (TRPL) spectra were recorded with an Edinburgh Instruments system under pulsed laser excitation at 655 nm. Fourier Transform Infrared Spectroscopy (FTIR) spectroscopy was performed using a Thermo Scientific Nicolet iS50 device, and film thickness was measured with a Dektak profilometer.

### 2.3. Device fabrication

FTO substrates, 2.5 cm x 2.5 cm in size, were initially cleaned for 20-minutes using a sequence of distilled water, acetone, and 2-propanol. Titanium dioxide (TiO<sub>2</sub>) was synthesized by the sol-gel method. The cleaned FTO glass substrates underwent a 7-minute oxygen plasma treatment, followed by the application of a TiO<sub>2</sub> solution using spin coating at 2000 rpm for 20 seconds to create a uniform layer. Finally, the coated films were annealed at 460°C for 1 hour to achieve the anatase crystal structure of TiO<sub>2</sub>. Then, a 0.1 M Li-TFSI solution prepared in anhydrous ACN was applied onto the TiO<sub>2</sub>-coated films at 3000 rpm for 40 seconds, followed by another 1 hour annealing at 460°C. To maintain a controlled environment, all coating operations for the subsequent layers were performed inside a glovebox. A triple-cation perovskite solution with the composition of Cs<sub>0.05</sub>(FA<sub>0.83</sub>MA<sub>0.17</sub>)<sub>0.95</sub>Pb(I<sub>0.83</sub>Br<sub>0.17</sub>)<sub>3</sub> was dissolved in an anhydrous DMF and DMSO (4:1 ratio) mixture [11,22].

The prepared perovskite solution was applied to the Li-TiO<sub>2</sub>-coated substrates through a two-step spin-coating process: the first step was performed at 2000 rpm for 25 seconds, followed by the second step at 4000 rpm for 20 seconds. During the second step, the surface was washed with 100  $\mu$ L of anhydrous CB at the 10<sup>th</sup> second. DCA was added to the CB at a concentration of 1 mg/mL. To enhance the solubility of DCA, it was kept in an ultrasonic bath at 50°C for 20 minutes. The anti-solvent process was carried out with both CB (control) and CB+DCA, and the perovskite thin films were annealed at 100°C for 1 hour to achieve a high-quality perovskite structure. Spiro-OMeTAD, was prepared by dissolving it in anhydrous CB at a concentration of 73 mg/mL. To this solution, 30  $\mu$ L of 4-tBP and 16  $\mu$ L of a Li-TFSI/acetonitrile solution (520 mg/mL) were added to enhance charge transport. The resulting mixture was uniformly deposited onto the substrate using spin coating at 4000 rpm for 20 seconds. To complete the device, a thin film of molybdenum trioxide (MoO<sub>3</sub>, 8 nm thick) was thermally evaporated onto the Spiro-OMeTAD layer, followed by a thicker layer of silver (Ag, 100 nm thick). The entire process was carried out under high vacuum conditions ( $2 \times 10^{-7}$  Torr). The active area of the devices is 0.095 cm<sup>2</sup>.

### 3. Results and Discussion

The configuration of the PSCs with the FTO/Li-TiO<sub>2</sub>/CsFAMA/Spiro-OMeTAD/MoO<sub>3</sub>/Ag is shown in Figure 1a. The triple-cation perovskite thin films were coated using the spin-coating method, aided by an anti-solvent [11]. During the perovskite thin film coating, DCA material was used within the CB anti-solvent to control the crystallization kinetics. The influence of DCA molecules on the perovskite was examined using various techniques, including XRD, AFM, PL, TRPL, UV-Vis spectroscopy, and FTIR spectroscopy. As shown in the XRD patterns in Figure 1b, the diffraction peaks from all perovskites were almost identical. Characteristic peaks associated with the CsFAMA perovskite structure were observed at  $2\theta$  values of 14.03°, 20.0°, 24.47°, 28.3°, 31.7°, 34.87°, 40.46°, and 43.0°, consistently appearing in all films treated with either the control or DCA molecules.[23] Notable differences were observed in the peak intensities at  $2\theta=14.03^\circ$  and  $28.3^\circ$ , corresponding to the (110) and (220) planes, respectively. Bakr et al. achieved a similar oriented growth using alkylamine ligands (AALs). The films treated with AALs demonstrated enhanced growth along the (110) orientation, showing a reduction in trap state density, as well as improvements in charge mobility and diffusion length [24]. The lack of any change in the peak positions of the perovskite indicates that the perovskite structure is not significantly affected by the DCA molecule used; however, it is understood that these molecules contributed to the oriented growth of the perovskite grain boundaries [25].

The absorption spectra in Figure 2a reveals that all perovskite thin films exhibit similar patterns. Since the perovskite structure is not significantly affected by the DCA molecule, no substantial differences in the bandgap energies are expected. The bandgap energy of the control film, calculated from the Tauc plots, is 1.612 eV, which is consistent with the literature (Figure 2b). [11,26]. For the perovskite sample modified with DCA within the anti-solvent, the bandgap energy was calculated to be 1.606 eV. The average film thicknesses of the perovskite films washed with CB and CB+DCA were found to be  $400 \pm 5$  nm and  $450 \pm 10$  nm, respectively. As the thickness of the perovskite thin films increases, light absorption also increases. Consequently, the film washed with CB+DCA exhibits the highest absorbance [27].

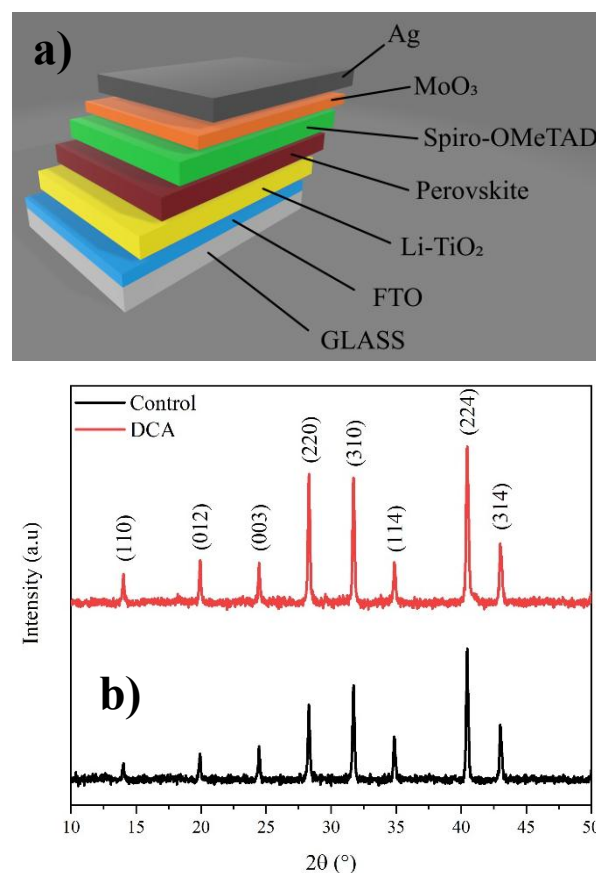


**Figure 1.** a) Device configuration, b) XRD spectra of control and DCA-modified triple cation perovskite thin films.

Figure 3a displays the PL spectra of perovskite thin films coated on glass substrates with and without the use of DCA molecules in anti-solvent. The PL peak at approximately 770 nm for the reference triple cation perovskite structure aligns with the literature. Notably, the PL intensities of the perovskite film coated with DCA were higher than those of the control film, suggesting that the use of DCA effectively reduces non-radiative recombination in the perovskite layer. Defects in perovskite films serve as trap centers for charge carriers,

leading to energy loss via non-radiative recombination pathways. To investigate the impact of the DCA molecules on the photoluminescence dynamics, TRPL decay measurements were conducted at the primary PL peak of 770 nm, using an excitation laser with a wavelength of 656 nm (Figure 3b). These components allow the extraction of two types of recombination regimes:  $\tau_1$ , dominated by interfacial recombination with a short carrier lifetime, and  $\tau_2$ , dominated by bulk recombination with a long carrier lifetime [28,29]. The  $\tau_2$  value of the DCA-modified perovskite thin film increased from 94.03 ns to 208.53 ns (Table 1). The longer carrier lifetime in the DCA-modified perovskite film indicates a significant reduction in non-radiative recombination of carriers due to the elimination of defects [30].

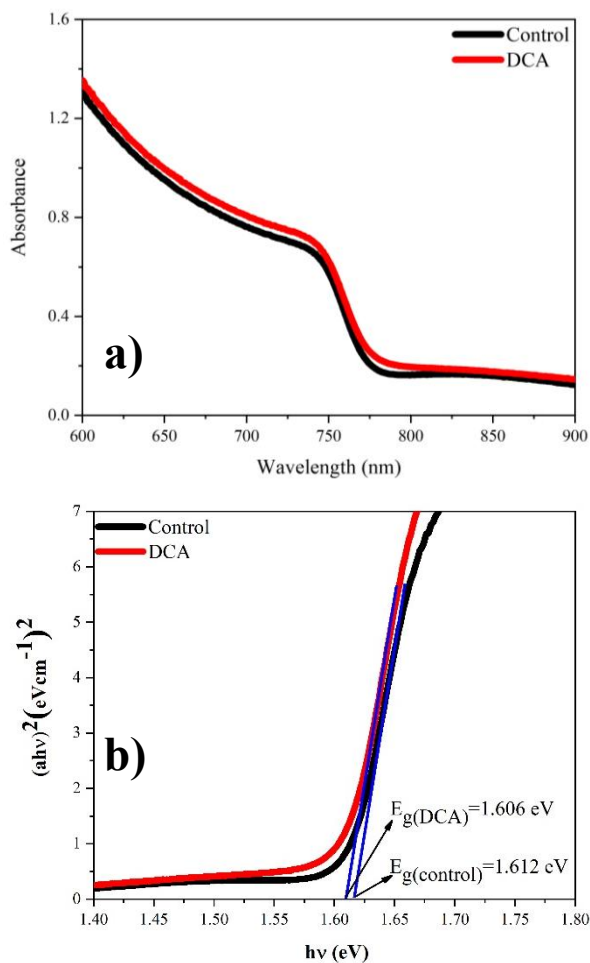


**Figure 2.** (a) UV-Vis spectra and (b) Tauc plots of control and DCA-modified triple cation perovskite thin films.

**Table 1.** TRPL parameters of control and DCA-modified perovskite thin films.

ID	$\tau_1$ (ns)	$\tau_2$ (ns)	$\chi^2$
Control	21.44	94.03	1.126
DCA	44.43	208.53	1.179

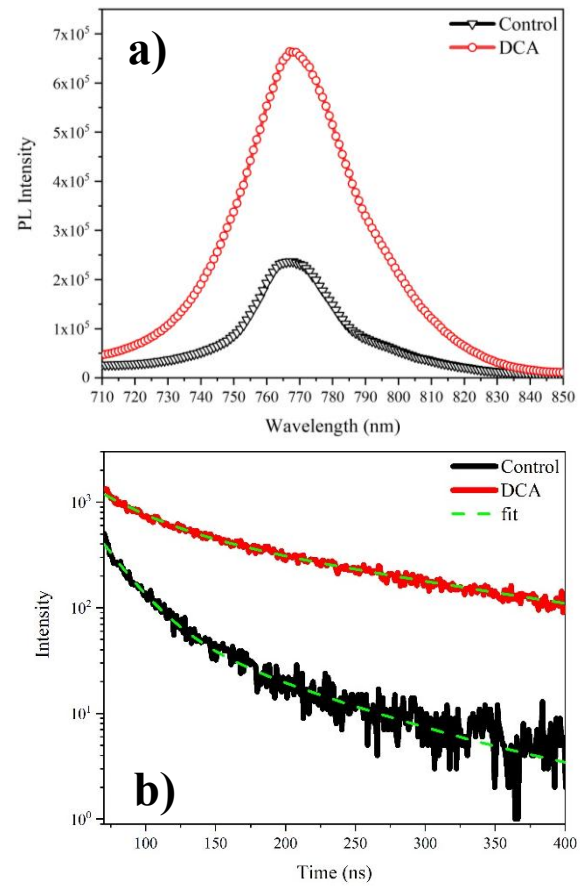


**Figure 3.** (a) PL and (b) TRPL spectra of control and DCA-modified triple cation perovskite thin films.

FTIR spectra were measured to observe the effect of the DCA molecule within the perovskite structure. To determine the interaction between the C=O bond in the DCA molecule and  $\text{Pb}^{+2}$  in the perovskite, FTIR spectra of both the control and DCA-modified thin films are presented in Figure 4. In the DCA-modified thin film, the characteristic peak of the C=O bond appears at a wavenumber of  $1681 \text{ cm}^{-1}$ , which is consistent with the literature [31,32]. The presence of the C=O stretching vibration peak at  $1681 \text{ cm}^{-1}$  in the film modified with this molecule clearly indicates that DCA has been incorporated into the perovskite film and interacts with  $\text{Pb}^{+2}$  within the perovskite structure. The electron pair on the oxygen atom of the C=O bond can provide strong coordination with  $\text{Pb}^{+2}$ , potentially forming nucleation centers around the DCA and supporting the slow and uniform growth of the perovskite layer. As a result of this effect, perovskite crystals grow gradually and evenly around the nucleation centers, forming a high-quality film with large grain size [31].



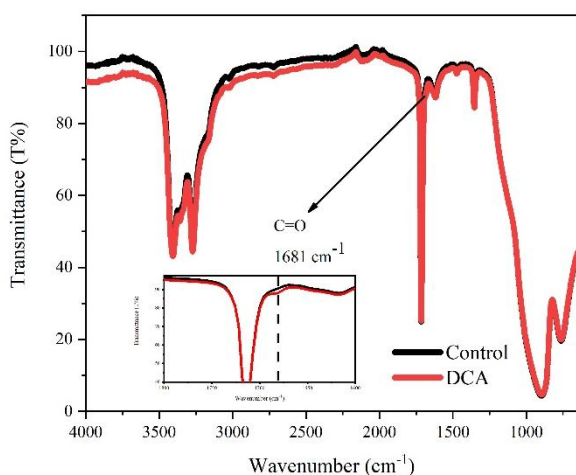


**Figure 4.** FTIR spectra of DCA-modified and unmodified perovskite thin films.

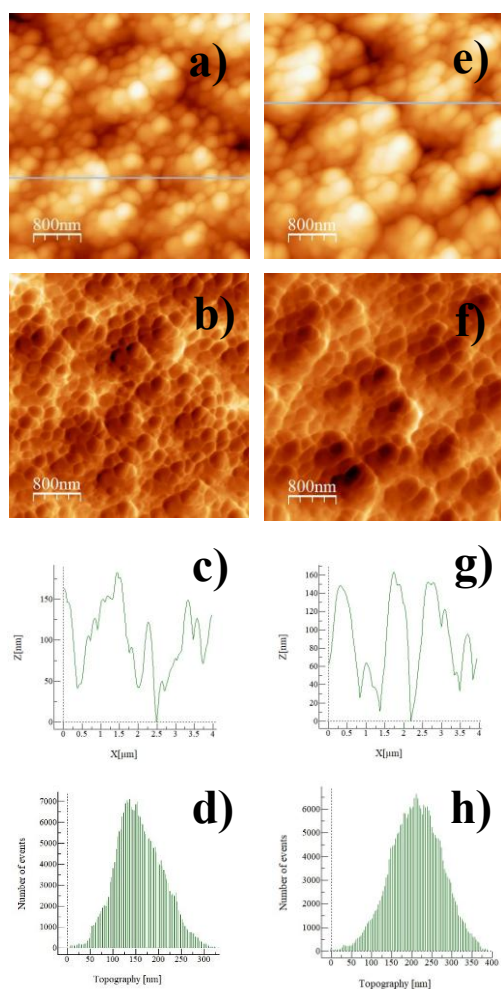


**Figure 5.** 4x4  $\mu\text{m}^2$  AFM images, phase images, profiles, and topographies of control (a–d) and DCA-modified (e–h) perovskite surfaces.

AFM was used to investigate the morphological properties of the perovskite thin films. Figure 5 presents AFM images, phase images, profiles, and topographic images obtained from a 4x4  $\mu\text{m}^2$  scan area, along with the root mean square (RMS) roughness values measured for surface roughness. The RMS roughness of the perovskite thin film washed only with CB was measured as 51 nm, whereas the RMS roughness of the DCA-modified film was measured as 65 nm. Although the RMS value of the DCA-modified film has slightly increased, a noticeable increase in grain sizes is observed. As can be clearly seen from the AFM images, the DCA molecule has altered the surface properties and crystal sizes of the perovskite film, a finding that is also supported by XRD measurements.

Considering all these analyses, when triple-cation perovskite solar cells are prepared using the DCA molecule, improvements in open-circuit voltage ( $V_{oc}$ ), short-circuit current density ( $J_{sc}$ ), and fill factor (FF) values are expected. This enhancement can be attributed to a reduction in charge carrier recombination within both the bulk and interfacial regions of the triple-cation perovskite structure [33,34]. The hysteresis index (HI) of the device produced with DCA is negligible compared to the control device. The performance enhancements observed in DCA-modified PSCs can be attributed to the beneficial effects of this molecule on carrier lifetime and film quality. In the control cell, the lifetime of short-lived carriers ( $\tau_1$ ) is measured at 21.44 ns, and the lifetime of long-lived carriers ( $\tau_2$ ) is 94.03 ns, indicating a high recombination rate that limits efficiency compared to the DCA-modified device. In contrast, in the DCA-modified film,  $\tau_1$  increases to 44.43 ns and  $\tau_2$  to 208.53 ns. These results demonstrate that DCA molecules improve the crystal structure, allowing carriers to move without recombination for longer periods and thus increasing efficiency by extending carrier lifetime within the cell [35]. Longer carrier lifetimes enhance the mobility of free carriers while reducing recombination losses, contributing to an increase in  $J_{sc}$  and FF, as shown in Figure 6 and Table 2. Thanks to these structural effects, a larger apparent grain size and a highly crystalline film are obtained from DCA-modified films. This not only increases carrier lifetime but also limits ion mobility by passivating defects, reducing hysteresis [36,37]. The DCA-modified PSCs exhibited significant improvements in performance parameters such as  $J_{sc}$ , FF and PCE compared to the control devices. Under reverse scan, the DCA-modified cells achieved a  $J_{sc}$  of 22.9  $\text{mA}/\text{cm}^2$  (vs. 21.7  $\text{mA}/\text{cm}^2$  for control), FF of 64.1% (vs. 58.1% for control), and PCE of 14.6% (vs. 12.6% for control). Furthermore, the HI was significantly reduced to 0.0579 in DCA-modified cells (vs. 0.125 for control). [37]. Through enhancement of film structure and increased carrier lifetimes, the DCA molecule improves device performance by increasing both  $J_{sc}$  and FF.



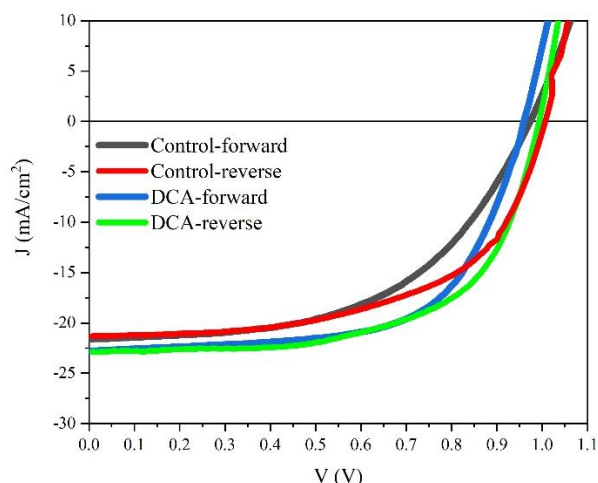


**Figure 6.** J-V curves obtained from devices fabricated with control and DCA-modified triple cation perovskite thin films under forward and reverse scan.

This study demonstrates that the addition of DCA additive to the anti-solvent during perovskite film formation can significantly enhance the structural and optoelectronic properties of PSCs. The DCA molecules affect crystallization kinetics, promoting crystal growth and enabling the production of films with lower defect densities. The perovskite films modified with DCA exhibited a substantial increase in PL intensity, indicating a significant suppression of non-radiative recombination in the perovskite layer and a reduction in trap state density. TRPL analyses revealed that DCA modification increased the carrier lifetime from  $\tau_2=94.03$  ns to 208.53 ns; these results suggest that DCA enhances device performance by allowing charge carriers to move longer without recombination through defect passivation. The observed increase in carrier lifetimes and the reduction in non-radiative recombination losses contribute to a notable improvement in  $J_{SC}$  and FF while also mitigating hysteresis effects. The findings obtained from DCA modification can be considered a significant step towards developing high-efficiency PSCs.

#### 4. Conclusion

**Table 2.** Electrical parameters obtained under forward and reverse scan from devices fabricated with control and DCA-modified triple cation PSCs.

	Scan direction	Jsc (mA/cm <sup>2</sup> )	Voc (mV)	FF (%)	PCE (%)	HI
<b>Control</b>	Forward	21.6	970	53.4	11.2	0.125
	Reverse	21.7	1000	58.1	12.6	
<b>DCA</b>	Forward	22.8	960	63.2	13.8	0.0579
	Reverse	22.9	995	64.1	14.6	

#### Acknowledgement

The authors gratefully acknowledge the financial support from the Presidency of the Republic of Turkey, Strategy and Budget Department (Project No: 16DPT002).

#### Author's Contributions

**Adem Mutlu:** Conceptualization, Methodology, Validation, Writing-original draft, Supervision, Writing-review and editing, Performed the analysis.

**Sevdiye Başak Turgut:** Collected data, Performed the analysis, Writing-review and editing.

#### Ethics

There are no ethical issues after the publication of this manuscript.

#### References

[1]. Khatoon vd., "Perovskite solar cell's efficiency, stability and scalability: A review", *Mater. Sci. Energy Technol.*, c. 6, ss. 437-459, 2023, doi: 10.1016/j.mset.2023.04.007.

[2]. N.-G. Park, "Perovskite solar cells: an emerging photovoltaic technology", *Mater. Today*, c. 18, sy 2, ss. 65-72, Mar. 2015, doi: 10.1016/j.mattod.2014.07.007.

[3]. B. Turedi vd., "Single-Crystal Perovskite Solar Cells Exhibit Close to Half A Millimeter Electron-Diffusion Length", *Adv. Mater.*, c. 34, sy 47, s. 2202390, Kas. 2022, doi: 10.1002/adma.202202390.

[4]. "best-research-cell-efficiencies chart, NREL". <https://www.nrel.gov/pv/assets/pdfs/best-research-cell-efficiencies.pdf>

[5]. H. Zhu vd., "Long-term operating stability in perovskite photovoltaics", *Nat. Rev. Mater.*, c. 8, sy 9, ss. 569-586, Eyl. 2023, doi: 10.1038/s41578-023-00582-w.

[6]. T. Ahmed Chowdhury, M. A. B. Zafar, M. S.-U. Islam, M. Shahinuzzaman, M. Aminul Islam, ve M. Uddin Khandaker, "Stability of perovskite solar cells: issues and prospects", *RSC Adv.*, c. 13, sy 3, ss. 1787-1810, 2023, doi: 10.1039/D2RA05903G.

[7]. G. Niu, W. Li, F. Meng, L. Wang, H. Dong, ve Y. Qiu, "Study on the stability of CH<sub>3</sub>NH<sub>3</sub>PbI<sub>3</sub> films and the effect of post-modification by aluminum oxide in all-solid-state hybrid solar cells", *J. Mater. Chem. A*, c. 2, sy 3, ss. 705-710, Ara. 2013, doi: 10.1039/C3TA13606J.

[8]. J. Bahadur, A. H. Ghahremani, S. Gupta, T. Druffel, M. K. Sunkara, ve K. Pal, "Enhanced moisture stability of MAPbI<sub>3</sub>

perovskite solar cells through Barium doping”, *Sol. Energy*, c. 190, ss. 396-404, Eyl. 2019, doi: 10.1016/j.solener.2019.08.033.

[9]. “Understanding the Cubic Phase Stabilization and Crystallization Kinetics in Mixed Cations and Halides Perovskite Single Crystals | Journal of the American Chemical Society”. *J. Am. Chem. Soc.* 2017, 139, 9, 3320–3323, <https://pubs.acs.org/doi/10.1021/jacs.6b12432>.

[10]. K. M. M. Salim vd., “Extended Absorption Window and Improved Stability of Cesium-Based Triple-Cation Perovskite Solar Cells Passivated with Perfluorinated Organics”, *ACS Energy Lett.*, Nis. 2018, doi: 10.1021/acsenenergylett.8b00328.

[11]. M. Saliba vd., “Cesium-containing triple cation perovskite solar cells: improved stability, reproducibility and high efficiency”, *Energy Environ. Sci.*, c. 9, sy 6, ss. 1989-1997, Haz. 2016, doi: 10.1039/C5EE03874J.

[12]. W. Tan, A. R. Bowring, A. C. Meng, M. D. McGehee, ve P. C. McIntyre, “Thermal Stability of Mixed Cation Metal Halide Perovskites in Air”, *ACS Appl. Mater. Interfaces* 2018, 10, 6, 5485–5491, <https://pubs.acs.org/doi/full/10.1021/acsami.7b15263>.

[13]. M. M. Tavakoli vd., “Highly Efficient Flexible Perovskite Solar Cells with Antireflection and Self-Cleaning Nanostructures”, *ACS Nano* 2015, 9, 10, 10287–10295, <https://pubs.acs.org/doi/full/10.1021/acsnano.5b04284>.

[14]. Q. Chen vd., “Planar Heterojunction Perovskite Solar Cells via Vapor-Assisted Solution Process”, *J. Am. Chem. Soc.* 2014, 136, 2, 622–625, <https://pubs.acs.org/doi/full/10.1021/ja411509g>.

[15]. Y. Han vd., “Degradation observations of encapsulated planar CH<sub>3</sub>NH<sub>3</sub>PbI<sub>3</sub> perovskite solar cells at high temperatures and humidity”, *J. Mater. Chem. A*, c. 3, sy 15, ss. 8139-8147, Mar. 2015, doi: 10.1039/C5TA00358J.

[16]. A. Mahapatra, D. Prochowicz, M. M. Tavakoli, S. Trivedi, P. Kumar, ve P. Yadav, “A review of aspects of additive engineering in perovskite solar cells”, *J. Mater. Chem. A*, c. 8, sy 1, ss. 27-54, Ara. 2019, doi: 10.1039/C9TA07657C.

[17]. L. Han vd., “Environmental-Friendly Urea Additive Induced Large Perovskite Grains for High Performance Inverted Solar Cells”, doi: 10.1002/solr.201800054.

[18]. N. K. Noel vd., “Enhanced Photoluminescence and Solar Cell Performance via Lewis Base Passivation of Organic–Inorganic Lead Halide Perovskites”, *ACS Nano* 2014, 8, 10, 9815–9821, <https://pubs.acs.org/doi/full/10.1021/nn5036476>.

[19]. D. Xin, S. Tie, R. Yuan, X. Zheng, J. Zhu, ve W.-H. Zhang, “Defect Passivation in Hybrid Perovskite Solar Cells by Tailoring the Electron Density Distribution in Passivation Molecules”, *ACS Publ.*, Kas. 2019, doi: 10.1021/acsami.9b15166.

[20]. J. Zhang vd., “Accelerated formation and improved performance of CH<sub>3</sub>NH<sub>3</sub>PbI<sub>3</sub>-based perovskite solar cells via solvent coordination and anti-solvent extraction”, *J. Mater. Chem. A*, c. 5, sy 8, ss. 4190-4198, Şub. 2017, doi: 10.1039/C6TA10526B.

[21]. K.-M. Lee vd., “Selection of anti-solvent and optimization of dropping volume for the preparation of large area sub-module perovskite solar cells”, *Sol. Energy Mater. Sol. Cells*, c. 172, ss. 368-375, Ara. 2017, doi: 10.1016/j.solmat.2017.08.010.

[22]. D. Liu vd., “Efficient planar heterojunction perovskite solar cells with Li-doped compact TiO<sub>2</sub> layer”, *Nano Energy*, c. 31, ss. 462-468, Oca. 2017, doi: 10.1016/j.nanoen.2016.11.028.

[23]. “Double-Halide Composition-Engineered SnO<sub>2</sub>-Triple Cation Perovskite Solar Cells Demonstrating Outstanding Performance and Stability | ACS Applied Energy Materials”. *ACS Appl. Energy*

*Mater.* 2020, 3, 9, 8595–8605, <https://pubs.acs.org/doi/10.1021/acsaem.0c01214>.

[24]. “Managing grains and interfaces via ligand anchoring enables 22.3%-efficiency inverted perovskite solar cells | Nature Energy”. *Nature Energy* volume 5, pages131–140 (2020), [https://www.nature.com/articles/s41560-019-0538-4?utm\\_source=acs&getft\\_integrator=acs](https://www.nature.com/articles/s41560-019-0538-4?utm_source=acs&getft_integrator=acs).

[25]. S.-G. Ko vd., “Effects of thiourea on the perovskite crystallization for fully printable solar cells”, *Sol. Energy Mater. Sol. Cells*, c. 196, ss. 105-110, Tem. 2019, doi: 10.1016/j.solmat.2019.03.045.

[26]. Y. Liu vd., “Bridging Effects of Sulfur Anions at Titanium Oxide and Perovskite Interfaces on Interfacial Defect Passivation and Performance Enhancement of Perovskite Solar Cells”, *ACS Omega*, Ara. 2021, doi: 10.1021/acsomega.1c04685.

[27]. T. Du vd., “Light-intensity and thickness dependent efficiency of planar perovskite solar cells: charge recombination versus extraction”, *J. Mater. Chem. C*, c. 8, sy 36, ss. 12648-12655, Eyl. 2020, doi: 10.1039/D0TC03390A.

[28]. J. Jiang vd., “Carrier lifetime enhancement in halide perovskite via remote epitaxy”, *Nat. Commun.*, c. 10, sy 1, s. 4145, Eyl. 2019, doi: 10.1038/s41467-019-12056-1.

[29]. J. Chang vd., “Crystallization and Orientation Modulation Enable Highly Efficient Doctor-Bladed Perovskite Solar Cells”, *Nano-Micro Lett.*, c. 15, sy 1, s. 164, Haz. 2023, doi: 10.1007/s40820-023-01138-x.

[30]. “Reversible Photoinduced Phase Segregation and Origin of Long Carrier Lifetime in Mixed-Halide Perovskite Films”. *Volume30, Issue28, July 9, 2020, 2002622*, [https://onlinelibrary.wiley.com/doi/epdf/10.1002/adfm.202002622?src=getft&utm\\_source=acs&getft\\_integrator=acs](https://onlinelibrary.wiley.com/doi/epdf/10.1002/adfm.202002622?src=getft&utm_source=acs&getft_integrator=acs).

[31]. S. S. Mali, J. V. Patil, D. W. Park, Y. H. Jung, ve C. K. Hong, “Intrinsic and extrinsic stability of triple-cation perovskite solar cells through synergistic influence of organic additive”, *Cell Rep. Phys. Sci.*, c. 3, sy 6, s. 100906, Haz. 2022, doi: 10.1016/j.xcrp.2022.100906.

[32]. S. Wang vd., “High-Performance Perovskite Solar Cells with Large Grain-Size obtained by using the Lewis Acid-Base Adduct of Thiourea”, doi: 10.1002/solr.201800034.

[33]. D. W. deQuilettes vd., “Reduced recombination via tunable surface fields in perovskite thin films”, *Nat. Energy*, c. 9, sy 4, ss. 457-466, Nis. 2024, doi: 10.1038/s41560-024-01470-5.



[34]. L. Fan vd., “Reducing charge-recombination losses in photovoltaic cells by spontaneous reconstruction of n/p homojunction in a monolithic perovskite film using black phosphorus nanosheets”, *Chem. Eng. J.*, c. 479, s. 147861, Oca. 2024, doi: 10.1016/j.cej.2023.147861.

[35]. D. Shi vd., “Low trap-state density and long carrier diffusion in organolead trihalide perovskite single crystals”, *Science*, c. 347, sy 6221, ss. 519-522, Oca. 2015, doi: 10.1126/science.aaa2725.

[36]. “Crystal Orientation and Grain Size: Do They Determine Optoelectronic Properties of MAPbI<sub>3</sub> Perovskite? | The Journal of Physical Chemistry Letters *J. Phys. Chem. Lett.* 2019, 10, 6010–6018, <https://pubs.acs.org/doi/10.1021/acs.jpclett.9b02757>.

[37]. “A multiscale ion diffusion framework sheds light on the diffusion–stability–hysteresis nexus in metal halide perovskites | Nature Materials”. *Nature Materials* volume 22, pages, 329–337 (2023), <https://www.nature.com/articles/s41563-023-01488-2>.

## Diagnostic Potential of miR-551b-3p in Lung Cancer: In Vitro and In Silico Experiments

Esen Çakmak<sup>1\*</sup> , İbrahim Seyfettin Çelik<sup>2</sup> 

<sup>1\*</sup> Department of Bioengineering and Sciences, Graduate School of Natural and Applied Sciences, Kahramanmaraş Sütçü İmam University, Kahramanmaraş, Türkiye

<sup>2</sup> Vocational School of Health Services, Department of Medical Services and Techniques, Kahramanmaraş Sütçü İmam University, Kahramanmaraş, Türkiye

\* [esencakmak@ksu.edu.tr](mailto:esencakmak@ksu.edu.tr)

\* Orcid No: 0000-0001-8805-3315

Received: 11 November, 2024

Accepted: 5 February, 2025

DOI: 10.18466/cbayarfbe.1582834

### Abstract

Lung cancer is a leading cause of cancer deaths worldwide. miRNAs have attracted attention as promising biomarkers in lung cancer diagnosis and prognosis. This study investigated the molecular mechanism of miR-551b-3p in lung cancer cells. The gene expression level of miR-551b-3p was investigated using qRT-PCR in healthy and cancerous lung cell lines. The target genes of miR-551b-3p and its function in cancer pathogenesis were also determined by in silico analyses. miR-551b-3p expression was higher in cancer cells compared to healthy lung cells ( $p < 0.01$ ). The expression level of miR-551b-3p was confirmed in silico in cancerous lung tissue. ERBB4 was identified as a target gene of miR-551b-3p and was down-regulated in cancer cells in comparison to healthy cells. Overexpression of miR-551b-3p and under expression of the ERBB4 gene decreased overall survival in cancer patients. A negative correlation was observed between miR-551b-3p and ERBB4 gene. miR-551b-3p expression was found to be closely associated with clinicopathological factors such as distant metastasis status, lymph node metastasis status and gender. miR-551b-3p target genes were enriched in cancer-related cellular processes. In conclusion, miR-551b-3p may be a potential alternative in treatment strategies as a therapeutic target in lung cancers.

**Keywords:** ERBB4, Lung cancer, miR-551b-3p, qRT-PCR

### 1. Introduction

Lung cancer is a high mortality cancer and is the first cancer diagnosed in men and the second cancer diagnosed in women [1]. Lung cancer is histologically classified into small cell lung cancer (SCLC) and non-small cell lung cancer (NSCLC), accounting for 15% and 85% of patients, respectively. NSCLC is subdivided into squamous cell carcinoma of the lung (SCLC), lung adenocarcinoma (LAC) and large cell carcinoma (LBC) [2-3]. Although surgery, chemotherapy and targeted therapies are commonly used to treat the disease, survival rates remain critical. The low survival rate may be due to conditions such as diagnosis at an advanced stage, metastases and high recurrence rates [4]. The lack of effective tools and treatment methods is a major problem for the early diagnosis and treatment in lung cancer [2]. Therefore, there is an urgent need to investigate new potential molecular markers and methods to understand the molecular mechanisms underlying lung cancer.

miRNAs play an important role in cancer biology. They can have oncogenic or tumor suppressor properties by affecting physiological processes such as growth, development and cell cycle of cancer cells through the genes they target [5]. Different miRNA markers are defined for different types of cancer, and while a miRNA may act as an oncogene in one type of cancer, it may act as a tumor suppressor in another [6]. In lung cancer, miR-138-5p and miR-200c were reported to be highly effective in preventing tumor development and progression by targeting PD-L1 [7]. miR-142-3p promoted invasion and metastasis of NSCLC cells by activating MAPK/ERK and NF- $\kappa$ B pathways [8]. miR-210 may lead to epidermal mesenchymal transition (EMT) by targeting the UPF1 gene and inducing the PTEN/PI3K/AKT pathway. This promotes migration and invasion of NSCLC [9].

There are few studies in the literature on the role of miR-551b-3p in cancer. In breast cancer, miR-551b-3p, which is upregulated by microRNA 551b-3p and transported to the nucleus by importin-8 (IPO8), activated STAT3 transcription. miR-551b-3p was associated with poor prognosis in breast cancer patients [10]. In lung cancer, downstream expression of miR-551b-3p causes overexpression lncRNA PVT1 and promotes cell viability, proliferation, migration and invasion [11]. LncRNA SMARCC2/miR-551b-3p/TMPRSS4 axis and miR-551b-3p have been reported to act as a tumor suppressor gene in gastric cancer [12]. In head and neck squamous cell carcinoma, miR-551a, miR-551b-3p and GLIPR2 gene triad partially regulate autophagy and is active in tumor growth, development and invasion [13].

This study aimed to investigate the molecular pathogenesis of miR-551b-3p in lung cancer. There are limited studies on the potential mechanism of miR-551b-3p in different types of cancer. Based on this, the gene expression levels of miR-551b-3p were investigated in a healthy lung cell line (BEAS-2B) and lung cancer cell lines (A549 and Calu-1), and its molecular mechanism was further investigated by in silico analyses.

## 2. Materials and Methods

### 2.1 Cell culture

A healthy human lung cell line (BEAS-2B) and cancer cell lines (A549 and Calu-1) were obtained from the ÜSKİM Health Laboratory (Kahramanmaraş, Turkey). Cells were cultivated at 37°C and 5% CO<sub>2</sub> in DMEM containing high glucose concentration (Gibco, Thermo Fisher Scientific, Waltham, MA, USA) supplemented with 10% FBS (Gibco), 1% penicillin (Gibco) and 100 µg/mL streptomycin (Gibco).

### 2.2 Transfection

miR-551b-3p mimic, miR-551b-3p inhibitor (anti-miR-551b-3p), miR-551b-3p mimic negative control and miR-551b-3p inhibitor negative control (anti-miR-NC) (Invitrogen, San Diego, CA) were purchased. One day before transfection, they were grown to 80% confluence in a 24-well plate at a density of  $5 \times 10^5$  per well. For miR-551b-3p mimic, inhibitors and negative controls, transfection was performed using reagent Lipofectamine 3000 (Invitrogen, San Diego, CA) according to the protocol of the manufacturer. The biological behavior of the cells was determined 24 hours after transfection.

### 2.3 RNA isolations and qRT-PCR

Total RNA was isolated using Trizol reagent (Invitrogen). The isolation was performed according to the manufacturer's protocols. Total RNA concentration and purity were measured by Thermo NanoDrop 2000 device. Complementary DNA (cDNA) was then

synthesized using QuantiTect Reverse Transcription Kit. qRT-PCR analyses were performed with ABI 7500 Fast Real Time PCR (Applied Biosystems, Foster City, CA, USA) and SYBR Green PCR kit (Takara, Shiga, Japan). miRNA isolation, RNA isolation, cDNA synthesis and PCR reaction were performed according to the manufacturer's protocol. PCR mixtures were made in a 10 µL volume consisting of 2 µL SYBR Green real-time PCR Master Mix, 1 µL cDNA, 0.5 µL Forward Primer (10 pmol), 0.5 µL Reverse Primer (10 pmol) and 6 µL. The PCR reaction was performed as pre-denaturation at 95°C for 10 min, denaturation at 95°C for 10 s, adhesion at 60°C for 20 s and amplification at 72°C for 10 s for 40 cycles. U6 for miRNA was used as endogenous controls. Negative controls were added during the experiment to control for contamination, and the experiments will be repeated 3 times independently. In addition, the expression of miR-551b-3p after the reaction was calculated by  $2^{-\Delta\Delta C_t}$  method. The primers used in this study are as follows: miRNA forward 5'-GCGACCCATACTTGGTTTCAG-3', miRNA reverse 5'-TCGTGAGATGAAGCACTGTAG-3', U6 forward 5'-CTCGCTTCGGCAGCACA-3' and U6 reverse 5'-AACGCTTCACGAATTTGCGT-3'.

### 2.4 Identification of target genes of miR-551b-3p

The mirWALK (<http://mirwalk.umm.uni-heidelberg.de/>), miRDB (<https://mirdb.org/mirdb/index.html>) and Target Scan HUMAN ([https://www.targetscan.org/vert\\_80/](https://www.targetscan.org/vert_80/)) databases were used to predict target genes. A Venn diagram was used to show commonalities among target genes (<https://bioinfogp.cnb.csic.es/tools/venny/index.html>).

### 2.5 Enrichment analysis

The PANTHER server (Protein Analysis Through Evolutionary Relationships, v 19.0) was used to identify biological processes, protein classes, cellular components, signalling pathways and molecular functions associated with the target genes of miR-551b-3p (<https://pantherdb.org/>). The PANTHER classification system is a comprehensive library describing the function, pathway and protein properties of genes and proteins and consists of a bioinformatics algorithm designed to facilitate high-throughput analyses [14].

### 2.6 KM-plotter survival analysis

Kaplan-Meier Plotter (<http://www.kmplot.com>) was used to analyze survival curves of miR-551b-3p. Gene expression was classified into high and low expression according to the median value. P value <0.05 indicates significance.



## 2.7 Association of miR-551b-3p with cancer pathogenesis

ULCAN (<https://ualcan.path.uab.edu/index.html>), an online platform based on the TCGA datasets, was used to determine the expression levels of miR-551b-3p and its target gene ERBB4 in lung cancer patients. At the same time, the expression level of miR-551b-3p and its cancer-pathogenic effects such as tumor development, stage, grade and survival were investigated using the Oncomir database (<https://oncomir.org/oncomir/index.html>).

## 2.8 Statistical analysis

Real-time PCR experiments were performed at least three times. Prism 8 (GraphPad) software was used for statistical data were analyzed by Student's t-test between two groups.  $P < 0.05$  was considered statistically significant.

## 3. Results

### 3.1 miR-551b-3p was more highly expressed in lung cancer cells compare to healthy lung cells

Expression levels were compared between healthy lung cell lines and cancer cell lines to determine the role of miR-551b-3p in lung cancer. miR-551b-3p was more highly expressed in the lung cancer cell line A549 and the Calu-1 healthy cell line BEAS-2B (Fig. 1a,1b,1c). According to the results of the analysis, no significant increase in miR-551b-3p was observed in healthy lung cells. In A549 cell lines, the gene expression level of miR-551b-3p mimic increased approximately 6-fold, while the gene expression level of miR-551b-3p inhibitor did not increase much. The gene expression level of miR-551b-3p mimic increased approximately 4-fold in Calu-1 cell lines. Very little increase was observed in the gene expression level of miR-551b-3p inhibitor.

The miRNA mimics and miRNA inhibitors were statistically compared between healthy and cancerous lung cell lines. As shown in Fig. 2a and Fig. 2b, as a result of statistical analysis, miR-551b-3p mimic showed a significant difference compared to healthy cells ( $p < 0.01$ ). The expression levels of the miRNA inhibitors in the cell lines did not show a significant increase.

### 3.2 miR-551b-3p targets the ERBB4 gene

To further investigate the molecular mechanism of miR-551b-3p, target genes were predicted by three different bioinformatics platforms. The number of target genes predicted in silico was determined to be 44 genes in total (Fig. 3). Among the target genes screened, the ERBB4 gene was found to be the overlapping gene in all platforms. The overlapping gene in miRDB and TargetSanHuman databases is GALNTL6, and the matching genes in miRDB and miRWalk databases are

CRB2, PDE4DIP, CDK17, SPATA31D3 and PGAM5. CTIF, PDE4C and ANKRD50 are overlapping genes in TargetSanHuman and miRWalk databases.

### 3.3 Enrichment analysis of miR-551b-3p target genes

The biological functions, pathway enrichment analyses and protein classifications of common genes targeted by miR-551b-3p were examined by Panther algorithm. According to the results of the analysis, it is seen that common target genes are concentrated in cases such as 'cellular process' (GALNTL6, ERBB4, PDE4DIP, PDE4C, CDK17, CRB2), 'biological regulation' (ERBB4, PDE4DIP, PDE4C, CTIF), 'metabolic processes' (GALNTL6, CDK17). In cellular components 'cellular anatomical formations' (GALNTL6, ERBB4, PDE4DIP, CTIF, CDK17, CDK17, CRB2) and in molecular properties 'catalytic activity' come to the forefront in processes in which genes (GALNTL6, ERBB4, CDK17, PDE4C) are enriched. In KEGG pathway analyses, the ERBB4 gene is concentrated in the 'cadherin signalling pathway' and 'EGF receptor pathway', and in protein classification, it is concentrated in protein subgroups such as 'metabolic interconversion enzymes', 'RNA metabolism proteins', 'protein modifying enzymes' (ERBB4, GALNTL6, PGAM5, PDE4C) (Fig. 4).

### 3.4 miR-551b-3p expression reduces overall survival in lung cancer patients

Kaplan-Meier (KM) plot, KM online tool was used to determine the prognostic significance of miR-551b-3p gene. The association between the expression levels of miR-551b-3p gene and overall survival rate (OS) in a total of 513 Lung adenocarcinoma patients was calculated by KM curve and log-rank test. The Kaplan-Meier survival analysis demonstrated that the overall survival rate was significantly reduced in lung cancer patients exhibiting expression of miR-551b-3p (HR 0.63,  $P: 0.0027$ ) expression (Fig. 5).

### 3.5 Overexpression of miR-551b-3p and low expression of ERBB4 are associated with tumor development

The expression level of miR-551b-3p was validated by analyzing its association with tumor development, correlations with tumor stage, tumor grade and clinical characteristics of patients. According to TCGA datasets in the ULCAN database, miR-551b-3p was significantly more expressed in lung cancer patients compared to normal lung tissues ( $p = 9.1 \times 10^{-11}$ ). Conversely, the ERBB4 gene was low expressed ( $p = 1.6 \times 10^{-12}$ ) in cancerous tissues (Fig. 6). When the correlation of miRNAs with clinical parameters is determined, it increases the potential of miRNA as a therapeutic target and biomarker. For this purpose, the relationship between miR-551b-3p and

clinical parameters was determined. The expression of miR-551b-3p was exhibited a significant correlation with pathological M status ( $p=4.64e^{-01}$ ), pathological N status

( $p=5.26e^{-01}$ ) and sex ( $p=2.59e^{-01}$ ) among clinical parameters (Table 1).

**Table 1.** Association of miR-551b-3p with clinical parameters in lung adenocarcinoma

Clinical Parameter	ANOVA P-value	ANOVA FDR	Multivariate Log Rank P-value	Multivariate Log Rank FDR
Pathologic M Status	$4.64e^{-01}$	$7.79e^{-01}$	$4.03e^{-02}$	$3.33e^{-01}$
Pathologic N Status	$5.26e^{-01}$	$9.99e^{-01}$	$3.71e^{-02}$	$3.40e^{-01}$
Sex	$2.59e^{-01}$	$5.84e^{-01}$	$3.74e^{-02}$	$3.03e^{-01}$

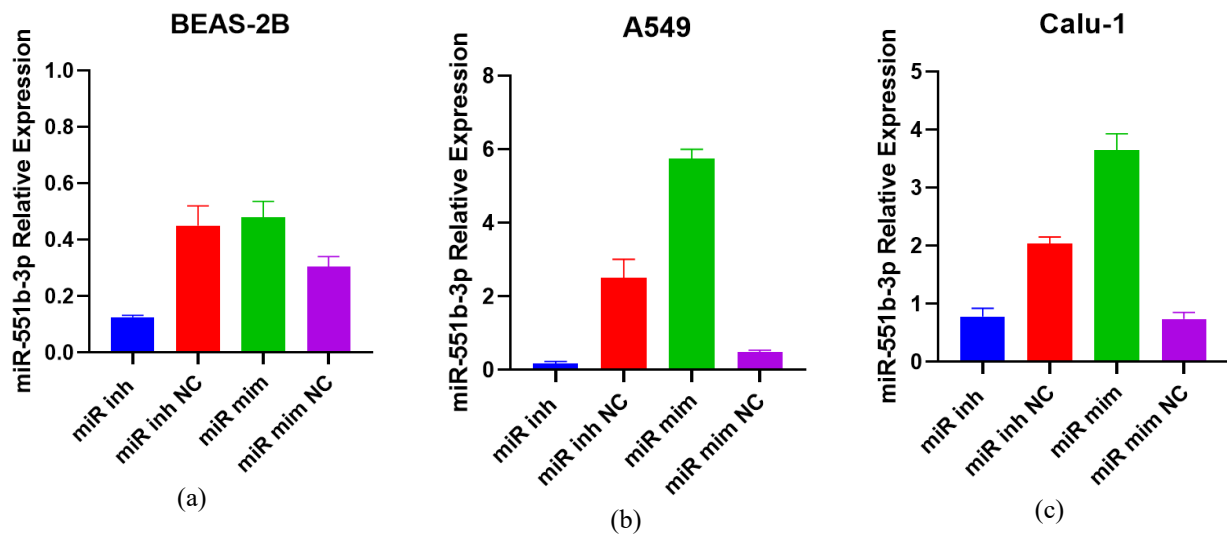


**Figure 1.** Gene expression levels of miR-551b-3p in cell lines. (a): miR-551b-3p expression level in BEAS-2B cell lines, (b): miR-551b-3p expression level in A549 cell lines, (c): miR-551b-3p expression level in Calu-1 cell lines. miR inh: miR-551-3p inhibitor, miR inh NC: miR-551-3p inhibitor negative control, miR mim: miR-551-3p mimic, miR mim NC: miR-551-3p mimic negative control.

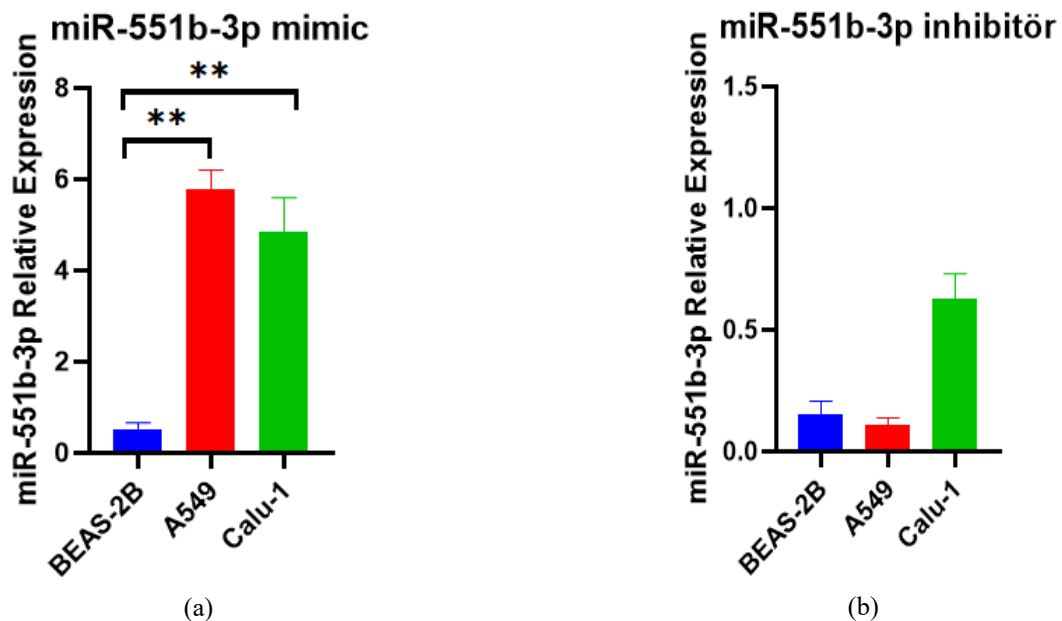


**Figure 2.** Expression levels of miR-551b-3p in healthy and cancerous lung cells in the presence of miRNA mimic and miRNA inhibitor

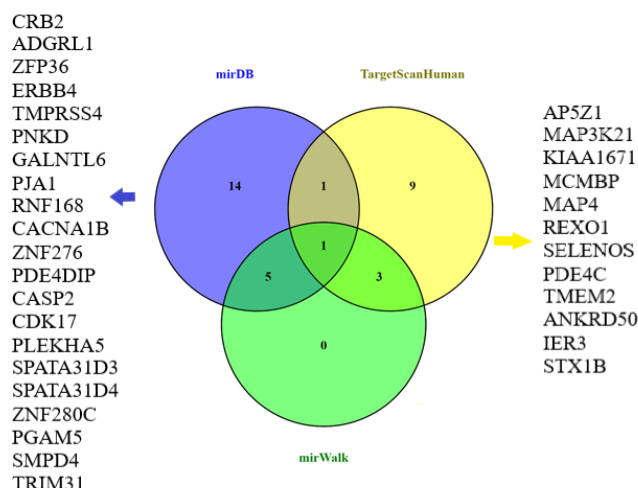


**Figure 3.** Venn diagram of overlapping target genes of miR-551b-3p in three separate in silico databases

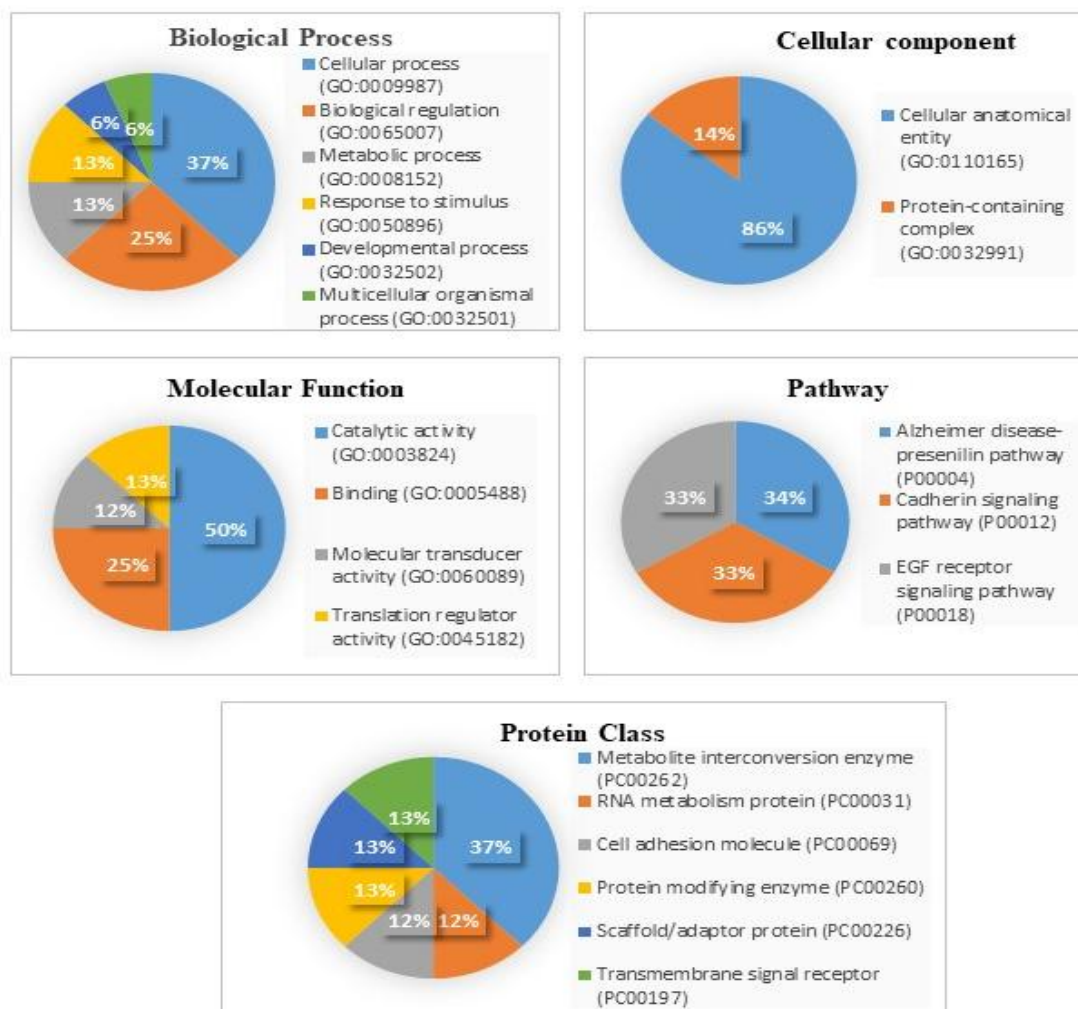


**Figure 4.** Grouping of miR-551b-3p target genes in biological function, pathway enrichment analysis and protein classification by in silico analysis

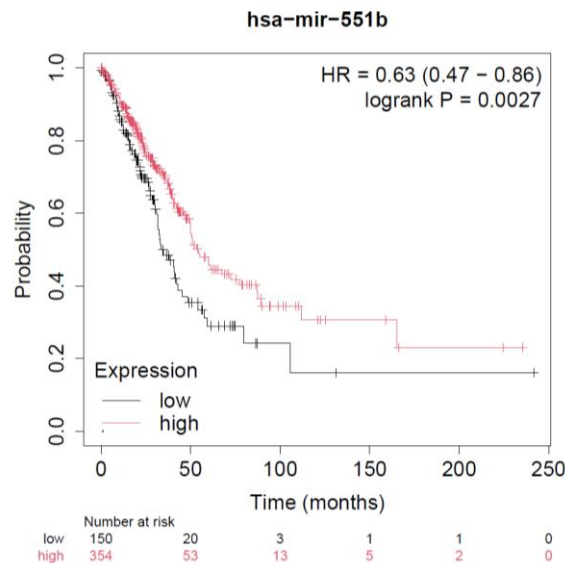


**Figure 5.** Survival analysis in lung cancer patients

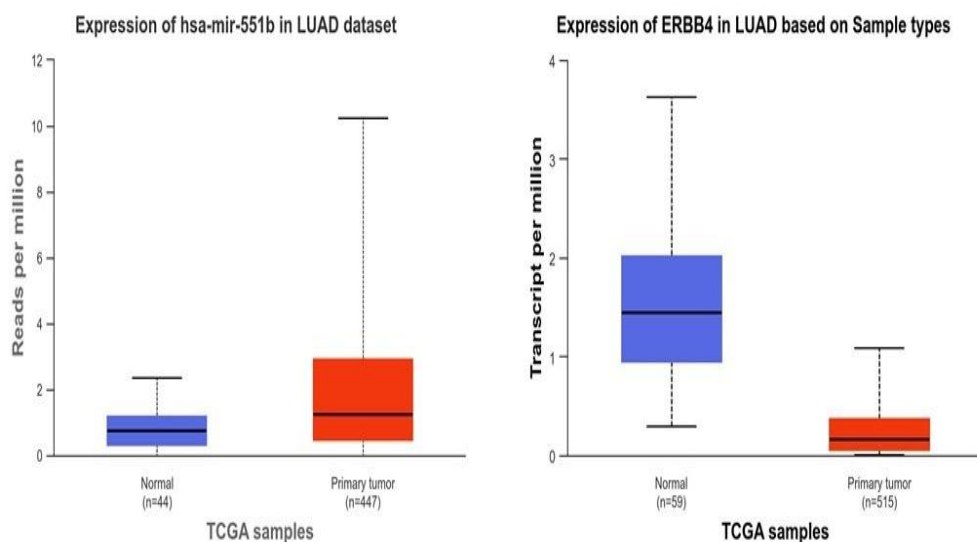


**Figure 6.** Expression level of miR-551b-3p and ERBB4 genes in lung cancer patients

#### 4. Discussion

miRNAs are known to be involved in many physiological processes, including cell growth and differentiation, apoptosis and tumor progression [15,16]. Dysregulation of miRNA gene expression is closely associated with pathological conditions of these processes. Many miRNAs play a crucial role in carcinoma and have even been proposed as biomarkers for diagnosis and treatment [17-19]. Whether a miRNA is an oncogene or a tumor suppressor, which genes it targets, in which pathways it is effective in cellular processes and in which pathways it causes dysregulation are important for determining the therapeutic role of miRNA.

The aim of this study was to define the biological role of miR-551b-3p in lung cancer cells. miR-551b-3p has been studied in very few cancer cells. According to the available evidence, miR-551b-3p is down-regulated in colorectal cancer [20], gastric cancer [21], breast cancer [22] and cholangiocarcinoma [23], whereas it is up-regulated in ovarian cancer [24] and head and neck cancer [13]. Bioinformatic analysis identified differentially expressed genes in thyroid cancer, and miR-551b-3p was found to be upregulated in cancer cells [25]. The expression level of miR-551b-3p was investigated in colorectal cancer. miR-551b-3p levels were significantly downregulated in CRC cell lines compared to healthy cell lines [20]. A study by Parashar et al. reported that microRNA 551b-3p was up-regulated in triple negative breast cancer [10]. miRNAs can be



over-expressed in some cancer cells and down-regulated in others. These differences in miRNA expression suggest that the mechanisms of miRNAs in tumor formation and development are different.

In lung cancer, only a few studies on miR-551b-3p are available in the literature and these are usually in silico analyses. miR-551b-3p has been reported to be upregulated in lung cancer in silico [26]. Using the TCGA datasets, the expression profiles of microRNA of 418 patients with lung adenocarcinoma (LUAD) were analyzed by bioinformatic analysis. Among the differentially expressed miRNAs, mir-551b-3p was demonstrated to be a prognostic marker for overall survival [27]. Charkiewicz et al. carried out miRNA profiling using next-generation sequencing on serum samples from patients with NSCLC and patients with non-cancerous lung disease. As a result of the analysis, they identified 28 upregulated miRNAs, including miR-551b-3p [28]. miR-551b-3p expression was investigated in lung cancer and was downregulated in tumor cell lines by comparison with normal cell lines [11]. In this study, RT-PCR analyses showed overexpression of the related miRNA in two different lung cancer cell lines compared to normal lung cell lines, and the results were confirmed by bioinformatic analysis. miR-551b-3p expression significantly decreased overall survival in lung cancer patients.

The majority of lung cancer patients are diagnosed at the metastatic stage due to limitations in diagnosis and treatment. However, traditional methods such as surgery and chemotherapy are not very effective in advanced stages of the disease due to disease recurrence and significantly reduce the survival rate of the disease [29]. Different expression patterns of miRNAs in processes such as cell migration, proliferation and metastasis may affect the survival rate of the disease. In particular, evaluating the clinicopathological conditions of patients and developing targeted therapies specific to the histological type of patients can provide significant advances in treatment [30]. For example, miR-106a has been shown to suppress the expression of tumor protein 53-induced nuclear protein 1 (TP53INP1) and is overexpressed in lung adenocarcinoma tissue with bone metastases. miR-106a silencing may offer a novel treatment for bone metastases in lung adenocarcinoma [31]. Expression of miR-551b-3p significantly reduced overall survival in lung cancer patients. Furthermore, miR-551b-3p expression was closely associated with clinicopathological factors such as distant metastasis status, lymph node metastasis status and gender. Decreasing the expression level of miR-551b-3p or silencing the gene may be an alternative treatment strategy and a potential molecular marker.

It is important to characterize miRNAs, which can alter the ability of cells to develop tumors, progress and respond to treatment [32]. In gallbladder cancer, in vivo, in vitro and in silico analyses have shown that miR-551b-

3p overexpression inactivates H6PD target gene expression and inhibits cell migration, invasion and EMT [33]. Overexpression of ERBB4, the target of miR-551b, was associated with poor prognosis in patients diagnosed with gastric cancer. miR-551b leads to inhibition of EMT and metastasis through downregulation of ERBB4 expression [34]. In patients with hepatocellular carcinoma, ERBB4 expression was shown to be downregulated and related to cellular differentiation and poorer prognosis [35]. In this study, ERBB4 was identified as a target gene of miR-551b-3p and found to have low levels of expression in lung cancer in comparison to normal tissue. ERBB4 belongs to the family of the ERBB receptor kinase. In cancer, the ERBB4 gene is generally known as a tumor suppressor, but there are also studies suggesting that it promotes tumor growth [34]. The ERBB4 gene is enriched in critical cancer-related processes such as cellular processes, translational regulatory activity, the cadherin signalling pathway and the EGF receptor signalling pathway.

## 5. Conclusion

In conclusion, the role of miR-551b-3p in lung cancer has been defined both in vitro and in silico. According to qRT PCR analyses, miR-551b-3p expression was higher in tumor cells from healthy cells. The expression level of miR-551b-3p was confirmed in silico in cancerous lung tissue compared to healthy tissues. The target gene of mir-551b-3p was identified as ERBB4 and showed a negative correlation with mir-551b-3p. mir-551b-3p expression decreased overall survival and was markedly related to distant metastasis, lymph node metastasis and gender. The results obtained suggest that miR-551b-3p may be a potential therapeutic target in lung cancer diagnosis and treatment. However, more detailed studies are needed to better understand mir-551b-3p tumor biology.

## Acknowledgement

This research was funded by Kahramanmaraş Sütçü İmam University Scientific Research Projects Coordination Unit for the research, grant number 2021/6-19 M.

## Author's Contributions

**Esen ÇAKMAK:** Drafted and wrote the manuscript, performed the experiment and result analysis.

**İbrahim Seyfettin ÇELİK:** Assisted in analytical analysis on the structure, supervised the experiment's progress, result interpretation and helped in manuscript preparation.

## Ethics

There are no ethical issues after the publication of this manuscript.

## References

- [1]. Leiter, A., Veluswamy, R.R., Wisnivesky, J. 2023. The global burden of lung cancer: current status and future trends. *Nature Reviews Clinical Oncology*; 20(9):624-639.
- [2]. Çakmak, E. 2022. A bioinformatics approach to identify potential biomarkers in non-small cell lung cancer. *Cumhuriyet Science Journal*; 43(1):6-13.
- [3]. Yang, Q., Wang, W., Cheng, D., Wang, Y., Han, Y., Huang, J. 2024. Non-coding RNA in exosomes: Regulating bone metastasis of lung cancer and its clinical application prospect. *Translational Oncology*; 46:102002.
- [4]. Lahiri, A., Maji, A., Potdar, P.D., Singh, N., Parikh, P. 2023. Lung cancer immunotherapy: progress, pitfalls, and promises. *Molecular Cancer*; 22(1):40.
- [5]. Chakraborty, A., Patton, D., Smith, B.F. 2023. miRNAs: potential as biomarkers and therapeutic targets for cancer. *Genes*; 14(7):1375.
- [6]. Çakmak, E. 2020. Computational and experimental tools of miRNAs in cancer. *Middle East Journal of Cancer*; 11(4):381-389.
- [7]. Zhang, Q., Pan, J., Xiong, D., Zheng, J., McPherson, K.N., Lee, S., You, M. 2023. Aerosolized miR-138-5p and miR-200c targets PD-L1 for lung cancer prevention. *Frontiers in Immunology*; 14:1166951.
- [8]. Cui, Y., Wu, X., Jin, J., Man, W. et al. 2023. CircHERC1 promotes non-small cell lung cancer cell progression by sequestering FOXO1 in the cytoplasm and regulating the miR-142-3p-HMGB1 axis. *Molecular Cancer*; 22(1):179.
- [9]. Yang, F., Yan, Y., Yang, Y., Hong, X., Wang, M., Yang, Z. et al. 2020. MiR-210 in exosomes derived from CAFs promotes non-small cell lung cancer migration and invasion through PTEN/PI3K/AKT pathway. *Cell signal*; 73:109675.
- [10]. Parashar, D., Geethadevi, A., Aure, M.R., Mishra, J., George, J. et al. 2019. miRNA551b-3p activates an oncostatin signaling module for the progression of triple-negative breast cancer. *Cell reports*; 29(13), 4389-4406.
- [11]. Wang, X., Cheng, Z., Dai, L., Jiang, T., Li, P., Jia, L. et al. 2021. LncRNA PVT1 facilitates proliferation, migration and invasion of NSCLC cells via miR-551b/FGFR1 axis. *OncoTargets and therapy*; 3555-3565.
- [12]. Yuan, H., Chen, Z., Bai, S., Wei, H., Wang, Y. et al. 2018. Molecular mechanisms of lncRNA SMARCC2/miR-551b-3p/TMPRSS4 axis in gastric cancer. *Cancer Letters*; 418, 84-96.
- [13]. Karanam, N.K., Ding, L., Vo, D.T., Giri, U., Yordy, J.S. et al. 2023. miR-551a and miR-551b-3p target GLIPR2 and promote tumor growth in high-risk head and neck cancer by modulating autophagy. *Advances in Cancer Biology-Metastasis*; 7:100085.
- [14]. Thomas, P.D., Ebert, D., Muruganujan, A., Mushayahama, T. et al. 2022. PANTHER: Making genome-scale phylogenetics accessible to all. *Protein Science*; 31(1):8-22.
- [15]. An, J., Zhang, M., Fu, Y., Zhang, D. et al. 2024. Emerging electrochemical biosensors for lung cancer-associated protein biomarker and miRNA detection. *International Journal of Biological Macromolecules*; 280(3):135972.
- [16]. Singh, S., Saxena, S., Sharma, H., Paudel, K.R., Chakraborty, A. et al. 2024. Emerging role of tumor suppressing microRNAs as therapeutics in managing Non-small cell lung cancer. *Pathology - Research and Practice*; 155222.
- [17]. Dong, Z.R., Cai, J.B., Shi, G.M., Yang, Y.F. et al. 2023. Oncogenic miR-93-5p/Gal-9 axis drives CD8 (+) T-cell inactivation and is a therapeutic target for hepatocellular carcinoma immunotherapy. *Cancer Letter*; 564:216186.
- [18]. Hsu, C.Y., Allela, O.Q.B., Mahdi, S.A.H., Doshi, O.P., Adil, M. et al. 2023. miR-136-5p: A key player in human cancers with diagnostic, prognostic and therapeutic implications. *Pathology - Research and Practice*; 54794.
- [19]. Liu, S., Ruan, Y., Chen, X., He, B., Chen, Q. 2024. miR-137: a potential therapeutic target for lung cancer. *Frontiers in Cell and Developmental Biology*; 12:1427724.
- [20]. Kim, K.S., Jeong, D., Sari, I.N., Wijaya, Y.T. et al. 2019. miR551b regulates colorectal cancer progression by targeting the ZEB1 signaling axis. *Cancers*; 11(5):735.
- [21]. Bai, S.Y., Ji, R., Wei, H., Guo, Q.H., Yuan H. et al. 2019. Serum miR-551b-3p is a potential diagnostic biomarker for gastric cancer. *Turkish Journal of Gastroenterology*; 30(5):415.
- [22]. Yang, Z., Xu, B., Wu, S., Yang, W., Luo, R., Geng, S. et al. 2022. Exosomal microRNA-551b-3p from bone marrow-derived mesenchymal stromal cells inhibits breast cancer progression via regulating TRIM31/Akt signaling. *Human Cell*; 235(6):1797-1812.
- [23]. Chang, W., Wang, Y., Li, W., Shi, L., Geng, Z. 2019. Micro RNA-551b-3p inhibits tumor growth of human cholangiocarcinoma by targeting Cyclin D1. *Journal of Cellular and Molecular Medicine*; 23(8):4945-4954.
- [24]. Chaluvally-Raghavan, P., Jeong, K.J., Pradeep, S., Silva, A.M., et al. 2016. Direct upregulation of STAT3 by MicroRNA-551b-3p deregulates growth and metastasis of ovarian cancer. *Cell Reports*; 15(7):1493-1504.
- [25]. Çağlar, H.O., Aytatlı, A., Karatas, O.F. 2024. In silico identification of differentially expressed microRNAs in thyroid cancer. *Human Gene*; 201306.
- [26]. Yu, H., Pang, Z., Li, G., Gu, T. 2021. Bioinformatics analysis of differentially expressed miRNAs in non-small cell lung cancer. *Journal of Clinical Laboratory Analysis*; 35(2):e23588.
- [27]. Lin, K., Xu, T., He, B.S., Pan, Y.Q., Sun, H.L., Peng, H.X. et al. 2016. MicroRNA expression profiles predict progression and clinical outcome in lung adenocarcinoma. *OncoTargets and therapy*; 5679-5692.
- [28]. Charkiewicz, R., Sulewska, A., Mroz, R., Charkiewicz, A., Naumnik, W. et al. 2023. Serum Insights: Leveraging the Power of miRNA Profiling as an Early Diagnostic Tool for Non-Small Cell Lung Cancer. *Cancers*; 15(20), 4910.
- [29]. Pandey, M., Mukhopadhyay, A., Sharawat, S. K., & Kumar, S. 2021. Role of microRNAs in regulating cell proliferation, metastasis and chemoresistance and their applications as cancer biomarkers in small cell lung cancer. *Biochimica et Biophysica Acta (BBA)-Reviews on Cancer*; 1876(1), 188552.
- [30]. Schegoleva, A. A., Khozyainova, A. A., Fedorov, A. A., Gerashchenko, T. S., Rodionov, E. O., Topolnitsky, E. B., ... & Denisov, E. V. 2021. Prognosis of different types of non-small cell lung cancer progression: current state and perspectives. *Cell Physiol Biochem*; 55(S2), 29-48.
- [31]. Han, L., Huang, Z., Liu, Y., Ye, L., Li, D., Yao, Z., ... & Yang, Z. 2021. MicroRNA-106a regulates autophagy-related cell death and EMT by targeting TP53INP1 in lung cancer with bone metastasis. *Cell death & disease*; 12(11), 1037.
- [32]. Pourdavoud, P., Pakzad, B., Mosallaei, M., Saadatian, Z., Esmaeilzadeh, E. et al. 2020. MiR-196: emerging of a new potential therapeutic target and biomarker in colorectal cancer. *Molecular Biology Reports*; 47:9913-9920.

[33]. Ji, T., Gao, L., Yu, Z. 2021. Tumor-suppressive microRNA-551b-3p targets H6PD to inhibit gallbladder cancer progression. *Cancer Gene Therapy*; 28(6), 693-705.

[34]. Song, G., Zhang, H., Chen, C., Gong, L., Chen, B., Zhao, S. et al. 2017. miR-551b regulates epithelial-mesenchymal transition and

metastasis of gastric cancer by inhibiting ERBB4 expression. *Oncotarget*; 8(28):45725.

[35]. Liu, Y., Song, L., Ni, H., Sun, L., Jiao, W., Chen, L. 2017. ERBB4 acts as a suppressor in the development of hepatocellular carcinoma. *Carcinogenesis*; 38(4):465-473.

# Co-pyrolysis of Different Coal Types with Biomass: Performance and Efficiency Evaluation by Thermogravimetric Analysis

Veysi Kamar<sup>1</sup> , Pınar Acar Bozkurt<sup>2\*</sup> 

<sup>1</sup> Graduate School of Natural and Applied Sciences, Ankara University, 06110, Ankara, Türkiye

<sup>2</sup> Department of Chemistry, Faculty of Science, Ankara University, 06100, Ankara, Türkiye

\* [p3acar@hotmail.com](mailto:p3acar@hotmail.com)

\*Orcid No: 0000-0001-8743-9734

Received: 17 March 2025

Accepted: 27 May 2025

DOI: 10.18466/cbayarfbe.1659482

## Abstract

In this study, the effect of co-pyrolysis of lignite and asphaltite, which are fossil energy sources with significant reserve potential in Turkey, with biomass sources such as walnut shell and hazelnut shell used as renewable energy sources on product efficiency and quality was investigated. The pyrolysis behavior of lignite, asphaltite, two types of biomass, lignite-biomass and asphaltite-biomass mixtures were investigated by non-isothermal thermogravimetric analysis (TGA) to evaluate the influence of biomass type, biomass mixing ratio and pyrolysis temperature on co-pyrolysis behavior. Pyrolysis experiments were carried out at three different temperatures (400, 460, and 520°C), first with the raw samples and then with mixtures at weight ratios of 25%, 50% and 75%. Possible synergistic effects were investigated by determining the mixture ratios and temperatures with the highest solid, liquid and gaseous product yields by analyzing the pyrolysis conversions. It was observed that the calorific values obtained before the pyrolysis process showed a significant increase after the process was applied. Increasing the amount of biomass added to lignite resulted in a 13.87% increase in calorific value and a positive synergy effect was indicated. Additionally, the addition of biomass to lignite and asphaltite reduced ash content and sulfur content.

**Keywords:** Asphaltite, Biomass, Co-pyrolysis, Lignite

## 1. Introduction

In recent years, there has been great interest in the utilization of agricultural wastes such as walnut shells, hazelnut shells, tea pulp, corn cobs, rice husks as biomass sources due to their renewability, low cost and abundant availability. Biomass can be cultivated in various locations, easily stored, contributes to socio-economic development, and has more favorable environmental impacts. Today, it is used in different industries for electricity generation, as a chemical feedstock, and as a liquid fuel. Due to these advantages, biomass energy has gained considerable importance for Turkey. Turkey ranks fourth in the world in walnut production, with an annual production of 287,000 tons. Additionally, based on the last decade's average, Turkey produces approximately 765,000 tons of hazelnut annually, accounting for about 70% of global production, with nearly half of this output consisting of shells [1]. Lignite is the most abundant type of coal in Turkey. According to 2024 data, 20.53 billion tons of our country's coal

reserve is lignite and approximately 19.32 billion tons of asphaltite is lignite [2].

In general, coal combustion is a major source of SO<sub>x</sub> and NO<sub>x</sub> emissions, which are the main causes of global climate change and acid rain. Biomass contains small amounts of nitrogen and phosphorus but almost no sulfur, so it produces lower emissions during its combustion. Therefore, it is considered that the co-utilization of biomass and coal can limit emission problems [3]. In our country, which has a high potential in terms of coal and biomass, this issue has been added to the chemistry and energy fields in the 11th and 12th Development Plans covering 2019-2023 in order to make these resources available for more efficient use [4]. Although a large number of studies have been carried out worldwide, especially in developed countries, studies in this field have gained momentum in Turkey in recent years. In this context, studies to be carried out for more efficient use of biomass and coal are of great importance.



Pyrolysis is the thermal decomposition of organic materials and is the first step in thermochemical conversion processes such as carbonization, gasification and combustion. It consists of a very complex set of reactions involving the formation of radicals and can be classified as a heterogeneous chemical reaction.

Some of the studies investigating the pyrolysis process of mixtures with different biomass/coal ratios by thermogravimetric analysis (TG) did not show any synergistic effect [5,6], whereas some of them showed opposite results [7-9]. In addition to these, different studies have confirmed the occurrence of synergy effect on the gas component of pyrolytic products, tar components and yields of these products [10,11].

The application of co-pyrolysis has been found to be both environmentally and economically beneficial [12]. The occurrence of synergy during co-pyrolysis is usually not certain and this effect is observed depending on the pyrolysis technique and fuels used. It has been reported that further research is needed to confirm the synergistic effect of the co-pyrolysis process and to better understand the mechanisms responsible for its synergistic effect [13,14].

Abnisa and Wan Daud [15], Mushtaq et al. [16] stated that there is limited research regarding the co-pyrolysis of coal/biomass blends. The non-isothermal thermogravimetric analysis of coal and corn stalk mixture at different heating rates indicated that the thermochemical reactivity of corn stalk is higher than that of coal [17]. The increase in tar yield and decrease in coke yield observed as the ratio of biomass to coal increased was attributed to the synergistic effect during the co-pyrolysis process [18-20].

In pyrolysis experiments, coal and biomass are two essential carbonaceous raw materials, and their co-pyrolysis has been proven to alter the fuel properties of the resulting oil and coke [21]. The co-processing of coal and biomass can increase product yield and reduce pollutant content [22]. The high H/C ratio of biomass can increase the decomposition of coal, whereas the minerals and inorganic components in coal can increase the decomposition of biomass. The effects hyper-coal yield obtained from a mixture of 80 wt% low rank coal and 20 wt% biomass on coke strength and structure were investigated. It was observed that oxygen and sulfur content decreased, ash content decreased significantly from 10.37 wt% to 0.86 wt%, and solvent thermal extraction, which was selected as the method, was found to be an effective technique to improve low-rank coal [23]. In the co-pyrolysis of low-metamorphic coal and pine sawdust, increasing the sawdust ratio from 10% to 50% resulted in an increase in tar yield from 11.58% to 16.62%. The addition of biomass shifted the pyrolysis process of coal to a low temperature region, decreased

the pyrolysis temperature of the coal sample, and increased the pyrolysis rate of the sample [24].

The aim of this study is to investigate the product yields to be obtained from the pyrolysis of two types of coal and biomass resources available in Turkey, which has approximately 20 billion tons of coal reserves and to determine the synergistic effects between them. For this purpose, both the more efficient utilization of the country's indigenous lignite and asphaltite, along with the valorization of currently underutilized biomass, reducing the environmental pollution of fossil-based coal, and activating it with biomass and increasing the efficiency of these two resources will provide a significant advantage.

## 2. Materials and Methods

### 2.1. Materials

In this study, the samples to be used as coal sources were lignite obtained from Edirne province and asphaltite sourced from Şırnak province. The biomass feedstocks consisted of walnut shells collected from the Çorum region and hazelnut shells obtained from the Black Sea region. All sample preparation and analysis procedures were conducted in accordance with ASTM standards.

The samples were first dried in an oven at 40°C for 24 hours according to ASTM D2013 standard and then ground to a particle size of less than 250 µm and stored in airtight plastic containers in the laboratory for use. Proximate analysis, including moisture, volatile matter, fixed carbon, and ash content analysis and elemental analysis (carbon, hydrogen, nitrogen, oxygen, and sulfur contents) of the samples were performed and the high heating value (HHV) was determined using a calorimeter bomb, and the results are given in Table 1. Elemental analysis was performed according to ASTM D5373 standard and calorific value determination was performed according to ASTM D5865 standard. The elemental analysis was carried out using a LECO CHN 628 analyzer and the oxygen content was calculated by difference. The sulfur content was determined in accordance with ASTM D4239 standard. The calorific values of the samples were determined by burning in a calorimeter bomb in a LECO AC 500 calorimeter.

### 2.2. Characterization

The thermogravimetric analysis (TGA) of raw samples and mixtures prepared at different ratios was performed using a LECO TGA 701 analyzer in the temperature range of 30°C -1000°C under a nitrogen atmosphere with at a flow rate of 100 mL/min. The ash content of combusted lignite and asphaltite samples was dissolved in acid, and the trace elements in the mineral matter content were determined using an ICP-OES analyzer. Due to the insufficient ash content in walnut and hazelnut

shell samples, the mineral matter content in their ash could not be determined. The X-ray fluorescence (XRF) analysis of the samples was performed using a Thermo Perform X model XRF analyzer.

### 2.3. Pyrolysis Experiments

The pyrolysis processes were carried out on the fixed bed pyrolysis system shown in Figure 1 according to TS 729 ISO 647 standard. A 30 g sample is placed into the retort. The collectors are weighed when empty and then properly connected to the retorts. After programming the control unit according to the desired temperature, the furnace is started to heat up. A thermocouple is inserted into the retort to measure the ambient temperature. Initially, the retorts remain elevated in the furnace, and once the preheating process is complete, the furnace is raised using a pneumatic mechanism and the retorts are placed in the oven. After the completion of the experiment, the collector and the liquid product are weighed together. The residual solid (coke) remaining in the retort is weighed. The amount of gas product is determined by subtracting the total weight of the liquid and residual coke.

In this stage of the experimental study, initially the samples (lignite-EL and asphaltite-SA as coal source; hazelnut shell-HS and walnut shell-WS as biomass source) in their raw forms without mixing, and then lignite-biomass and asphaltite-biomass mixtures were mixed at 25% (wt), 50% (wt) and 75% (wt) by weight were pyrolyzed at 400°C, 460°C, and 520°C. Following the pyrolysis process, solid, liquid, and gaseous product yields were determined, and the pyrolysis conversion was calculated.



**Figure 1.** The fixed bed pyrolysis system.

## 3. Results and Discussion

### 3.1. Pre-analysis of Samples

The pre-analysis results of the raw samples and the lignite-biomass and asphaltite-biomass mixtures prepared at three different ratios are presented in Table 1. When the results are analyzed, it is observed that the calorific heating value increased by 13.87% with the increase in the amount of biomass added to lignite, whereas the calorific heating value decreased by 7.3% with the increase in the amount of biomass added to asphaltite.

Lignite and asphaltite samples have high ash contents of 33.88% and 41.12%, respectively, while walnut and hazelnut shells selected as biomass samples have very low ash contents of 0.45% and 0.80%, respectively. The addition of biomass to lignite and asphaltite samples reduces their ash content. Furthermore, the volatile matter content of the biomass samples is considerably higher compared to lignite and asphaltite. The high volatile matter content of these samples contributes to their high calorific value [25].

**Table 1.** Proximate analysis of samples.

Sample	Moisture (wt %)	Ash (wt %)	Volatile matter (wt %)	Fixed carbon (wt %)	Calorific value (kcal/kg)
SA	0.71	41.12	43.97	14.21	4650
EL	8.02	33.88	34.12	23.98	3507
WS	6.45	0.45	75.93	17.17	4201
HS	8.29	0.80	72.28	18.64	4193
EL75-WS25	7.71	25.06	45.28	21.96	3680
EL50-WS50	7.25	16.72	55.16	20.87	3854
EL25-WS75	6.81	8.46	65.48	19.25	4027
EL75-HS25	8.26	25.72	43.05	22.97	3678
EL50-HS50	8.27	11.68	58.65	21.41	3850
EL25-HS75	8.30	8.78	61.49	21.44	4022
SA75-WS25	2.08	34.29	49.03	14.60	4537
SA50-WS50	3.46	23.33	58.37	14.84	4425
SA25-WS75	4.86	11.30	68.91	14.93	4313
SA75-HS25	2.53	34.22	48.26	14.99	4535
SA50-HS50	4.36	23.37	56.74	15.52	4421
SA25-HS75	6.25	12.10	64.49	17.16	4307

**Table 2.** Elemental analysis of samples.

Sample	C	H	N	O*	S	H/C	O/C
SA	45.88	3.56	1.22	42.28	7.06	0.93	0.69
EL	40.38	2.94	1.21	52.41	3.06	0.87	0.97
WS	48.62	5.39	0.38	45.58	0.03	1.33	0.70
HS	48.79	5.16	0.53	45.50	0.02	1.27	0.70
EL75-WS25	42.44	2.69	1.00	51.36	2.51	0.76	0.91
EL50-WS50	44.50	3.35	0.80	49.67	1.68	0.90	0.84
EL25-WS75	46.56	4.02	0.59	47.97	0.86	1.04	0.77
EL75-HS25	42.48	2.57	1.04	51.40	2.51	0.73	0.91
EL50-HS50	44.59	3.13	0.87	49.73	1.68	0.84	0.84
EL25-HS75	46.69	3.68	0.70	48.07	0.86	0.95	0.77
SA75-WS25	46.57	3.78	1.01	43.28	5.36	0.97	0.70
SA50-WS50	47.25	4.09	0.80	44.27	3.59	1.04	0.70
SA25-WS75	47.94	4.39	0.59	45.27	1.81	1.10	0.71
SA75-HS25	46.61	3.68	1.05	43.30	5.36	0.95	0.70
SA50-HS50	47.34	3.87	0.88	44.32	3.59	0.98	0.70
SA25-HS75	48.06	4.06	0.70	45.37	1.81	1.01	0.71

\* calculated from the difference

The elemental analysis results of the samples are presented in Table 2. It was found that the carbon and hydrogen contents of walnut and hazelnut shells selected as biomass sources are very close to each other. Compared to the raw lignite and asphaltite samples, the mixtures formed using these biomass sources exhibited increased carbon and hydrogen content. The sulfur content of the lignite and asphaltite samples was determined to be 3.06% and 7.06%, respectively, which is consistent with existing studies in the literature [26,27]. It was observed that increasing the amount of biomass added to the lignite and asphaltite samples gradually decreased the sulfur content of the asphaltite mixture to 1.81% and the lignite mixture to 0.86%.

The pyrolysis of coal produces limited liquid yields due to its low H/C ratios. To enhance the quality of liquid products, providing an additional hydrogen source is

essential. Therefore, the co-pyrolysis of coal and biomass has been suggested as an effective process to improve product yields [28]. When walnut and hazelnut shell were added to lignite, the highest H/C molar ratio was obtained at a 75% mixing ratio of biomass. The H/C ratios of the lignite samples with biomass addition ranged between 0.73 and 1.04. Similarly, increasing the amount of biomass in the asphaltite samples resulted in higher H/C molar ratios, ranging from 0.95 to 1.10. The increase in the H/C molar ratio, indicating higher hydrogen content, enhances volatile matter content and calorific value, ultimately leading to the production of high-quality products. This trend is consistent with previous results suggesting that biomass addition increases hydrogen content and reduces fixed carbon dominance in coal blends, thereby improving combustion reactivity [28, 33].

**Table 3.** Mineral matter content in ash of lignite and asphaltite samples

Samples (ppm)	Al	B	Ba	Be	Bi	As	Ca	Cd	Co	Cr
EL	36533	253	292	5	<0.1	71	41054	1	16	103
SA	6502	45	164	2	<0.1	89	19719	62	7	235
(LOD)	0.065	0.072	0.083	0.024	0.035	0.029	0.087	0.011	0.013	0.028
	Cu	Fe	K	Li	Mg	Mn	Mo	Na	Ni	P
EL	17	47125	6805	24	19959	381	3	4425	120	255
SA	119	17800	3263	11	23814	86	1500	856	1717	3879
(LOD)	0.009	0.033	0.093	0.048	0.082	0.071	0.063	0.071	0.043	0.084
	Pb	Si	Sn	Sr	Ti	V	Zn	Se	Zr	
EL	43	962	18	840	380	109	126	3.8	36.9	
SA	17	624	18	588	39	3156	3559	69.4	7.1	
(LOD)	0.058	0.092	0.035	0.036	0.088	0.063	0.039	0.063	0.067	

Table 3 presents the mineral matter contents of the coal and asphaltite ash samples, along with the corresponding LOD (limit of detection) values for each element. The inclusion of LOD values ensures analytical transparency and facilitates the accurate interpretation of trace element concentrations by clarifying the detection limits associated with each analyte. The high mineral matter content in lignite and asphaltite resulted in a high ash content. During the conversion of coal by thermal processes, certain elements in coal ash, such as Na, Al, Mg, and Ca, may exhibit catalytic effects. The mineral matter or ash content affects the adsorption capacity of coal seams [29]. Interactions between chlorine (Cl), sulfur (S), and alkali and alkaline earth metals (AAEM) are critical factors affecting ash formation, transformation, and accumulation during biomass and coal gasification and combustion. These problems lead to slag formation, agglomeration, corrosion, and other issues related to the safety performance of gasifiers and boilers [30].

### 3.2. Thermogravimetric Analysis Results of the Samples

The TGA and DTA curves obtained as a result of the analysis of the raw samples to investigate their thermal degradation are given in Figure 1.

The results of TGA analysis show that hazelnut shell, walnut shell, lignite, and asphaltite samples begin to decompose at low temperatures, and their decomposition continues up to approximately 950°C. At 950°C, mass losses are nearly 100% for walnut shell, 97% for hazelnut shell, 63% for lignite, and approximately 51% for asphaltite. The mass loss observed between 65-160°C in hazelnut shell, walnut shell, and lignite samples is attributed to moisture loss in their structures, whereas no significant mass loss is observed in the asphaltite sample at these temperatures, indicating that the sample is dry.

The decomposition rate defines the rate at which a substance breaks down as a result of change over time. For hazelnut and walnut shell samples, mass loss occurs at lower temperatures, leading to a significant increase in the decomposition rate.

The TGA and DTA analysis results exhibit highly similar decomposition curves for both biomass samples. Due to the high volatile matter content of walnut and hazelnut shell samples, the total mass losses observed in their TGA curves are higher than those of lignite and asphaltite samples. The two sharp peaks observed in the DTA curves of the biomass samples can be attributed to the decomposition of hemicellulose and cellulose, respectively [31]. There are two clearly visible peaks around 255°C and 305°C in the hazelnut shell sample and 280°C and 330°C in the walnut shell sample. It can be said that significant degradation of plant-based organic matter occurs within the 250-350°C temperature range, with the degradation rate beginning to decrease from 380°C onward, stabilizing around 400°C, and lignin degradation continuing at higher temperatures. The higher decomposition temperature of walnut shell compared to hazelnut shell may be attributed to its more hemicellulose and lignin content. It has been reported that the thermal degradation of hemicellulose occurs in the 200-260°C temperature range, thermal degradation of cellulose in between 240-350°C, and thermal degradation of lignin in the temperature range of 280-500°C [32]. Based on this data, observed the low-temperature peaks (255°C and 280°C) in biomass samples are likely due to hemicellulose degradation, while at the high-temperature peaks (305°C and 330°C) can be attributed to cellulose degradation. Hemicellulose has an amorphous and moderately rigid structure, whereas cellulose consists of straight-chain molecules with a stronger structure. Therefore, the degradation of cellulose occurs at higher temperatures.

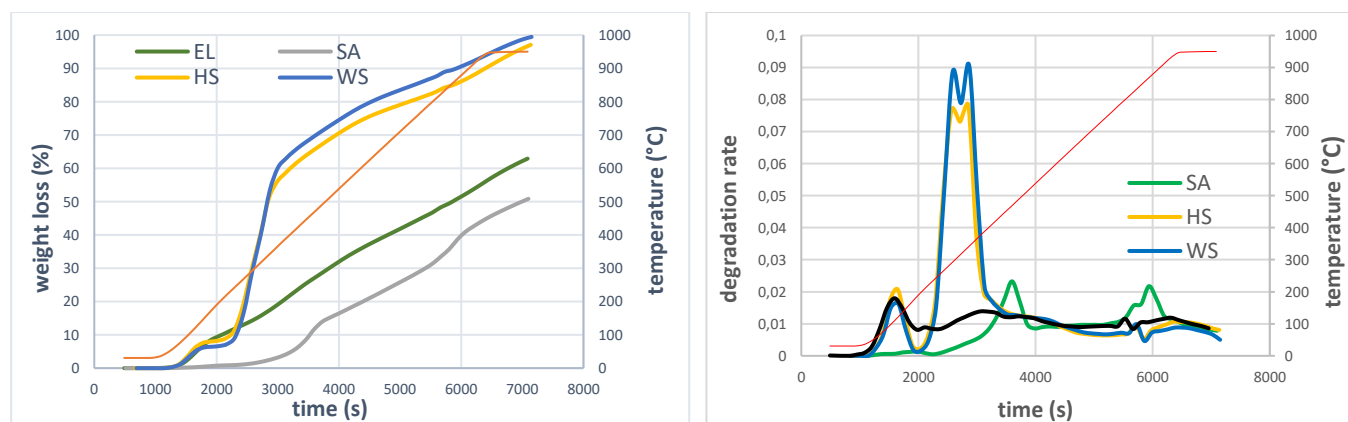


**Figure 1.** TGA and DTA curves for lignite (EL), asphaltite (SA) and biomass (HS and WS)



As the coal rank increases, the main pyrolytic decomposition regions shift to higher temperatures due to the strength of the bonds in the structure of the sample. The macromolecular components of biomass are linked by weak ether bonds, which exhibit low thermal resistance even at low temperatures. On the other hand, coal molecules have stronger pyrolytic aromatic hydrocarbons and C=C bonds, which show higher resistance to thermal degradation. Therefore, it can be said that lignite and asphaltite samples decompose at higher temperatures compared to biomass due to the presence of their C=C bonds. The degradation of coal samples occurred at approximately 255°C and 865°C. The degradation rate of biomass samples is considerably higher than that of coal, and these degradation rates are observed as sharp peaks in the DTA curves. In contrast, the degradation peak of coal is more widespread, indicating that the degradation process occurs over a wider temperature range.

In the lignite sample, a steady increase in mass loss is observed in the temperature range of 255-450°C, remains constant after 450°C, a peak occurs again around 800°C and remains constant again after 850°C. When the DTA curve of the asphaltite sample is analyzed, a degradation progressing at a constant rate up to 230°C is observed, but after 250°C, a rapid degradation peak is observed up to around 465°C. The degradation continues steadily in the temperature range of 510-800°C. It is observed that the first shoulder peak appears at 820°C, followed by a more distinct peak at 865°C, with decomposition proceeding in a horizontal manner from 900°C onwards. Unlike the biomass and lignite samples, the degradation rate of the asphaltite sample increases between 850-900°C, leading to further mass loss.

### 3.3. Thermogravimetric Analysis Results of the Mixture Samples

The TGA and DTA curves obtained as a result of the analysis of the mixture samples to investigate their thermal degradation are given in Figure 2 and 3, respectively.

In all TGA and DTA curves, it is observed that as the biomass ratio added to the lignite and asphaltite samples increases, both mass loss and degradation rates increase for the mixtures. This observation is attributed to the fact that the degradation in the structure of lignocellulosic biomass occurs at lower temperatures and at a faster rate. Additionally, as seen in the curves obtained from the analysis results, the degradation temperature decreases as the biomass mass ratio increases. The observed decrease in decomposition temperatures with increasing biomass ratio indicates the catalytic influence of biomass on thermal degradation behavior, consistent with previous studies showing that biomass facilitates the early release of volatiles and accelerates thermal breakdown of the blend [24, 31].

### 3.4. Experimental and Hypothetical (Theoretical) Thermogravimetric Analysis Results

Hypothetical values are calculated from the formula given in Equation 3.1 using the TGA and DTA data obtained as a result of the experiments.

$$W_{\text{hypothetical}} = X_{\text{coal}} \times W_{\text{coal}} + X_{\text{biomass}} \times W_{\text{biomass}} \quad (3.1)$$

$$\Delta W = W_{\text{experimental}} - W_{\text{hypothetical}}$$

Here,  $W_{\text{coal}}$  and  $W_{\text{biomass}}$  represent the mass loss amounts obtained in the raw form for coal and biomass,  $X_{\text{coal}}$   $X_{\text{biomass}}$  represents the mixing ratios of coal and biomass, respectively. The  $W_{\text{hypothetical}}$  value is calculated for each sample using the data from TGA curves. The  $\Delta W$  synergistic value is used to describe the deviation between the experimental value and the calculated (hypothetical) value in the co-pyrolysis process. When the experimental values of coal and biomass samples mixed in different ratios are compared with the calculated values of the raw samples, a noticeable increase in the samples indicates a positive synergistic effect, whereas a noticeable decrease indicates a negative synergistic effect. In other words, if  $\Delta W$  is significantly greater than zero, this is a positive synergistic effect; if the value is significantly less than zero, it is a negative synergistic effect.

The TGA and DTA curves obtained for the experimental and theoretical (hypothetical) calculations of the asphaltite-hazelnut shell mixtures prepared at three different ratios are given in Figure 4. As the amount of biomass added to asphaltite increases, both the experimental and theoretical results show an increase in mass loss, along with an increase in the rate and amount of degradation. In the TGA result of the asphaltite-hazelnut shell mixtures, the experimental and theoretical curves exhibit similar trends, and the pyrolytic transformations are close to each other. Increasing mass losses in experimental values around 240°C are higher than the theoretical values. At around 370°C, while the theoretical and experimental values for the SA75-HS25 and SA50-HS50 mixtures are quite close to each other, the experimental mass loss values for the SA25-HS75 mixture are lower than the theoretical values, indicating a negative synergistic effect. In the DTA result, the first peak, occurring around 110°C, indicates that the experimental values undergo degradation at lower temperatures, while the degradation rates are quite similar. In the second peak, which begins around 310°C, a decrease is observed in both the degradation amount and temperature in the experimental values.

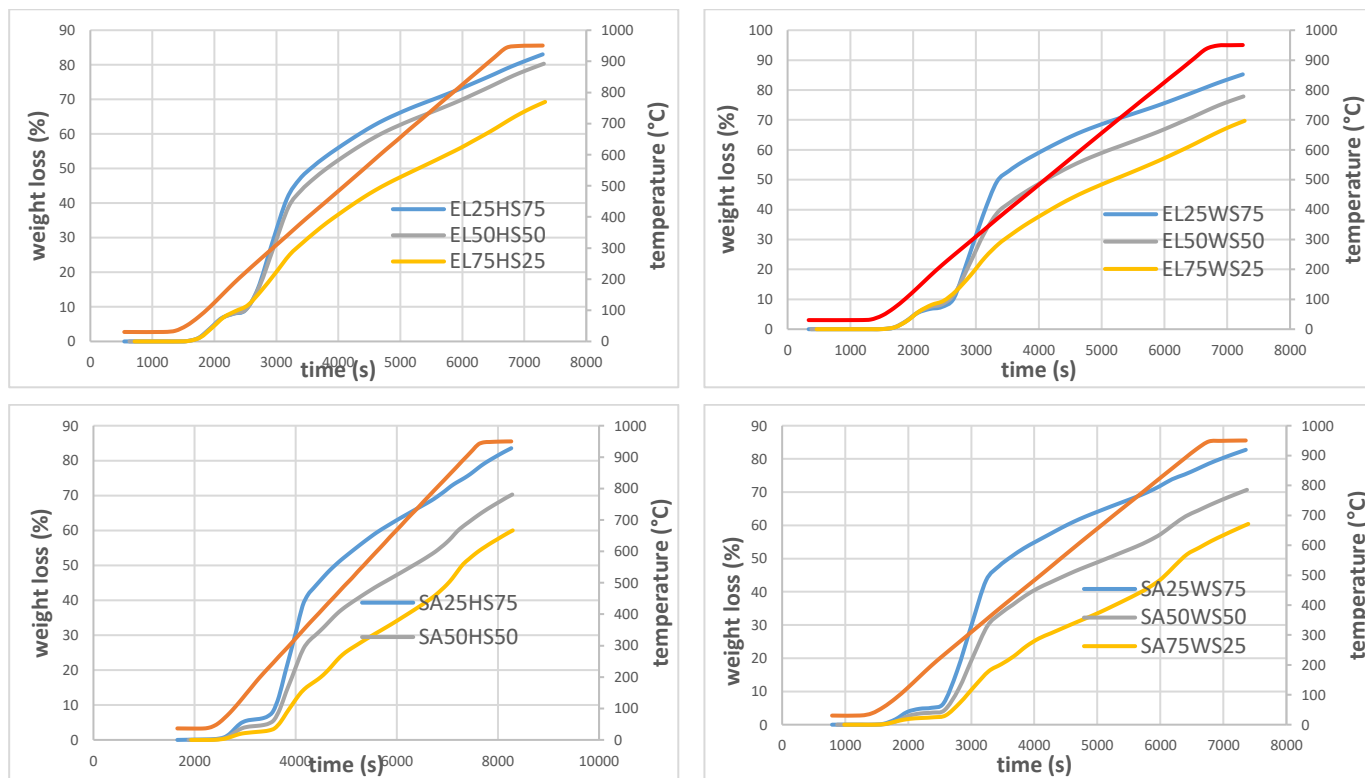


**Figure 2.** TGA curves for lignite-biomass and asphaltite-biomass mixtures at different ratio.

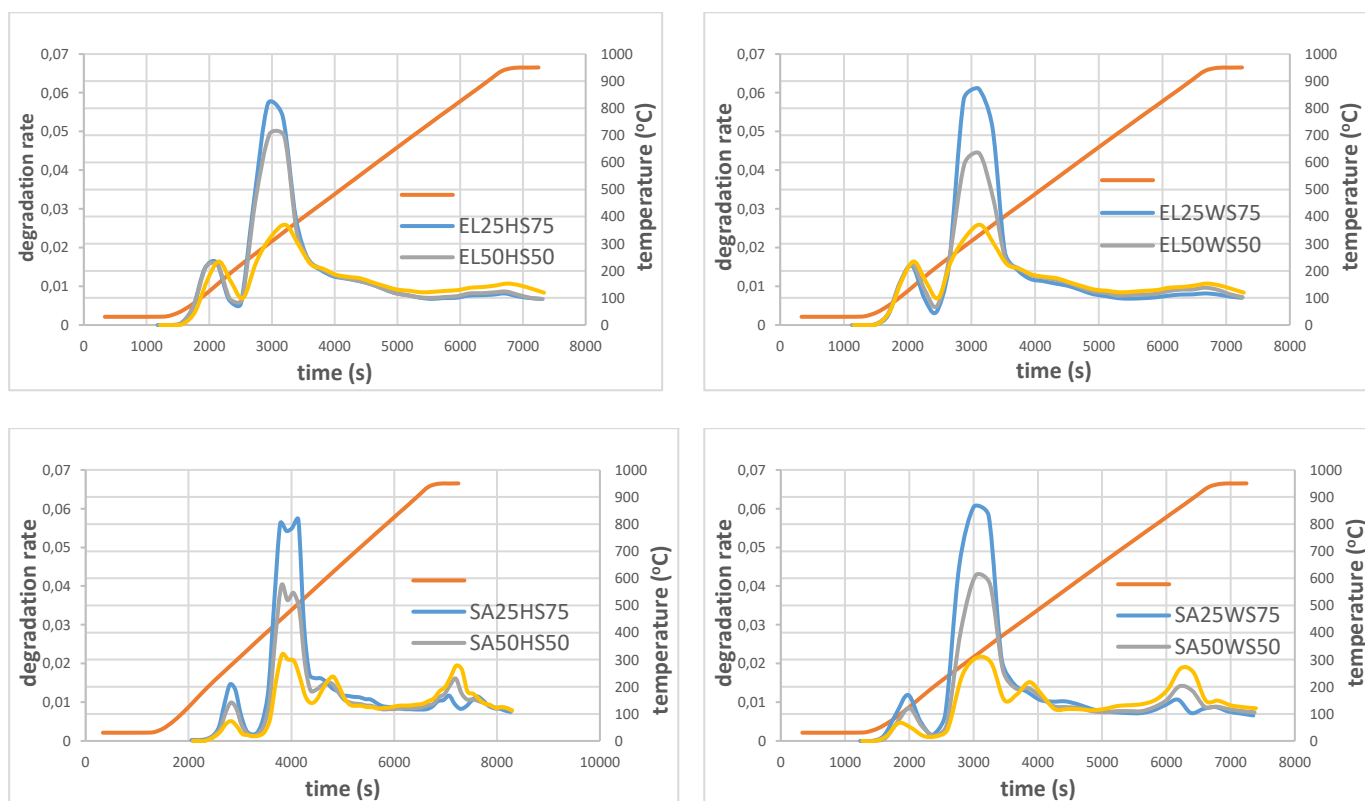


**Figure 3.** DTA curves for lignite-biomass and asphaltite-biomass mixtures at different ratio.

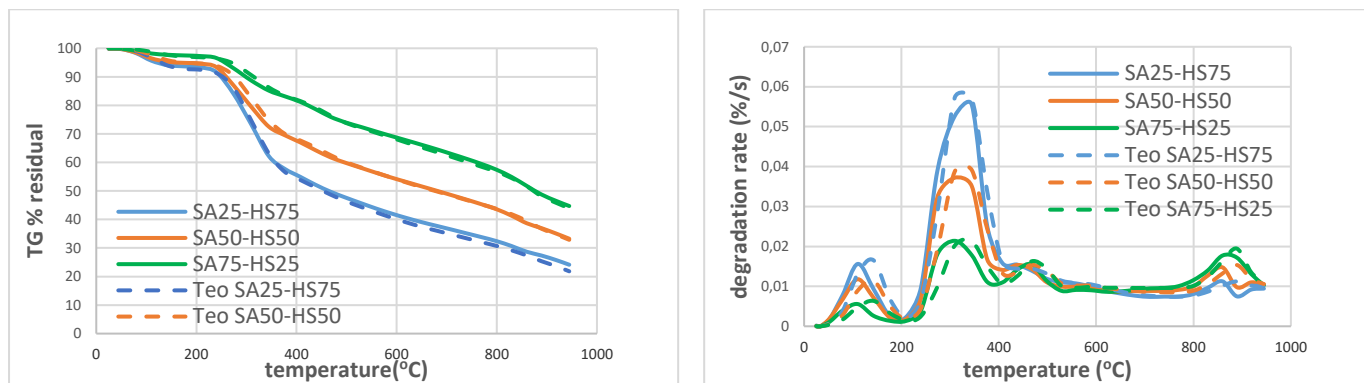


**Figure 4.** TGA and DTA curves for experimental and theoretical calculations of asphaltite (SA)-biomass (HS) mixture samples.

The TGA and DTA curves obtained for the experimental and theoretical (hypothetical) calculations of the asphaltite–walnut shell mixtures prepared at three different ratios are given Figure 5. In the TGA result, the mass loss observed at the first peak at around 245°C, in the experimental values is greater than the theoretical values. Up to around 380°C, the mass loss values of the experimental curves for all mixtures are higher than the theoretical values. After these temperature values, while

the SA50-WS50 and SA75-WS25 mixture curves are quite close to each other, the experimental mass loss values for the SA25-WS75 mixture are higher than the theoretical values. For the DTA result, in the first peak, occurring at around 110°C, it is observed that the experimental values undergo degradation at lower temperatures, while the degradation rates are quite similar. In the second peak, which begins around 310°C, a decrease is observed in both the degradation amount and temperature in the experimental values.

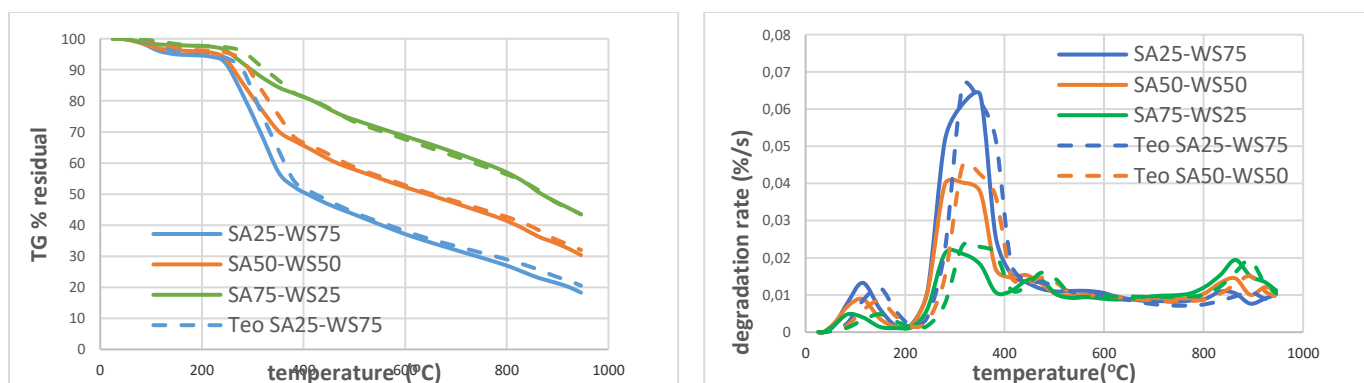


**Figure 5.** TGA and DTA curves for experimental and theoretical calculations of asphaltite (SA)-biomass (WS) mixture samples.

The TGA and DTA curves obtained for the experimental and theoretical (hypothetical) calculations of the lignite–hazelnut shell mixtures prepared at three different ratios are given in Figure 6. In the TGA result, the mass loss increases rapidly after 250–260°C. For all mixture samples, the theoretical values are greater than the experimental values, indicating a negative synergistic effect. For the DTA result, a decrease in both the degradation amount and rate is observed in the experimental values compared to the theoretical values. In the first peak, high degradation is observed around 130°C and this situation is similar in all mixtures. In the second peaks, around 330°C, the experimental values exhibit lower degradation amounts and rates compared to

the theoretical values. Although no change is observed in the degradation temperatures, the theoretical degradation rate and amount are greater than the experimental values, resulting in a significant difference.

The TGA and DTA curves obtained for the experimental and theoretical (hypothetical) calculations of the lignite–walnut shell mixtures prepared at three different ratios are given in Figure 7. In the TGA result, mass loss increases rapidly around 240°C. The theoretical and experimental mass loss values for the EL75-WS25 and EL50-WS50 mixtures are quite close to each other. However, for the EL25-WS75 mixture, the experimental values for mass loss are considerably higher than the theoretical values, indicating a synergistic effect. For the DTA result, the experimental and theoretical degradation

rates are close to each other at the first peak occurring around 130–140°C. In the second peak, which begins around 300°C, the degradation rate of the theoretical value is considerably higher than the experimental value.

The experimental values have shifted to higher temperatures compared to the theoretical values and have occurred at lower degradation rates.

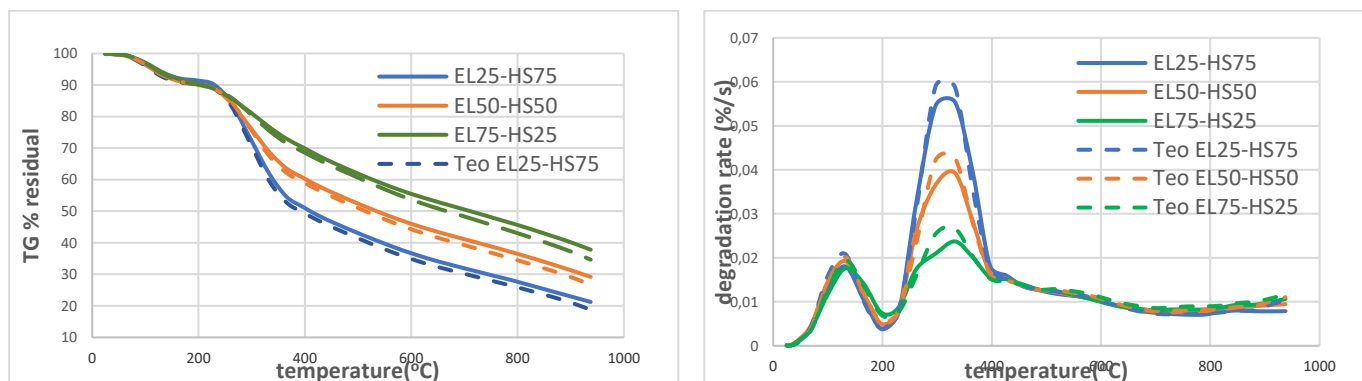


**Figure 6.** TGA and DTA curves for experimental and theoretical calculations of lignite (EL)-biomass (HS) mixture samples.

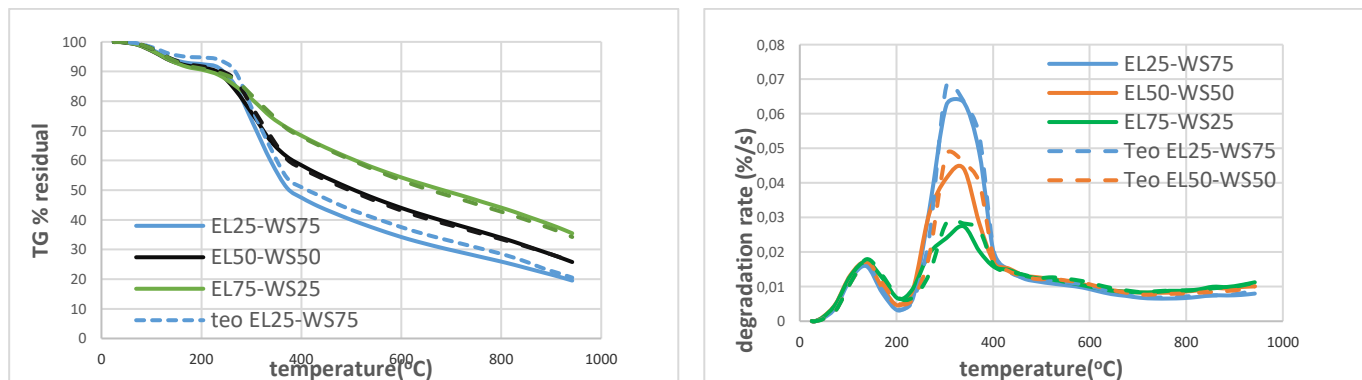


**Figure 7.** TGA and DTA curves for experimental and theoretical calculations of lignite (EL)-biomass (WS) mixture samples.

### 3.5. Pyrolyzed product yields

Coal and biomass samples were firstly pyrolyzed in their raw form and then after being mixed at varying ratios (25%, 50%, 75%) at three different temperatures of 400°C, 460°C, and 520°C. These temperatures were selected based on all TGA and DTA data, as it was determined that reasonable overall conversions were achieved within this temperature range. This selection is justified by the fact that mass loss of the samples begin around 300°C and reach their highest values within the 450–550°C temperature range. The calculated yields of solid, liquid, and gaseous products obtained after pyrolysis at 400°C, 460°C, and 520°C are presented in Table 4.

The results obtained from the table show that solid product yield decreases with increasing temperature. This is an expected outcome, as coal and biomass undergo more thermal decomposition at higher pyrolysis temperatures. The liquid product yield generally increases with temperature; however, no significant change is observed in the hazelnut shell sample. After 460°C, while the liquid yield continues to increase in the walnut shell sample, the increase slows down in the asphaltite sample. In the lignite sample, the liquid yield increases in parallel with the temperature rise. The gas product yields of the raw samples increase at 400°C and 460°C but begin to decline at 520°C. The only exception is the hazelnut shell sample, where gas product yield continues to increase with rising temperature.



**Table 4.** Product yields obtained from the pyrolysis experiments of raw and mixed samples at 400°C, 460°C, and 520°C.

Sample	Solid (%)			Liquid (%)			Gas (%)		
Temperature(°C)	400	460	520	400	460	520	400	460	520
SA	93.06	74.18	74.25	3.53	13.47	14.99	3.41	12.35	10.76
WS	36.06	32.62	30.22	56.08	57.19	62.79	7.86	10.19	6.99
HS	39.79	37.25	34.89	52.06	52.99	53.25	8.15	9.76	11.86
EL	86.00	80.44	75.85	13.60	18.17	23.68	0.40	1.39	0.47
EL25-HS75	59.03	48.40	45.73	36.96	44.30	45.01	4.01	7.30	9.26
EL50-HS50	64.13	59.19	55.92	32.09	35.70	37.03	3.78	5.11	7.05
EL75-HS25	70.54	70.39	66.32	27.93	25.93	27.15	1.53	3.68	6.53
EL25-WS75	48.31	44.57	41.56	45.67	46.96	48.72	6.02	8.47	9.72
EL50-WS50	61.39	56.69	53.51	35.90	35.99	38.72	2.71	7.32	7.77
EL75-WS25	75.21	69.29	64.64	23.99	26.66	29.25	0.80	4.05	6.11
SA25-HS75	55.53	51.00	46.78	44.35	42.71	44.86	0.12	6.29	8.36
SA50-HS50	64.37	62.23	58.17	35.12	29.92	34.51	0.51	7.85	7.32
SA75-HS25	83.48	69.62	65.15	15.36	22.56	24.93	1.16	7.82	9.92
SA25-WS75	52.71	46.83	43.38	41.65	45.68	46.32	5.64	7.49	10.30
SA50-WS50	67.02	59.56	55.46	26.21	34.08	36.56	6.77	6.36	7.98
SA75-WS25	82.75	68.80	65.64	15.46	24.05	22.93	1.79	7.15	11.43

Examining the mixture samples, it is observed that as the ratio of biomass (hazelnut shell and walnut shell) added to lignite increases, the solid product yield decreases, and this decrease becomes more pronounced with increasing temperature. Consequently, the decrease in solid product yield leads to an increase in liquid and gas product yields. The same trend is also observed in the asphaltite sample. It has been reported in the literature that co-pyrolysis of lignite and biomass mixtures is beneficial for gas and liquid production and that these changes are due to synergistic effect [13, 18, 24]. During co-pyrolysis, a synergistic effect occurs due to hydrogen transfer from biomass with high H/C content to coal [33]. Moreover, the variation in gas and liquid product yields with increasing temperature and biomass ratio is attributed to enhanced devolatilization and secondary cracking reactions, which is in agreement with previous studies emphasizing the temperature sensitivity of product distribution during co-pyrolysis [13, 18, 33]. The highest solid product yield is observed at 400°C for the EL75-HS25, EL75-WS25, SA75-HS25, and SA75-WS25 mixtures, while the highest liquid product yield is observed at 520°C for the EL25-HS75, EL25-WS75, SA25-HS75, and SA25-WS75 mixtures. Therefore, the optimum temperature values are determined as 400°C,

where solid product yield is at its maximum, and 520°C, where liquid product yield is at its highest.

After the pyrolysis processes at 400°C, 460°C, and 520°C, the solid products obtained from the raw samples were elementally analyzed, H/C and O/C molar ratios were determined and the results obtained are shown in Table 5. As can be seen from the table, the H/C and O/C molar ratio values for the solid products obtained from pyrolysis process of the raw samples (asphaltite, lignite, walnut shell and hazelnut shell) decrease with increasing temperature.

The elemental analysis results of the raw and mixture samples that yielded the highest solid product yield at the optimum temperature of 400°C are presented in Table 6, while the comparative calorific values are shown in Figure 8.

The comparison of the H/C and O/C molar ratio values of the solid products obtained from the pyrolysis experiments in 400°C for the mixture samples showed an increase with the addition of biomass to lignite and a slight decrease with the addition of biomass to asphaltite.

**Table 5.** Elemental analysis results of the solid products obtained from the pyrolysis experiments of raw samples at 400°C, 460°C, and 520°C.

Sample (dry basis%)	Asphaltite			Lignite			Walnut shell			Hazelnut shell		
Temperature (°C)	400	460	520	400	460	520	400	460	520	400	460	520
Carbon (C)	45.55	39.08	38.74	43.83	44.99	45.42	77.74	81.80	87.12	77.76	81.39	86.97
Hydrogen (H)	3.38	1.94	1.37	2.44	2.07	1.79	3.51	3.10	2.79	3.35	2.97	2.62
Nitrogen (N)	1.17	1.28	1.30	1.45	1.49	1.39	0.73	0.74	0.76	0.77	0.78	1.23
Oxygen (O)*	49.90	57.70	58.59	52.58	51.45	51.40	18.02	14.36	9.33	18.12	14.36	9.18
H/C molar ratio	0.89	0.60	0.42	0.67	0.55	0.47	0.54	0.45	0.38	0.52	0.44	0.36
O/C molar ratio	0.82	1.11	1.13	0.89	0.86	0.85	0.17	0.13	0.08	0.17	0.14	0.08

**Table 6.** Elemental analysis results of the solid products obtained from the pyrolysis experiments at 400°C.

Sample (dry basis%)	C	H	O	N	S	H/C	O/C
WS	77.74	3.51	18.01	0.73	0.01	0.54	0.17
HS	77.76	3.35	18.11	0.77	0.01	0.52	0.17
EL	43.83	2.44	49.23	1.45	3.05	0.67	0.84
SA	45.55	3.38	43.28	1.17	6.62	0.89	0.71
EL75-W25	48.73	2.89	44.45	1.64	2.29	0.71	0.68
EL75-HS25	51.01	2.95	42.14	1.61	2.29	0.69	0.62
SA75-WS25	50.58	3.62	39.38	1.40	5.02	0.86	0.58
SA75-HS25	50.29	3.59	39.46	1.63	5.03	0.86	0.59

\* Calculated from the difference

Comparing the calorific values of the solid products obtained pyrolysis at 400°C, it is observed that the calorific value of the walnut shell sample increased from 4531 kcal/kg to 6494 kcal/kg, while the calorific value of the hazelnut shell sample increased from 4625 kcal/kg to 6440 kcal/kg after pyrolysis. The pyrolysis of walnut shell and hazelnut shell, selected as biomass sources, resulted in the production of high-calorific biochar. A similar comparison for the selected coal sources shows that the calorific value of the lignite sample increased by 41 kcal/kg, whereas a decrease was observed in the asphaltite sample. As seen, the co-pyrolysis of lignite and asphaltite with biomass led to the production of more environmentally friendly, cleaner, and higher-calorific biochar, indicating an improvement in fuel quality.

#### 4. Conclusion

In this study, the performance and efficiency evaluation of the pyrolysis process of coal samples, which have significant reserves in our country, together with two different types of biomass was investigated using the thermogravimetric analysis (TGA) method.

The addition of biomass to lignite and asphaltite samples decreases both the ash and sulfur content. It is observed that the volatile matter content of the biomass samples is significantly higher compared to the lignite and asphaltite samples. The high volatile matter content of these samples contributes to an increase in their calorific value. Furthermore, increasing the amount of biomass added to lignite and asphaltite samples results in a higher H/C molar ratio. The increase in the H/C molar ratio, meaning a higher hydrogen content, leads to an increase in volatile matter and enhances the calorific value, ultimately yielding a higher-quality product.

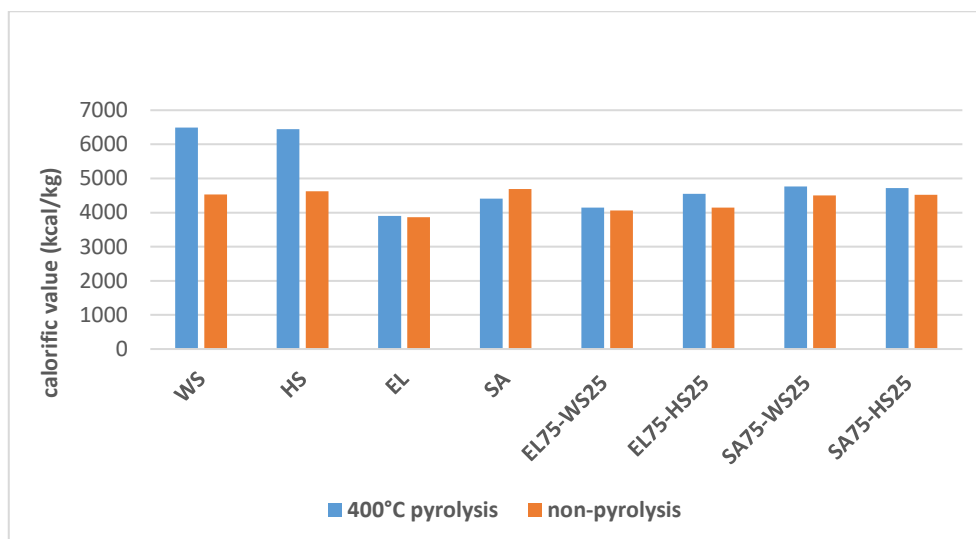


**Figure 8.** Calorific values of the solid products obtained from the pyrolysis experiments at 400°C.

Due to their high volatile matter content in walnut and hazelnut shell samples, the total mass loss in the TGA curves is higher compared to lignite and asphaltite samples. For the mixture samples, analysis of the TGA and DTA curves indicates that as the ratio of biomass added to lignite and asphaltite increases, both the mass loss and degradation rates increase across all mixtures, while the decomposition temperature decreases. When the experimental values of the coal and biomass samples mixed at different ratios are compared with the calculated values of the raw samples, a synergistic effect is observed, which is consistent with the results reported in previous studies, where co-pyrolysis of coal and biomass led to enhanced volatile production and improved thermal conversion efficiency through chemical interactions between the fuel components [18, 19].

In the pyrolysis process, the increase in temperature results in a decrease in solid product yield while leading to an increase in liquid and gas product yields. For the calorific values of solid products at 400°C temperature; while high calorific value biochar was obtained by pyrolysis of walnut and hazelnut shell samples, a slight increase in the calorific value of the lignite sample was observed as a result of the pyrolysis process, while a decrease occurred in the asphaltite sample. After pyrolysis with the addition of biomass to lignite and asphaltite, more environmentally friendly, cleaner and higher quality biochar with high calorific value was obtained. From this study, it can be concluded that the co-pyrolysis of coal and biomass can yield hybrid coal with a higher calorific value and greater environmental compatibility. The calorific value of the hybrid coal obtained from this study is comparable to that of bituminous coal, making it a suitable and more eco-friendly option for power plants. Similar results were also reported in studies indicating that co-pyrolysis of biomass with coal enhances the heating value and

combustion behavior due to synergistic hydrogen transfer and reductions in ash and sulfur content [33].

This study is thought to provide a significant advantage by enabling the more efficient utilization of lignite and asphaltite, the valorization of waste biomass, and the reduction of environmental pollution through the enhancement of coal with biomass, thereby improving the efficiency of both resources.

#### Author's Contributions

**Veysi Kamar:** Supervised the experiment's progress, result interpretation and helped in manuscript preparation.

**Pınar Acar Bozkurt:** Drafted and wrote the manuscript, performed the analytical analysis and result.

#### Ethics

There are no ethical issues after the publication of this manuscript.


#### References

- [1]. GAP Bölge Kalkınma Programı 2022. <http://www.gap-dogu-kalkinma.com2021-2023> (accessed at 10.05.2024), Tarım ve orman Bakanlığı, Tarımsal Araştırmalar (TAGEM), <http://www.tarimorman.gov.tr/TAGEM> (accessed at 10.05.2024).
- [2]. Türkiye Kömür İşletmeleri 2025. [www.tki.gov.tr](http://www.tki.gov.tr). (accessed at 20.01.2025).
- [3]. Merdun, H, Sezgin, İV.2018. Products distribution of catalytic co-pyrolysis of greenhouse vegetable wastes and coal. *Energy*; 162: 953-963.
- [4]. 12. Kalkınma Planı 2024. [https://www.sbb.gov.tr/wp-content/uploads/2023/12/On-Ilkinci-Kalkinma-Planı\\_](https://www.sbb.gov.tr/wp-content/uploads/2023/12/On-Ilkinci-Kalkinma-Planı_) (accessed at 18.01.2025).

- [5]. Vuthaluru, HB. 2004. Thermal behaviour of coal/biomass blends during co-pyrolysis. *Fuel Processing Technology*; 85(2-3): 141–155.
- [6]. Kastanaki E, Vamvuka, D, Grammelis, P, Kakaras E. 2002. Thermogravimetric studies of the behavior of lignite-biomass blends during devolatilization. *Fuel Processing Technology*; 77-78: 159–166.
- [7]. Aboyade, A, Carrier, OM, Meyer, EL, Knoetze, H, Gorgens, JF. 2013. Slow and pressurized co-pyrolysis of coal and agricultural residues. *Energy Conversion and Management*; 65: 198–207.
- [11]. Li, S, Chen, X, Wang, L, Liu A, Yu, G. 2013. Co-pyrolysis behaviors of sawdust and Shenfu coal in drop tube furnace and fixed bed reactor. *Bioresource Technology*; 148: 24-29.
- [12]. Wang, YJ, Ying, H, Sun, H, Jiang, JF, Gao, YW, Yu, WJ. 2013. Co-pyrolysis characteristics of torrefied pine sawdust with different rank coals. *Bio Resources*; 8(4): 5169-5183.
- [13]. Wu, Z, Li, Y, Xu, D, Meng, H. 2019. Co-pyrolysis of lignocellulosic biomass with low-quality coal: Optimal design and synergistic effect from gaseous products distribution. *Fuel*; 236: 43-54.
- [14]. Collard, FX, Blin, J. 2014. A review on pyrolysis of biomass constituents: mechanisms and composition of the products obtained from the conversion of cellulose, hemicelluloses and lignin. *Renewable and Sustainable Energy Reviews*; 38: 594-608.
- [15]. Abnisaand WM, Wandaud, A. 2014. A review on co-pyrolysis of biomass: an optional technique to obtain a high-grade pyrolysis oil. *Energy Conversion and Management*; 87: 71-85.
- [16]. Mushtaq, F, Mat, R, Ani, FN. 2014. A review on microwave assisted pyrolysis of coal and biomass for fuel production. *Renewable and Sustainable Energy Reviews*; 39: 555-574.
- [17]. Chen, X, Liu, L, Zhang, L, Zhao, Y, Zhang, Z, Xie, X, Qiu, P, Chen, G, Pei, J. 2018. Thermogravimetric analysis and kinetics of the co-pyrolysis of coal blends with corn stalks. *Thermochimica Acta*; 659: 59-65.
- [18]. Meng, H, Wang, S, Wu, Z, Zhao, J, Chen, L, Li, J. 2019. Thermochemical behavior and kinetic analysis during co-pyrolysis of starch biomass model compound and lignite. *Energy Procedia*; 158: 400-405.
- [19]. Yi, S, He, XM. 2016. Synergistic effect in low-temperature co-pyrolysis of sugarcane bagasse and lignite. *Korean Journal Chemical Engineering*; 33(10): 2923-2929.
- [20]. Hu, J, Shao, J, Yang, H, Lin, G, Chen, Y, Wang, X, Zhang, W, Chen H. 2017. Co-gasification of coal and biomass: Synergy, characterization and reactivity of the residual char. *Bioresource Technology*; 244(1): 1-7.
- [21]. Li, C, Su, Y, Zhang, L, Li, Q, Zhang, S, Hu X. 2022. Sequential pyrolysis of coal and biomass: Influence of coal-derived volatiles on property of biochar. *Applications in Energy and Combustion Science*; 9: 1-13.
- [22]. Singh, K., Zondlo, J. 2017. Co-processing coal and torrefied biomass during direct liquefaction. *Journal of the Energy Institute*; 90(4): 497-504.
- [23]. Zhao, J, Liu, H, Zhang, H, Song, X, Zuo, H, Wang, G, Xu, Z, Wu, M, Zhang, Z, Chi, R. 2023. Metallurgical performance and structural characteristics of cokes of hypercoal prepared from the mixture of low-rank coal and biomass residue. *Fuel*; 332: 1-11.
- [8]. Chen, X, He, Y. 2012. Co-pyrolysis characteristics of microalgae *Chlorella vulgaris* and coal through TGA. *Bioresource Technology*; 117: 264–273.
- [9]. Shui, H, Shan, C, Cai, Z, Wang, Z, Lei, Z, Ren, S, Pan, C. 2011. Co-liquefaction behavior of a sub-bituminous coal and sawdust. *Energy*; 36(11): 6645–6650.
- [10]. Wei, L, Zhang, S, Xu, P. 2011. Effects of feedstock on co-pyrolysis of biomass and coal in a free-fall reactor. *Journal of Fuel Chemistry and Technology*; 39(10): 728–734.
- [24]. Zhang, P, Chen, Z, Zhang, Q, Zhang, S, Ning, X, Zhou, J. 2022. Co-pyrolysis characteristics and kinetics of low metamorphic coal and pine sawdust. *RSC Advances*; 12: 21725-21735.
- [25]. Mohamed, A, Coşkun, T, Garib, A. 2024. Enhancing lignite coal quality with biomass waste in slow pyrolysis Fischer-Tropsch reactor. *Journal of Engineering Research*; In press.
- [26]. Ma, M, Bai, Y, Song, X, Wang, J, Su, W, Yao, M, Yua, G. 2020. Investigation into the co-pyrolysis behaviors of cow manure and coal blending by TG–MS. *Science of the Total Environment*; 728: 1-9.
- [27]. Cao, Y, He, M, Dutta, S, Luo, G, Zhang, S, Tsang, DCW. 2021. Hydrothermal carbonization and liquefaction for sustainable production of hydrochar and aromatics. *Renewable and Sustainable Energy Reviews*; 152: 1-18.
- [28]. Wei, J, Wang, M, Wang, F, Song, X, Yu, G, Liu, Y, Vuthaluru, H, Xu, J, Xu, Y, Zhang H, Zhang, S. 2021. A review on reactivity characteristics and synergy behavior of biomass and coal Co-gasification, *International Journal of Hydrogen Energy*; 46(33): 17116-17132.
- [29]. Busch, A, Gensterblum, Y. 2011. CBM and CO<sub>2</sub>-ECBM related sorption processes in coal: A review. *International Journal of Coal Geology*; 87(2): 49-71.
- [30]. Wang, YJ, Ying, H, Sun, Y, Jiang, JF, Jiang, JC, Gao, YW, Yu, WJ. 2013. Co-pyrolysis characteristics of torrefied pine sawdust with different rank coals. *Bioresources*; 8(4): 5169-5183.
- [31]. Acma, HH, Yaman, S. 2007. Synergy in devolatilization characteristics of lignite and hazelnut shell during co-pyrolysis. *Fuel*; 86(3): 373–380.
- [32]. Gonzales, JF., Roman, S, Encinar, JM, Martinez, G. 2009. Pyrolysis of various biomass residues and char utilization for the production of activated carbons. *Journal of Analytical and Applied Pyrolysis*; 85(1-2): 134-141.
- [33]. Quan, C, Gao, N. 2016. Co-pyrolysis of biomass and coal: A review of effects of co-pyrolysis parameters, product properties and synergistic mechanisms. *Biomed Research Internatiol*; 2016: 1-11.



## Tribonacci numbers as sum or difference of powers of 2

Fatih Erduvan<sup>1\*</sup> 

<sup>1</sup> MEB, İzmit Namık Kemal Anatolia High School, Kocaeli, Türkiye

\* [erduvanmat@hotmail.com](mailto:erduvanmat@hotmail.com)

\* Orcid No: 0000-0001-7254-2296

Received: 6 August 2024

Accepted: 25 February 2025

DOI: 10.18466/cbayarfbe.1528991

### Abstract

This paper investigates Tribonacci numbers can be expressed as either the sum or difference of two distinct powers of 2. Namely, we address the problem of expressing Tribonacci numbers in the form

$$T_n = 2^x \pm 2^y$$

in positive integers with  $1 \leq y \leq x$ . Our findings reveal specific instances where such representations are possible, including examples like the seventh Tribonacci number expressed both as the sum and the difference of powers of 2. Additionally, we identify Tribonacci numbers that can be represented as the differences of Mersenne numbers, specifically, the numbers 2, 4, 24, and 504. These results enhance the understanding of the structural properties of Tribonacci sequences and their relationships with exponential and Mersenne-based number systems.

**Keywords:** Diophantine equations, Tribonacci numbers, Baker's Theory.

### 1. Introduction

The exploration of the properties of linear recurrence sequences has a rich history and has produced an extensive body of literature. The quest to find all integer solutions to Diophantine equations with Fibonacci numbers has drawn considerable interest from mathematicians, leading to a diverse array of literature on the subject. Tribonacci numbers are a generalization of Fibonacci numbers and therefore, it is inevitable that equations containing Tribonacci numbers will also be interesting. Let  $(T_n)$  be the sequence of Tribonacci numbers defined by  $T_0 = 0, T_1 = T_2 = 1$  and

$$T_{n+3} = T_{n+2} + T_{n+1} + T_n \quad \text{for } n \geq 0.$$

In recent years, many studies have been seen involving integer sequences and powers integers. Readers can see these works in [1-9]. Especially, the equation

$$T_n = 2^a + 3^b + 5^c + \delta$$

related to Tribonacci numbers has been solved by Irmak and Szalay in [10]. Here, variables are non-negative integers with  $0 \leq \delta \leq 10$  and  $0 \leq a, b \leq c$ .

In this paper, using the linear forms in logarithms, we obtain large upper bounds thanks to Lemma 2.1 and then, we reduce these bounds using Lemma 2.2. Now, we give our main theorem.

**Theorem 1.1:** Let  $T_n$  be n-th Tribonacci number. The only solutions to the Diophantine equations

$$T_n = 2^x + \epsilon 2^y \tag{1}$$

in non-negative integers with  $1 \leq y \leq x$  and  $\epsilon = \pm 1$  are given by

$$\epsilon = 1: \quad (n, x, y) = (4, 1, 1), (7, 4, 3);$$

$$\epsilon = -1: \quad (n, x, y) = \{(0, x, x), (3, 2, 1), (4, 3, 2), (7, 5, 3), (12, 9, 3)\}.$$

### 2. The Tools

In this section, we will remind you about Tribonacci numbers and linear forms in logarithms. We will also give some lemmas that are necessary to prove the main theorem. The characteristic equation

$$\psi(x) := x^3 - x^2 - x - 1 = 0$$

has roots  $\alpha, \beta, \gamma = \bar{\beta}$  where

$$\alpha = \left(\frac{1+(s_1+s_2)}{3}\right), \bar{\gamma} = \beta = \left(\frac{2-(s_1+s_2)+\sqrt{-3}(s_1-s_2)}{6}\right)$$

and

$$s_1 = \sqrt[3]{19 + 3\sqrt{33}}, s_2 = \sqrt[3]{19 - 3\sqrt{33}}.$$

Binet formula for this number is

$$T_n = a\alpha^n + b\beta^n + c\gamma^n \text{ for all } n \geq 0, \quad (2)$$

where

$$a = \frac{1}{(\alpha-\beta)(\alpha-\gamma)}, b = \frac{1}{(\beta-\alpha)(\beta-\gamma)}, \text{ and } c = \frac{1}{(\gamma-\alpha)(\gamma-\beta)}.$$

Moreover,  $a = \frac{\alpha}{\alpha^2+2\alpha+3}$  and the minimal polynomial of  $a$  over  $\mathbb{Z}$  is given by  $44x^3 + 44x - 1$ . Zeros of this equation are  $a, b$  and  $c$ . With simple calculations, it can be shown the following estimates hold:

$$1.83 < \alpha < 1.84, 0.73 < |\beta| = |\gamma| < \alpha^{1/2} < 0.74$$

and

$$0.18 < a < 0.19, 0.35 < |b| = |c| < 0.36.$$

Let

$$e(n) := T_n - a\alpha^n = b\beta^n + c\gamma^n.$$

Then, from the above inequalities we conclude that

$$|e(n)| := \frac{1}{\alpha^{n/2}} \quad (3)$$

for  $k \geq 1$ . The relation between  $T_n$  with  $\alpha$  is given by

$$\alpha^{n-2} \leq T_n \leq \alpha^{n-1} \text{ for all } n \geq 1. \quad (4)$$

Baker's Theory, developed by Alan Baker, is an important theory on number theory and Diophantine equations. This theory specifically includes the concepts of linear form and logarithmic height and plays a large role in the context of solving Diophantine equations. Now, we present materials related to this theory. Let  $\gamma$  be an algebraic number of degree  $d$  over  $\mathbb{Q}$  with minimal primitive polynomial

$$c_0x^d + c_1x^{d-1} + \dots + c_d = c_0 \sum_{i=1}^d (x - \gamma^{(i)}) \in \mathbb{Z}[x],$$

with  $\gamma^{(i)}$ 's are conjugates of  $\gamma$  and  $c_0 > 0$ . Then logarithmic height of  $\gamma$  is given

$$h(\gamma) = \frac{1}{d} (\log c_0 + \sum_{i=1}^d \log(\max\{|\gamma^{(i)}|, 1\})).$$

The following properties are given in [11].

$$h(\gamma_1 \mp \gamma_2) \leq \log 2 + h(\gamma_1) + h(\gamma_2)$$

$$h(\gamma_1 \gamma_2^{\pm 1}) \leq h(\gamma_1) + h(\gamma_2)$$

$$h(\gamma_1^r) = |r|h(\gamma_1).$$

The following two lemmas can be found in [12,13].

**Lemma 2.1.** Let  $\gamma_1, \gamma_2, \dots, \gamma_n$  be positive real algebraic numbers and let  $b_1, b_2, \dots, b_n$  be nonzero integers. Let  $D$  be the degree of the number field  $\mathbb{Q}(\gamma_1, \gamma_2, \dots, \gamma_n)$  over  $\mathbb{Q}$ . Let

$$B \geq \max\{|b_1|, |b_2|, \dots, |b_n|\},$$

$$A_i \geq \max\{D \cdot h(\gamma_i), |\log \gamma_i|, (0.16)\}$$

for all  $i = 1, 2, \dots, n$ . If

$$\Gamma := \gamma_1^{b_1} \cdot \gamma_2^{b_2} \cdots \gamma_n^{b_n} - 1 \neq 0$$

then

$$|\Gamma| > \exp(-1.4 \cdot 30^{n+3} \cdot n^{4.5} \cdot D^2 \cdot (1 + \log D) \cdot (1 + \log B) \cdot A_1 \cdot A_2 \cdots A_n).$$

**Lemma 2.2.** Let  $\eta$  be irrational number,  $M$  be a positive integer and  $\frac{p}{q}$  be a convergent of the continued fraction of  $\eta$  such that  $q > 6M$ , and let  $A, B, \mu$  be some real numbers with  $A > 0$  and  $B > 1$ . Put

$$\varepsilon := \|\mu q\| - M\|\eta q\|,$$

where  $\|\cdot\|$  denotes the distance from the nearest integer. If  $\varepsilon > 0$ , then there is no positive integer solution  $(r, s, t)$  to the inequality

$$0 < |r\eta - s + \mu| < A \cdot B^{-t}$$

subject to the restrictions that

$$r \leq M \text{ and } t \geq \frac{\log(Aq/\varepsilon)}{\log B}.$$

We give the following lemma without proof since its proof can be easily seen.

**Lemma 2.3.** If the real numbers  $x$  and  $K$  satisfy

$$|e^x - 1| < K < 3/4,$$

then  $|x| < 2K$ .

### 3. Proof of Main Theorem

In the case  $x = y$ , we have the trivial solution

$(n, x, y) = (0, x, x)$  for  $\epsilon = -1$  and the only solution  $(n, x, y) = (4, 1, 1)$  for  $\epsilon = 1$ , from [14]. From now on, we will take  $1 \leq y < x$ . As  $y \leq x - 1$  and  $x \geq 2$ , we can say

$$2 < 2^{x-1} = 2^x - 2^{x-1} \leq 2^x - 2^y < T_n$$

by the equation (1). So, we get  $n \geq 3$ . Now let's find a relationship between  $n$  and  $x$ . Considering (1), we obtain

$$T_n \leq 2^x + 2^y \leq 2^x + 2^{x-1} = 3 \cdot 2^{x-1} < \alpha^{1.9+1.2(x-1)}.$$

If we combine the above inequality and (4), we get

$$n < 1.7 + 1.2x \quad (5)$$

Using (2) and (3), we arrange the equation (1) as

$$|\Gamma| = |a \cdot \alpha^n \cdot 2^{-x} - 1| \leq \frac{1}{\alpha^{\frac{n}{2} \cdot 2^x}} + \frac{1}{2^{x-y}} < \frac{1.21}{2^{x-y}} \quad (6)$$

and

$$\begin{aligned} |\Gamma'| &= |(a^{-1}(1 \pm 2^{y-x}))^{-1} \cdot \alpha^n \cdot 2^{-x} - 1| \\ &\leq \frac{1}{\alpha^{\frac{n}{2} \cdot 2^x \cdot |1 \pm 2^{y-x}|}} \\ &< \frac{0.81}{2^x}. \end{aligned} \quad (7)$$

Here, we have used that  $\alpha^{\frac{n}{2}} < 0.401$  for  $n \geq 3$  and

$$|1 \pm 2^{y-x}|^{-1} < 2$$

for  $1 \leq y < x$ . To apply Lemma 2.1, we take

$$(\gamma_1, b_1) := (a, 1)$$

$$(\gamma'_1, b'_1) := ((a^{-1}(1 \pm 2^{y-x}))^{-1}, -1)$$

$$(\gamma_2, b_2) = (\gamma'_2, b'_2) := (\alpha, n)$$

$$(\gamma_3, b_3) = (\gamma'_3, b'_3) := (2, -x)$$

in the inequalities (6) and (7). Moreover,  $D = D' = 3$ . Now, we show that

$$\Gamma := a \cdot \alpha^n \cdot 2^{-x} - 1 \neq 0.$$

If  $\Gamma = 0$ , then we can write  $a \cdot \alpha^n = 2^x \in \mathbb{Z}$ , which is not possible. Similarly,

$$\Gamma' := (a^{-1}(1 \pm 2^{y-x}))^{-1} \cdot \alpha^n \cdot 2^{-x} - 1 \neq 0.$$

Using the definition and properties of logarithmic height, we get

$$h(\gamma_1) = h(a) = \frac{\log 44}{3},$$

$$\begin{aligned} h(\gamma'_1) &= h((a^{-1}(1 \pm 2^{y-x}))^{-1}), \\ &< \frac{\log 44}{3} + (x - y) \log 2 + \log 2, \\ &< 3.9(x - y) \log 2, \end{aligned}$$

$$h(\gamma_2) = h(\gamma'_2) = h(\alpha) = \frac{\log \alpha}{3},$$

and

$$h(\gamma_3) = h(\gamma'_3) = h(2) = \log 2.$$

Thus, we can write

$$A = A_1 \cdot A_2 \cdot A_3 = \log 44 \cdot \log \alpha \cdot \log 8,$$

$$A' = A'_1 \cdot A'_2 \cdot A'_3 := 11.7(x - y) \log 2 \cdot \log \alpha \cdot \log 8.$$

The inequality (5) lead to  $B = B' := 1.7 + 1.2x$ . Let

$$T = (-1.4) \cdot 30^6 \cdot 3^{4.5} \cdot 3^2 \cdot \log 9.$$

From Lemma 2.1, the inequalities (6) and (7) give us

$$1.21 \cdot 2^{-(x-y)} > |\Gamma| > \exp((T \cdot (3.5 \log x) \cdot A))$$

i.e.,

$$x - y < 6.55 \cdot 10^{13} \cdot \log x \quad (8)$$

and

$$0.81 \cdot 2^{-x} > |\Gamma'| > \exp((T \cdot (3.5 \log x) \cdot A'))$$

i.e.,

$$x < 1.41 \cdot 10^{14} \cdot (x - y) \cdot \log x, \quad (9)$$

where we have used

$$1 + \log(1.7 + 1.2x) < 3.5 \log x$$

for  $x \geq 2$ . The inequalities (8) and (9) tell us

$$x < 9.24 \cdot 10^{27} \cdot (\log x)^2$$

or  $x < 4.93 \cdot 10^{31}$ . From (5), we obtain

$$n < 5.92 \cdot 10^{31}. \quad (10)$$

Let

$$z := n \log \alpha - x \log 2 + \log a$$

and

$$z' := n \log \alpha - x \log 2 - \log((a^{-1}(1 \pm 2^{y-x})).$$

From (6) and (7), we can write

$$|\Gamma| := |e^z - 1| < \frac{1.21}{2^{x-y}} < 0.61$$

for  $x - y \geq 1$  and

$$|\Gamma'| := |e^{z'} - 1| < \frac{0.81}{2^x} < 0.21.$$

for  $x \geq 2$ . According to Lemma 2.3, we can say

$$|z| = |n \log \alpha - x \log 2 + \log \alpha| < \frac{2.42}{2^{x-y}}$$

and

$$|z'| = |n \log \alpha - x \log 2 - \log((a^{-1}(1 \pm 2^{y-x}))| < \frac{1.62}{2^x}.$$

With necessary arrangement, these inequalities convert to

$$0 < \left| n \left( \frac{\log \alpha}{\log 2} \right) - x + \frac{\log \alpha}{\log 2} \right| < \frac{3.5}{2^{x-y}} \quad (11)$$

and

$$0 < \left| n \left( \frac{\log \alpha}{\log 2} \right) - x - \frac{\log((a^{-1}(1 \pm 2^{y-x}))}{\log 2} \right| < \frac{2.34}{2^x}. \quad (12)$$

To apply Lemma 2.2, we choose

$$\eta = \eta' := \frac{\log \alpha}{\log 2}, \mu := \frac{\log \alpha}{\log 2}, A := 3.5, B := 2, t := x - y$$

and

$$\mu' := \frac{\log((a^{-1}(1 \pm 2^{y-x}))}{\log 2}, A' := 2.34, B' := 2, t' := x$$

by considering (11) and (12). To reduce  $x - y$ , we take

$$n < 5.92 \cdot 10^{31} = M$$

from (10) in the equation (11). We find that  $q_{62} > 6M$  for  $\eta$ . Moreover, we compute

$$\varepsilon := \|\mu q_{62}\| - M \|\eta q_{62}\| > 0.37.$$

Thanks to Lemma 2.2, we have

$$x - y \leq \frac{\log(\frac{Aq_{62}}{\varepsilon})}{\log B} \leq 112.61,$$

and so  $x - y \leq 112$ . This upper bound and (9) give us

$$x < 6.48 \cdot 10^{18}.$$

The above inequality and (5) imply that

$$n < 7.78 \cdot 10^{18}. \quad (13)$$

Considering (12) and (13), we choose

$$n < 7.78 \cdot 10^{18} = M'.$$

It can be seen that  $q_{33} > 6M'$  for  $\eta'$ . Furthermore, we compute

$$\varepsilon := \|\mu q_{33}\| - M \|\eta q_{33}\| > 0.001.$$

From Lemma 2.2, we conclude that

$$x \leq \frac{\log(\frac{Aq_{33}}{\varepsilon})}{\log B} \leq 78.86.$$

From this, we get  $x \leq 78$  and so  $n \leq 95$ . With help a computer program, we get the only solutions displayed as

$$24 = T_7 = 2^4 + 2^3, \quad 2 = T_3 = 2^2 - 2^1,$$

$$4 = T_4 = 2^3 - 2^2, \quad 24 = T_7 = 2^5 - 2^3,$$

$$504 = T_{12} = 2^9 - 2^3$$

for  $1 \leq y < x \leq 78$  and  $3 \leq n \leq 95$ . Therefore, the proof ends.

Mersenne numbers are given by  $2^a - 1$  for  $a \geq 1$ . Difference of two Mersenne numbers is expressed as  $2^a - 2^b$  for  $a, b \geq 1$ .

**Corollary 3.1:** Tribonacci numbers that can be written as the difference of two Mersenne numbers are 2, 4, 24 and 504.

#### 4. Conclusion and Suggestion

Recently, investigators have used linear forms in logarithms and reduction method in many of their studies. It turned out that the Diophantine equation produced the interesting result, which is Tribonacci numbers in the form of the difference of two Mersenne numbers. This result not only show cases the power of logarithmic forms in solving Diophantine equations but also provides a deeper understanding of the interplay between different number-theoretic structures.

As a more general version of this study, solutions to these equations can be investigated by substituting various integer sequences for 2 in these equations. By doing so, one can explore a broader class of Diophantine equations that involve powers of integers, such as powers of primes or other specially constructed sequences. This approach could yield new insights into the nature of integer solutions and their distribution, potentially revealing deeper symmetries in number theory.



## Acknowledgement

The authors thank the anonymous reviewers for their contribution to this paper.

## Author's Contributions

**Fatih Erduvan:** Supervision, Methodology, Validation, Writing-original draft, Investigation

## Ethics

There are no ethical issues after the publication of this manuscript.

## References

- [1]. Bravo, JJ, Luca, F. 2014. Powers of two as sums of two Lucas numbers. *Journal of Integer Sequences*; 17(1): article no 14.8.3.
- [2]. Bravo, EF, Bravo, JJ. 2015. Powers of two as sums of three Fibonacci numbers. *Lithuanian Mathematical Journal*; 55(3). 301-311.
- [3]. Bravo, JJ, Gómez, CA, Luca, F. 2016. Powers of two as sums of two k-Fibonacci numbers. *Miskolc Mathematical Notes*; 17(1): 85-100.
- [4]. Bravo, JJ, Faye, B, Luca, F. 2017. Powers of two as sums of three Pell numbers. *Taiwanese Journal of Mathematics*; 21(4): 739-751.
- [5]. Erduvan, F, Keskin, R. 2019. Non-negative integer solutions of the equation  $F_n - F_m = 5^a$ . *Turkish Journal of Mathematics*; 43(3): 1115-1123.
- [6]. Demirtürk, B. 2019. On the Diophantine equation  $L_n - L_m = 2 \cdot 3^a$ . *Periodica Mathematica Hungarica*; 79(2): 210-217.
- [7]. Tiebekabe, P, Diouf, I. 2021. Powers of three as difference of two Fibonacci numbers. *JP Journal of Algebra, Number Theory and Applications*; 49(2): 185-196.
- [8]. Aboudja, H., Hernane, M, Rihane, SE, Togbé, A. 2021. On perfect powers that are sums of two Pell numbers. *Periodica Mathematica Hungarica*; 82: 11-15.
- [9]. Şiar, Z, Keskin, R. 2020. On the Diophantine equation  $F_n - F_m = 2^a$ . *Colloquium Mathematicum*; 159: 119-126.
- [10]. Irmak, N, Szalay, L. 2016. Tribonacci Numbers Close to the Sum  $2^a + 3^b + 5^c$ . *Mathematica Scandinavica*; 118: 27-32.
- [11]. Y. Bugeaud, 2018. "Linear Forms in Logarithms and Applications" IRMA Lectures in Mathematics and Theoretical Physics 28, Zurich, *European Mathematical Society*, 1-176.
- [12]. Y. Bugeaud, M. Mignotte S. Siksek, 2006. "Classical and modular approaches to exponential Diophantine equations I. Fibonacci and Lucas perfect powers" *Annals of Mathematics*, 163(3), 969-1018.
- [13]. J.J. Bravo, C.A. Gomez, F. Luca, 2016. "Powers of two as sums of two k-Fibonacci numbers" *Miskolc Mathematical Notes*, 17(1), 85-100.
- [14]. Bravo, J.J., Luca, F. (2012). Powers of two in generalized Fibonacci sequences. *Revista Colombiana de Matemáticas*, 46(1), 67-79.

# Binary Classification of Alzheimer's Disease Using Siamese Neural Network for Early Stage Diagnosis

Ruken Tekin<sup>1\*</sup> , Tuğba Özge Onur<sup>1</sup> 

<sup>1</sup> Dept. of Electrical-Electronics, Faculty of Engineering, Zonguldak Bülent Ecevit University, Zonguldak, Türkiye

\* [r.tekin@fbe.karaelmas.edu.tr](mailto:r.tekin@fbe.karaelmas.edu.tr)

\* Orcid No: 0000-0003-4732-7580

Received: 7 August 2024

Accepted: 9 February 2025

DOI: 10.18466/cbayarfbe.1529546

## Abstract

Alzheimer's Disease (AD) is a cognitive disease. In individuals with disease, increased brain cell loss is observed over time. This situation leads to deficiencies in memory and thinking ability over time. As a result, significant impairments occur in individuals' ability to perform primary function. According to research results, the rate of thos disease doubles every five years among people aged between 65 and 85. The causes of AD are unknown and nowadays not definite cure. Early diagnosis of the disease in clinical cure as it has the potential to slow or stop progression. This study aimed to make a prediction based on Magnetic Resonance (MR) images. Images in the standard Alzheimer dataset obtained from the open access database Kaagle were enhanced by applying Gaussian and Median filters. Siamese Neural Network (SNN) categorizes disease stages by learning the similarity between these images. Two categories of images were used from the dataset: Very Mild Dementia (VMD) and Non-Dementia (ND). According to this proposed study, the training accuracy was %99.62 and the validation accuracy %97.67.

**Keywords:** Siamese Neural Network, Machine Learning, Alzheimer Disease, Magnetic Resonance Imaging

## 1. Introduction

Alzheimer's disease is a neurodegenerative cognitive disorder [1]. Among people with AD, the continuous death of brain cells causes damage to memory and thinking functions, leaving the person unable to carry out even daily activities [2]. AD has a prevalence of 3-11% in people over the age of 65 and 20-47% over the age of 85. Studies in different regions of the world have shown that the incidence of people with AD doubles every five years [3].

Alzheimer's is generally divided four parts. These are Mild Cognitive Impairment (MCI), Mild Dementia, Moderate Dementia and Severe Dementia. MCI, as in this stage many people may experience memory loss due to age. This does not mean that every older person has MCI, but it can lead to dementia in others. Mild dementia (MID) is a condition seen in people who have cognitive impairments during the day, sometimes affecting their daily lives. In this phase of the disease,

loss of memory, people' s personal behavior status disorder manifests itself as the inability continue daily life or difficulty in doing so. In moderate dementia, it becomes noticeably more complex for people to carry out daily activities. The symptoms are mild but equivalent to high-level dementia. Individuals may become suspicious or angry for irrational reasons. Sleep problems are also likely to occur. In the severe phase of dementia, symptoms can be worse. Individuals may lose their ability to communicate and need care. People in this stage may have loss of control on bladder and unable to perform simple activities such as holding their own head in a normal posture or sitting in a chair [4].

Clinically, the cause of AD remains unclear and there is currently no treatment for the disease [5]. Diagnosing AD at an early state may provide an opportunity to slow or halt progression. Early prediction and diagnosis of AD is therefore significant in clinical treatment [6]. Research has revealed that there are different biomarkers in patients' brains that help early diagnosis of AD [7]. These changes in the brain are used to diagnose AD in clinical

settings by magnetic resonance imaging (MRI) and positron emission tomography (PET)[8].

With MR imaging, structural and functional information of the brain can be obtained by utilising the tissue contrast of the images. PET imaging can provide metabolic and molecular information of the brain [9]. Additionally, with these methods, AD is diagnosed qualitatively, but also the sensitivity of the threshold can be measured, which can be identified at different stages of the disease [10].

Machine learning and deep learning methods serve as robust instruments for creating predictive models based on MRI [11]. There are similar works in the literature for the predictive diagnosis and diagnostic problem. Lu and others [12] suggested new multimodal deep neural network. The model achieved 82.4% accuracy in predicting MCI and detected that these patients developed Alzheimer's in the following three years. Gupta et al [13] suggested a diagnostic model for AD classification based on the Alzheimer's Disease Neuroimaging Initiative (ADNI) and National Questionnaire Scale dataset. By combining features from various parts of the brain in MRI data, this method classified people with AD with a success rate of 96.42% compared to Healthy Control (HC). Ahmed and others [14] suggested an ensemble Convolutional Neural Network (CNN) model. The study was designed to automate AD classification using sMRI. It adopted a patch-based approach specifically targeting the left and right hippocampus areas. In experiments on ADNI and the National Research Center for Dementia (NRCD) databases, accuracy rates of 85.55% and 90.05% were obtained, respectively. Nawaz et al [15] proposed the use of a trained AlexNet model for Alzheimer's detection. The model leveraging deep features attained a classification with a success rate of 99.21%. Shi and others [16] suggested deep polynomial network. This study achieved 55.34% success for AD. Liu and others [17] suggested deep SNNs to detect brain asymmetries related to AD and MCI. The dataset obtained from the ADNI database was used. In this study, the accuracy rate for MCI and AD classification is 92.72%. Xiaowang Bi and others [18] proposed deep metric learning and CNN for Alzheimer's disease-healthy control (AD-HC), healthy control- Mild Cognitive Impairment (HC-MCI) binary classification. They used MRI in the ADNI database and obtained 65% accuracy for MCI-HC classification and 83% accuracy for AD-HC classification.

This paper proposes SNNs, a machine learning method for identification of early stage AD utilizing MR images. This study, a binary classification was made between people with very mild dementia, an early stage of AD, and people without dementia. Segmented 2-dimensional (2D) MRI were used and Median and Gaussian filters were applied. Multilayer CNN was built to augment the

SNN. The results were evaluated with Accuracy (Acc), Sensitivity (Sens), and Specificity (Spec) success evaluation metrics and the results are explained in Section 4.

## 2. Materials and Methods

This part explains the material and methodology used to process and classify MRI datasets. Figure 1 represent processing steps of the proposed model. In this model, the dataset is acquired and preprocessed. Gaussian and Median filters are used in the preprocessing step. Then the dataset is trained and classified with SNNs.

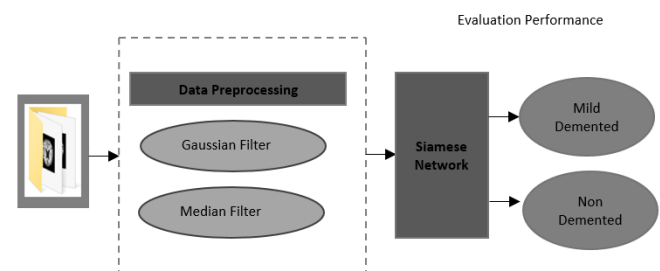


Figure 1. Stages of the study.

### 2.1. MRI Alzheimer's Dataset

The AD dataset was acquired by Kaggle. The dataset contains a total of 6400 MR images belonging to four classes: MID, Moderate Dementia (MOD), ND and VMD. The original size of the images in the dataset is  $176 \times 208$ .

In this study, 700 VMD samples and 700 ND samples were randomly selected and used. Figure 2 below shows some images resized to  $176 \times 176$ .

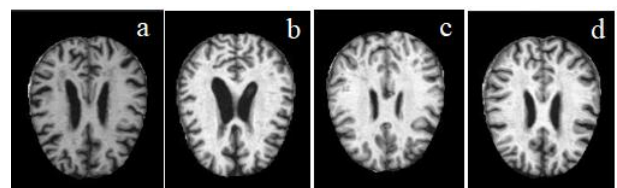


Figure 2. (a) Mild Demented, (b) Moderate Demented, (c) Non Demented, (d) Very Mild Demented

### 2.2. Data Preprocessing

In this study, Gaussian and Median filters were used to enhance MR images.

#### 2.2.1. Gaussian Filter

Gaussian filter was applied to the images. This linear filter assigns weighted values to each element, determined by the Gaussian function's shape. The filter is usually very effective in eliminating leakage noise [19]. Using Equation (1), the value of each member of the

Gaussian filter can be calculated or determined. In this equation,  $\sigma$  represents the standard deviation of the Gaussian Kernel and  $c$  represents the normalization constant.

$$h(x, y) = \frac{1}{c} e^{-\frac{x^2 + y^2}{2\sigma^2}} \quad (1)$$

### 2.2.1. Median Filter

Median filtering is an image processing method used to enhance images. This nonlinear method preserves helpful information in the image [20]. The preservation of helpful information is achieved by converting the original pixel gray value of an image into the average gray value of the pixels in a given neighbourhood. The numerical formula for the median filtered  $K(u, v)$  image for the  $J(x, y)$  image is shown in Equation (2),

$$J(x, y) = \underset{(u, v \in R_{xy})}{\text{median}}\{K(u, v)\} \quad (2)$$

### 2.3. Siamese Neural Network

Siamese Neural Network was proposed to solution signature authentication challenge [21]. The objective is verifying that the signatures belong to the person concerned. SNN is trained based on similarity discrimination between two input images. Figure 3 expresses the way this model works. The similarity of the images is determined by associating input images based on weight parameters shared across the neural networks. In cases where the weight parameters extracted on two images give approximately analogous results, the images are decided to be identical.

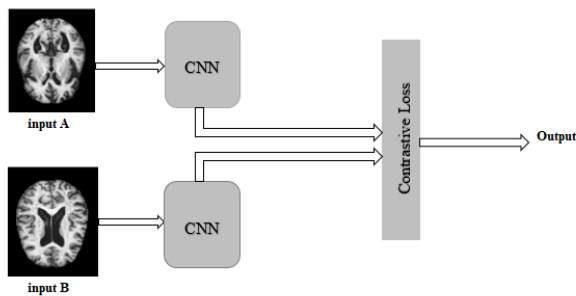


**Figure 3.** Working principle of SNN.

In the SNN model, a threshold value is utilised for this purpose and the gap between the output produced by the two neural networks is calculated. If this diff is less than the threshold, the output indicates that the images are analogous or identical; otherwise, the model produces an output indicating that the results are different [22].

Each pixel in the image has a numerical value. The distance between the pixels is usually calculated using the Euclidean distance given in Equation (3). Here, the

variable  $U$  symbolises the interval, and the variables  $x$  and  $y$  symbolise the two vectors generated within the neural networks.

$$U = \sqrt[2]{\sum_{i=1}^n (x^i - y^i)^2} \quad (3)$$

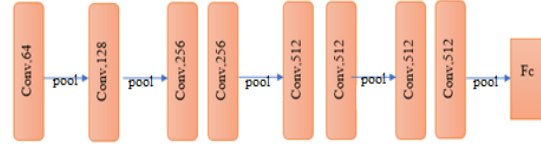


**Figure 4.** CNN architecture.

### 2.3.1. Contrastive Loss Function

The comparative loss function computes the loss for every pair of placements, aiming for reduced distances between similar pairs and increased distances between dissimilar pairs. The comparative loss is calculated by the formula given by Equation (4),

$$L = (1 - y) * D^2 + y * \max(0, m - D)^2 \quad (4)$$

where:

L: Comparative loss for the pair.

D: Distance or difference between embeddings.

y: Label indicating whether the pair is similar or dissimilar (0 for similar, 1 for dissimilar).

m: Margin parameter defining the dissimilarity threshold.

### 2.4. Evaluation Index

The study's performance was assessed using the Acc, Sens, and Spec metrics.

In the equations below, letters are given according to the situations of the people. A refers to patients with a correct diagnosis. B, C and D refer to healthy individuals who have been correctly diagnosed; healthy individuals who were misdiagnosed; sick individuals who have been misdiagnosed, respectively.

Acc is calculated by Equation (5) and expresses the ratio of the number of people that can be properly predicted and categorized.

$$Acc = \frac{A+B}{A+B+C+D} \quad (5)$$

The term Sens denotes the proportion of correctly identified patients in the overall number of patients and is calculated by Equation (6).

$$Sens = \frac{A}{A+D} \quad (6)$$

The term Spec denotes the proportion of correctly identified healthy individuals relative to the total number of individuals without any health issues, computed as outlined in Equation (7).

$$Spec = \frac{B}{B+C} \quad (7)$$

Precision, recall and F1-score are the criteria that analyse the performance of the classification models. These measures are formulated with reference to the confusion matrix in Table 1.

**Table 1.** Cofusion matrix

	PREDICTED	
	True Posivites (TP)	False Negives (FN)
	False Posivites (FP)	True Negives (TN)
ACTUAL		

The areas where the model makes correct predictions are expressed as True Positive and True Negative, while the areas where the model makes incorrect predictions are False Positive and False Negative.

Precision indicates the accuracy of Positive class predictions, calculated as the ratio of True Positives to all Positive predictions.

$$Precision = \frac{TP}{TP+FP} \quad (8)$$

Recall (Rec) is a metric that shows how much of what is expected to be positively predicted is positively predicted.

$$Rec = \frac{TP}{TP+FN} \quad (9)$$

The F1 Score represents the harmonic mean of Precision and Recall.

$$F_1 = 2 * \frac{precision*recall}{precision+recall} \quad (10)$$

### 3. Training and Evaluation

In this study, Very Mild Demented and Non Demented MR images were taken as two different inputs and used for comparison. The images were preprocessed before being trained with the neural network. The images were resized as 176 x 176. Then Gaussian and Median filters were applied to improve the images.

To obtain a successful model in machine learning, the parameters must be estimated correctly. In order to accomplish this, the dataset is segmented into a training set and a validation set. Training set is the set in which the model is taught what is desired to be taught, while the validation set is the set utilized to measure how well the model has learned what has been taught [22]. Here the dataset is divided 80% training data and 20% validation data.

Within framework of the SNN used in differentiating the stages of AD, positive and negative image pairs were generated for similarity learning. For this pair generation step, two different images are selected; if the images belong to the same class, they are considered as positive pairs, and if they belong to different classes, they are considered as negative pairs. The features of the images are then extracted with CNN. The evaluation of the similarity relationship among images is conducted through the utilization of the Euclidean distance metric. Error estimation of the relationship is calculated with Contrastive loss function.

The structure of the CNN model consists of 8 convolution layers, 5 pooling layers, 3 fully dependent layers, 1 dropout layer and 2 normalization layers. Rectified Linear Unit (ReLU) is used as the activation function. In the CNN model of this study, average pooling was used as the pooling layer.

### 4. Results

Python programming language was utilized to create the model. The experiments were conducted using TensorFlow and Keras libraries in Google Colab Pro (Google) environment, a cloud service for deep learning research. The proposed model was tested using 32GB RAM and Tensor Processing Unit (TPU) speed.

The model was trained with 50 epoch parameters, 16 batch sizes and a learning rate of 0.0001. Training was performed on 700 very mild dementia samples and 700 non-dementia samples randomly selected from the dataset. Adaptive moment (Adam) was used as the optimization method.

Figure 5 shows the values obtained during the training for the model. Figure 5 (a) graphs the values obtained from training and validation data. Figure 5 (b) shows the accuracy and 5 (c) shows the sensitivity/specificity graphs. When the accuracy graph is analyzed; the fact that the performances of the training and validation sets have similar increases shows that the model does not face the issue of overlearning. The training accuracy of the model was 99.62% and the validation accuracy was 97.67%. Table 2 indicate other outcome of the model.



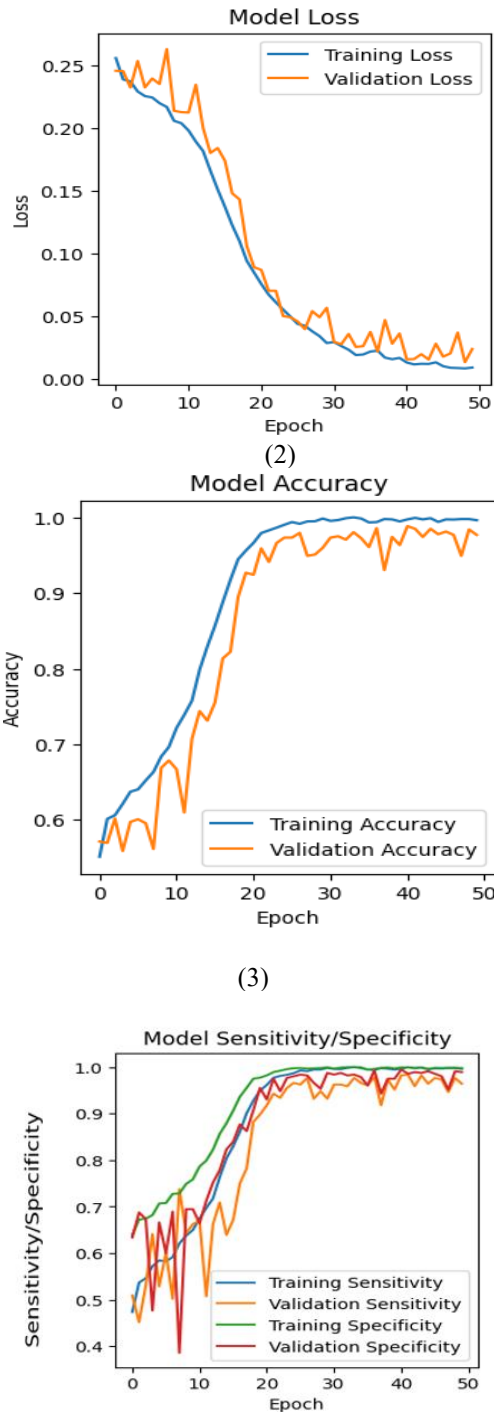


**Figure 5.** Training process (a) loss, (b) accuracy, (c) sensitivity/specificity of SNN model.

**Table 2.** AD diagnosis results

Metrics	Acc (%)	Loss (%)	Sens (%)	Spec (%)
Train Data	99.62	0.89	99.61	99.8
Validation Data	97.67	0.23	96.42	98.92

In order to compare the outputs of the study, a confusion matrix was created, shown in Figure 6. The performance of the model on the dataset is depicted by the confusion matrix. This matrix was created based on test data of two different categories. When the confusion matrix is analyzed, 554 data belonging to the Very Mild Demented class were true classified, while 6 data were mistake predicted. In addition, while 540 images in the Non Demented class were correctly predicted, 20 images were incorrectly predicted.

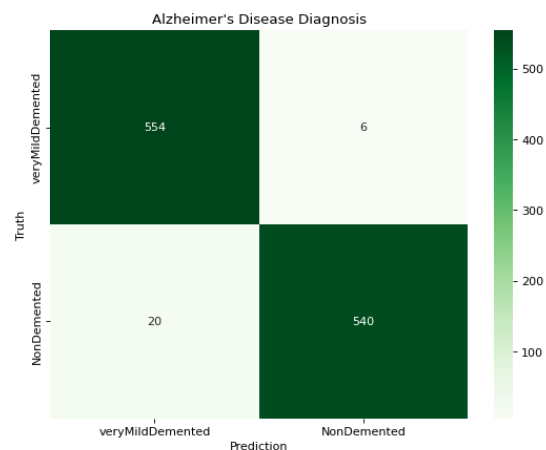


**Figure 6.** Confusion matrix of the model.

Table 3 shows the model's precision results, recall values and F1 score values calculated according to the confusion matrix.

**Table 3.** Performance indices of individual class.

Diseases	Precision	Recall	F1- score
Very Mild Demented	0.97	0.99	0.98
Non-Demented	0.99	0.96	0.98

## 5. Discussion

In the Discussion section, we evaluate different classification methods used for the early diagnosis of AD. As mentioned in the introduction, there are many studies in the literature that perform MRI classification for AD using different methods. Table 4 presents the classification studies in the literature for AD diagnosis together with the corresponding Acc scores obtained from the datasets, facilitating direct comparison.

**Table 4.** The performance of this study and other studies in the literature for the diagnosis of the disease

Ref	Dataset	Modality	Acc(%)
<b>Binary Classification of Alzheimer's Disease Using Siamese Network for Early Stage Diagnosis (this study)</b>	<b>Kaggle (2 class / VMD-ND)</b>	<b>MRI</b>	<b>97.67</b>
	ADNI and GARD (2 class / AD-HC)	sMRI	94.03
	ADNI (2 class / MCI-AD)	MRI	92.72
	ADNI (2 class / MCI-HC)	MRI	65

\*Acc: Accuracy, AD: Alzheimer's Disease, ADNI: Alzheimer's Disease Neuroimaging Initiative HC: Health Care, GARD: Gwangju Alzheimer's and Related Dementia, MCI: Mild Cognitive Impairment, MRI: Magnetic Resonance Imaging, ND: Non Dementia sMRI: Structural Magnetic Resonance VMD:Very Mild Dementia

The ensemble-based classifier method [14] trained the model on the ADNI dataset and performed validation on the GARD dataset. The method achieved 94.03% accuracy in AD-HC classification. The Siamese network method [17] used the ADNI dataset and obtained 92.72% accuracy on MCI-AD and MRI images. The deep metric learning method [18] provided 65% accuracy on MCI-HC MR images in the ADNI dataset. This study achieved 97.67% accuracy when run on the Kaggle dataset. In line with these results, it is proved that the proposed work gives better results.

## 6. Conclusion

Alzheimer is an irremediable disease that impact the aged individuals and profoundly impacts their lives. It's important to diagnose the disease early to effectively control it. Machine learning enables the creation of models to predict disease with MR images. Promising results are obtained for use in clinical treatment.

In this study, SNN is proposed for early detection of AD. In the literature, SNN model has been used for AD classification, for example, in Siamese network [17] and Deep Metric Learning [18], the features of images were extracted using CNN and the similarity between the images was evaluated by Euclidean distance. The proposed work differs in terms of the complexity of the data set and the CNN model. At the same time, the MR images used in this study are 2D segmented images

enhanced by image processing. Compared to the other studies in the literature, the proposed work has proven to provide better results.

The model proposed in this study and tested using Kaggle data for the sorting of disease phases achieved an accuracy of 97.67%. According to the obtained results, the suggested model was found to be suitable for the binary classification problem.

In the future, it is believed that the success of the study can be increased if the dataset is enlarged, image processing algorithms are developed and hybrid with specialized CNN models are used.

## Author's Contributions

**Ruken Tekin:** Methodology, investigation, software, resources, data curation, original draft preparation.

**Tuğba Özge Onur:** Methodology, formal analysis, validation, writing—review and editing, visualization, supervision.

## Ethics

There are no ethical issues after the publication of this manuscript.

## References

- [1]. M. Vasileios, A. Alexiou, Biomarkers for Alzheimer's Disease Diagnosis, *Current Alzheimer Research*, vol. 14, no. 11, pp. 1149-1154, 2017.
- [2]. S. Przedborski, M. Vila, V. Jackson-Lewis, Neurodegeneration: what is it and where are we?, *The Journal of Clinical Investigation*, vol. 111, no. 1, pp. 3-10, 2003.
- [3]. Türkiye Alzheimer Derneği Resmi Web Sitesi. (2 January 2024). Alzheimer Hastalığı Nedir?, <https://www.alzheimerderneği.org.tr/>.
- [4]. S. Murugan, C. Venkatesan, M. G. Sumithra, X. Gao, B. Elakkiya, M. Akila, M. Subramanian, DEMNET: A Deep Learning Model for Early Diagnosis of Alzheimer Diseases and Dementia From MR Images, *IEEE Access*, vol. 9, pp. 90319-90329, 2021.
- [5]. S. Basaia, F. Agosta, L. Wagner, E. Canu, G. Magnani, R. Santangelo, M. Filippi, Automated classification of Alzheimer's disease and mild cognitive impairment using a single MRI and deep neural networks, *NeuroImage Clinical*, vol. 21, 2019.
- [6]. S. Qiu, P. Joshi, M. I. Miller, C. Xue, X. Zhou, C. Karjadi, G. H. Chang, A. S. Joshi, B. Dwyer, S. Zhu, M. C. Kaku, Y. Zhou, Y. J. Alderazi, A. Swaminathan, S. Kedar, M. Saint-Hilaire, S. H. Auerbach, J. Yuan, E. Sartor, R. Au, V. B. Kolachalama, Development and validation of an interpretable deep learning framework for Alzheimer's disease classification, *Brain*, vol. 143, pp. 1920-1933, 2020.
- [7]. Z. Wan, Y. Dong, Z. Yu, H. Lv, Z. Lv, Semi-Supervised Support Vector Machine for Digital Twins Based Brain Image Fusion, *Frontiers in Neuroscience*, vol. 15, 2021.
- [8]. S. Pala, Alzheimer hastalığının erken teşhisi için biyobelirteçlere dayalı stratejik yol haritası derleme çeviri çalışması, *Tıbbi Politika Yazısı*, 2021.

- [9]. Zhang, X. Y., Yang, Z. L., Lu, G. M., Yang, G. F., Zhang, L. J., PET/MR Imaging: New Frontier in Alzheimer's Disease and Other Dementias. *Frontiers in Molecular Neuroscience*, vol. 10, 2017.
- [10]. Barthel H., Schroeter M. L., Hoffmann K. T., Sabri O., PET/MR in dementia and other neurodegenerative diseases, *Seminars in Nuclear Medicine*, vol. 45, pp. 224–233, 2015
- [11]. B. A. Mohammed, E. M. Senan, T. H. Rassem, N. M. Makbol, A. A. Alanazi, Z. G. Al-Mekhlafi, T. S. Almurayziq, F. A. Ghaleb, Multi-Method Analysis of Medical Records and MRI Images for Early Diagnosis of Dementia and Alzheimer's Disease Based on Deep Learning and Hybrid Methods, *Electronics*, vol. 10, no. 22, 2021.
- [12]. D. Lu, K. Popuri, G. W. Ding, R. Balachandar, M. F. Beg, Multimodal and Multiscale Deep Neural Networks for the Early Diagnosis of Alzheimer's Disease using structural MR and FDG-PET images, *Scientific Reports*, vol. 8, 2017.
- [13]. Y. Gupta, K. H. Lee, K. Y. Choi, J. J. Lee B. Kim, G. Kwon, Early diagnosis of Alzheimer's disease using combined features from voxel-based morphometry and cortical, subcortical, and hippocampus regions of MRI T1 brain images, *PloS One*, vol. 14, no. 10, 2019.
- [14]. S. Ahmed, K. Y. Choi, J. J. Lee, B. C. Kim, G. Kwon, K. H. Lee, H. B. Jung, Ensembles of Patch-Based Classifiers for Diagnosis of Alzheimer Diseases, *IEEE Access*, vol. 7, pp. 73373-73383, 2019.
- [15]. H. Nawaz, M. Maqsood, S. Afzal, F. Aadil, I. Mehmood, S. Rho, A deep feature-based real-time system for Alzheimer disease stage detection, *Multimedia Tools and Applications*, vol. 80, pp. 1-19, 2021.
- [16]. J. Shi, X. Zheng, Y. Li, Q. Zhang, S. Ying, Multimodal Neuroimaging Feature Learning With Multimodal Stacked Deep Polynomial Networks for Diagnosis of Alzheimer's Disease, *IEEE Journal of Biomedical and Health Informatics*, vol. 22, no. 1, pp. 173-183, 2018.
- [17]. C. F. Liu, S. Padhy, S. Ramachandran, V. Wang, A. Efimov, A. Bernal, L. Shi, M. Vaillant, J. T. Ratnanather, A. V. Faria, B. Caffo, M. S. Albert, M. I. Miller, Using deep Siamese neural networks for detection of brain asymmetries associated with Alzheimer's Disease and Mild Cognitive Impairment, *Magnetic Resonance Imaging*, vol. 64, pp. 190-199, 2019.
- [18]. X. Bi, W. Liu, H. Liu, Q. Shang, Artificial Intelligence-based MRI Images for Brain in Prediction of Alzheimer's Disease, *Journal of Healthcare Engineering*, vol. 165, 2021.
- [19]. T. M. Khan, D. G. Bailey, M. A. U. Khan, Y. Kong, Efficient Hardware Implementation For Fingerprint Image Enhancement Using Anisotropic Gaussian Filter, *IEEE Transactions on Image Processing*, vol. 26, no. 5, pp. 2116-2126, 2017.
- [20]. Y. Lee, S. A. Kassam, Generalized median filtering and related nonlinear filtering techniques, *IEEE Transactions on Acoustics, Speech, and Signal Processing*, vol. 33, no. 3, pp. 672-683, 1985.
- [21]. J. Bromley, J. W. Bentz, L. Bottou, I. Guyon, Y. Lecun, E. Sckinger, R. Shah, "Signature Verification Using A Siamese Time Delay Neural Network, *International Journal of Pattern Recognition Artificial Intelligence*, vol. 7, pp. 669-688, 1993.
- [22]. M. Toğaçar, Z. Cömert, B. Ergen, Siyam Sinir Ağlarını Kullanarak Türk İşaret Dilindeki Rakamların Tanımlanması, *Dokuz Eylül Üniversitesi Mühendislik Fakültesi Fen Ve Mühendislik Dergisi*, vol. 23, no. 68, pp. 349-56, 2021.

# Four Dimensional Matrix Operators on the Double Series Spaces of Weighted Means

Feride Çalışır<sup>1</sup> , Canan Hazar Güleç<sup>2\*</sup> 

<sup>1,2</sup> Department of Mathematics, Pamukkale University, Denizli, Türkiye

\* [gchazar@pau.edu.tr](mailto:gchazar@pau.edu.tr)

\* Orcid No: 0000-0002-8825-5555

Received: 6 May 2024

Accepted: 14 April 2025

DOI: 10.18466/cbayarfbe.1479195

## Abstract

The main purpose in this study is to investigate some topological and algebraic properties of the double series space  $|\bar{N}_{p,q}|_k$  defined by the absolute double weighted summability methods for  $k \geq 1$ . Beside this, we determine the  $\alpha$ -dual of the double series space  $|\bar{N}_{p,q}|_1$  and the  $\beta(bp)$ - and  $\gamma$ -duals of the double series space  $|\bar{N}_{p,q}|_k$  for  $k \geq 1$ . Finally, we characterize some new four dimensional matrix transformation classes  $(|\bar{N}_{p,q}|_k, v)$ ,  $(|\bar{N}_{p,q}|_1, v)$  and  $(|\bar{N}_{p,q}|_1, \mathcal{L}_k)$ , where  $v$  denotes any spaces of double sequences  $\mathcal{M}_u$  and  $\mathcal{C}_p$ . Hence, we extend some results about weighted means to double sequences.

**Keywords:** Double sequences, Dual spaces, Four dimensional weighted means, Four dimensional matrix transformations, Pringsheim convergence.

## 1. Introduction

Recently, there has been an increased interest in studies concerned on sequence spaces (see, [1-11]). Also, an important area of study in sequence spaces is the generalization of single-sequence spaces to double sequence spaces [12-16]. The initial works on double sequences have been given by Bromwich [17]. Also, Zeltser [18] has studied both the theory of topological double sequence spaces and the theory of summability of double sequences in her PhD thesis. Later on, they were studied by Hardy [19], Móricz [20], Móricz and Rhoades [21], Mursaleen [22], Mursaleen and Başar [23], Demiriz and Duyar [24], Demiriz and Erdem [25] and many others.

A double sequence  $x = (x_{rs})$  is a double infinite array of elements  $x_{rs}$  for all  $r, s \in \mathbb{N}$ , where  $\mathbb{N} = \{0, 1, 2, \dots\}$ . We denote the set of all real or complex valued double sequences by  $\Omega$  which forms a vector space with coordinatewise addition and scalar multiplication of double sequences. Any vector subspace of  $\Omega$  is called as a *double sequence space*. We denote the space of all bounded double sequences by  $\mathcal{M}_u$ , i.e.,

$$\mathcal{M}_u = \left\{ x = (x_{mn}) \in \Omega : \|x\|_\infty = \sup_{m,n \in \mathbb{N}} |x_{mn}| < \infty \right\},$$

which is a Banach space with the norm  $\|\cdot\|_\infty$ . Consider the double sequence  $x = (x_{mn}) \in \Omega$ . If for every given  $\epsilon > 0$  there exists  $n_0 = n_0(\epsilon) \in \mathbb{N}$  and  $L \in \mathbb{C}$  such that  $|x_{mn} - L| < \epsilon$  for all  $m, n > n_0$ , the double sequence  $x = (x_{mn}) \in \Omega$  is called *convergent* to the limit point  $L$  in the *Pringsheim's sense*, where  $\mathbb{C}$  denotes the complex field. Then, we write  $p - \lim_{m,n \rightarrow \infty} x_{mn} = L$ , and  $L \in \mathbb{C}$  is called the Pringsheim limit of  $x$ . By  $\mathcal{C}_p$ , we denote the space of all convergent double sequences in the Pringsheim's sense [26]. Unlike single sequences,  $p$ -convergent double sequences need not be bounded. Namely, the set  $\mathcal{C}_p - \mathcal{M}_u$  is not empty. Indeed, following Boos [27], if we define the sequence  $x = (x_{mn})$  by

$$x_{mn} = \begin{cases} m; n = 0, m \in \mathbb{N} \\ n; m = 0, n \in \mathbb{N} \\ 0; m, n \in \mathbb{N} - \{0\} \end{cases}$$

for all  $m, n \in \mathbb{N}$ , then it is trivial that  $x \in \mathcal{C}_p - \mathcal{M}_u$ , since  $p - \lim_{m,n \rightarrow \infty} x_{mn} = 0$  but  $\|x\|_\infty = \infty$ . Therefore, we consider the set  $\mathcal{C}_{bp}$  of double sequences which are both convergent in Pringsheim's sense and bounded, i.e.,  $\mathcal{C}_{bp} = \mathcal{C}_p \cap \mathcal{M}_u$ . Hardy [19] proved that a sequence in the space  $\mathcal{C}_p$  is said to be *regularly convergent* if it is a single convergent sequence with respect to each index and,  $\mathcal{C}_r$  denotes the set of all such sequences.

Here and after, we assume that  $\vartheta$  denotes any of the symbols  $p$ ,  $bp$ , or  $r$ , and  $k'$  denotes the conjugate of  $k$ , that is,  $\frac{1}{k} + \frac{1}{k'} = 1$  for  $1 < k < \infty$ , and  $\frac{1}{k'} = 0$  for  $k = 1$ .

Let  $x = (x_{mn})$  be a double sequence and define the sequence  $s = (s_{mn})$  via  $x$  by

$$s_{mn} = \sum_{i=0}^m \sum_{j=0}^n x_{ij}$$

for all  $m, n \in \mathbb{N}$ . Then, the pair of  $(x, s)$  and the sequence  $s = (s_{mn})$  are called as a double series and the sequence of partial sums of the double series, respectively. For brevity, here and in what follows we use the abbreviation  $\sum_{i,j} x_{ij}$  for the summation  $\sum_{i=0}^{\infty} \sum_{j=0}^{\infty} x_{ij}$ . If the double sequence  $(s_{mn})$  is convergent in the  $\vartheta$ -sense, then the double series  $\sum_{i,j} x_{ij}$  is said to be convergent in the  $\vartheta$ -sense and it is denoted that  $\vartheta - \sum_{i,j} x_{ij} = \vartheta - \lim_{m,n \rightarrow \infty} s_{mn}$ .

Quite recently, Başar and Sever have introduced the Banach space  $\mathcal{L}_k$  of double sequences as

$$\mathcal{L}_k = \left\{ x = (x_{mn}) \in \Omega : \sum_{m,n} |x_{mn}|^k < \infty \right\},$$

which corresponds to the well-known classical sequence space  $\ell_k$  of single sequences [28]. Also, for the special case  $k = 1$ , the space  $\mathcal{L}_k$  is reduced to the space  $\mathcal{L}_u$ , which was introduced by Zeltser [18].

Let  $\lambda$  and  $\mu$  be two double sequence spaces, and  $A = (a_{mnij})$  be any four dimensional complex infinite matrix. Then, we say that  $A$  defines a four dimensional matrix mapping from  $\lambda$  into  $\mu$ , if for every double sequence  $x = (x_{ij}) \in \lambda$ ,  $Ax = \{(Ax)_{mn}\}_{m,n \in \mathbb{N}}$ , the  $A$ -transform of  $x$ , is in  $\mu$ , where

$$(Ax)_{mn} = \vartheta - \sum_{i,j} a_{mnij} x_{ij} \quad (1.1)$$

provided that the double series exists for each  $m, n \in \mathbb{N}$ . By  $(\lambda, \mu)$ , we denote the set of such all four dimensional matrices transforming from the space  $\lambda$  into the space  $\mu$ . Thus,  $A = (a_{mnij}) \in (\lambda, \mu)$  if and only if the double series on the right side of (1.1) converges in the sense of  $\vartheta$  for each  $m, n \in \mathbb{N}$  and  $Ax \in \mu$  for all  $x \in \lambda$ .

The  $\alpha$ -dual  $\lambda^\alpha$ ,  $\beta(\vartheta)$ -dual  $\lambda^{\beta(\vartheta)}$  in regard to the  $\vartheta$ -convergence for  $\vartheta \in \{p, bp, r\}$ , and  $\gamma$ -dual  $\lambda^\gamma$  of the double sequence space  $\lambda$  are defined by, respectively,

$$\lambda^\alpha := \left\{ a = (a_{kl}) \in \Omega : \sum_{k,l} |a_{kl} x_{kl}| < \infty, \text{ for all } (x_{kl}) \in \lambda \right\},$$

$$\lambda^{\beta(\vartheta)} := \left\{ a = (a_{kl}) \in \Omega : \vartheta - \sum_{k,l} a_{kl} x_{kl} \text{ exists, for all } (x_{kl}) \in \lambda \right\},$$

and

$$\lambda^\gamma := \left\{ a = (a_{kl}) \in \Omega : \sup_{m,n \in \mathbb{N}} \left| \sum_{k,l=0}^{m,n} a_{kl} x_{kl} \right| < \infty, \text{ for all } (x_{kl}) \in \lambda \right\}.$$

We define the  $\vartheta$ -summability domain  $\lambda_A^{(\vartheta)}$  of  $A = (a_{mnij})$  in a space  $\lambda$  of double sequences by

$$\lambda_A^{(\vartheta)} = \left\{ x = (x_{ij}) \in \Omega : Ax = \left( \vartheta - \sum_{i,j} a_{mnij} x_{ij} \right)_{m,n \in \mathbb{N}} \text{ exists and is in } \lambda \right\}.$$

We write throughout for simplicity in notation for all  $m, n, k, l \in \mathbb{N}$  that

$$\begin{aligned} \Delta_{10} x_{mn} &= x_{mn} - x_{m+1,n}, \\ \Delta_{01} x_{mn} &= x_{mn} - x_{m,n+1}, \\ \Delta_{11} x_{mn} &= \Delta_{01}(\Delta_{10} x_{mn}) = \Delta_{10}(\Delta_{01} x_{mn}) \end{aligned}$$

and

$$\begin{aligned} \Delta_{10}^{kl} a_{mnkl} &= a_{mnkl} - a_{m+1,k+1,l}, \\ \Delta_{01}^{kl} a_{mnkl} &= a_{mnkl} - a_{m,n,k+1,l+1}, \\ \Delta_{11}^{kl} a_{mnkl} &= \Delta_{01}^{kl}(\Delta_{10}^{kl} a_{mnkl}) = \Delta_{10}^{kl}(\Delta_{01}^{kl} a_{mnkl}). \end{aligned}$$

Now, we give some definitions about fundamental four dimensional matrix methods. The four dimensional Cesàro matrix  $C = (c_{mnij})$  of order one is defined by

$$c_{mnij} = \begin{cases} \frac{1}{mn}, & 1 \leq i \leq m, \quad 1 \leq j \leq n \\ 0, & \text{otherwise} \end{cases}$$

for all  $m, n, i, j \in \mathbb{N} - \{0\}$  [23]. The four dimensional Cesàro matrix  $C = (c_{mnij})$  is extended by means of the four dimensional Riesz matrix.

Let  $p = (p_k)$ ,  $q = (q_k)$  be two sequences of positive numbers, and  $P_n = \sum_{k=0}^n p_k$ , and  $Q_n = \sum_{k=0}^n q_k$ . Then, the four dimensional Riesz matrix  $R^{pq} = (r_{mnij}^{pq})$  is defined by

$$r_{mnij}^{pq} = \begin{cases} \frac{p_i q_j}{P_m Q_n}, & 0 \leq i \leq m, \quad 0 \leq j \leq n \\ 0, & \text{otherwise} \end{cases}$$

for all  $m, n, i, j \in \mathbb{N}$  [29]. Note that in the case  $p_k = q_k = 1$  for all  $k \in \mathbb{N}$ , the Riesz matrix  $R^{pq}$  is reduced to the four dimensional Cesàro matrix of order one.



Let  $\sum_{i,j} x_{ij}$  be an infinite double series with partial sums  $(s_{mn})$ . The double weighted mean transformation  $R_{mn}^{pq}$  of a double sequence  $s = (s_{mn})$  by means of the four dimensional Riesz matrix is defined as

$$R_{mn}^{pq}(s) = \frac{1}{P_m Q_n} \sum_{i=0}^m \sum_{j=0}^n p_i q_j s_{ij}, \quad (m, n \in \mathbb{N}).$$

We say that  $s = (s_{mn})$  is  $(\bar{N}, p_n, q_n)$  summable or Riesz summable to some number  $\ell$  if, (see, [30])

$$p - \lim_{m,n \rightarrow \infty} R_{mn}^{pq}(s) = \ell.$$

A double series  $\sum_{i,j} x_{ij}$  is called summable  $|\bar{N}, p_n, q_n|_k$  or absolute double weighted summability ([31]), if

$$\sum_{m=0}^{\infty} \sum_{n=0}^{\infty} \left( \frac{P_m Q_n}{p_m q_n} \right)^{k-1} |\Delta_{11} R_{m-1, n-1}^{pq}(s)|^k < \infty,$$

where,  $k \geq 1$  and for  $m, n \geq 1$

$$\begin{aligned} \Delta_{11}(R_{m-1, n-1}^{pq}) &= R_{m0}^{pq} - R_{m-1, 0}^{pq}, \\ \Delta_{11}(R_{-1, n-1}^{pq}) &= R_{0n}^{pq} - R_{0, n-1}^{pq}, \end{aligned}$$

and

$$\Delta_{11}(R_{m-1, n-1}^{pq}) = R_{mn}^{pq} - R_{m-1, n}^{pq} - R_{m, n-1}^{pq} + R_{m-1, n-1}^{pq}.$$

Further, it is easily seen that

$$\begin{aligned} R_{mn}^{pq}(s) &= \frac{1}{P_m Q_n} \sum_{i=0}^m \sum_{j=0}^n p_i q_j s_{ij} \\ &= \frac{1}{P_m Q_n} \sum_{i=0}^m \sum_{j=0}^n x_{ij} (P_m - P_{i-1})(Q_n - Q_{j-1}) \\ &= \sum_{i=0}^m \sum_{j=0}^n x_{ij} \left(1 - \frac{P_{i-1}}{P_m}\right) \left(1 - \frac{Q_{j-1}}{Q_n}\right). \end{aligned} \quad (1.2)$$

Also, throughout the paper for brevity, we show  $R_{mn}^{pq}(s)$  defined as in (1.2) by  $R_{mn}^{pq}$ .

So, we can calculate for  $m, n = 0$ ,

$$\Delta_{11} R_{m-1, n-1}^{pq} = x_{00}, \quad (1.3)$$

and, for  $m, n \geq 1$ ,

$$\Delta_{11} R_{m-1, -1}^{pq} = \frac{p_m}{P_m P_{m-1}} \sum_{i=1}^m P_{i-1} x_{i0}, \quad (1.4)$$

$$\Delta_{11} R_{-1, n-1}^{pq} = \frac{q_n}{Q_n Q_{n-1}} \sum_{j=1}^n Q_{j-1} x_{0j}, \quad (1.5)$$

and

$$\begin{aligned} &\Delta_{11} R_{m-1, n-1}^{pq} \\ &= \frac{p_m q_n}{P_m P_{m-1} Q_n Q_{n-1}} \sum_{i=1}^m \sum_{j=1}^n P_{i-1} Q_{j-1} x_{ij}. \end{aligned} \quad (1.6)$$

Now, considering Sarigöl [31], we show the double series space  $|\bar{N}_{p,q}|_k$  by the set of all double series summable by absolute double weighted summability method  $|\bar{N}, p_m, q_n|_k$ , that is,

$$\begin{aligned} &|\bar{N}_{p,q}|_k \\ &= \{x = (x_{ij}) \in \Omega \\ &: \sum \sum x_{ij} \text{ is summable } |\bar{N}, p_m, q_n|_k\}, \end{aligned}$$

which is a Banach space [15].

Many single sequence spaces have been defined by using the matrix domain of Riesz means [32,33,34]. Bodur and Güleç [13] have essentially studied some topological properties of double series space  $|C_{1,1}|_k$ , determined certain dual spaces and characterized the classes of four dimensional matrix transformations. Also, Yeşilkayagil and Başar [29,35] have introduced the spaces  $(\mathcal{M}_u)_{R^{qt}}, (\mathcal{C}_p)_{R^{qt}}, (\mathcal{C}_{bp})_{R^{qt}}, (\mathcal{C}_r)_{R^{qt}}$  and  $(\mathcal{L}_s)_{R^{qt}}$  as the domain of four dimensional Riesz mean  $R^{qt}$  in the spaces  $\mathcal{M}_u, \mathcal{C}_p, \mathcal{C}_{bp}, \mathcal{C}_r$  and  $\mathcal{L}_s$ , respectively. In this paper, we investigate some topological and algebraic properties of the absolutely double series space  $|\bar{N}_{p,q}|_k$  taking account of absolute double weighted summability method for  $k \geq 1$ . Beside this, we determine the  $\alpha$ -dual of the double series space  $|\bar{N}_{p,q}|_1$  and the  $\beta(bp)$ - and  $\gamma$ -duals of the double series spaces  $|\bar{N}_{p,q}|_k$  for  $k \geq 1$ . Finally, we characterize some new classes of the four dimensional matrix transformations.

## 2. The Absolutely Double Series Space of Double Weighted Means

In this section, we give some properties of the absolutely double weighted series spaces  $|\bar{N}_{p,q}|_k$  for  $k \geq 1$ . Also, we determine the  $\alpha$ -dual of the double series space  $|\bar{N}_{p,q}|_1$ ,  $\beta(bp)$ - and  $\gamma$ -duals of the double series spaces  $|\bar{N}_{p,q}|_k$  for  $1 \leq k < \infty$ .

**Theorem 2.1.** The set  $|\bar{N}_{p,q}|_k$  becomes a linear space with the coordinatewise addition and scalar multiplication, and  $|\bar{N}_{p,q}|_k$  is a Banach space with the norm

$$\|x\|_{|\bar{N}_{p,q}|_k} = \left( \sum_{m=0}^{\infty} \sum_{n=0}^{\infty} \left( \frac{P_m Q_n}{p_m q_n} \right)^{k-1} |\Delta_{11} R_{m-1, n-1}^{pq}|^k \right)^{1/k} \quad (2.1)$$

and it is linearly norm isomorphic to the space  $\mathcal{L}_k$  for  $1 \leq k < \infty$ , where  $R_{mn}^{pq}$  is defined as in (1.3 – 1.6).

**Proof.** Since the initial assertion is routine verification and so we omit it.

To prove the fact that  $|\bar{N}_{p,q}|_k$  is norm isomorphic to the space  $\mathcal{L}_k$ , we should show the existence of a linear and norm preserving bijection between the spaces  $|\bar{N}_{p,q}|_k$  and  $\mathcal{L}_k$  for  $1 \leq k < \infty$ . Consider the transformation  $U$  defined by

$$U : |\bar{N}_{p,q}|_k \rightarrow \mathcal{L}_k$$

$$x \rightarrow y = U(x),$$

where  $U(x) = (U_{mn}(x)) = (y_{mn})$  is stated by

$$U_{mn}(x) = y_{mn} = \left( \frac{P_m Q_n}{p_m q_n} \right)^{1-1/k} \Delta_{11} R_{m-1, n-1}^{pq} \quad (2.2)$$

for  $m, n \geq 0$  and  $\Delta_{11} R_{m-1, n-1}^{pq}$  is given as in (1.3 – 1.6). The linearity of  $U$  is clear. Also,  $x = \theta$  whenever  $U(x) = \theta$ , where  $\theta$  denotes the zero vector. This says us that  $U$  is injective.

Let  $y = (y_{mn}) \in \mathcal{L}_k$  and define the sequence  $x = (x_{mn})$  via  $y = (y_{mn})$  by

$$x_{mn} = \frac{1}{P_{m-1}Q_{n-1}} \Delta_{11} \left( y_{m-1, n-1} \left( \frac{P_{m-1}Q_{n-1}}{P_{m-1}Q_{n-1}} \right)^{1/k} P_{m-2}Q_{n-2} \right), \quad (2.3)$$

$$x_{m0} = \frac{1}{P_{m-1}} \bar{\Delta}_{10} \left( y_{m0} \left( \frac{P_m}{P_m} \right)^{1/k} P_{m-1} \right), \quad (2.4)$$

$$x_{0n} = \frac{1}{Q_{n-1}} \bar{\Delta}_{01} \left( y_{0n} \left( \frac{Q_n}{Q_n} \right)^{1/k} Q_{n-1} \right), \quad (2.5)$$

for  $m, n \geq 1$ , and

$$x_{00} = y_{00}, \quad (2.6)$$

where  $\bar{\Delta}_{10}$  and  $\bar{\Delta}_{01}$  refer to the back difference notations, that is,  $\bar{\Delta}_{10}(x_{mn}) = x_{m,n} - x_{m-1,n}$ ,

$\bar{\Delta}_{01}(x_{mn}) = x_{m,n} - x_{m,n-1}$  for all  $m, n \in \mathbb{N}$ .

In that case, it is seen that

$$\|x\|_{|\bar{N}_{p,q}|_k} = \|U(x)\|_{\mathcal{L}_k} = \left( \sum_{m,n} |U_{mn}(x)|^k \right)^{1/k} = \|y\|_{\mathcal{L}_k} < \infty$$

for  $1 \leq k < \infty$ . So, this yields that  $U$  is surjective and norm preserving. Thus,  $U$  is a linear and norm preserving bijection which says the spaces  $|\bar{N}_{p,q}|_k$  and  $\mathcal{L}_k$  are norm isomorphic for  $1 \leq k < \infty$ , as desired.

Now, we may show that  $|\bar{N}_{p,q}|_k$  is a Banach space with the norm defined by (2.1). To prove this, we can consider "Let  $(E, \rho)$  and  $(F, \sigma)$  be semi-normed spaces and  $\Psi : (E, \rho) \rightarrow (F, \sigma)$  be an isometric isomorphism. Then  $(E, \rho)$  is complete if and only if  $(F, \sigma)$  is complete. In particular,  $(E, \rho)$  is a Banach space if and only if  $(F, \sigma)$  is a Banach space." which can be found section (b) of Corollary 6.3.41 in [27]. Since the transformation  $U$  defined from  $|\bar{N}_{p,q}|_k$  into  $\mathcal{L}_k$  by (2.2) is an isometric isomorphism and the double sequence space  $\mathcal{L}_k$  is a Banach space from Theorem 2.1 in [28], we deduce that the space  $|\bar{N}_{p,q}|_k$  is a Banach space. This is the result that we desired.

Now, we calculate the  $\alpha$ -,  $\beta(bp)$ - and  $\gamma$ - duals of the double series spaces  $|\bar{N}_{p,q}|_k$  for  $k \geq 1$ . Before we give some results based on their duals, we need to state the following significant lemma which is essential for proving next theorems.

**Lemma 2.2.** [35] Let  $A = (a_{mnij})$  be any four dimensional infinite matrix. At that case, the following statements are satisfied:

(a) Let  $0 < k \leq 1$ . Then,  $A = (a_{mnij}) \in (\mathcal{L}_k, \mathcal{M}_u)$  iff

$$\Lambda_1 = \sup_{m,n,i,j \in \mathbb{N}} |a_{mnij}| < \infty. \quad (2.7)$$

(b) Let  $1 < k < \infty$ . Then,  $A = (a_{mnij}) \in (\mathcal{L}_k, \mathcal{M}_u)$  iff

$$\Lambda_2 = \sup_{m,n \in \mathbb{N}} \sum_{i,j} |a_{mnij}|^{k'} < \infty. \quad (2.8)$$

(c) Let  $0 < k \leq 1$  and  $1 \leq k_1 < \infty$ . Then,  $A = (a_{mnij}) \in (\mathcal{L}_k, \mathcal{L}_{k_1})$  iff

$$\sup_{i,j \in \mathbb{N}} \sum_{m,n} |a_{mnij}|^{k_1} < \infty.$$

(d) Let  $0 < k \leq 1$ . Then,  $A = (a_{mnij}) \in (\mathcal{L}_k, \mathcal{C}_{bp})$  iff the condition (2.7) holds and there exists a  $(\lambda_{ij}) \in \Omega$  such that

$$bp - \lim_{m,n \rightarrow \infty} a_{mnij} = \lambda_{ij}. \quad (2.9)$$

(e) Let  $1 < k < \infty$ . Then,  $A = (a_{mnij}) \in (\mathcal{L}_k, \mathcal{C}_{bp})$  iff (2.8) and (2.9) are satisfied.

To shorten the following theorems and their proofs, let us denote the sets  $E_k$  with  $k \in \{1, 2, 3, 4\}$  as follows for  $\xi = (\xi_{mn}) \in \Omega$ :

$$E_1 = \left\{ \xi \in \Omega : \sup_{i,j \in \mathbb{N}} \sum_{m,n} |f_{mnij}| < \infty \right\}, \quad (2.10)$$

$$E_2 = \left\{ \xi \in \Omega : bp - \lim_{m,n \rightarrow \infty} d_{mnij}^{(k)} \text{ exists} \right\}, \quad (2.11)$$

$$E_3 = \left\{ \xi \in \Omega : \sup_{m,n,i,j \in \mathbb{N}} |d_{mnij}^{(1)}| < \infty \right\}, \quad (2.12)$$

$$E_4 = \left\{ \xi \in \Omega : \sup_{m,n \in \mathbb{N}} \sum_{i,j} |d_{mnij}^{(k)}|^{k'} < \infty \right\}, \quad (2.13)$$

where the four dimensional matrices  $D^{(k)} = (d_{mnij}^{(k)})$  and  $F = (f_{mnij})$  are defined by

$$d_{mnij}^{(k)} = \begin{cases} \xi_{00}, & m = n = 0, \\ \xi_{m0} \left( \frac{P_m}{p_m} \right)^{1/k}, & n = 0 \text{ and } i = m, \\ \xi_{0n} \left( \frac{Q_n}{q_n} \right)^{1/k}, & m = 0 \text{ and } j = n, \\ P_{i-1} \left( \frac{P_i}{p_i} \right)^{1/k} \Delta_{10} \left( \frac{\xi_{i0}}{P_{i-1}} \right), & n = 0 \text{ and } 1 \leq i \leq m-1, \\ Q_{j-1} \left( \frac{Q_j}{q_j} \right)^{1/k} \Delta_{01} \left( \frac{\xi_{0j}}{Q_{j-1}} \right), & m = 0 \text{ and } 1 \leq j \leq n-1, \\ \Delta_{11} \left( \frac{\xi_{ij}}{P_{i-1}Q_{j-1}} \right) \left( \frac{P_iQ_j}{p_iq_j} \right)^{1/k} P_{i-1}Q_{j-1}, & 1 \leq i \leq m-1 \text{ and } 1 \leq j \leq n-1, \\ \Delta_{10} \left( \frac{\xi_{in}}{P_{i-1}} \right) \left( \frac{P_iQ_n}{p_iq_n} \right)^{1/k} P_{i-1}, & 1 \leq i \leq m-1 \text{ and } j = n, \\ \Delta_{01} \left( \frac{\xi_{mj}}{Q_{j-1}} \right) \left( \frac{P_mQ_j}{p_mq_j} \right)^{1/k} Q_{j-1}, & i = m \text{ and } 1 \leq j \leq n-1, \\ \xi_{mn} \left( \frac{P_mQ_n}{p_mq_n} \right)^{1/k}, & i = m \text{ and } j = n, \\ 0, & \text{otherwise,} \end{cases} \quad (2.14)$$

and

$$f_{mnij} = \begin{cases} \xi_{00}, & m = n = 0, \\ \xi_{m0} \frac{P_m}{p_m}, & n = 0 \text{ and } i = m, \\ -\frac{\xi_{m0}P_{m-2}}{p_{m-1}}, & n = 0 \text{ and } i = m-1, \\ \xi_{0n} \frac{Q_n}{q_n}, & m = 0 \text{ and } j = n, \\ -\frac{\xi_{0n}Q_{n-2}}{q_{n-1}}, & m = 0 \text{ and } j = n-1, \\ \frac{\xi_{mn}P_{m-2}Q_{n-2}}{p_{m-1}q_{n-1}}, & i = m-1 \text{ and } j = n-1, \\ -\frac{\xi_{mn}P_{m-2}Q_n}{p_{m-1}q_n}, & i = m-1 \text{ and } j = n, \\ -\frac{\xi_{mn}Q_{n-2}P_m}{p_mq_{n-1}}, & i = m \text{ and } j = n-1, \\ \xi_{mn} \frac{P_mQ_n}{p_mq_n}, & i = m \text{ and } j = n, \\ 0, & \text{otherwise} \end{cases} \quad (2.15)$$

respectively.

Now, we give the theorems determining the  $\alpha$ -dual of the double series space  $|\bar{N}_{p,q}|_1$  and  $\beta(bp)$ - and  $\gamma$ -duals of the double series spaces  $|\bar{N}_{p,q}|_k$  for  $k \geq 1$ .

**Theorem 2.3.** Let the set  $E_1$  and the four dimensional matrix  $F = (f_{mnij})$  be defined as in (2.10) and (2.15), respectively. Then,  $(|\bar{N}_{p,q}|_1)^\alpha = E_1$ .

**Proof.** Let  $x = (x_{mn}) \in |\bar{N}_{p,q}|_1$ ,  $\xi = (\xi_{mn}) \in \Omega$ . Taking account of relations in (2.3 – 2.6) for  $m, n \geq 0$ , we can calculate the following equalities:  
for  $m, n \geq 1$ ,

$$\begin{aligned}\xi_{mn}x_{mn} &= \frac{\xi_{mn}}{P_{m-1}Q_{n-1}} \left( \left( \frac{P_m Q_n}{p_m q_n} \right) P_{m-1} Q_{n-1} y_{mn} \right. \\ &\quad - \left( \frac{P_m Q_{n-1}}{p_m q_{n-1}} \right) P_{m-1} Q_{n-2} y_{m,n-1} \\ &\quad - \left( \frac{P_{m-1} Q_n}{p_{m-1} q_n} \right) P_{m-2} Q_{n-1} y_{m-1,n} \\ &\quad \left. + \left( \frac{P_{m-1} Q_{n-1}}{p_{m-1} q_{n-1}} \right) P_{m-2} Q_{n-2} y_{m-1,n-1} \right) \\ &= \frac{\xi_{mn}}{P_{m-1}Q_{n-1}} \\ &\quad \sum_{i=m-1}^m \sum_{j=n-1}^n (-1)^{m+n-(i+j)} \left( \frac{P_i Q_j}{p_i q_j} \right) y_{ij} P_{i-1} Q_{j-1} \\ &= (Fy)_{mn},\end{aligned}$$

for  $n = 0$  and  $m \geq 1$ ,

$$\begin{aligned}\xi_{m0}x_{m0} &= \xi_{m0} \frac{1}{P_{m-1}} \left( \left( \frac{P_m}{p_m} \right) P_{m-1} y_{m0} \right. \\ &\quad \left. - P_{m-2} \left( \frac{P_{m-1}}{p_{m-1}} \right) y_{m-1,0} \right) \\ &= \xi_{m0} \frac{1}{P_{m-1}} \sum_{i=m-1}^m (-1)^{m-i} \left( \frac{P_i}{p_i} \right) P_{i-1} y_{i0} \\ &= (Fy)_{m0},\end{aligned}$$

for  $m = 0$  and  $n \geq 1$ ,

$$\begin{aligned}\xi_{0n}x_{0n} &= \xi_{0n} \frac{1}{Q_{n-1}} \left( \left( \frac{Q_n}{q_n} \right) Q_{n-1} y_{0n} \right. \\ &\quad \left. - Q_{n-2} \left( \frac{Q_{n-1}}{q_{n-1}} \right) y_{0,n-1} \right) \\ &= \xi_{0n} \frac{1}{Q_{n-1}} \sum_{j=n-1}^n (-1)^{n-j} \left( \frac{Q_j}{q_j} \right) Q_{j-1} y_{0j} \\ &= (Fy)_{0n},\end{aligned}$$

and for  $n = m = 0$ ,

$$\xi_{00}x_{00} = \xi_{00}y_{00} = (Fy)_{00},$$

where the four dimensional matrix  $F = (f_{mnij})$  is defined by (2.15). In this fact, we obtain that  $\xi x = (\xi_{mn}x_{mn}) \in \mathcal{L}_u$  whenever  $x \in |\bar{N}_{p,q}|_1$  if and only if  $Fy \in \mathcal{L}_u$  whenever  $y \in \mathcal{L}_u$ . This implies that  $\xi = (\xi_{mn}) \in (|\bar{N}_{p,q}|_1)^\alpha$  iff  $F \in (\mathcal{L}_u, \mathcal{L}_u)$ . Then, we deduce by using (c) of Lemma 2.2 with  $k_1 = k = 1$  that

$$\sup_{i,j \in \mathbb{N}} \sum_{m,n} |f_{mnij}| < \infty.$$

Hence, we get  $(|\bar{N}_{p,q}|_1)^\alpha = E_1$ , as desired.

This step concludes the proof.

**Theorem 2.4.** Let the sets  $E_2, E_3, E_4$  and the four dimensional matrix  $D^{(k)} = (d_{mnij}^{(k)})$  be defined as in (2.11 – 2.13) and (2.14), respectively. Then, we have

$$\left( |\bar{N}_{p,q}|_1 \right)^{\beta(bp)} = E_2 \cap E_3 \text{ and } \left( |\bar{N}_{p,q}|_k \right)^{\beta(bp)} = E_2 \cap E_4 \text{ for } 1 < k < \infty.$$

**Proof.** Let  $\xi = (\xi_{mn}) \in \Omega$  and  $x = (x_{mn}) \in |\bar{N}_{p,q}|_k$  be given. Then, we deduce from Theorem 2.1 that there exists a double sequence  $y = (y_{ij}) \in \mathcal{L}_k$ . Therefore, by using the equations (2.3 – 2.6) we can calculate that

$$\begin{aligned}z_{mn} &= \sum_{i=0}^m \sum_{j=0}^n \xi_{ij} x_{ij} \\ &= \xi_{00} y_{00} + \sum_{i=1}^m \xi_{i0} y_{i0} \left( \frac{P_i}{p_i} \right)^{1/k} \\ &\quad - \sum_{i=2}^m \xi_{i0} y_{i-1,0} \left( \frac{P_{i-1}}{p_{i-1}} \right)^{1/k} \frac{P_{i-2}}{P_{i-1}} \\ &\quad + \sum_{j=1}^n \xi_{0j} y_{0j} \left( \frac{Q_j}{q_j} \right)^{1/k} - \sum_{j=2}^n \xi_{0j} y_{0,j-1} \left( \frac{Q_{j-1}}{q_{j-1}} \right)^{1/k} \frac{Q_{j-2}}{Q_{j-1}} \\ &\quad + \sum_{i=1}^m \sum_{j=1}^n \frac{\xi_{ij}}{P_{i-1} Q_{j-1}} r_{ij},\end{aligned} \quad (2.16)$$

where

$$r_{ij} = \Delta_{11} \left( y_{i-1,j-1} \left( \frac{P_{i-1} Q_{j-1}}{p_{i-1} q_{j-1}} \right)^{1/k} P_{i-2} Q_{j-2} \right)$$

for every  $i, j \in \mathbb{N}$ . Also, by the generalized Abel transformation for double sequences we obtain that

$$\begin{aligned}u_{mn} &= \sum_{k,l=0}^{m,n} a_{kl} x_{kl} \\ &= \sum_{k,l=0}^{m-1,n-1} s_{kl} \Delta_{11} a_{kl} + \sum_{k=0}^{m-1} s_{kn} \Delta_{10} a_{kn} \\ &\quad + \sum_{l=0}^{n-1} s_{ml} \Delta_{01} a_{ml} + s_{mn} a_{mn},\end{aligned}$$

where

$$s_{mn} = \sum_{k,l=0}^{m,n} x_{kl}$$

for every  $m, n \in \mathbb{N}$  [29]. With the generalized Abel transformation for double sequences, we can calculate relation (2.16) as follows:

$$\begin{aligned}z_{mn} &= \xi_{00} y_{00} + \xi_{m0} y_{m0} \left( \frac{P_m}{p_m} \right)^{1/k} \\ &\quad + \sum_{i=1}^{m-1} y_{i0} P_{i-1} \left( \frac{P_i}{p_i} \right)^{1/k} \Delta_{10} \left( \frac{\xi_{i0}}{P_{i-1}} \right) \\ &\quad + \xi_{0n} y_{0n} \left( \frac{Q_n}{q_n} \right)^{1/k} \\ &\quad + \sum_{j=1}^{n-1} y_{0j} Q_{j-1} \left( \frac{Q_j}{q_j} \right)^{1/k} \Delta_{01} \left( \frac{\xi_{0j}}{Q_{j-1}} \right)\end{aligned}$$

$$\begin{aligned}
 & + \sum_{i,j=1}^{m-1,n-1} \Delta_{11} \left( \frac{\xi_{ij}}{P_{i-1}Q_{j-1}} \right) y_{ij} \left( \frac{P_i Q_j}{p_i q_j} \right)^{1/k} P_{i-1} Q_{j-1} \\
 & + \sum_{i=1}^{m-1} \Delta_{10} \left( \frac{\xi_{in}}{P_{i-1}Q_{n-1}} \right) y_{in} \left( \frac{P_i Q_n}{p_i q_n} \right)^{1/k} P_{i-1} Q_{n-1} \\
 & + \sum_{j=1}^{n-1} \Delta_{01} \left( \frac{\xi_{mj}}{P_{m-1}Q_{j-1}} \right) y_{mj} \left( \frac{P_m Q_j}{p_m q_j} \right)^{1/k} P_{m-1} Q_{j-1} \\
 & + \xi_{mn} y_{mn} \left( \frac{P_m Q_n}{p_m q_n} \right)^{1/k} \\
 & = \sum_{i=0}^m \sum_{j=0}^n d_{mnij}^{(k)} y_{ij} \\
 & = (D^{(k)}(y))_{mn}.
 \end{aligned}$$

Thus, we see that  $\xi x = (\xi_{mn} x_{mn}) \in \mathcal{CS}_{bp}$  whenever  $x = (x_{mn}) \in |\bar{N}_{p,q}|_k$  if and only if  $z = (z_{mn}) \in \mathcal{C}_{bp}$  whenever  $y = (y_{ij}) \in \mathcal{L}_k$ . This leads to the fact that  $\xi = (\xi_{mn}) \in (|\bar{N}_{p,q}|_k)^{\beta(bp)}$  if and only if  $D^{(k)} \in (\mathcal{L}_k, \mathcal{C}_{bp})$ , where the four dimensional matrix  $D^{(k)} = (d_{mnij}^{(k)})$  is defined in (2.14) for every  $m, n, i, j \in \mathbb{N}$ . Hence, we deduce  $(|\bar{N}_{p,q}|_1)^{\beta(bp)} = E_2 \cap E_3$  and  $(|\bar{N}_{p,q}|_k)^{\beta(bp)} = E_2 \cap E_4$  for  $1 < k < \infty$  from parts (d) and (e) of Lemma 2.2, respectively.

**Theorem 2.5.** Let the sets  $E_3$ ,  $E_4$  and the four dimensional matrix  $D^{(k)} = (d_{mnij}^{(k)})$  be defined as in (2.12), (2.13) and (2.14), respectively. Then,  $(|\bar{N}_{p,q}|_1)^{\beta(bp)} = E_3$  and  $(|\bar{N}_{p,q}|_k)^{\beta(bp)} = E_4$  for  $1 < k < \infty$ .

**Proof.** The proof of this theorem is similar to the proof Theorem 2.4 using Parts (a) and (b) of Lemma 2.2 in place of parts (d) and (e) of Lemma 2.2, respectively. To avoid the repetition of similar statements, we omit the details.

### 3. Characterizations of Some Classes of Four Dimensional Matrices

In the present section, we characterize some four dimensional matrix mappings from the double series spaces  $|\bar{N}_{p,q}|_1$  and  $|\bar{N}_{p,q}|_k$  to the double sequence spaces  $\mathcal{M}_u$ ,  $\mathcal{C}_{bp}$  and  $\mathcal{L}_k$  for  $1 \leq k < \infty$ .

**Theorem 3.1.** Suppose that  $A = (a_{mnij})$  be an arbitrary four dimensional infinite matrix. Then, the following statements hold:

(a)  $A = (a_{mnij}) \in (|\bar{N}_{p,q}|_1, \mathcal{M}_u)$  if and only if

$$A_{mn} \in (|\bar{N}_{p,q}|_1)^{\beta(bp)} \quad (3.1)$$

and

$$\sup_{m,n,i,j \in \mathbb{N}} \left| \Delta_{11}^{(i,j)} \left( \frac{a_{mnij}}{P_{i-1}Q_{j-1}} \right) \left( \frac{P_i Q_j}{p_i q_j} \right) P_{i-1} Q_{j-1} \right| < \infty. \quad (3.2)$$

(b) Let  $1 < k < \infty$ . Then,  $A = (a_{mnij}) \in (|\bar{N}_{p,q}|_k, \mathcal{M}_u)$  if and only if

$$A_{mn} \in (|\bar{N}_{p,q}|_k)^{\beta(bp)} \quad (3.3)$$

and

$$\sup_{m,n \in \mathbb{N}} \sum_{i,j} \left| \Delta_{11}^{(i,j)} \left( \frac{a_{mnij}}{P_{i-1}Q_{j-1}} \right) \left( \frac{P_i Q_j}{p_i q_j} \right)^{1/k} P_{i-1} Q_{j-1} \right|^{k'} < \infty. \quad (3.4)$$

**Proof.** Part (a) can be proved using Lemma 2.2 (a) in a manner similar to that used in the proof of part (b) of Theorem 3.1. To avoid repeating similar statements, we prove for  $1 < k < \infty$ .

(b) Let  $1 < k < \infty$  and  $x = (x_{ij}) \in |\bar{N}_{p,q}|_k$ . Then, from Theorem 2.1 there exists a double sequence  $y = (y_{mn}) \in \mathcal{L}_k$  via  $x$  by (2.2). Then, using the equalities (2.3 – 2.6), for  $(s, t)$ th rectangular partial sum of the series  $\sum_{i,j} a_{mnij} x_{ij}$ , we obtain that

$$(Ax)_{mn}^{[s,t]} = \sum_{i,j}^{s,t} a_{mnij} x_{ij} \quad (3.5)$$

$$= a_{mn00} y_{00} + a_{mns0} y_{s0} \left( \frac{P_s}{p_s} \right)^{1/k} + a_{mn0t} y_{0t} \left( \frac{Q_t}{q_t} \right)^{1/k}$$

$$\begin{aligned}
 & + \sum_{i=1}^{s-1} y_{i0} P_{i-1} \left( \frac{P_i}{p_i} \right)^{1/k} \Delta_{10}^{(ij)} \left( \frac{a_{mni0}}{P_{i-1}} \right) \\
 & + \sum_{j=1}^{t-1} y_{0j} Q_{j-1} \left( \frac{Q_j}{q_j} \right)^{1/k} \Delta_{01}^{(ij)} \left( \frac{a_{mn0j}}{Q_{j-1}} \right)
 \end{aligned}$$

$$+ \sum_{i,j=1}^{s-1,t-1} \Delta_{11}^{(ij)} \left( \frac{a_{mnij}}{P_{i-1}Q_{j-1}} \right) y_{ij} \left( \frac{P_i Q_j}{p_i q_j} \right)^{1/k} P_{i-1} Q_{j-1}$$

$$+ \sum_{i=1}^{s-1} \Delta_{10}^{(ij)} \left( \frac{a_{mnit}}{P_{i-1}Q_{t-1}} \right) y_{it} \left( \frac{P_i Q_t}{p_i q_t} \right)^{1/k} P_{i-1} Q_{t-1}$$

$$+ \sum_{j=1}^{t-1} \Delta_{01}^{(ij)} \left( \frac{a_{mnsj}}{P_{s-1}Q_{j-1}} \right) y_{sj} \left( \frac{P_s Q_j}{p_s q_j} \right)^{1/k} P_{s-1} Q_{j-1}$$

$$+ a_{mnst} y_{st} \left( \frac{P_s Q_t}{p_s q_t} \right)^{1/k}$$

$$= \sum_{i,j}^{s,t} g_{stij}^{mn} y_{ij} = (G_{mn} y)_{[s,t]}$$

for every  $t, s, m, n \in \mathbb{N}$ , where the four dimensional matrix  $G_{mn} = (g_{stij}^{mn})$  is defined by



$$g_{stij}^{mn} = \begin{cases} a_{mn00}, & s = t = 0, \\ a_{mns0} \left( \frac{p_s}{p_s} \right)^{1/k}, & t = 0 \text{ and } i = s, \\ a_{mn0t} \left( \frac{q_t}{q_t} \right)^{1/k}, & s = 0 \text{ and } j = t, \\ P_{i-1} \left( \frac{p_i}{p_i} \right)^{1/k} \Delta_{10}^{(ij)} \left( \frac{a_{mni0}}{P_{i-1}} \right), & t = 0 \text{ and } 1 \leq i \leq s-1, \\ Q_{j-1} \left( \frac{q_j}{q_j} \right)^{1/k} \Delta_{01}^{(ij)} \left( \frac{a_{mn0j}}{Q_{j-1}} \right), & s = 0 \text{ and } 1 \leq j \leq t-1, \\ \Delta_{11}^{(ij)} \left( \frac{a_{mnij}}{P_{i-1}Q_{j-1}} \right) \left( \frac{P_iQ_j}{p_iq_j} \right)^{1/k} P_{i-1}Q_{j-1}, & 1 \leq i \leq s-1 \text{ and } 1 \leq j \leq t-1, \\ \Delta_{10}^{(ij)} \left( \frac{a_{mnit}}{P_{i-1}} \right) \left( \frac{P_iQ_t}{p_iq_t} \right)^{1/k} P_{i-1}, & 1 \leq i \leq s-1 \text{ and } j = t, \\ \Delta_{01}^{(ij)} \left( \frac{a_{mnsj}}{Q_{j-1}} \right) \left( \frac{P_sQ_j}{p_sq_j} \right)^{1/k} Q_{j-1}, & i = s \text{ and } 1 \leq j \leq t-1, \\ a_{mnst} \left( \frac{p_sq_t}{p_sq_t} \right)^{1/k}, & i = s \text{ and } j = t \\ 0, & \text{otherwise} \end{cases}$$

for every  $s, t, i, j \in \mathbb{N}$ . Then, from (3.5), we have

$$(Ax)_{mn}^{[s,t]} = (G_{mn}\mathcal{Y})_{[s,t]}. \quad (3.6)$$

Therefore, it follows from (3.6) that the  $bp$ -convergence of  $(Ax)_{mn}^{[s,t]}$  and the statement  $G_{mn} \in (\mathcal{L}_k, \mathcal{C}_{bp})$  are equivalent for all  $x \in |\bar{N}_{p,q}|_k$  and  $m, n \in \mathbb{N}$ . Hence, the condition (3.3) is satisfied for each fixed  $m, n \in \mathbb{N}$ , that is,  $A_{mn} \in (|\bar{N}_{p,q}|_k)^{\beta(bp)}$  for each fixed  $m, n \in \mathbb{N}$  and  $1 < k < \infty$ .

If we take  $bp$ -limit in the terms of the matrix  $G_{mn} = (g_{stij}^{mn})$  while  $s, t \rightarrow \infty$ , we obtain that

$$bp - \lim_{s,t \rightarrow \infty} g_{stij}^{mn} = \left( \frac{P_iQ_j}{p_iq_j} \right)^{1/k} P_{i-1}Q_{j-1} \Delta_{11}^{(i,j)} \left( \frac{a_{mnij}}{P_{i-1}Q_{j-1}} \right). \quad (3.7)$$

With the relation (3.7), we can define the four dimensional matrix  $G = (g_{mnij})$  as

$$g_{mnij} = \left( \frac{P_iQ_j}{p_iq_j} \right)^{1/k} P_{i-1}Q_{j-1} \Delta_{11}^{(i,j)} \left( \frac{a_{mnij}}{P_{i-1}Q_{j-1}} \right).$$

In this situation, we deduce from the equations (3.6) and (3.7) that

$$bp - \lim_{s,t \rightarrow \infty} (Ax)_{mn}^{[s,t]} = bp - \lim (Gy)_{mn}. \quad (3.8)$$

Thus, one can write that  $A = (a_{mnij}) \in (|\bar{N}_{p,q}|_k, \mathcal{M}_u)$  if and only if  $G \in (\mathcal{L}_k, \mathcal{M}_u)$ , by considering the relation (3.8).

Therefore, using Lemma 2.2 (b), we calculate that

$$\sup_{m,n \in \mathbb{N}} \sum_{i,j} \left| \left( \frac{P_iQ_j}{p_iq_j} \right)^{1/k} P_{i-1}Q_{j-1} \Delta_{11}^{(i,j)} \left( \frac{a_{mnij}}{P_{i-1}Q_{j-1}} \right) \right|^{k'} < \infty,$$

which gives the condition (3.4).

So, we conclude that  $A = (a_{mnij}) \in (|\bar{N}_{p,q}|_k, \mathcal{M}_u)$  if and only if the conditions (3.3) and (3.4) are satisfied.

This step completes the proof.

**Theorem 3.2.** Suppose that  $A = (a_{mnij})$  be an arbitrary four dimensional infinite matrix. In that case, the following statements hold:

(a)  $A = (a_{mnij}) \in (|\bar{N}_{p,q}|_1, \mathcal{C}_{bp})$  if and only if (3.1), (3.2) are satisfied, and there exists  $(\alpha_{ij}^{(1)}) \in \Omega$  such that

$$bp - \lim_{m,n \rightarrow \infty} \left( \frac{P_iQ_j}{p_iq_j} \right) P_{i-1}Q_{j-1} \Delta_{11}^{(i,j)} \left( \frac{a_{mnij}}{P_{i-1}Q_{j-1}} \right) = \alpha_{ij}^{(1)}.$$

(b) Let  $1 < k < \infty$ . Then,  $A = (a_{mnij}) \in (|\bar{N}_{p,q}|_k, \mathcal{C}_{bp})$  if and only if (3.3), (3.4) are satisfied, and there exists  $(\alpha_{ij}^{(k)}) \in \Omega$  such that

$$bp - \lim_{m,n \rightarrow \infty} \left( \frac{P_iQ_j}{p_iq_j} \right)^{1/k} P_{i-1}Q_{j-1} \Delta_{11}^{(i,j)} \left( \frac{a_{mnij}}{P_{i-1}Q_{j-1}} \right) = \alpha_{ij}^{(k)}.$$

**Proof.** This theorem is easily proved by proceeding as in the proof of Theorem 3.1 by using parts (d) and (e) of Lemma 2.2.

**Theorem 3.3.** Suppose that  $A = (a_{mni j})$  be an arbitrary four dimensional infinite matrix. Then,  $A \in \left( |\bar{N}_{p,q}|_1, \mathcal{L}_k \right)$  if and only if (3.1) and

$$\sup_{i,j \in \mathbb{N}} \sum_{m,n} \left| \frac{P_i Q_j}{p_i q_j} P_{i-1} Q_{j-1} \Delta_{11}^{(i,j)} \left( \frac{a_{mni j}}{P_{i-1} Q_{j-1}} \right) \right|^k < \infty$$

holds for  $1 \leq k < \infty$ .

**Proof.** This theorem is easily proved by proceeding as in the proof of Theorem 3.1 by using part (c) of Lemma 2.2.

### Acknowledgement

We would like to thank the anonymous reviewers and the editor for their very helpful comments and valuable suggestions.

### Author's Contributions

**Feride Çalışır:** Drafted and wrote the manuscript, performed the experiment and result analysis.

**Canan Hazar Güleç:** Assisted in analytical analysis on the structure, supervised the experiment's progress, result interpretation and helped in manuscript preparation.

### Ethics

There are no ethical issues after the publication of this manuscript.

### References

- [1]. Demiriz, S., Erdem, S., 2024. Mersenne matrix operator and its application in p-summable sequence space. *Communications in Advanced Mathematical Sciences*; 7(1): 42-55.
- [2]. Devletli U., Kara, M.I., 2023. New Banach sequence spaces defined by Jordan totient function. *Communications in Advanced Mathematical Sciences*; 6(4): 211-225.
- [3]. Ellidokuzoğlu, H.B., Demiriz, S., Köseoğlu, A., 2018. On the paranormed binomial sequence spaces. *Universal Journal of Mathematics and Applications*; 1(3): 137-147.
- [4]. Hazar Güleç, G.C., 2019. Characterization of some classes of compact and matrix operators on the sequence spaces of Cesàro means. *Operators and Matrices*; 13(3): 809-822.
- [5]. Hazar Güleç, G.C., 2020. Compact matrix operators on absolute Cesàro spaces. *Numerical Functional Analysis and Optimization*; 41(1): 1-15.
- [6]. Hazar Güleç, G.C., Sarıgöl, M.A., 2020. Matrix mappings and norms on the absolute Cesàro and weighted spaces. *Quaestiones Mathematicae*; 43(1): 117-130.
- [7]. İlkan M., Bayrakdar, M.A., 2021. A study on matrix domain of Riesz-Euler totient matrix in the space of p-absolutely summable sequences. *Communications in Advanced Mathematical Sciences*; 4(1): 14-25.
- [8]. Polat, H., 2018. Some new Cauchy sequence spaces, *Universal Journal of Mathematics and Applications*; 1(4): 267-272.
- [9]. Sezer, S.A., Çanak, İ., 2023. On the convergence of weighted mean summable improper integrals over  $R \geq 0$ . *The Journal of Analysis*; 31(2): 1029-1039.
- [10]. Sezer, S.A., Çanak, İ., 2023. Tauberian theorems concerning weighted mean summable integrals. *Periodica Mathematica Hungarica*; 87: 315-323.
- [11]. Önder, Z., Savaş, E., Çanak, İ., 2023. On the weighted generator of double sequences and its Tauberian conditions. *Advances in Operator Theory*; 8(3): 38.
- [12]. Başar, F., Savaşçı, M.Y., Double Sequence Spaces and Four-Dimensional Matrices (1st ed.). Chapman and Hall/CRC, 2022.
- [13]. Bodur, O., Güleç, C.H., 2024. Characterizations of some new classes of four-dimensional matrices on the double series spaces of first order Cesàro means. *Mathematical Sciences and Applications E-Notes*; 12(4): 196-206.
- [14]. Ceylan, A.I., Güleç, C.H., 2024. A new double series space derived by factorable matrix and four-dimensional matrix transformations. *AIMS Mathematics*; 9(11): 30922-30938.
- [15]. Sarıgöl, M.A., 2023. Four dimensional matrix mappings on double summable spaces. *Filomat*; 37: 1277-1290.
- [16]. Sarıgöl, M. A., 2023. Four dimensional matrix mappings and applications. *Kuwait Journal of Science*; 50(2A): 1-12.
- [17]. Bromwich, T. J., An Introduction to the Theory of Infinite Series; Macmillan, New York, 1965.
- [18]. Zeltser, M., 2022. On conservative matrix methods for double sequence spaces. *Acta Mathematica Hungarica*; 95(3): 225-242.
- [19]. Hardy, G. H., 1917. On the convergence of certain multiple series. *Proceedings of the Cambridge Philosophical Society*; 19: 86-95.
- [20]. Móricz, F., 1991. Extensions of the spaces  $c$  and  $c_0$  from single to double sequences. *Acta Mathematica Hungarica*; 57, (1-2): 129-136.
- [21]. Móricz, F., Rhoades, B.E., 1988. Almost convergence of double sequences and strong regularity of summability matrices. *Mathematical Proceedings of the Cambridge Philosophical Society*; 104 (2): 283-294.
- [22]. Mursaleen, M., 2004. Almost strongly regular matrices and a core theorem for double sequences. *Journal of Mathematical Analysis and Applications*; 293(2): 523-531.
- [23]. Mursaleen, M., Başar, F., 2014. Domain of Cesàro mean of order one in some spaces of double sequences. *Studia Scientiarum Mathematicarum Hungarica*; 51: 335-356.
- [24]. Demiriz, S., Duyar, O., 2015. Domain of difference matrix of order one in some spaces of double sequences. *Gulf Journal of Mathematics*; 3(3): 85-100.
- [25]. Demiriz, S., Erdem, S., 2020. Domain of Euler-totient matrix operator in the space  $\mathcal{L}_p$ . *Korean Journal of Mathematics*; 28(2): 361-378.
- [26]. Pringsheim, A., 1900. Zur theorie der zweifach unendlichen Zahlenfolgen. *Mathematische Annalen*; 53: 289-321.
- [27]. Boos, J., Classical and Modern Methods in Summability; Oxford University Press, New York, 2000.
- [28]. Başar, F., Sever, Y., 2009. The space  $\mathcal{L}_k$  of double sequences. *Mathematical Journal of Okayama University*; 51: 149-157.

- [29]. Yeşilkayagil, M., Başar, F., 2018. Domain of Riesz mean in some spaces of double sequences. *Indagationes Mathematicae*; 29(3): 1009-1029.
- [30]. Alotaibi, A.M., Çakan, C., 2012. The Riesz convergence and Riesz core of double sequences. *Journal of Inequalities and Applications*; 2012, 56.
- [31]. Sarıgöl, M.A., 2021. On equivalence of absolute double weighted mean methods. *Quaestiones Mathematicae*; 44(6): 755-764.
- [32]. Altay, B., Başar, F., 2006. Some paranormed Riesz sequence spaces of non-absolute type. *Southeast Asian Bulletin of Mathematics*; 30(4): 591-608.
- [33]. Başarır, M., Kara, E.E., 2011. On compact operators on the Riesz Bm-difference sequence space. *Iranian Journal of Science and Technology (Sciences)*; 35(4): 279-285.
- [34]. Sarıgöl, M.A., 2016. Norms and compactness of operators on absolute weighted mean summable series. *Kuwait Journal of Science*; 43(4): 68-74.
- [35]. Yeşilkayagil, M., Başar, F., 2017. On the domain of Riesz mean in the space  $\mathcal{L}_k^*$ . *Filomat*; 31(4): 925-940.